

# **Measurements of Reynolds Stress and its Contribution to the Momentum Balance in the HSX Stellarator**

by

Robert S. Wilcox

A dissertation submitted in partial fulfillment of  
the requirements for the degree of

Doctor of Philosophy  
(Electrical Engineering)

at the

University of Wisconsin–Madison

2014

Date of final oral examination: 12/2/2014

The dissertation is approved by the following members of the Final Oral Committee:

David T. Anderson, Professor, Electrical Engineering

Amy E. Wendt, Professor, Electrical Engineering

Chris C. Hegna, Professor, Engineering Physics

Paul W. Terry, Professor, Physics

Joseph N. Talmadge, Associate Scientist, Electrical Engineering

© Copyright by Robert S. Wilcox 2014

All Rights Reserved

## ABSTRACT

In a magnetic configuration that has been sufficiently optimized for quasi-symmetry, the neoclassical transport and viscosity can be small enough that other terms can compete in the momentum balance to determine the plasma rotation and radial electric field. The Reynolds stress generated by plasma turbulence is identified as the most likely candidate for non-neoclassical flow drive in the HSX stellarator. Using multi-tipped Langmuir probes in the edge of HSX in the quasi-helically symmetric (QHS) configuration, the radial electric field and parallel flows are found to deviate from the values calculated by the neoclassical transport code PENTA using the ambipolarity constraint in the absence of externally injected momentum. The local Reynolds stress in the parallel and perpendicular directions on a surface is also measured using the fluctuating components of floating potential and ion saturation current measurements. Although plasma turbulence enters the momentum balance as the flux surface averaged radial gradient of the Reynolds stress, the locally measured quantity implies a significant contribution to the momentum balance. If extrapolated to a flux surface average, this locally measured Reynolds stress gradient is calculated to result in a flow drive many times larger than the observed flows. Probe measurements made at two locations on the device in regions with different magnetic geometry indicate very different, but consistently large Reynolds stress drive terms. The large variation of the local Reynolds stress on a flux surface suggests that a small number of measurement locations is insufficient to properly sample the flux surface averaged quantity. Contrary to expectations, measurements in configurations with the quasi-symmetry intentionally degraded deviate more from the neoclassically calculated velocity profiles than those in the QHS configuration. Measured density fluctuations and the Reynolds stress are reduced in these cases, indicating that additional terms may be important in the momentum balance.

For my parents, Betty and Steven Wilcox



## ACKNOWLEDGMENTS

This work could not have been done without the help and support of many people, both within and beyond the HSX group. First and foremost, I would like to thank my advisor, David Anderson, for the guidance and support throughout the course of my studies, starting many years ago when he gave an inspiring lecture in my undergraduate electromagnetics course about magnetic confinement and fusion energy. His unique combination of scientific aptitude, real-world knowledge and enthusiasm are invaluable assets to his students and the university, as well as to the world fusion community. Discussions with Chris Hegna and Paul Terry were vitally important to gaining a deeper understanding of the transport mechanisms at play in this work. In addition to Professors Anderson, Terry and Hegna, I would like to thank Professor Amy Wendt and Joe Talmadge for serving on my thesis committee.

Joe Talmadge provided scientific guidance through the course of this work, and most often asks the probing questions that need to be investigated when linking experiments to theory. Simon Anderson painstakingly maintained many of the systems on HSX and aided greatly in day-to-day operations and on-the-spot data analysis in order to make adjustments to experiments during run days. Konstantin Likin, Chuanbao Deng, Santhosh Kumar, Kan Zhai and Paul Probert all provided crucially important expertise into the diagnostic systems of HSX that they helped design and build, and they kept everything up and running as experiments were performed. Mike Frankowski passed away during my time at HSX, but I remember him fondly for the conversations we had and the help that he provided in the design and construction of the Langmuir probe system. He is dearly missed.

During the course of my research, I traveled to Madrid and worked alongside Carlos Hidalgo, Boudewijn van Milligen and Arturo Alonso, and published a paper based in part on this collaboration. I learned much from this exchange and I am very appreciative of their guidance and hospitality.

My time at HSX was made much more enjoyable by the company of my fellow graduate students. Jeremy Lore passed his knowledge of Thomson scattering to me before leaving, and his research and career advice were always helpful. Alexis Briesemeister's CHERS measurements were an important piece of evidence in support of my work, and she always provided much-needed enthusiasm around the office. Chris Clark has an incredibly wide range of knowledge, and observing his thorough, systematic approach to problems has helped me immensely as a scientist. John Schmitt always came to work with an enviable combination of an excellent work ethic and positive attitude. I benefited greatly from Enrico Chlechowicz's unique German perspective on whatever topic was at hand, whether it was physics, politics, or food and drink. My time at HSX overlapped significantly with Gavin Weir and Carson Cook. We shared many good times and fruitful discussions at conferences and around the office. Laurie Stephey perfectly embodies the hopeful optimism that brings most of us into the field of fusion, and it is encouraging to know that there are people like her in the world. There have been many nights after work that I enjoyed drinks and "talking shop" at the Library and elsewhere with Adrian Akerson, Jason Smoniewski, Carlos Ruiz, and Tom Dobbins, as well.

I would also like to thank my parents, Steve and Betty, who have been very supportive of my pursuits, as well as my sisters, Annie and Julie. My family has always provided a solid grounding and a support structure that I found more necessary than ever as I worked through graduate school. My girlfriend Peggy has been patient with my long hours in the lab, and she has made the process of finishing this dissertation much more tolerable than it might have otherwise been.

Finally, I would like to acknowledge the financial support of the United States Department of Energy, who provided the funding over the course of this work.

# TABLE OF CONTENTS

	Page
<b>ABSTRACT</b> . . . . .	i
<b>ACKNOWLEDGMENTS</b> . . . . .	iii
<b>LIST OF FIGURES</b> . . . . .	viii
<b>1 Introduction</b> . . . . .	1
1.1 Need for fusion energy . . . . .	1
1.2 Magnetic confinement of plasma . . . . .	5
1.2.1 Tokamaks . . . . .	6
1.2.2 Conventional stellarators . . . . .	8
1.2.3 Optimized stellarators . . . . .	11
1.3 HSX . . . . .	14
1.3.1 Quasi-helical symmetry and predicted effects . . . . .	15
<b>2 Momentum balance and intrinsic flows</b> . . . . .	23
2.1 Rotation and $E_r$ determination in the absence of external momentum sources . . . . .	26
2.1.1 $E_r$ determination in unoptimized stellarators . . . . .	26
2.2 Neoclassical transport and radial electric field calculations . . . . .	28
2.2.1 VMEC . . . . .	29
2.2.2 DKES . . . . .	30
2.2.3 PENTA . . . . .	36
2.3 Momentum balance . . . . .	38
2.3.1 Reynolds stress . . . . .	40
2.3.2 Maxwell/kinetic stress . . . . .	43
2.3.3 Ion orbit loss . . . . .	45
2.3.4 Charge exchange drag force . . . . .	46
2.3.5 ECRH-driven electron flux . . . . .	48
2.3.6 Turbulent parallel flow acceleration . . . . .	50
2.4 Rotation in configurations approaching quasi-symmetry . . . . .	50
2.4.1 Magnetic configurations in HSX . . . . .	53

	Page
2.4.2 Effective ripple . . . . .	55
2.4.3 Observations of intrinsic rotation in tokamaks . . . . .	58
2.5 Predictions of limits of non-neoclassical $E_r$ determination in HSX . . . . .	60
2.5.1 Helander and Simakov estimates . . . . .	60
2.5.2 Calculations of closeness to quasi-symmetry by Calvo et. al. . . . .	63
2.5.3 Comparison of non-ambipolar neoclassical particle flux to total experi- mental particle flux . . . . .	67
2.6 Previous comparisons of measured flows in HSX to neoclassical calculations . . .	69
2.6.1 Flow damping . . . . .	69
2.6.2 CHERS intrinsic flow measurements . . . . .	70
2.6.3 Probe floating potential . . . . .	72
2.7 Measurements of Reynolds stress in other devices . . . . .	73
<b>3 Experimental setup . . . . .</b>	<b>85</b>
3.1 Langmuir probes . . . . .	85
3.1.1 Floating potential . . . . .	86
3.1.2 Ion saturation current . . . . .	91
3.1.3 Mach probes . . . . .	92
3.2 Reynolds stress probe design . . . . .	94
3.3 Probe positioning and magnetic geometry . . . . .	97
3.3.1 Probe alignment to the magnetic field . . . . .	99
3.3.2 Radial positioning of probes . . . . .	100
3.3.3 Magnetic geometry at probe locations . . . . .	103
3.4 Probe perturbation tests . . . . .	107
<b>4 Measurements of <math>E_r</math> and <math>V_{  }</math> and comparisons with neoclassical modeling . . . . .</b>	<b>113</b>
4.1 Neoclassical ambipolarity calculations . . . . .	113
4.1.1 Inputs to PENTA . . . . .	114
4.1.2 Calculated neoclassical particle fluxes and ambipolar solution for $E_r$ . . . .	116
4.1.3 Sensitivity studies . . . . .	118
4.2 Raw Langmuir probe data and synthesis . . . . .	120
4.3 Radial electric field measurements . . . . .	123
4.3.1 Measurement of $T_e$ from fluctuating signals . . . . .	124
4.3.2 $E_r$ profile and comparison to neoclassical calculations . . . . .	128
4.4 Parallel flow measurements . . . . .	131
4.4.1 Pfirsch-Schlüter component of the parallel ion flow . . . . .	132
4.4.2 Total measured $V_{  }$ profiles and comparison to neoclassical calculations in QHS . . . . .	134

## Appendix

	Page
4.5 $E_r$ and $V_{  }$ measurements in other configurations . . . . .	136
4.5.1 $E_r$ and $V_{  }$ measurements in the Mirror configuration . . . . .	137
4.5.2 $E_r$ and $V_{  }$ measurements in the Flip-1-4 configuration . . . . .	140
<b>5 Measurements of Reynolds stress using Langmuir probes . . . . .</b>	<b>146</b>
5.1 Local Reynolds stress measurements . . . . .	147
5.1.1 Reynolds stress profiles in the QHS configuration . . . . .	149
5.1.2 Time averaging of the Reynolds stress . . . . .	152
5.1.3 Contribution of turbulent particle flux to Reynolds stress . . . . .	154
5.1.4 Potential sources of measurement error . . . . .	156
5.2 Momentum evolution and steady state solution . . . . .	158
5.3 Contribution of Reynolds stress to flows in different configurations . . . . .	162
5.3.1 Expectation of Reynolds stress scaling . . . . .	162
5.3.2 Measured Reynolds stress and calculated resulting flows . . . . .	164
<b>6 Conclusions . . . . .</b>	<b>171</b>
6.1 Summary and discussion of results . . . . .	171
6.1.1 Possible additional sources of momentum . . . . .	173
6.1.2 Implications for other devices . . . . .	174
6.2 Suggestions for future work . . . . .	174
6.2.1 Quantify ECRH-driven electron flux . . . . .	175
6.2.2 Parameter scans, measure flows using <b>CHERS</b> . . . . .	175
6.2.3 Gyrokinetic Reynolds stress simulations . . . . .	176
6.2.4 Add ion heating . . . . .	178
 <b>APPENDICES</b>	
Appendix A: Zonal flows . . . . .	181
Appendix B: Alternative configurations in HSX . . . . .	192

## LIST OF FIGURES

Figure	Page
1.1 Concentration of $\text{CO}_2$ in the earth's atmosphere over time . . . . .	2
1.2 Average annual global temperatures . . . . .	3
1.3 2012 U.S. electrical energy production by source . . . . .	4
1.4 Generic tokamak device . . . . .	6
1.5 The ITER tokamak . . . . .	8
1.6 LHD . . . . .	9
1.7 Particle diffusivity versus collisionality for stellarators and tokamaks . . . . .	10
1.8 $ B $ contours in Boozer coordinates for different magnetic geometries . . . . .	13
1.9 HSX . . . . .	14
1.10 $ B $ along a field line in the edge of HSX ( $r/a=0.8$ ) . . . . .	15
1.11 Colored Poincare plots of magnetic surfaces for several cross sections in HSX . . . . .	16
1.12 A main modular coil and planar auxiliary coil of HSX. . . . .	17
2.1 Plasma temperature and density profiles in DIII-D with and without an H-mode pedestal	25
2.2 Stellarator neoclassical particle fluxes . . . . .	28
2.3 DKES transport coefficients vs $E_r$ . . . . .	31
2.4 $E_r$ in W7-AS from CXRS . . . . .	32
2.5 Calculated and measured $E_r$ in LHD . . . . .	34
2.6 $E_r$ resonance for C and H . . . . .	36

Figure	Page
2.7 $V_{\parallel}$ measured by CHERS in HSX vs DKES and PENTA . . . . .	37
2.8 Flow velocity in the helical direction of symmetry and cross-symmetry direction in HSX as measured by CHERS . . . . .	41
2.9 Tests of the assumption that fluctuations are electrostatic . . . . .	44
2.10 Comparison of ECE signals after ECRH turn-off with and without evidence of a suprathermal electron population . . . . .	49
2.11 Rotational transform profiles for the QHS and Mirror configurations . . . . .	54
2.12 Boozer spectra for the dominant harmonics in the QHS, Flip-1-4 and Mirror configurations . . . . .	55
2.13 Effective ripple in HSX QHS, Flip-1-4 and Mirror configurations compared to other devices . . . . .	56
2.14 Normalized collisionality $\nu^*$ for thermal electrons and ions in the QHS configuration of HSX. . . . .	58
2.15 Comparison of effective ripple in HSX to Helander and Simakov criteria for non-neoclassical rotation . . . . .	62
2.16 $\alpha$ from Calvo et. al. along with the parameters with which it is to be compared . . . .	65
2.17 $\alpha$ in the Mirror configuration. . . . .	66
2.18 Comparison of calculated neoclassical non-ambipolar particle flux to total experimentally measured particle flux in HSX . . . . .	68
2.19 Measured flow damping rates in HSX . . . . .	70
2.20 Measured $E_r$ profile from CHERS in QHS . . . . .	71
2.21 Azimuthal rotation in the CSDX linear device . . . . .	73
3.1 Floating potential circuit for HSX Langmuir probes. . . . .	87
3.2 Calculated contribution of $T_e$ to $V_{fl}$ measurements for probes in HSX. . . . .	89
3.3 Circuit for measuring the ion saturation current in HSX. . . . .	92

Appendix	
Figure	Page
3.4 Pictures of the Reynolds stress probe . . . . .	95
3.5 Top view of HSX with locations of Reynolds stress probes indicated. . . . .	97
3.6 Magnetic surface cross sections at probe insertion locations . . . . .	98
3.7 Poincaré plot of the 12/11 island chain at the location of the high-field side probe. . . .	99
3.8 Radial locations of Reynolds stress probes along the axis of the probe slide from VMEC equilibria . . . . .	101
3.9 Radial profiles of $I_{sat}$ signals at the LFS probe position in (a) the QHS and (b) Mirror configurations. . . . .	102
3.10 Magnetic field strength and normal curvature on a surface in the QHS configuration, with probe locations . . . . .	104
3.11 Magnetic field strength and normal curvature on a surface in the Mirror configuration, with probe locations . . . . .	105
3.12 Magnetic field strength and normal curvature on a surface in the Flip-1-4 configura- tion, with probe locations . . . . .	106
3.13 Low field side probe perturbation test . . . . .	108
3.14 High field side probe perturbation test . . . . .	109
4.1 (a) $T_e$ and (b) $n_e$ profiles from Thomson scattering in QHS plasmas and their fits used as inputs to PENTA. . . . .	114
4.2 Ion temperature measurements from CHERS . . . . .	116
4.3 Neoclassical ion and electron particle fluxes as a function of $E_r$ for calculated by PENTA for HSX experimental parameters in QHS, and the predicted radial $E_r$ profile resulting from these calculations . . . . .	117
4.4 Neoclassical particle fluxes as a function of $E_r$ for Mirror and QHS . . . . .	118
4.5 Approximate limits of the neoclassical ambipolar solutions calculated by PENTA given conservative estimates of experimental measurement uncertainties. . . . .	119



Appendix	
Figure	Page
4.6 Raw data and averages taken from pins measuring (a) floating potential and (b) ion saturation current. . . . .	121
4.7 Auto-power spectrum of fluctuations from a probe pin measuring the floating potential.	122
4.8 Auto-power spectra of fluctuations from probe pins measuring (a) the ion saturation current and (b) the floating potential, with and without an applied digital filter at 250 kHz. . . . .	123
4.9 Electron temperature profiles estimated from $V_{fl}$ and $I_{sat}$ fluctuations using the Reynolds stress probes in the QHS configuration . . . . .	126
4.10 Electron temperature profiles estimated from $V_{fl}$ and $I_{sat}$ fluctuations using the Reynolds stress probes in the Mirror configuration . . . . .	128
4.11 Potential profile and resulting $E_r$ measured by the LFS probe in the QHS configuration	129
4.12 Potential profile measured by the perturbative HFS probe in the QHS configuration. . .	131
4.13 Parallel ion flow divided by the local magnetic field strength ( $B \approx 1$ T) as a function of $E_r$ for a selection of radial locations in the edge of the QHS configuration, calculated by PENTA. . . . .	133
4.14 Contributions of Pfirsch-Schlüter flows to $V_{  i}$ in the QHS configuration . . . . .	134
4.15 Parallel ion flow in the QHS configuration measured by the (a) LFS and (b) HFS mach probes, compared with neoclassical predictions from PENTA. . . . .	135
4.16 Potential profile and resulting $E_r$ measured by the LFS probe in the Mirror configuration	137
4.17 Parallel ion flow divided by the local magnetic field strength ( $B \approx 1$ T) as a function of $E_r$ for a selection of radial locations in the edge of the Mirror configuration, calculated by PENTA. . . . .	138
4.18 Parallel ion flow in the Mirror configuration measured by the (a) LFS and (b) HFS mach probes, compared with neoclassical predictions from PENTA. . . . .	139
4.19 Potential profile and resulting $E_r$ measured by the LFS probe in the Flip-1-4 configuration . . . . .	141

Appendix	
Figure	Page
4.20	Parallel ion flow in the Flip-1-4 configuration measured by the (a) LFS and (b) HFS mach probes, compared with neoclassical predictions from PENTA. . . . . 142
5.1	Probability density functions of radial and bi-normal velocity fluctuations from the LFS probe . . . . . 149
5.2	Radial profiles of (a) $\langle \tilde{v}_r \tilde{v}_\theta \rangle$ and (b) $\langle \tilde{v}_r \tilde{v}_\parallel \rangle$ measured by the LFS probe in the QHS configuration, along with polynomial fits. . . . . 150
5.3	Radial profiles of (a) $\langle \tilde{v}_r \tilde{v}_\theta \rangle$ and (b) $\langle \tilde{v}_r \tilde{v}_\parallel \rangle$ measured by the HFS probe in the QHS configuration, along with polynomial fits. . . . . 151
5.4	Radial profiles of $\langle \tilde{v}_r \tilde{v}_\theta \rangle$ measured by the LFS probe in the QHS configuration and linear fits using a range of time windows for mean subtraction. . . . . 153
5.5	Gradients of the radial Reynolds stress profiles in the QHS configuration using a range of time windows for mean subtraction, for (a) $\langle \tilde{v}_r \tilde{v}_\theta \rangle$ and (b) $\langle \tilde{v}_r \tilde{v}_\parallel \rangle$ profiles from the LFS probe and (c) $\langle \tilde{v}_r \tilde{v}_\theta \rangle$ and (d) $\langle \tilde{v}_r \tilde{v}_\parallel \rangle$ profiles from the HFS probe. . . . . 154
5.6	Neutral particle density for viscosity calculations, as modeled by DEGAS . . . . . 159
5.7	Momentum evolution in the QHS configuration near $r/a=0.9$ resulting from the bi-normal component of the Reynolds stress measured by the LFS probe. . . . . 160
5.8	Parallel flow inferred from the saturated evolution of Equation 5.5 in the QHS configuration using both the parallel and bi-normal components of the Reynolds stress drive measured by the (a) LFS and (b) HFS probes. . . . . 161
5.9	Normalized density fluctuation profiles in the QHS, Flip-1-4 and Mirror configurations 163
5.10	Radial profiles of (a) $\langle \tilde{v}_r \tilde{v}_\theta \rangle$ and (b) $\langle \tilde{v}_r \tilde{v}_\parallel \rangle$ measured by the LFS probe in the Mirror configuration, along with polynomial fits. . . . . 165
5.11	Radial profiles of (a) $\langle \tilde{v}_r \tilde{v}_\theta \rangle$ and (b) $\langle \tilde{v}_r \tilde{v}_\parallel \rangle$ measured by the HFS probe in the Mirror configuration, along with polynomial fits. . . . . 165
5.12	Saturated parallel flows resulting from Reynolds stress profiles in the Mirror configuration using the (a) LFS and (b) HFS probes. . . . . 166
5.13	Radial profiles of (a) $\langle \tilde{v}_r \tilde{v}_\theta \rangle$ and (b) $\langle \tilde{v}_r \tilde{v}_\parallel \rangle$ measured by the LFS probe in the Flip-1-4 configuration, along with polynomial fits. . . . . 166

## Appendix

Figure	Page
5.14 Radial profiles of (a) $\langle \tilde{v}_r \tilde{v}_\theta \rangle$ and (b) $\langle \tilde{v}_r \tilde{v}_{  } \rangle$ measured by the HFS probe in the Flip-1-4 configuration, along with polynomial fits. . . . .	167
5.15 Saturated parallel flows resulting from Reynolds stress profiles in the Flip-1-4 configuration using the (a) LFS and (b) HFS probes. . . . .	167
A.1 Auto-bicoherence of $E_\theta$ fluctuations at several radial locations in QHS, with and without an applied bias . . . . .	184
A.2 Auto-bicoherence of fluctuations for discharges in (a) $E_\theta$ signals in TJ-II and (b) $I_{\text{sat}}$ signals in CCT . . . . .	185
A.3 Long-range correlations of low-frequency fluctuations in QHS and FL14 . . . . .	186
A.4 GAM oscillation frequency and damping rate in HSX using the Watari single helicity model . . . . .	189
B.1 Effective ripple for several configurations in HSX . . . . .	194
B.2 Poincare plots for 2.5% n=1 configuration. . . . .	196
B.3 Poincare plots for 11% n=2 configuration. . . . .	197
B.4 Effective ripple for non-stellarator symmetric configurations. . . . .	197

# Chapter 1

## Introduction

This chapter begins with a motivation for the research of magnetic confinement fusion energy in Section 1.1 and an overview of the physics behind magnetic confinement of plasmas. Following that, a brief discussion of the difference between tokamaks, unoptimized stellarators and various forms of stellarator optimization is given in Section 1.2. Finally, the HSX stellarator is introduced in Section 1.3, which is the device in which the experiments documented in later chapters have been performed.

### 1.1 Need for fusion energy

Global climate change has emerged as one of the greatest challenges to economic and political stability in the coming century. The scientific consensus is that the release of greenhouse gases into the atmosphere by human activity is responsible for rapid global climate change and must be addressed quickly to avoid the worst of the consequences [1]. Specifically, the concentration of carbon dioxide in the atmosphere has increased dramatically since the industrial revolution with the wide-scale combustion of fossil fuels as an energy source [2]. Figure 1.1(a) shows the concentration of atmospheric CO<sub>2</sub> measured at the Mauna Loa Observatory in Hawaii since 1958 [3]. Figure 1.1(b) then plots the same data alongside historical CO<sub>2</sub> concentrations taken from bubbles in Antarctic ice core samples [4]. It is clear from the scale and speed of change in the historical

data that human activity is now dominating the natural climate cycles that drove atmospheric CO<sub>2</sub> concentrations for hundreds of thousands of years.

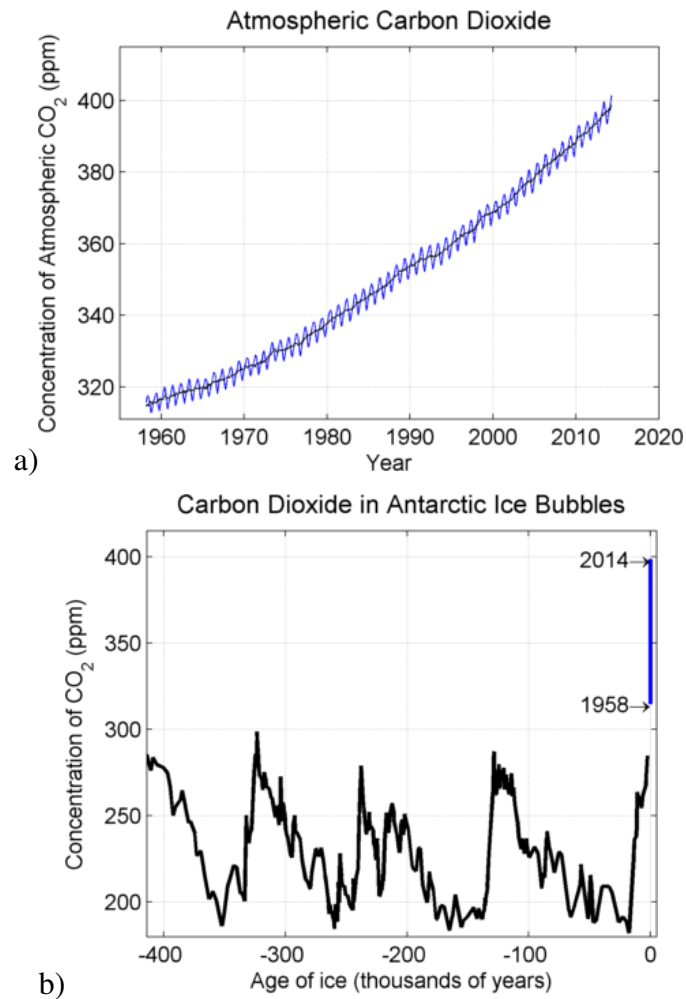


Figure 1.1 Concentration of CO<sub>2</sub> in the earth's atmosphere over time, (a) measured at Mauna Loa Observatory, Hawaii [3]. The seasonally adjusted curve (black) is plotted over monthly average measurements (blue). (b) CO<sub>2</sub> concentration from Antarctic ice bubble samples [4] plotted in black along with the contemporary measurements in blue, for historical perspective.

While other anthropogenic greenhouse gases currently contribute substantially to global temperature increase in the short term (methane is responsible for an estimated 60% of that caused by CO<sub>2</sub> [5]), carbon dioxide is especially destabilizing to the earth's climate in the long term because of its lifetime in the atmosphere. It takes tens to hundreds of thousands of years for CO<sub>2</sub> to be

removed en masse by natural processes once it is released into the atmosphere [6], compared to the  $<10$  year atmospheric lifetime of methane, which is broken down by organic processes [7].

Meanwhile, global temperatures have been increasing at an alarming rate, as plotted in Figure 1.2 [8]. This trend has been largely attributed to the increase in greenhouse gas concentration in the atmosphere, and it will continue on the timescale of a few decades, even if no more anthropogenic greenhouse gases are released [9]. If emissions continue their current pace, the consequences for global food and water supplies, among many other things, would be dire.

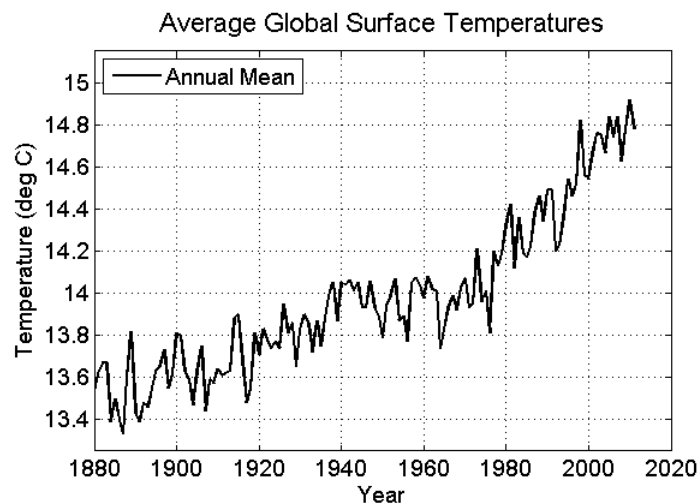


Figure 1.2 Average annual global temperatures, as measured by meteorological stations [8].

Because of these detrimental effects of additional atmospheric  $\text{CO}_2$ , there is a need for energy sources that do not emit  $\text{CO}_2$  as a byproduct. Unfortunately, this will not be a simple or inexpensive task. To demonstrate how much alternative energy production would be needed to replace fossil fuels in our economy, U.S. electricity generation is plotted in Figure 1.3, broken down by source (data from [10]).

Solar energy generation (which includes both solar thermal and photovoltaic) has grown substantially in recent years, but still makes up only a tiny fraction of total US electrical capacity (0.1% in 2012, up from 0.02% in 2009 [10]). While solar and wind energy are attractive solutions that

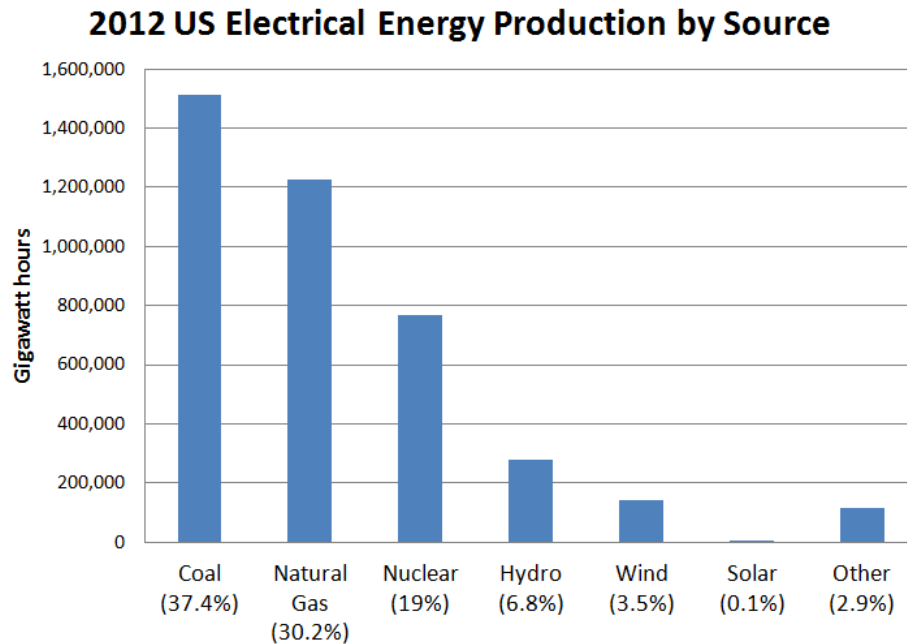


Figure 1.3 2012 U.S. electrical energy production by source (data from [10]).

could be greatly expanded, their low power density and variability with time of day and weather have made them less effective as baseline power sources than coal, natural gas and conventional nuclear fission power plants. Fission power stations are an option, but concerns over safety, waste management and proliferation of nuclear materials make it politically unattractive in many parts of the world. There are also finite reserves of uranium on earth, which would not last for many decades of a fission-based energy economy [11]. This last problem could be mitigated by using thorium, which is much more abundant on earth than uranium-235, to breed uranium-233 [12], although the breeding process has not yet been demonstrated commercially.

One potentially revolutionary technology for the long term is nuclear fusion, which uses abundantly available deuterium and lithium as fuel and produces no harmful byproducts such as greenhouse gases or long-lasting nuclear waste. In a world with growing energy needs, fusion power could be an integral part of the solution.

## 1.2 Magnetic confinement of plasma

In an exothermic nuclear fusion reaction, two light nuclei combine to form one larger one, destroying a small amount of mass and releasing energy in the process. For two elements to fuse, electrons must first be stripped from their nuclei, and the positively charged ions must have enough energy to overcome the electrostatic force and get close enough for the strong nuclear force to take effect. There are two main approaches to this problem. The first, inertial confinement, involves compressing a pellet of fuel long enough for the fusion reactions to cascade and burn through as much of the fuel as possible before blowing apart and releasing all of the energy. The National Ignition Facility at Lawrence Livermore National Lab is the most advanced and ambitious attempt at inertial confinement fusion to date [13]. From an engineering standpoint, this is an incredibly difficult problem due to the required symmetry of the fuel pellet and its compression, the pulsed nature of the energy source and the short timescale over which the energy is released and the inefficiencies and recirculating power involved in the lasers used to compress the pellet. Recent results showed that more fusion energy was produced than energy absorbed by the fuel pellet [14], which was a major milestone for fusion research efforts. However, this would need to be scaled up by many orders of magnitude in terms of incident energy absorption efficiency, fuel burn-up efficiency, laser electrical efficiency and pulse rep rate in order to approach an economically useful power source.

The more common approach to a fusion reactor worldwide (in terms of research expenditures) has been magnetic confinement. With this technique, magnetic fields are used to confine a fully ionized hot plasma in some form of a steady state. Ideally, once the plasma has been heated up to “ignition,” external heating could be turned off and all thermal losses from the plasma would be recovered from heating by the fusion reactions. In this case, the fusion gain (fusion energy output / energy input) could approach infinity, and the plasma would be considered fully “burning.”



While there are unstable, non-steady state magnetic confinement fusion devices, such as Z-pinches and field-reversed configurations, these confinement schemes are not being pursued as vigorously as devices which have the potential to achieve a continuous “burning” reaction.

### 1.2.1 Tokamaks

The most common and advanced of all magnetic confinement devices is the tokamak. A tokamak implements a magnetic confining field in the shape of an axisymmetric torus, with the majority of its field generated using planar external coils. Because  $\nabla \cdot \mathbf{B} = 0$ , however, the magnetic field strength exhibits a  $1/R$  dependence which leads to a  $\nabla B$  drift of individual particles that destroys confinement. To account for this, tokamaks drive a large toroidal current to provide an additional magnetic field component in the “poloidal” direction, which completes the basic confining field and organizes the plasma into a series of nested flux surfaces on which single particle orbits are confined. This current is generally driven predominantly by induction using a central solenoid, although current can also be driven using injected neutral beams or RF waves. A basic schematic design of a tokamak is given in Figure 1.4 [15].

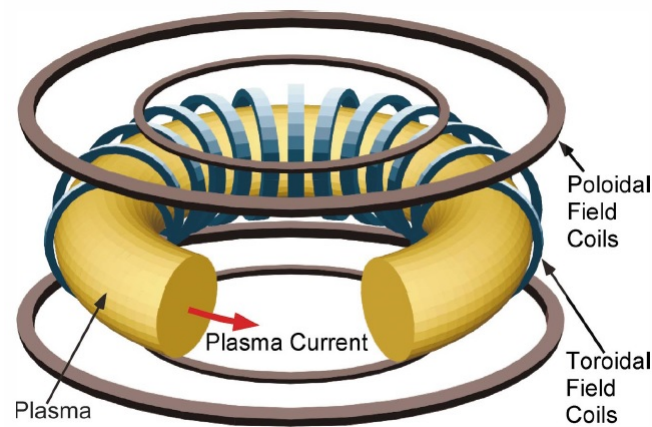


Figure 1.4 Generic tokamak device [15].

The main magnetic field strength in a high aspect ratio tokamak can be described approximately by the expression

$$\frac{|B|}{B_0} \approx 1 - \epsilon \cos \theta, \quad (1.1)$$

where  $\epsilon = r/R_0$  is the local inverse aspect ratio and  $B_0$  is the magnitude of the magnetic field on axis. Both the magnetic field strength and vector components do not change with the toroidal angle, so that ideally, the device can be described as axisymmetric.

The axisymmetry of a tokamak provides several benefits to confinement and to the simplicity of the design. An axisymmetric magnetic configuration is guaranteed to have closed flux surfaces and an equilibrium which can be described using the Grad-Shafranov equation. Particle transport is intrinsically ambipolar, meaning that ion and electron transport is the same regardless of the value of the electric field, and the plasma is free to rotate because there is no neoclassical flow damping in the toroidal direction with perfect axisymmetry. The design is relatively simple because all coils are planar and many of the components can be replicated identically around the device. An axisymmetric divertor as a reactor exhaust solution has the advantage of being continuous around the device and can be located distantly away from the main plasma, where flux expansion may be larger and neutral recycling can be reduced by local pumping [16].

The ITER tokamak is currently under construction in Cadarache, France. It is expected to be the first magnetic fusion device to exceed scientific break-even (fusion power out / heating power in  $> 1$ ), with an estimated 500 MW of fusion power generated using 50 MW of input power [17]. A schematic drawing of ITER is shown in Figure 1.5, including a standard-sized person underneath the device for scale.

However, because of the inductive current drive, ITER will still be a pulsed device, and the path forward to a tokamak with a steady state, non-inductive current drive is unclear. While electron cyclotron current drive or lower hybrid current drive are available as additional current sources,

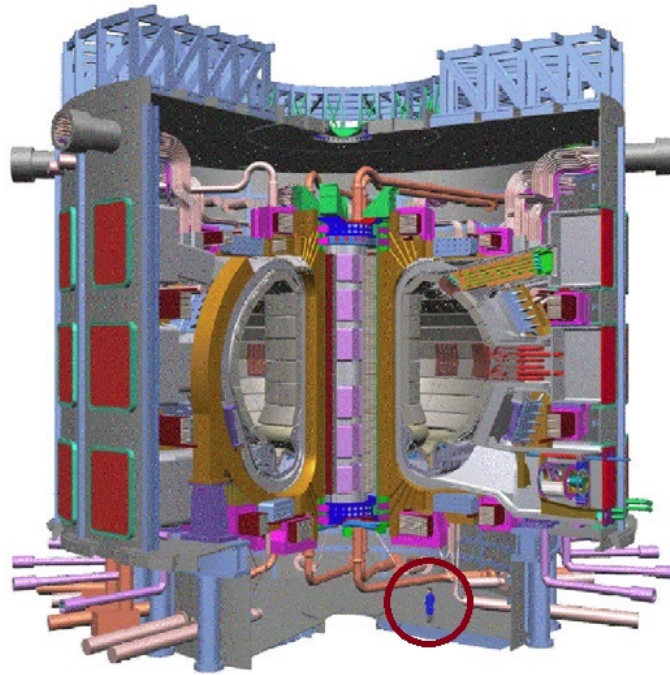


Figure 1.5 The ITER tokamak, with person for scale [17].

their electrical efficiency is poor and recirculating power in a reactor drives its cost up substantially. Current driven instabilities and disruptions also raise the possibility that a tokamak may be problematic for use as a fusion reactor. Although the tokamak is presently the leading candidate for a magnetic confinement device to become a reactor, there is a clear need to explore additional options.

### 1.2.2 Conventional stellarators

Another magnetic confinement scheme which has received a great deal of attention and experimental research is the stellarator. The main advantage of a stellarator is that it removes the current drive requirement of a tokamak and avoids disruptions by producing all (or at least the majority) of the confining field using external coils rather than relying on the plasma current. To

generate closed magnetic surfaces without a driven current, the poloidal component of the confining field must be at least partially provided by external coils and the magnetic configuration must necessarily become three dimensional.

Stellarators use external coils to provide 3-dimensional plasma shaping, often using helical windings, in order to generate the additional field component necessary for confinement rather than driving a plasma current. An example of a conventional stellarator which implements helical windings, LHD, is given in Figure 1.6 [15].

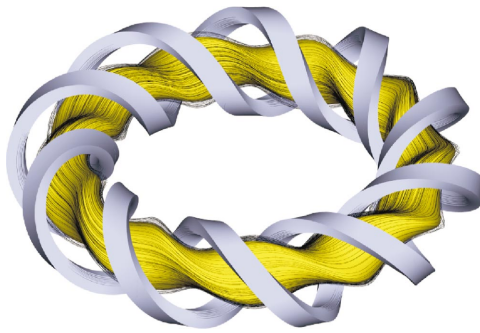


Figure 1.6 LHD: a conventional stellarator with helical windings (from [15]).

Introducing non-axisymmetric components to the magnetic field structure in these 3-dimensional systems has implications for trapped particle confinement. For a stellarator with multiple harmonics in the magnetic field spectrum, there are also multiple classes of trapped particles. When the collisionality is higher than the bounce frequency (the frequency at which a particle trajectory is reflected due to the magnetic mirror effect), this has only small effects on the particle diffusivity, which therefore scales similarly to that of a tokamak. To demonstrate this, particle diffusivity is plotted as a function of collisionality for several values of  $E_r$  in a stellarator in Figure 1.7, along with the diffusivity in a tokamak.

For zero radial electric field, the stellarator diffusivity matches that of an equivalent tokamak in the plateau and Pfirsch-Schlüter collisionality regimes. In the low collisionality regime, however, particles on average do not undergo collisions before bouncing multiple times. In a tokamak, these

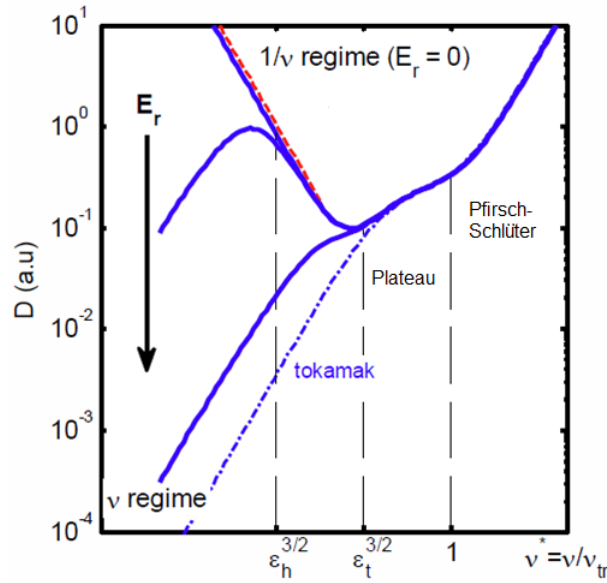


Figure 1.7 Particle diffusivity versus collisionality for stellarators and tokamaks [18].

bounce points are on the same flux surface, even as the particle precesses toroidally around the device. For a conventional stellarator with multiple helical ripples in the magnetic field strength, the bounce points of trapped particle orbits can be on different radial surfaces, as a trapped particle does not necessarily complete a full banana orbit before reaching another region of locally high  $|B|$ . This leads to a collisionless radial displacement of the trapped particle out of the device.

The net result of these single particle losses in the absence of collisions is a loss cone in velocity space, similar to that in magnetic mirror devices. When some collisions are present, this effect then scales unfavorably with  $1/\nu$  in the low collisionality regime where hot, reactor-relevant plasmas are most likely to operate. As demonstrated by LHD, these neoclassical losses then dominate once stellarator plasmas become hot and collisionless [19]. Achieving reactor-relevant plasma parameters becomes extremely difficult when there are collisionless loss orbits into which particles diffuse.

A finite radial electric field reduces the trapped particle losses and improves the neoclassical confinement, as demonstrated by the decreased diffusivity with increasing values of  $E_r$  in Figure 1.7. The improvement of confinement scales with  $E_r/v$ , where  $v$  is the particle velocity, however, so that the radial electric field required to confine alpha particles becomes untenably large as devices scale toward a reactor.

### 1.2.3 Optimized stellarators

Using modular, non-planar toroidal field coils of varying shapes, a more carefully crafted magnetic field can be generated which provides good confinement of collisionless trapped particles. One such magnetic field optimization is called quasi-symmetry. In a quasi-symmetric magnetic configuration, the magnetic field strength (but not necessarily the vector components of the field) is constant in some direction in a particular straight field line coordinate system, denoted Boozer coordinates [20]. With perfect quasi-symmetry, this optimization produces tokamak-like neoclassical particle and energy confinement without the need for externally driven currents. Similar to the form of the tokamak field in Equation 1.1, in a quasi-symmetric magnetic configuration, the magnetic field strength can be written as

$$\frac{|B|}{B_0} \approx 1 - \epsilon_h \cos(N\zeta - M\alpha), \quad (1.2)$$

where  $\zeta$  and  $\alpha$  are the toroidal and poloidal angles in Boozer coordinates and  $N$  and  $M$  are the toroidal and poloidal mode numbers of the quasi-symmetric system, respectively. If  $N=0$ , the configuration is quasi-axisymmetric, if  $M=0$ , it is quasi-poloidally symmetric, and any configuration with finite values of both  $N$  and  $M$  is quasi-helically symmetric. It can be shown that  $M = 1$  is the only acceptable poloidal mode number for a configuration which approaches quasi-symmetry, due to a boundary condition near the axis [21, 22]. The predicted and experimentally observed effects of quasi-symmetry on plasma confinement will be explored further in later sections.

One thing to note is that no configuration exists, let alone could be built, that is perfectly quasi-symmetric without also being axisymmetric [23]. However, no real tokamak device is perfectly axisymmetric either, but at some point the symmetry is sufficient enough that other dynamics, such as turbulence, begin to dominate the non-axisymmetric effects on neoclassical confinement and flow damping. This should also be true for quasi-symmetric systems.

Using a more general form of optimization, a quasi-isodynamic configuration (QI, or equivalently quasi-omnigenous, QO) has been implemented in the W7-X stellarator [24], which has completed construction in Greifswald, Germany and is undergoing commissioning at the time of this writing. This optimization attempts to ensure that the longitudinal adiabatic invariant  $J = \oint v_{\parallel} dl$  is constant on a flux surface so that the average radial drift of a collisionless particle off of a flux surface vanishes [25]. One result of this optimization is poloidally continuous  $|B|$  contours on a magnetic surface. While all quasi-symmetric systems are also quasi-isodynamic, QI relaxes the requirement that the magnetic field strength has a direction of symmetry on a flux surface in straight field line coordinates. This allows the design to be optimized for additional targets, such as reduced bootstrap current, without sacrificing good trapped particle confinement. By not maintaining a direction of symmetry in the magnetic field strength, however, neoclassical transport is no longer intrinsically ambipolar at any value of  $E_r$ , and large, arbitrary flows would not be possible in the QI device [26, 27].

To illustrate the distinctions between these various magnetic configurations, Figure 1.8 compares the magnetic field strength on a surface versus toroidal and poloidal angle using Boozer coordinates in (a) a classical stellarator (WEGA [28]), (b) a single field period of a stellarator optimized for quasi-isodynamicity (similar to W7-X, figure from [29]), (c) a stellarator optimized for quasi-helical symmetry (HSX) and (d) an axisymmetric tokamak. Dotted lines indicate the direction of the magnetic field lines, which are straight lines by definition in Boozer coordinates.

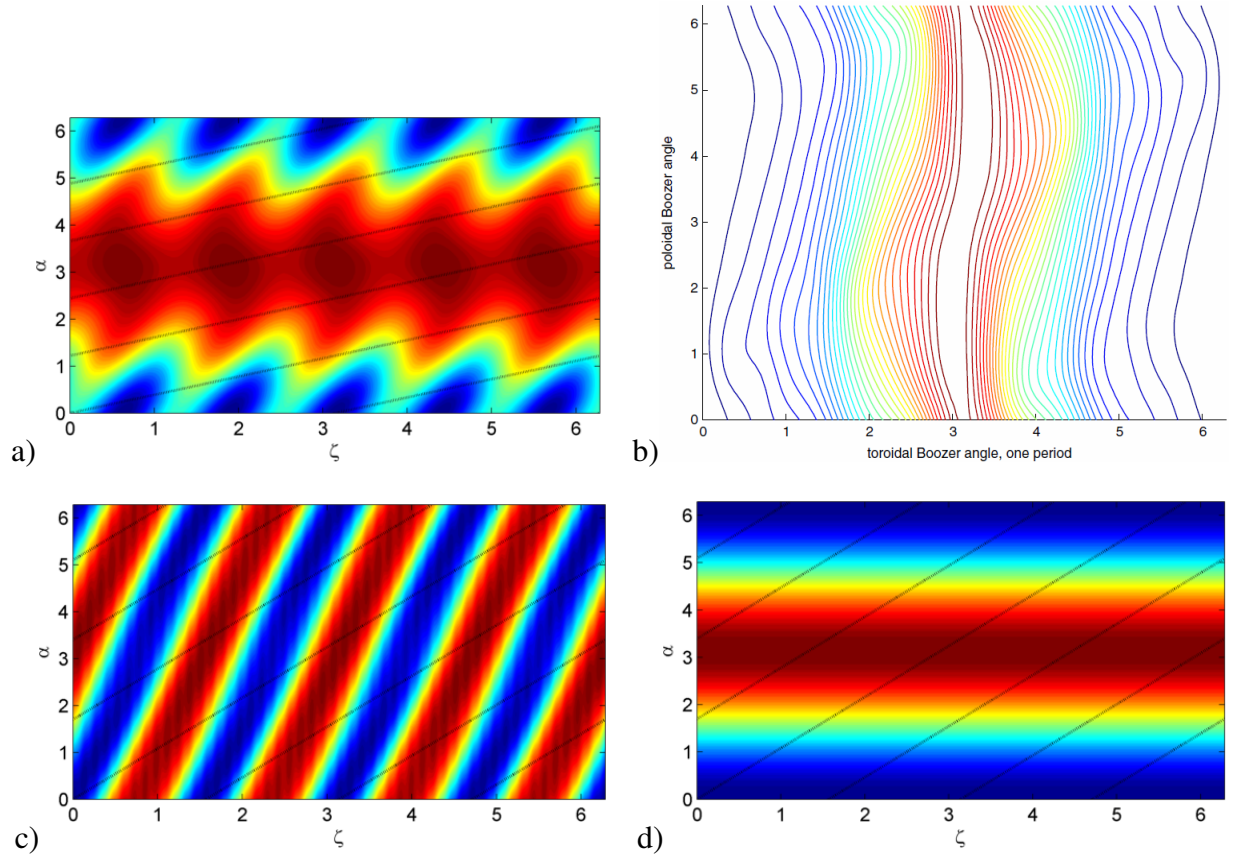


Figure 1.8  $|B|$  contours in Boozer coordinates for (a) WEGA, a classical stellarator [28], (b) W7-X, a quasi-isodynamic stellarator [29], (c) HSX, a quasi-helically symmetric stellarator and (d) an axisymmetric tokamak.

From Figure 1.8, the transition and overlap between the different magnetic field configurations begins to become clear. All quasi-symmetric systems are quasi-isodynamic, but the inverse is not true. It is also the case that all axisymmetric systems are quasi-symmetric. A trapped particle in the quasi-helically symmetric field will precess in the helical direction in a similar way that it would precess toroidally in an axisymmetric field without any average outward radial drift, because bounce points remain on the same surface.

One result of QI optimization that is apparent from Figure 1.8(b) is poloidally continuous  $|B|$  contours. This also allows the trapped particles to precess poloidally without a radial drift, but not in such a way that allows large flows to develop unless the configuration is also quasi-symmetric.



Recent work suggests, however, that the optimization scheme used in W7-X may greatly reduce the turbulent transport even without sheared flows due to the stabilization of trapped particle modes [30].

### 1.3 HSX

The Helically Symmetric eXperiment (HSX), pictured in Figure 1.9, is a 4-field period modular coil stellarator that is optimized for quasi-helical symmetry, with  $N=4$  and  $M=1$  in Equation 1.2 [31, 32]. HSX plasmas are heated using electron cyclotron resonance heating (ECRH) with two separate gyrotrons, each with a maximum injected heating power of  $\sim 100$  kW. All of the experiments presented here have been performed using only a single gyrotron source. Because only the electrons are heated directly and charge exchange losses are large, the ions are relatively cold and collisional. The temperature of  $C^{6+}$  ions has been measured using CHERS to peak at  $\sim 60$  eV in the core, compared to  $\sim 2$  keV electrons [33].

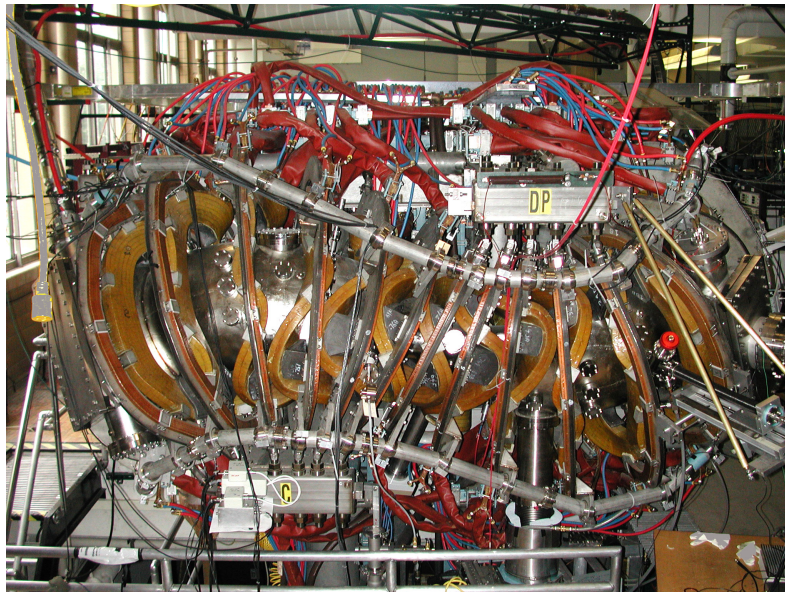


Figure 1.9 HSX.

### 1.3.1 Quasi-helical symmetry and predicted effects

HSX has been optimized to be quasi-symmetric in a helical direction on a flux surface. This property results in improvements to plasma confinement through several channels. First and most importantly, the neoclassical direct-loss orbits and large excursions from the magnetic surfaces that are traditionally associated with stellarators are removed, leading to improved neoclassical particle and energy confinement in the low collisionality regime [20, 34]. Many of the other effects described here are direct consequences of this. The magnitude of the magnetic field along a field line for one toroidal transit in the edge of HSX (at  $r/a=0.8$ ) is plotted in Figure 1.10, demonstrating the dominance of the single mode, as in a tokamak.

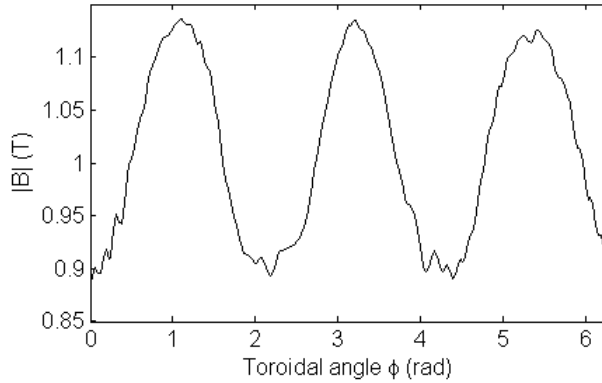


Figure 1.10  $|B|$  along a field line in the edge of HSX ( $r/a=0.8$ ).

This modulation of the magnetic field strength on a flux surface can be seen additionally in the cross sections of a flux surface. Figure 1.11 is a plot of magnetic surfaces in HSX at three different toroidal locations, with the color of each point indicating the strength of the magnetic field at that point.

In addition to the main coils that provide the magnetic field for the optimized quasi-helically symmetric magnetic configuration (QHS), HSX has a set of auxiliary coils that can be energized to intentionally break the designed optimization. Each of the six unique planar coils can be energized to generate a magnetic field in either direction, allowing a wide range of magnetic configurations

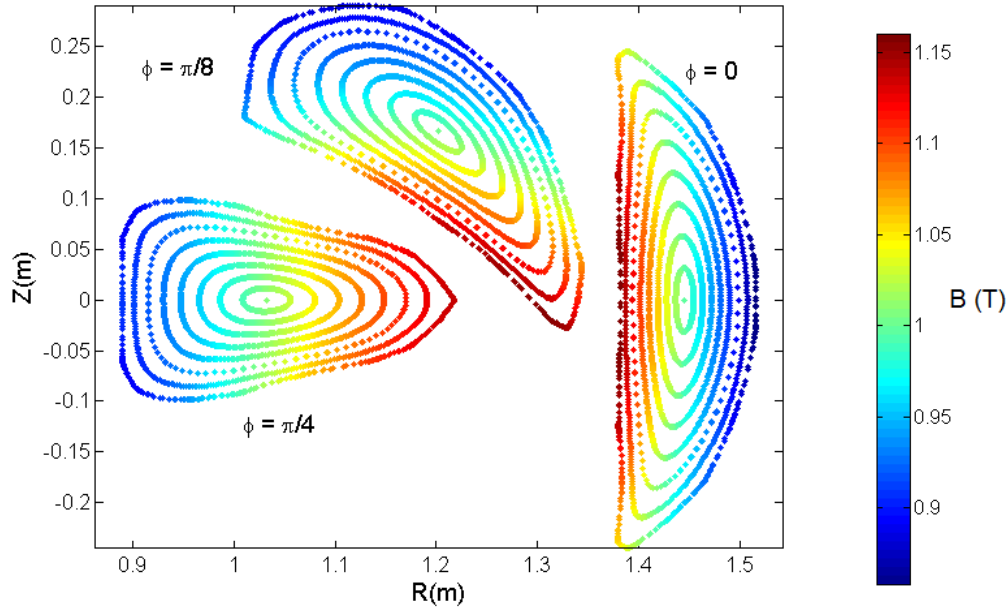


Figure 1.11 Colored Poincaré plots of magnetic surfaces for several cross sections in HSX, indicating magnetic field strength at each point.

to test various effects of the magnetic field structure on confinement. A picture of a modular main coil and an associated planar auxiliary coil is given in Figure 1.12.

The Mirror configuration is a particular magnetic configuration that is designed to break the symmetry in the magnetic field strength as much as possible while keeping other parameters, such as the rotational transform and plasma volume, close to their value in the QHS configuration. This allows a more direct comparison of confinement and transport properties with and without the optimization. A more complete analysis of the characteristics of this configuration will be presented in Section 2.4.1.

A second effect of optimizing the magnetic field for quasi-symmetry is that the neoclassical flow damping in the direction of symmetry is reduced [35]. Large flows in the direction of symmetry are then expected to be allowed, and these have been confirmed in HSX [33]. Experimentally,

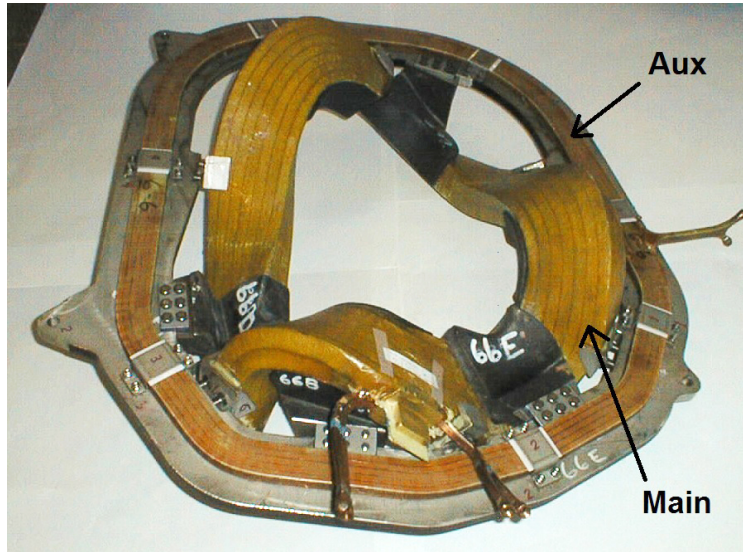


Figure 1.12 A main modular coil and planar auxiliary coil of HSX.

however, the measured flow damping in both the optimized and unoptimized magnetic configurations is significantly larger than the neoclassically calculated values [35]. This demonstrates that when the neoclassical optimization is sufficient, non-neoclassical effects become important, as they are in tokamaks, which are approximately axisymmetric.

Another predicted beneficial effect of quasi-symmetric optimization, as yet to be confirmed experimentally, is the enhancement of zonal flows with reduced ripple-trapped particle losses [36, 37, 38]. This effect has been used to explain results in the Large Helical Device, where a reduction in anomalous transport was observed with a change of configuration to a regime that was optimized to reduce neoclassical transport, despite larger linear growth rates of the microinstabilities [39]. The reduction in anomalous transport was attributed to an enhanced coupling of the turbulence to zonal flows when the neoclassical trapped particle losses are reduced [36, 38]. An experimental investigation into this effect was performed in HSX [40] and is presented briefly in Appendix A. The results were inconclusive, as no evidence of zonal flows was observed without an applied bias

in either the quasi-symmetric configuration or the configuration with the symmetry intentionally broken.

One additional predicted effect of quasi-symmetry is related to these others and is the topic under investigation in this dissertation. If a magnetic configuration is close enough to quasi-symmetry, then the plasma should “rotate freely”; that is to say that the rotation velocity and radial electric field are free parameters and are not determined solely by the neoclassical non-ambipolar particle transport as they typically are in stellarators. In a configuration which is near quasi-symmetry but not perfectly quasi-symmetric, the competition between the neoclassical term and other terms in the momentum balance determine the plasma rotation. The rotation can be driven by a number of mechanisms, such as neutral beams or ion orbit loss, but the Reynolds stress is identified as a likely cause of the rotation in HSX. The Reynolds stress is the term in the momentum balance which accounts for locally fluctuating turbulent fluid velocities. These forcing mechanisms will be discussed in detail in Chapter 2, and the experimental examination of the Reynolds stress will be the focus of much of this document.

The remainder of this document is broken up into five chapters. First, the theory of intrinsic rotation in magnetically confined plasmas is presented in Chapter 2 along with previous experimental results, from both HSX and other devices. In Chapter 3, the experimental setup for the studies in HSX is introduced, including the design of the Langmuir probe system and the methods used in data processing and analysis. The measurements of the radial electric field and parallel flows using these probes are then presented in Chapter 4 and are compared with neoclassical models and calculations of the predicted flows. Chapter 5 presents the measured Reynolds stress profile using the two probes and the calculated flow drive that would result from these profiles and compares this inferred flow to the measured values from Chapter 4. Conclusions are then given in Chapter 6, along with some suggestions for future work.

## References

1. Bray, D. The scientific consensus of climate change revisited. *Environmental science & policy* **13**, 340–350 (2010).
2. Hansen, J., Sato, M., Kharecha, P., *et al.* Climate change and trace gases. *Philosophical Transactions of the Royal Society A: Mathematical, Physical and Engineering Sciences* **365**, 1925–1954 (2007).
3. Tans, P. & Keeling, R. *Trends in Atmospheric Carbon Dioxide* tech. rep. (NOAA/ESRL, 2012).
4. Petit, J. R., Jouzel, J., Raynaud, D., *et al.* Climate and atmospheric history of the past 420,000 years from the Vostok ice core, Antarctica. *Nature* **399**, 429–436 (1999).
5. Shindell, D. T., Faluvegi, G., Koch, D. M., *et al.* Improved attribution of climate forcing to emissions. *Science* **326**, 716–718 (2009).
6. Archer, D., Eby, M., Brovkin, V., *et al.* Atmospheric lifetime of fossil fuel carbon dioxide. *Annual Review of Earth and Planetary Sciences* **37**, 117 (2009).
7. Lelieveld, J., Crutzen, P. J. & Dentener, F. J. Changing concentration, lifetime and climate forcing of atmospheric methane. *Tellus B* **50**, 128 (1998).
8. Hansen, J., Reudy, R., Sato, M., *et al.* A closer look at United States global surface temperature change. *Journal of Geophysical Research* **106**, 23947–23963 (2001).
9. Meehl, G. A., Washington, W. M., Collins, W. D., *et al.* How much more global warming and sea level rise? *Science* **307**, 1769 (2005).
10. *Summary electricity statistics 2001-2012* (<http://www.eia.gov/electricity/data.cfm>) tech. rep. (U.S. Energy Information Administration, 2013).

11. Deffeyes, K. S. & MacGregor, I. D. World uranium resources. [Use of log-curves in estimation]. *Scientific American* (1980).
12. Moir, R. W. & Teller, E. Thorium-fueled underground power plant based on molten salt technology. *Journal of Nuclear Technology* **151**, 334 (2005).
13. Moses, E. I. The National Ignition Facility (NIF): A path to fusion energy. *Energy Conversion and Management* **49**, 1795–1802 (2008).
14. Hurricane, O. A., Callahan, D. A., Casey, D. T., *et al.* Fuel gain exceeding unity in an inertially confined fusion implosion. *Nature* **506**, 343–348 (2014).
15. Boozer, A. H. Physics of magnetically confined plasmas. *Reviews of Modern Physics* **76**, 1071 (2005).
16. Feng, Y, Sardei, F, Grigull, P, *et al.* Physics of island divertors as highlighted by the example of W7-AS. *Nuclear Fusion* **46**, 807–819 (2006).
17. Shimada, M, Campbell, D. J., Mukhovatov, V, *et al.* ITER Physics Basis, Chapter 1: Overview and summary. *Nuclear Fusion* **47**, S1–S17 (2007).
18. Lore, J. *Jeremy Lore's Dissertation, University of Wisconsin - Madison* 2010.
19. Takahashi, H., Osakabe, M., Nagaoka, K., *et al.* Extension of the operational regime in high-temperature plasmas and the dynamic-transport characteristics in the LHD. *Nuclear Fusion* **53**, 073034 (2013).
20. Boozer, A. H. Transport and isomorphic equilibria. *Physics of Fluids* **26**, 496 (1983).
21. Calvo, I., Parra, F. I., Velasco, J. L. & Alonso, J. A. Stellarators close to quasisymmetry. *Plasma Physics and Controlled Fusion* **55**, 125014 (2013).
22. Cary, J. R. & Shasharina, S. G. Omnigenity and quasihelicity in helical plasma confinement systems. *Physics of Plasmas* **4**, 3323 (1997).

23. Garren, D. A. & Boozer, A. H. Existence of quasihelically symmetric stellarators. *Physics of Fluids B: Plasma Physics* **3**, 2822 (1991).
24. Erckmann, V., Hartfuss, H.-J., Kick, M., *et al.* in *Fusion Engineering, 1997. 17th IEEE/NPSS Symposium* **1** (IEEE, 1997), 4048.
25. Mynick, H. E. Transport optimization in stellarators. *Physics of Plasmas* **13**, 058102 (2006).
26. Helander, P. & Simakov, A. Intrinsic Ambipolarity and Rotation in Stellarators. *Physical Review Letters* **101**, 145003 (2008).
27. Landreman, M. & Catto, P. J. Neoclassical flow, current, and electric field in a quasi-isodynamic stellarator. *Plasma Physics and Controlled Fusion* **53**, 035016 (2011).
28. *Private communication with Enrico Chlechowicz*, 2014.
29. Subbotin, A. A., Mikhailov, M. I., Shafranov, V. D., *et al.* Integrated physics optimization of a quasi-isodynamic stellarator with poloidally closed contours of the magnetic field strength. *Nuclear Fusion* **46**, 921–927 (2006).
30. Proll, J. H. E., Helander, P., Connor, J. W. & Plunk, G. G. Resilience of Quasi-Isodynamic Stellarators against Trapped-Particle Instabilities. *Physical Review Letters* **108**, 245002 (2012).
31. Nührenburg, J. & Zille, R. Quasi-helically symmetric toroidal stellarators. *Physics Letters A* **129**, 113 (1988).
32. Anderson, F. S. B., Almagri, A. F., Anderson, D. T., *et al.* The Helically Symmetric Experiment, (HSX) goals, design and status. *Fusion Technology* **27**, 273 (1995).
33. Briesemeister, A., Zhai, K., Anderson, D. T., Anderson, F. S. B. & Talmadge, J. N. Comparison of the flows and radial electric field in the HSX stellarator to neoclassical calculations. *Plasma Physics and Controlled Fusion* **55**, 014002 (2013).



34. Canik, J., Anderson, D. T., Anderson, F. S. B., *et al.* Experimental Demonstration of Improved Neoclassical Transport with Quasihelical Symmetry. *Physical Review Letters* **98**, 085002 (2007).
35. Gerhardt, S., Talmadge, J. N., Canik, J. & Anderson, D. T. Experimental Evidence of Reduced Plasma Flow Damping with Quasisymmetry. *Physical Review Letters* **94**, 015002 (2005).
36. Sugama, H. & Watanabe, T. Dynamics of Zonal Flows in Helical Systems. *Physical Review Letters* **94**, 115001 (2005).
37. Mynick, H. E. & Boozer, A. H. Zonal flows in toroidal systems. *Physics of Plasmas* **14**, 072507 (2007).
38. Watanabe, T., Sugama, H. & Ferrando-Margalet, S. Reduction of Turbulent Transport with Zonal Flows Enhanced in Helical Systems. *Physical Review Letters* **100**, 195002 (2008).
39. Yamada, H., Watanabe, K. Y., Yamazaki, K., *et al.* Energy confinement and thermal transport characteristics of net current free plasmas in the Large Helical Device. *Nuclear Fusion* **41**, 901 (2001).
40. Wilcox, R. S., van Milligen, B. P., Hidalgo, C., *et al.* Measurements of bicoherence and long-range correlations during biasing in the HSX stellarator. *Nuclear Fusion* **51**, 083048 (2011).

## Chapter 2

### Momentum balance and intrinsic flows

In this chapter, the theoretical basis behind plasma rotation will be presented for the experiments discussed in later chapters. The calculation and experimental observation of intrinsic (non-driven) rotation in stellarators is discussed in Sections 2.1 and 2.2. In Section 2.3, different terms in the momentum balance equation are examined for their contribution to toroidal plasmas in general, and HSX plasmas in particular. A discussion of the rotation and radial electric field determination in devices which approach quasi-symmetry is presented in Section 2.4, and some theories of the limits of non-neoclassical radial electric field determination are then applied to HSX in Section 2.5. Section 2.6 summarizes some previous measurements in HSX which are applicable to this work and helped motivate it. The Reynolds stress term is identified as the most likely non-neoclassical contributor to momentum balance in HSX, and measurements of Reynolds stress and its contribution to the momentum balance in other devices are then presented in Section 2.7.

Plasma flows have many beneficial effects in magnetic confinement devices. They can stabilize the MHD equilibrium [41], shield error fields from penetrating into the plasma and generating islands [42], and have been shown to heal existing islands in stellarator configurations [43]. One of the most beneficial results of sustained plasma flows is the reduction of turbulent heat and particle losses in the presence of sheared  $E \times B$  flows [44]. In particular, this flow shear can enable access to H-mode confinement [45].

One of the great stumbling blocks to a magnetic confinement fusion reactor continues to be anomalous thermal and particle transport, thought to be driven by microinstabilities that are destabilized by temperature and density gradients across the minor radius of the torus. The magnitude of the achievable gradients in large part determines the machine size for fusion devices. The larger a device is, the more expensive its construction and maintenance becomes, with everything from raw materials to labor and tooling. A larger device size also generates more engineering hurdles as the plasma volume and total heat fluxes to plasma facing components increase, which further amplifies the complexity of design. Therefore the cost of experimental devices (and, eventually, a reactor) is largely dependent on the achievable gradients across the minor radius of the plasma. It is necessary, then, to search for mechanisms which can reduce the energy transport driven by microturbulence.

There is one simple mechanism for suppressing turbulent transport that has been shown to be effective across a broad range of magnetic confinement devices. If the shearing rate of the radial electric field  $\partial E_r / \partial r$  is greater than the growth rate of a given instability, then the turbulence will be quenched and that mode will no longer drive transport as long as this  $E \times B$  shear is present [44, 46]. This relatively simple model has been used to explain confinement improvement in experiments with great success, and it is now considered the fundamental mechanism for minimizing transport in an environment with linearly destabilized turbulent modes [45]. While optimizing the shaping of magnetic configurations may result in significant reductions in turbulent transport [30, 47], no other mechanism has experimentally demonstrated access to the steep pressure gradients in the way that  $E \times B$  flow shear has been shown to do, especially to the extent that occurs in H-modes [45].

Figure 2.1 demonstrates the effect of an H-mode pedestal on the plasma parameters across the plasma volume from measurements taken before and after an L-mode to H-mode transition in the DIII-D tokamak [48]. The electron temperature ( $T_e$ , Figure 2.1(a)), ion temperature ( $T_i$ , Figure

2.1(b)) and electron density ( $n_e$ , Figure 2.1(c)) each have substantially larger values in the core of the plasma following the L-H transition. The transport changes are localized to a small radial region at the edge of the confinement volume, but the integrated effect of these steep edge gradients over the interior plasma volume is dramatic.

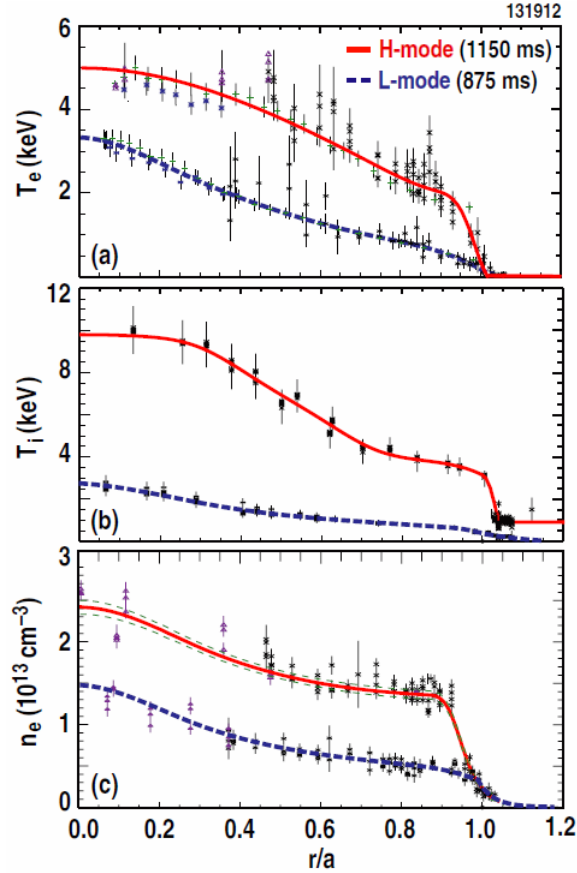


Figure 2.1 (a) Electron temperature, (b) ion temperature and (c) electron density profiles for a DIII-D discharge with and without an H-mode pedestal [48].

Without the benefit of the H-mode pedestal, a reactor device's size would need to be increased in order to achieve the high temperatures necessary for fusion reactions to occur ( $T_i \approx 10$  keV). It is unclear whether a device which is unable to achieve a similar level of confinement as one with an H-mode would be suitable for a reactor, but it would certainly be larger and more expensive to build. If having a direction of symmetry in the magnetic field strength in a stellarator aids in

the development of sheared flows and the subsequent reduction of turbulent transport, whether via an H-mode or other sheared flows, then quasi-symmetric optimization may greatly reduce the necessary size and cost of an eventual stellarator reactor.

## 2.1 Rotation and $E_r$ determination in the absence of external momentum sources

As plasma confinement devices scale toward a reactor, intrinsic flows generated by the plasma itself will dominate the momentum input from neutral beams [49]. Ideally, a reactor would not require any externally injected momentum once it was ignited and would therefore rely on the plasma's intrinsic flows for stability and confinement. Poloidal or toroidal rotation driven by alpha particles alone has been shown to be insufficient for either avoidance of MHD instabilities or suppression of microturbulence [50], so other mechanisms for intrinsic rotation need to be investigated.

HSX is well-positioned to study intrinsic plasma flows, as it has no momentum injection, but has been optimized to have a helical direction of symmetry along which the flow damping is minimized [35]. The optimization of the magnetic field is not perfect, however, and the deviation from ideal quasi-symmetry may be important to the resulting intrinsic flows. The implications of this work may apply to tokamaks with non-axisymmetric perturbations as well as other stellarators which have been optimized for quasi-symmetry.

### 2.1.1 $E_r$ determination in unoptimized stellarators

For a generic toroidal plasma in MHD equilibrium, the relationship between the flows, radial electric field, and pressure gradient is given by the radial force balance [45]

$$E_r = \frac{1}{Z_i e n_i} \nabla P_i - \mathbf{V}_i \times \mathbf{B}, \quad (2.1)$$

where  $E_r = -\nabla\Phi(\psi)$ ,  $\Phi$  is the plasma potential which is assumed to be a constant on surface  $\psi$ ,  $Z_i$  is the ion charge state,  $e$  is the elementary charge,  $n_i$  is the ion density,  $P_i = n_i T_i$  is the ion pressure,

$T_i$  is the ion temperature,  $\mathbf{V}_i$  is the ion flow velocity, and  $\mathbf{B}$  is the equilibrium magnetic field. Radial force balance is achieved in magnetic confinement devices on a fast timescale compared to radial transport processes, and it is therefore commonly used to determine the radial electric field from the measured velocity and plasma pressure [45].

In classical (unoptimized) stellarators, neoclassical particle transport is different for each particle species and depends strongly on the radial electric field [51, 52]. This leads to a radial current when the ion and electron fluxes are different, which quickly changes the potential (and  $E_r$ ) on the surfaces until particle fluxes are brought into equilibrium. At this point,  $J_r = 0$  at some set value of  $E_r$  for each surface, so that

$$\sum_i Z_i \Gamma_i(E_r) = \Gamma_e(E_r) \quad (2.2)$$

where  $\Gamma_j$  is the particle flux for species  $j$ . Equation 2.2 is referred to as the ambipolarity constraint, and neglecting all other sources of differential particle flux and torque, it results in plasmas which necessarily have their radial electric field (and subsequently their rotation velocity) set to this neoclassically determined value for each flux surface. As a typical example of the calculation of the radial electric field using the ambipolarity constraint, the neoclassical particle fluxes as a function of  $E_r$  for a pure-hydrogen stellarator plasma with  $T_i \approx T_e$  are plotted in Figure 2.2 (reproduced from [53]).

For a single species plasma, the ambipolarity constraint is satisfied where the curves in Figure 2.2 intersect so that  $\Gamma_i(E_r) = \Gamma_e(E_r)$ , which occurs at three values of  $E_r$  in this example. The middle solution is unstable, so that there are only two stable roots at which  $E_r$  can reach equilibrium, labeled the “ion root” and “electron root” solutions in the plot. On the magnetic surface for which this plot was made, the plasma is only able to have one of these two values for  $E_r$  in steady state, and associated with each of these is a particular perpendicular flow velocity according to Equation 2.1. For all of the HSX plasmas studied in this work, only ion root solutions to the ambipolarity

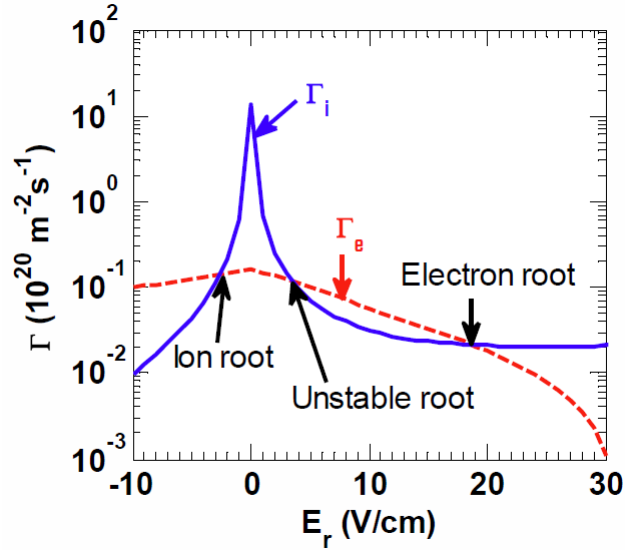


Figure 2.2 Neoclassical ion and electron particle fluxes as a function of  $E_r$  for a stellarator plasma with  $T_i \approx T_e$ , reproduced from [53].

condition are calculated to exist in the edge region where probes can be used to take measurements in the plasma.

## 2.2 Neoclassical transport and radial electric field calculations

To calculate the neoclassically predicted radial electric field using the ambipolarity condition, a series of coupled numerical codes are used to calculate the particle fluxes as a function of  $E_r$  and solve the ambipolarity constraint (Equation 2.2) given experimentally measured plasma profiles in HSX. A brief overview of these codes and the procedure used to make the neoclassical calculations, which are necessary to compare against measurements in HSX, will be described in this section. The assumptions and simplifications that each code makes and the validity and implications of these assumptions will also be addressed.

### 2.2.1 VMEC

The Variational Moments Equilibrium Code (VMec) [54] is the standard tool used for most stellarator computational modeling to solve for the 3D equilibrium. VMec takes a vacuum magnetic field, a plasma pressure profile and the net toroidal current distribution as an input and uses radial force balance assuming no rotation ( $\mathbf{J} \times \mathbf{B} = \nabla p$ ) to calculate the total plasma current distribution in all directions to construct a series of nested flux surfaces. The spatial locations of the surfaces are represented in Fourier harmonics. The resulting calculated current distributions can be compared to experiment to determine which calculated equilibrium is most likely being observed given the measured current distribution, a process known as equilibrium reconstruction. Some of this work has been done in HSX in Reference [55], and it is currently being continued and expanded by Enrico Chlechowicz. Because closed, nested flux surfaces are assumed in VMec, islands cannot be resolved using this tool, although several equilibrium solvers exist or are under development which are capable of solving for equilibria with magnetic islands present, including SIESTA [56], PIES [57] and SPEC [58]. Discussions of the advantages and limitations of each of these codes is beyond the scope of this work.

For HSX neoclassical transport calculations used in this work and elsewhere, a vacuum VMec equilibrium is used as opposed to including finite-beta effects due to the large computational costs of the neoclassical calculations for each equilibrium using DKES (discussed in the next section). The use of a vacuum equilibrium is justified due to the absence of any external current drive and the low values of  $\beta$  in HSX plasmas, where  $\beta = 2\mu_0 nT/B^2$  is the ratio of the plasma pressure to magnetic pressure.  $\beta < 0.5\%$  for all plasmas in HSX, and  $\beta < 0.1\%$  outside the very core ( $r/a > 0.2$ ), plotted later in Figure 2.9(a). Finite- $\beta$  effects on the plasma shaping are therefore expected to be small, especially in the edge where measurements with probes are taken for this work.



Comparisons of calculated vacuum and finite-pressure equilibria confirm that this simplification is valid for HSX, as the difference in plasma shaping is negligible.

### 2.2.2 DKES

The Drift Kinetic Equation Solver (DKES) [52, 59] is a common tool used for stellarators to calculate the neoclassical transport coefficients as a function of radial electric field and particle collisionality based on a VMEC equilibrium. The coefficients calculated from DKES are then used along with measured plasma parameters ( $T_e$ ,  $T_i$  and  $n_e$ ) to determine the particle transport for each species and subsequently the neoclassical value of the radial electric field, as demonstrated by finding the intersection of the curves in Figure 2.2.

Due to the large computational cost of the DKES calculations as well as a problem of slow convergence at low collisionality, analytic extrapolations are used to extend the domain of the transport coefficient calculations to the lowest values of collisionality [60, 61]. The particle diffusivity calculated by DKES as a function of normalized collisionality  $\nu^* = \nu/v_p$ , where  $v_p$  here is the particle velocity, is plotted in Figure 2.3 for several values of the normalized radial electric field  $e_{field} = E_r/(Bv_p)$ . These calculations are for a surface at about  $r/a=0.9$ , where the transport at low collisionality is large relative to surfaces further inside the plasma (see Figure 2.13). The extrapolated points are plotted in blue.

The transport coefficients calculated by DKES for the Mirror configuration used in this work are also plotted in Figure 2.3 for  $E_r=0$  in red (and green for the extrapolated values). The surfaces which are represented here are near  $r/a=0.9$  for both configurations. This comparison shows that the transport is over an order of magnitude higher in the low collisionality regime for the Mirror configuration than it is for QHS, and electrons in HSX are generally in this range of collisionality.

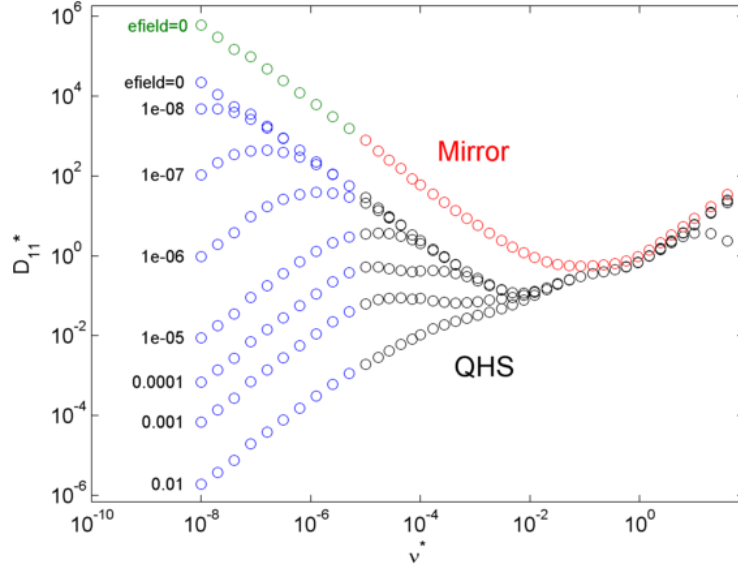


Figure 2.3 DKES particle transport coefficient for different values of  $E_r$  for the QHS configuration and a single curve for the Mirror configuration ( $E_r=0$ ) for comparison. Both surfaces represented are near  $r/a=0.9$ .

The simplification of using a single VMEC equilibrium to generate a single DKES database for each magnetic configuration, as discussed in the previous section, is necessary due to the computational cost of running DKES for each equilibrium. The changes in shaping with finite pressure are small for the low- $\beta$  HSX plasmas studied here, especially in the edge where probe measurements are made.

When stellarators are not optimized to reduce ripple-trapped particle losses, there is a large non-ambipolar particle loss which drives the radial electric field towards the neoclassical ambipolar solution at low collisionality, as discussed in Section 2.1.1. In unoptimized stellarators, the radial electric field values calculated by DKES or similar neoclassical transport codes are often consistent with flows measured in those devices [62, 63]. An example of this is given in Figure 2.4 (from reference [62]), which plots the calculated values of  $E_r$  for the stellarator W7-AS along with measured values of  $E_r$  from CXRS in plasmas with (a) on-axis and (b) off-axis ECRH.

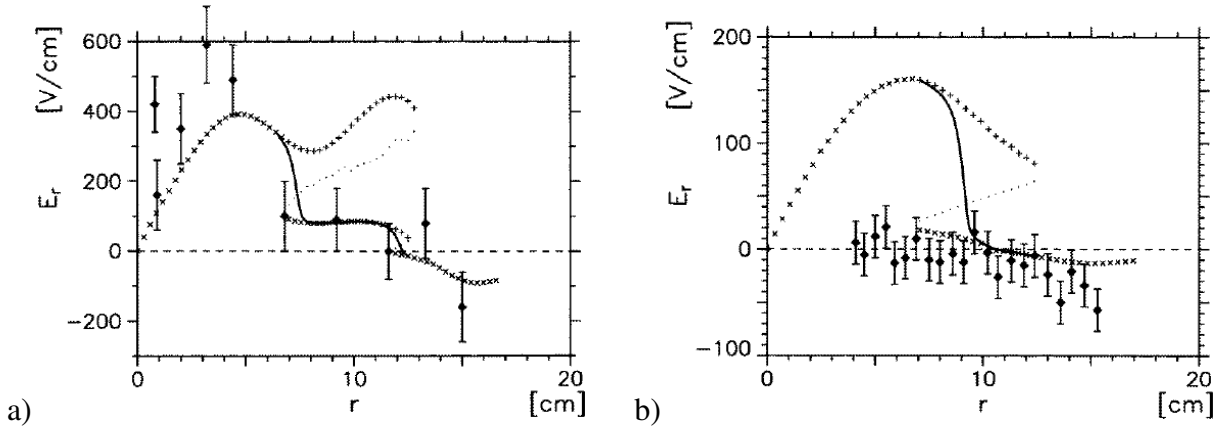


Figure 2.4 CXRS measurements of  $E_r$  in W7-AS using (a) on-axis and (b) off-axis ECRH heating, each compared to calculations using DKES. Figures reproduced from [62].

While there are some discrepancies in the core in both cases in Figure 2.4, the DKES calculations match reasonably consistently with the measurements in the radial regions where there is only an ion root solution predicted. Later, this will be contrasted with HSX measurements which do not even qualitatively match the neoclassically calculated solutions for the radial electric field.

### 2.2.2.1 DKES approximations

The DKES code makes several assumptions to simplify the kinetic equation and make the computation of the transport coefficients more tractable. Most of these assumptions are expected to be valid for the experimental parameters used in this work, particularly for values in the edge where  $E_r$  and  $V_{||}$  are calculated to be small. It is nevertheless important to keep all assumptions and simplifications in mind as comparisons are made between modeling and experiment.

First, the transport calculated by DKES is assumed to be radially local, based on the surfaces generated using VMEC. This assumption fails when there are helically trapped particles which drift collisionlessly out of the confinement regime, as is possible in stellarator plasmas with low collisionality. The collisionless loss orbits are not properly accounted for using a single-surface diffusive model. There are expected to be very few particles in these loss orbits in the edge of HSX

where these studies are being performed in the QHS configuration, although it may be a factor in the radial electric field determination in configurations in which the quasi-symmetry is broken.

The flow ordering used by DKES assumes that the flow velocity  $V \ll v_{ti}$  where  $v_{ti}$  is the thermal ion velocity, so that the distribution function is an unshifted Maxwellian. Ions in HSX are relatively cold ( $< \sim 60$  eV), so that this assumption can be broken with modest values of flow, but experimentally it is well satisfied for the main hydrogen ion species for all of the calculated values presented in this work.

DKES also assumes that particles are monoenergetic, meaning that the potential change as a particle drifts off of a flux surface is not accounted for and does not affect the particle velocity. This should not have any effect on the calculations for the low values of  $E_r$  which are calculated in the edge of HSX.

Another standard assumption that simplified neoclassical transport codes like DKES make is that the particle orbit width is zero and particle trajectories can be well-described by defining a magnetic surface. This assumption should be valid for the relatively cold particles in HSX, especially in the edge region where experiments reported in this paper are performed, but these effects have also been shown to be small in even hotter plasmas in LHD [63]. Figure 2.5 (reproduced from [63]) compares the calculated radial electric field in LHD using DCOM/NNW [64], a code that makes the standard neoclassical assumptions (similar to DKES), with values calculated using FORTEC-3D. FORTEC-3D [65] is a drift-kinetic  $\delta f$  Monte Carlo code which retains much more of the neoclassical physics, including finite orbit width effects. Although the DCOM/NNW calculations are done using Monte Carlo methods rather than the spectral methods of DKES, the two codes demonstrate good agreement when compared with each other [64]. Both the DCOM/NNW and FORTEC-3D calculations are made using an initial guess for the solution of the ambipolar

$E_r$ , which is given by the straight dotted line in Figure 2.5, and are then plotted against the experimental measurements. Both calculations also rely on VMEC as a framework to represent the underlying equilibrium.

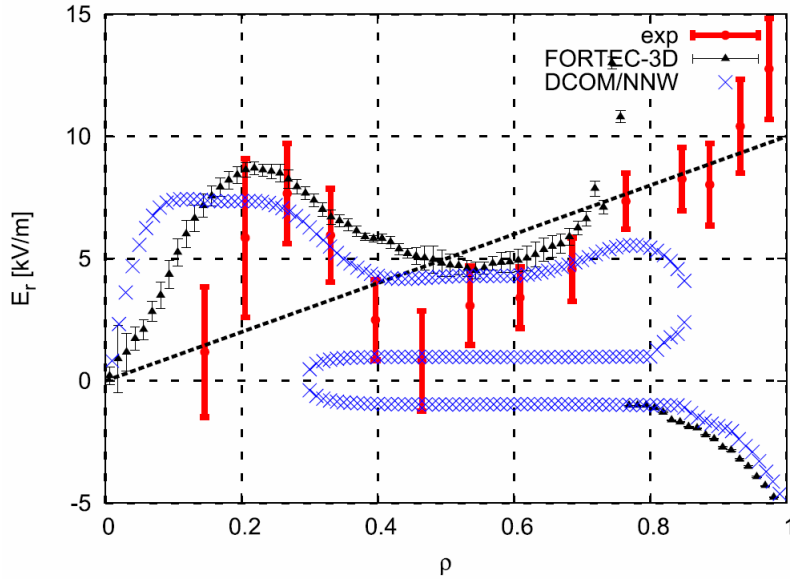


Figure 2.5 Predicted  $E_r$  in LHD calculated from the Monte Carlo code FORTEC-3D, the simplified neoclassical code DCOM/NNW, and the measured values from experiment (reproduced from [63]).

The two different methods of calculating the  $E_r$  profile given in Figure 2.5 are in reasonable agreement with each other across most of the minor radius. For relatively cold plasmas in the edge of HSX, this should give confidence that some of the assumptions made by DKES do not change the result significantly compared to calculations which include a more complete representation of the neoclassical physics. Because LHD is not neoclassically optimized, one would expect the neoclassical calculations to agree with the experimental measurements, which they do reasonably well everywhere except the outer 20% of the minor radius. This region happens to be where the experiments in HSX presented here will be focused, so it is important to keep in mind that there may be additional physics that is not captured by these neoclassical codes in the edge region, such as non-diffusive fluxes caused by collisionless loss orbits.

There are known problems with the DKES neoclassical calculations when the value of  $E_r$  approaches the helical ion resonance [53], which is the value of the radial electric field at which a single particle's parallel velocity causes it to approximately follow the  $|B|$  contours on a magnetic surface for a given mode in the magnetic spectrum, causing the particle to experience zero effective transform due to that mode. This resonant value of  $E_r$  for particle species  $a$  is expressed as [66]

$$E_r^{res} = \left| \frac{m - n/\iota}{m} \right| v_{Ta} B_\theta, \quad (2.3)$$

where  $m$  and  $n$  are the poloidal and toroidal mode numbers of the magnetic ripple term causing the resonance,  $v_{Ta}$  is the thermal velocity of the particle species  $a$ , and  $\iota$  is the rotational transform ( $1/q$ ). The physics of the resonance will not be discussed in further detail in this work, aside from the fact that the neoclassical calculations made by DKES break down at radial electric field values approaching  $E_r^{res}$  due to the monoenergetic assumption made while solving for the transport coefficients [67].

The helical ion resonance has been shown to be unimportant for low values of  $E_r$ , however, given approximately by  $E_r < \frac{1}{3} E_r^{res}$  [68]. The error in the calculation of  $E_r$  due to the resonance will therefore not play a role in the calculations for main hydrogen ions at the edge of HSX, which is the main focus of this work, but it may be an important factor for impurity species such as carbon or heavier ions if the calculated value of  $E_r$  is large enough. The resonant values of  $E_r$  for the main  $n=4$ ,  $m=1$  component of the magnetic spectrum for both carbon and hydrogen species are plotted in Figure 2.6, which is based on measured ion temperatures from CHERS and calculated in Alexis Briesemeister's dissertation [69]. The shaded areas are the errorbars of the measurement.

Based on radiated power measurements, the relative density of impurities is small in the hydrogen plasmas presented here with boronized walls. It is therefore not expected that the problem of calculations near the resonance will be encountered in the course of this work, because the

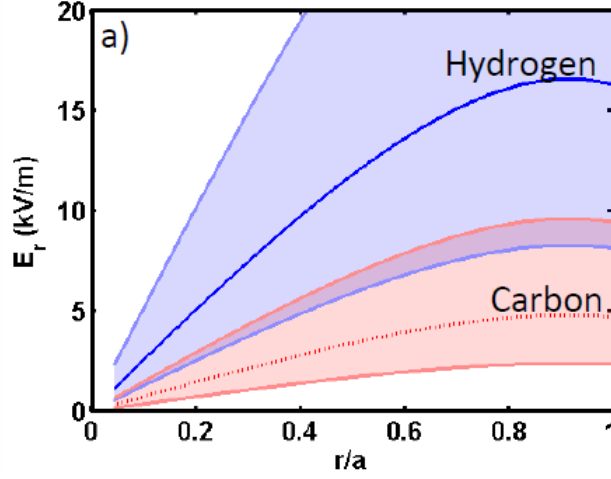


Figure 2.6  $E_r^{\text{res}}$  for carbon and hydrogen species from measured ion temperatures (reproduced from [69]).

neoclassically calculated values of  $E_r$  for these experiments satisfies  $E_r < \frac{1}{3}E_r^{\text{res}}$  for thermal hydrogen ions. It is still mentioned as a possible source of error in the neoclassical calculations, if both impurity concentrations are larger than expected and the predicted  $E_r$  approaches  $\sim \frac{1}{3}E_r^{\text{res}}$ .

One last simplification made by DKES which may be invalid is the use of a pitch angle scattering collision operator that does not conserve momentum. This simplification is addressed with the code PENTA, which will be explained in the next section.

### 2.2.3 PENTA

The DKES code uses a pitch angle scattering collision operator because this approximation greatly simplifies the equations to be solved with a significant reduction in the computational expense. Unfortunately, this operator does not conserve momentum. This is sufficient for stellarators not optimized for quasi-symmetry, as neoclassical flow damping is large in all directions. Because of this, DKES is the standard tool used to analyze neoclassical transport in stellarators. When the neoclassical flow damping in any direction is reduced sufficiently, however, corrections must be

made to these DKES transport coefficients to account for momentum conservation with collisions between unlike particle species [53].

The PENTA code [53, 70] uses the monoenergetic diffusion coefficients calculated by DKES, along with the thermodynamic drive terms from experimental plasma profiles, and calculates the particle flows and cross-field fluxes as a function of  $E_r$ . In the process, PENTA uses a moments method to correct for momentum conservation [71].

Calculating the predicted parallel flows in the QHS configuration of HSX using only the DKES neoclassical calculations, without momentum correction, finds the flows to be much smaller than what is measured using CHERS, while the PENTA calculations, which correct for momentum conservation, are around the same magnitude as the measured flows [33]. These CHERS measurements and the corresponding neoclassical calculations are shown in Figure 2.7 for HSX (from [33]).

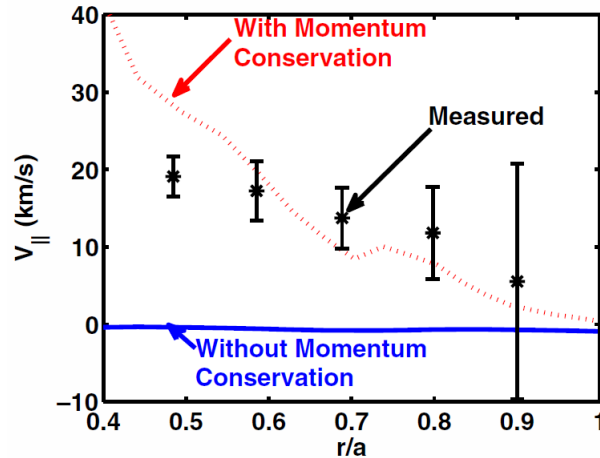


Figure 2.7  $V_{||}$  measured by CHERS in HSX vs calculations which include momentum conservation (red, using PENTA) and calculations without momentum conservation (blue, using DKES) (from [33]).

PENTA is the tool used for neoclassical calculations in HSX, because it is the most accurate one available with reasonable computational expense. Monte Carlo codes such as FORTEC-3D [65] are available which are expected to be more accurate, but these are extremely computationally



expensive, especially when multiple runs need to be performed for any change in plasma parameters. Early comparisons between particle flux and radial electric field predictions using PENTA, FORTEC-3D and another neoclassical code SFINCS [68] show that each of them produce similar results for HSX experimental parameters in the edge [72].

## 2.3 Momentum balance

In stellarators with multiple large terms in the magnetic spectrum and without driven momentum sources, the neoclassical term in the momentum balance is dominant due to the non-ambipolar particle flux and large neoclassical flow damping in all directions. When these neoclassical terms are reduced through optimization toward a quasi-symmetric magnetic configuration and there is a direction in which the flow damping is reduced as there is in a tokamak, other terms in the momentum balance equation may become important. Experimentally, large flow velocities are regularly observed in the direction of symmetry in tokamaks in the absence of injected momentum [49]. In DIII-D experiments with balanced co- and counter-injected beams (resulting in zero net injected momentum), the resulting rotation profile is indicative of a large amount of apparent torque generated by the plasma [73]. When beams were used to zero out all plasma rotation, the torque which was deposited to accomplish this zero rotation profile was approximately the same as an entire neutral beam (one of three), suggesting that the “intrinsic torque” provided by the plasma was approximately the same as a single neutral beam in this case [73].

In HSX, there are large flows measured in the direction of symmetry in the absence of injected momentum [74]. Because the flows in the symmetric direction in HSX may be analogous to those in the toroidal direction in a tokamak, first the momentum balance in a tokamak will be explored to find which terms may apply in a quasi-symmetric configuration such as HSX. When all possible non-ambipolar sources are included and the restriction is imposed that the net radial current must sum to zero on the time scale of the radial force balance, the momentum evolution equation in the

toroidal direction in a tokamak can be described as [75]

$$\begin{aligned}
 \underbrace{\frac{1}{V'} \frac{\partial}{\partial t} (V' L_t)}_{\text{inertia}} &\simeq - \underbrace{\langle \mathbf{e}_\zeta \cdot \nabla \cdot \bar{\pi}_{i\parallel}^{NA} \rangle}_{\text{non-res. NA } \tilde{B}_\parallel} - \underbrace{\langle \mathbf{e}_\zeta \cdot \nabla \cdot \bar{\pi}_{i\perp} \rangle}_{\text{classical, neoclassical}} \\
 &\quad - \underbrace{\frac{1}{V'} \frac{\partial}{\partial \rho} (V' \Pi_{iRS\zeta})}_{\text{ion Reynolds stress}} + \underbrace{\langle \mathbf{e}_\zeta \cdot \tilde{\mathbf{J}} \times \tilde{\mathbf{B}} \rangle}_{\text{Maxwell stress}} \\
 &\quad + \underbrace{\langle \mathbf{e}_\zeta \cdot \tilde{\mathbf{J}}_{\parallel mn}^{NA} \times \tilde{\mathbf{B}}_{\perp mn}^{NA} \rangle}_{\text{Resonant NA } \tilde{B}_{mn}} - \underbrace{\dot{\rho}_{\psi_p} \partial L_t / \partial \rho}_{\dot{\psi}_p \neq 0 \text{ transient}} \\
 &\quad + \underbrace{\langle \mathbf{e}_\zeta \cdot \sum_S \bar{\mathbf{S}}_{sm} \rangle}_{\text{mom. sources}},
 \end{aligned} \tag{2.4}$$

where  $L_t \equiv m_i n_{i0} \langle R^2 \bar{V}_i \cdot \nabla \zeta \rangle$  is the angular momentum in the toroidal ( $\zeta$ ) direction,  $\langle \dots \rangle$  indicates an average over the flux surface and an overbar indicates a time average.

The first term is the neoclassical non-ambipolar particle transport due to deviations from perfect axi-symmetry in a tokamak (or quasi-symmetry in a stellarator), and the second term is the neoclassical viscosity. These terms were examined in Section 2.2 and are calculated using the PENTA code for HSX. It should be noted that even in tokamaks, when the non-axisymmetric component of the magnetic field becomes large enough (due to large toroidal field ripple or non-resonant magnetic perturbations, for example), the intrinsic toroidal rotation velocity can be dominated by neoclassical processes [76].

In HSX, the plasma  $\beta$  is very low across the minor radius (always  $<0.5\%$  everywhere, and usually  $<0.1\%$  outside of the core region ( $r/a > 0.2$ )), so that fluctuating magnetic terms may be neglected (this is demonstrated more rigorously in Section 2.3.2). This leads to a simplified expression in which, in the absence of external sources, the neoclassical terms and the Reynolds stress are the only relevant contributions to the momentum balance in steady state HSX plasmas. The Reynolds stress term will now be explored, along with a few other terms which may be important in some situations, but are not expected to play a dominant role in HSX discharges.

### 2.3.1 Reynolds stress

The Reynolds stress,  $\nabla \cdot \langle \rho \mathbf{V} \mathbf{V} \rangle$ , is the main term in which fluid fluctuations enter into the momentum balance, and is therefore the term in which electrostatic microturbulence is expected to play a role in confined plasmas. It is a divergence term, so it requires a boundary to “push off” of in order to provide net rotation, otherwise it only transports momentum from one place to another. In tokamaks, the Reynolds stress is often assumed to play a dominant role in toroidal momentum balance due to the minimized role of neoclassical effects in the symmetric direction [77]. In addition to flow in the toroidal direction, Reynolds stress can also drive mean poloidal flow in a tokamak edge when waves propagate through the separatrix [78, 79].

The Reynolds stress term can be decomposed into three components, including a diffusive term proportional to the gradient of the velocity, a pinch term proportional to the velocity, and a residual stress term which is proportional to neither the velocity nor its gradient. For the Reynolds stress in some arbitrary direction  $\beta$  within a flux surface, such as the direction of symmetry in a tokamak or a quasi-symmetric stellarator, the Reynolds stress is often decomposed and expressed as [77, 80]

$$\langle \tilde{v}_r \tilde{v}_\beta \rangle = -\mu_\perp \nabla v_\beta + V_{pinch} v_\beta + \Gamma_\beta^{RS} \quad (2.5)$$

where  $\mu_\perp$  is the perpendicular momentum diffusivity,  $V_{pinch}$  is a convective pinch velocity and  $\Gamma_\beta^{RS}$  is referred to as the “residual stress”.

When collisionless trapped electron modes are the dominant instability, as they are expected to be in HSX [81, 82], perpendicular momentum diffusivity is predicted to have the same magnitude as ion and electron thermal diffusivity ( $\mu_\perp \approx \chi_i \approx \chi_e$ ) [77]. Experimentally in tokamaks, this has been found to be a valid approximation to within a small factor ( $< \sim 2$ ) in TFTR [83], DIII-D [84] and ASDEX Upgrade [85]. Studying the momentum diffusivity will not be a focus of this work, but it would certainly play a role in momentum transport if the neoclassical flow damping term were small enough.

The second component of the Reynolds stress is the anomalous pinch, the part proportional to  $v_\beta$  in Equation 2.5. In systems which have been sufficiently optimized for quasi- or true axisymmetry and which have no injected momentum, a momentum pinch is required in order to enable a peaked flow profile. Gyrokinetic theory predicts that the momentum pinch is generally directed inwards, regardless of the mode of the turbulence which drives the fluctuations [86]. One exception is the thermoelectric pinch, which can go either direction when large ion temperature gradients are present [86], but this is not expected to be the case in HSX plasmas. Turbulent momentum pinches have been used to explain core toroidal rotation in tokamaks with no momentum input, where momentum is generated at the edge of the plasma by various mechanisms and is convected inward by the momentum pinch component of the Reynolds stress [77, 87]. As an indication that there may be a turbulent momentum pinch in HSX, the flow velocity in the helical direction of symmetry as measured by CHERS is plotted in Figure 2.8 (reproduced from [74]).

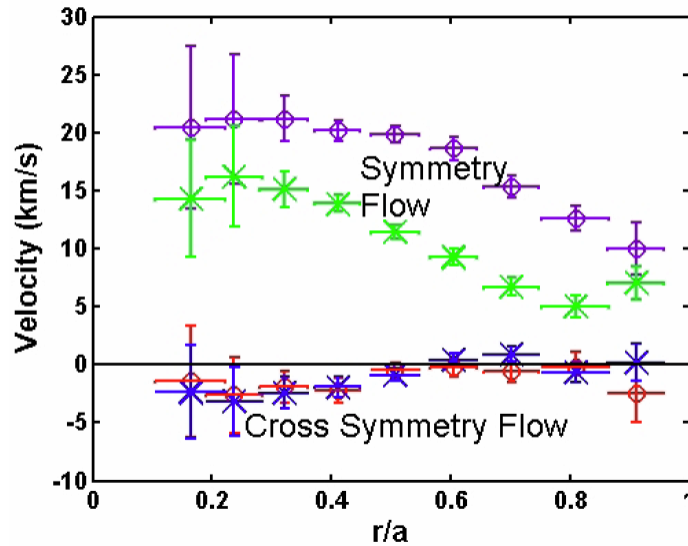


Figure 2.8 Flow velocity in the helical direction of symmetry and cross-symmetry direction in HSX as measured by CHERS with 100 kW (purple O's) and 50 kW (green X's) of injected ECRH [74].

As shown in Figure 2.8, the flow is mostly in the direction of symmetry and the velocity profile in the direction of symmetry is peaked in the core of HSX. In the absence of energetic neutral beams which inject momentum in the core of the plasma, momentum must be injected from the edge and transported inward via a momentum pinch if there is core rotation. This flow profile could be due to neoclassical forces, as discussed in sections 2.1 and 2.2, or it could be a turbulent momentum pinch if the neoclassical term in the momentum balance equation is subdominant to the Reynolds stress term. The increase in rotation velocity with heating power would be expected if turbulence were driving the flows, due to increased fluctuation levels caused by instabilities being more destabilized. The measurement of the competition between the neoclassical and Reynolds stress terms is the subject of this work, although the momentum pinch itself is not the direct target of study.

The remaining component of the Reynolds stress, termed the “residual stress”, is the component of the momentum transport which is neither proportional to the flow velocity nor its gradient [88]. In the absence of other momentum sources, this term is necessarily the source from which any fluctuation-driven intrinsic flow must arise assuming a  $V = 0$  initial condition. The momentum generated by the residual stress can then be transported elsewhere via diffusion or the momentum pinch. One way that this residual stress can be measured experimentally is by producing plasmas with zero rotation but which have a finite applied neutral beam torque. Because the diffusive and pinch terms vanish in the absence of flows, this gives a measurement of the residual stress. Using this technique, experiments in DIII-D found that the bulk of the residual stress is generated at the edge [89], which agrees with the prediction made by theory that any residual stress must be generated by breaking the symmetry in the  $k_{\parallel}$  spectra of the turbulence [88]. In tokamaks, edge symmetry breaking is only expected when there is up-down asymmetry, which would correspond

to the breaking of stellarator symmetry in HSX. HSX maintains stellarator symmetry in the confinement region in all configurations examined here, however, so it is not clear where the necessary  $k_{\parallel}$  asymmetry would arise, unless torque could propagate in from the scrape off layer.

While the Reynolds stress and processes described in this section represent the most likely contributions to the momentum balance aside from the neoclassical term in HSX, as they are predicted to be in tokamak devices, there are additional terms that have been ignored which may also play a role. Some of these will be explored in the next sections.

### 2.3.2 Maxwell/kinetic stress

In plasmas in some devices, the fluctuating magnetic component of the field drives relevant levels of flow through the Maxwell (or kinetic) stress,  $\tilde{\mathbf{J}} \times \tilde{\mathbf{B}}$  [90]. In the MST reversed field pinch, the Maxwell stress has been measured using probes and magnetic diagnostics to be large and, along with the measured Reynolds stress, accounts for the observed rotation following reconnection events [91]. In the stellarator TJ-II, there are also observed magnetic fluctuations which have been linked to the generation of poloidal rotation near resonant low-order rational surfaces [92].

In HSX, the plasma beta is low and there are no low order rational surfaces in the confinement region. There are therefore, as expected, no observations of fluctuating magnetic modes which may drive rotation in a similar manner. There is microturbulence, however, which can exhibit electromagnetic behavior that may provide torque via the Maxwell stress, but it will be shown that the fluctuations in HSX can be considered electrostatic for most purposes, and therefore they do not provide torque in this manner.

For the turbulence to be considered electrostatic, the parallel Alfvén frequency must be fast compared to the thermal electron transit frequency and the drift frequency [93, 94]. For parallel dynamics, this translates to a criteria that the normalized plasma pressure  $\beta = 2\mu P/B^2$  must

satisfy the expression

$$\beta \ll \frac{m_e}{M_i}, \quad (2.6)$$

where  $\frac{m_e}{M_i}$  is the electron to ion mass ratio. This expression is valid for the edge of HSX, as demonstrated in Figure 2.9(a), which plots the mass ratio for hydrogen ions as well as the plasma  $\beta$  calculated from fitted temperature and density inputs to PENTA. These inputs are based on Thomson scattering measurements for  $T_e$  and  $n_e$  and CHERS measurements for  $T_i$  in a QHS plasma with 50 kW of input heating.

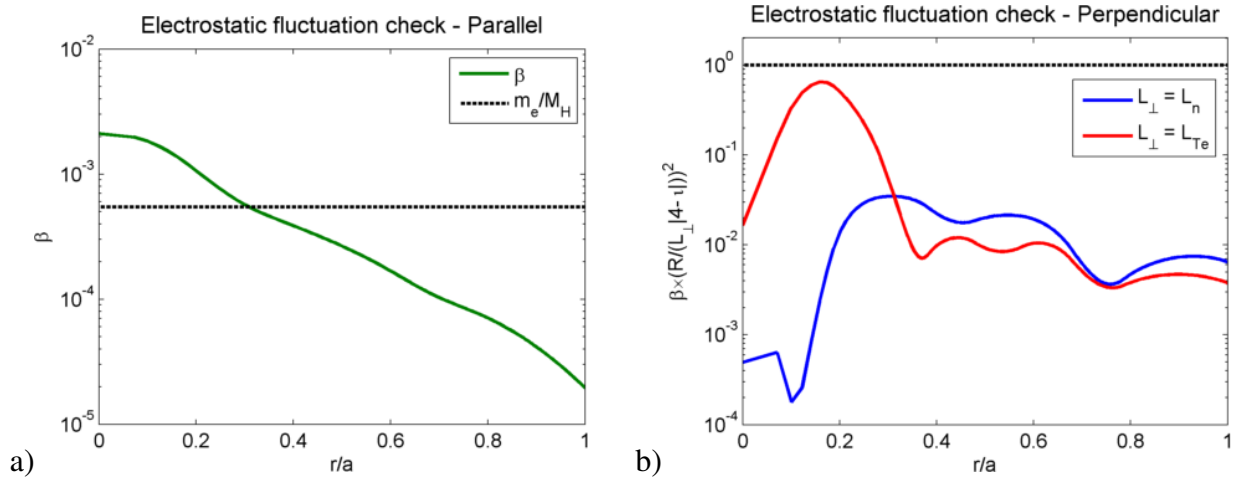


Figure 2.9 Tests of the assumption that fluctuations are electrostatic: (a) plasma  $\beta$  across the minor radius as compared to the mass ratio, and (b) the ratio of  $\beta$  to the quantity on the right hand side of Equation 2.7.

For perpendicular drift dynamics, which should be more relevant for drift wave phenomena than the parallel dynamics, the plasma  $\beta$  must be compared to the ratio of the magnetic connection length ( $qR$  in a tokamak,  $\frac{R}{|N-M\iota|}$  in a quasi-symmetric stellarator) to the perpendicular gradient scale length. For the fluctuations to be considered electrostatic, then [93, 94]

$$\beta \ll \left( \frac{L_{\perp} |N - M\iota|}{R} \right)^2, \quad (2.7)$$

where  $L_{\perp}$  is the perpendicular gradient scale length for the parameter which destabilizes the dominant instability. For HSX, the density gradient is expected to be driving turbulence in the edge, so

that  $L_{\perp} = L_n = \left| \frac{n_e}{\nabla n_e} \right|$ . The flux surface averaged density gradient scale length is on the order of  $\sim 2 - 3$  cm in the edge of HSX. As seen in Figure 2.9(b), the relationship in Equation 2.7 is well-satisfied across the minor radius of HSX, especially in the edge where these studies are performed, and the drift wave turbulence can therefore safely be assumed to be electrostatic.

Because the turbulence may be considered electrostatic and there is no expectation or observation of tearing modes in these plasmas, Maxwell stress is not expected to play a role in the momentum balance, and will therefore be neglected in this work.

### 2.3.3 Ion orbit loss

In tokamaks, thermal ion orbit loss has been invoked as a mechanism to explain intrinsic torque observed near the separatrix [95, 96]. Because co-moving ions drift inward and counter-moving ions drift outward (where co- and counter- are in reference to the direction of plasma current in a tokamak), there is a preferential loss of counter-moving ions near the separatrix in a tokamak which leads to some finite amount of co-directed rotation at the edge. Thermal ion orbit loss models have been shown to account for about half of the intrinsic toroidal rotation localized in the far edge (outside of  $r/a \approx 0.98$ ) in experiments at DIII-D, although the remaining torque could not be accounted for [96].

In HSX, the mean free path of ions near the last closed flux surface is short, on the order of  $\sim 3$  m. At the same time, parallel connection lengths to the wall for particles sourced within an ion gyroradius from the last closed flux surface are long due to the lack of a tokamak-like X-point (10's to 100's of meters or more, depending on the field line), so that particle momentum is not quickly lost to the wall when orbit excursions take particles outside of the confinement region.

In addition to this, the radial excursion of ions off a flux surface which would lead to ion orbit loss scales with the ion banana orbit width. In a tokamak, this is  $\Delta r = v_{||i} / \omega_{c\theta}$ , where  $v_{||i}$  is the parallel ion velocity and  $\omega_{c\theta} = ZB_{\theta} / m_i$  is the poloidal ion cyclotron frequency. In HSX, this ion



banana width can be approximated by using a large aspect ratio expansion for  $B_\theta$  along with the conversion  $q \Rightarrow 1/\iota_{eff}$ , where the effective rotational transform for HSX is  $\iota_{eff} = |n - m\iota| \approx 3$ . The equation for the half-width of an ion banana orbit  $\Delta r$  in a quasi-symmetric stellarator then becomes

$$\Delta r \approx \frac{v_{||i} m_i}{\iota_{eff} e B_0} \frac{R_0}{r}, \quad (2.8)$$

where  $r$  and  $R_0$  are the minor and major radii of the device, respectively, and  $B_0$  is the main magnetic field strength. Based on Equation 2.8, the half width of a banana orbit near the last closed flux surface in HSX for a thermal ion would be  $\sim 2$  mm, only about 3 times as large as the ion gyroradius. Because of the combination of high collisionality, long connection lengths and small banana width, ion orbit loss is not expected to play a large role in the momentum balance in HSX.

### 2.3.4 Charge exchange drag force

HSX has a non-negligible neutral particle density throughout the plasma radius. Due to the relatively low density of the plasma, the mean-free path of a hydrogen atom with the energy of molecular disassociation is long compared to the minor radius of the device, so that there is finite atomic hydrogen density throughout the volume of the plasma. While the neutral particle density is only a small fraction of the plasma density, charge exchange with neutral particles may still represent a significant contribution to the momentum balance and must be considered.

Charge exchange drag produces a non-ambipolar radial particle flux because it acts only on the ions and drives them in the  $\mathbf{F}_{CX} \times \mathbf{B}$  direction, where  $\mathbf{F}_{CX}$  is the charge exchange drag force which is directed counter to the direction of ion flow. If the poloidal direction is defined as  $\hat{\mathbf{e}}_\theta$  for this simple explanation, this corresponds to flow from a positive  $E_r$  (positive  $\mathbf{v}_{E \times B} \Rightarrow$  positive  $\frac{E_r}{B} \hat{\mathbf{e}}_\theta$ ), then  $\mathbf{F}_{CX}$  is in the negative  $\hat{\mathbf{e}}_\theta$  direction for flow caused by a positive  $E_r$ . The toroidal direction  $\phi$  is defined as the direction of the main toroidal field  $\mathbf{B} \sim B_0 \hat{\phi}$  (this all results in the right-handed

coordinate ordering:  $(\rho, \phi, \theta)$ ). The ion flux resultant from the  $\mathbf{F}_{CX} \times \mathbf{B}$  force is then in the positive  $\hat{\rho}$  direction, which causes a radial current  $\mathbf{J}_{r,CX}$  in the positive  $\hat{\rho}$  direction. This radial charge flux will lead to a smaller value of  $E_r$  and therefore a reduced drive for the flows being driven by the original  $E_r$ . This result is intuitively satisfying, in that volumetric charge exchange cannot “spin up” the plasma by acting as a force on only positively charged particles, and charge exchange indeed acts only as a drag on the plasma rotation. It will always drive the radial electric field back towards zero.

While volumetric charge exchange may not affect the plasma potential structure, poloidal asymmetry in charge exchange has been shown to affect the radial electric field in tokamaks in the Pfirsch-Schlüter collisionality regime when neutral fractions are as small as  $10^{-3}$  [97, 98]. This arises from poloidal asymmetries in the neutral fueling which cause local cooling and flows to develop within a surface. While this may possibly have some effect on the rotation in HSX, it is expected that this effect is small relative to others in the experiments presented here. The high aspect ratio of the device reduces the effects of local cooling from recycling particles compared to a lower-aspect ratio tokamak, and the presence of hydrogen neutrals throughout the volume of the plasma leads to the expectation that charge exchange losses are not especially localized. The region near the puff may be an exception, but once the hydrogen atoms disassociate from the molecule, their mean free paths through the plasma are long so that their spatial distribution would not be localized.

Although the charge exchange mechanism is not used to explain rotation drive in HSX, it should nonetheless be taken into account in the full momentum balance as a damping mechanism if the flows are to be calculated. Particularly in the QHS configuration, neutral damping was found to be the dominant calculated damping mechanism in previous studies in HSX, although experimental damping rates were found to be higher [99].

### 2.3.5 ECRH-driven electron flux

In a configuration with collisionless loss orbits, additional rotation can be induced due to electrons being heated into these loss cones in velocity space. In this case, a more positive radial electric field is generated than what may be calculated neoclassically by DKES and PENTA due to the preferential loss of electrons in the heating region [100]. Heuristically, this effect should be larger when using X-mode heating than it is when using O-mode, due to the heating mechanism pumping energy directly into the perpendicular velocity in X-mode, which drives a population of deeply trapped particles.

In HSX, O-mode heating is used in the 1 T plasma experiments presented here, which is calculated to drive a significantly smaller non-thermal portion of the distribution function than the X-mode heating used in 0.5 T plasmas, based on modeling using the GNET code [101]. The effect of the core heating on the distribution function diminishes towards the edge of the plasma where the experiments presented here are performed, as well.

For all of the discharges studied here, the density was kept high enough so that there was no indication of a suprathermal electron population. When the line averaged density as measured by the interferometer is larger than  $\sim 3 \times 10^{18} \text{ m}^{-3}$  for the heating powers used here, the plasma stored energy as measured by the diamagnetic loop and by the Thomson scattering system are in agreement to within experimental errorbars. At lower densities, the diamagnetic loop observes a measurably higher stored energy than the Thomson scattering, which does not properly interpret the high energy tail in the distribution function caused by the ECRH due to the assumption of a thermalized distribution function.

Another indication of a suprathermal electron population is the persistence of a signal on the electron cyclotron emission diagnostic (ECE) and the diamagnetic loop long after the bulk plasma stored energy has decayed away. The ECE signals after ECRH turn-off are plotted in Figure 2.10

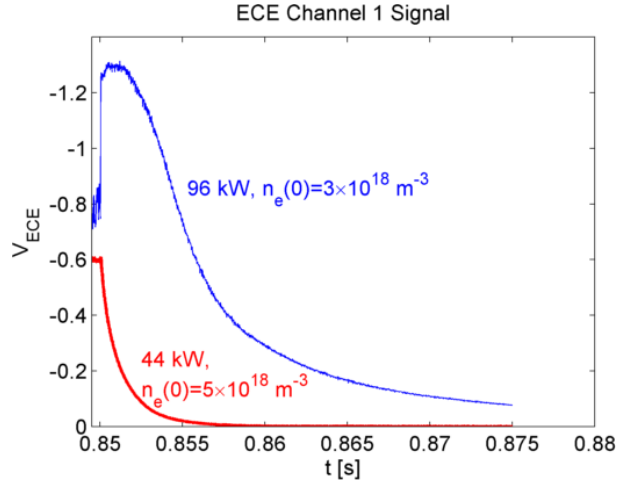


Figure 2.10 Comparison of ECE signals after ECRH turn-off from a set of 96 kW, low density discharges with evidence of a suprathermal electron population and a set of 44 kW, high density discharges without it [courtesy of Gavin Weir].

for two sets of discharges with different heating powers and densities using a sample frequency channel which primarily observes emission from the edge. For the discharges with 44 kW of injected heating and a core density  $n_e(0) = 5 \times 10^{18} \text{ m}^{-3}$  from Thomson scattering, there is a smooth exponential decay of the radiation temperature as soon as the heating is turned off. For the discharges with 96 kW of injected heating and a core density  $n_e(0) = 3 \times 10^{18} \text{ m}^{-3}$ , where the power per particle is much higher, there are multiple timescales to the decay, and there is significant signal remaining long after the end of the discharge, which is indicative of a suprathermal electron population. These indicators were again not present in any of the discharges studied in this work, which were all high-density plasmas with 44 kW of injected heating. This should give confidence in the assumption of a reasonably thermalized distribution function.

The effect of the ECRH on the distribution function is therefore not taken into account in this work, although it may play a role in some cases, particularly in configurations which deviate significantly from quasi-symmetry, where a significant portion of the high energy velocity distribution

will be in a loss cone. ECRH-driven particle losses would always lead to a more-positive radial electric field.

### 2.3.6 Turbulent parallel flow acceleration

A mechanism of turbulent acceleration of parallel flows which is distinct from the divergence of the Reynolds stress has recently been invoked as another possible source of intrinsic rotation in tokamaks [102]. In the presence of an ion temperature gradient, gyrokinetic theory shows that a drive term exists which is not proportional to either the velocity or its gradient. This allows it to spin up a plasma from rest, similar to the residual stress component of the Reynolds stress.

While this new mechanism deserves investigation by the magnetic confinement community, it will not be experimentally examined for this work in HSX, but is mentioned here for completeness. The probes used here are specifically designed to measure the divergence of the Reynolds stress, which does not capture the physics of this torque mechanism. This derivation has also not yet been performed for stellarators, nor has it been examined for modes other than ion temperature gradient turbulence, although presumably the physics is similar in stellarators as they are in tokamaks.

## 2.4 Rotation in configurations approaching quasi-symmetry

Unlike a classical stellarator, which has multiple terms in its magnetic spectrum and therefore multiple classes of trapped particles which lead to non-ambipolar particle transport, the ambipolarity constraint is satisfied automatically (total charge flux  $\sum_a q_a \Gamma_a(E_r) = 0$  for all values of  $E_r$ ) for an ideal tokamak [103, 104] or a perfectly quasi-symmetric stellarator [20, 26]. Intrinsic rotation in these configurations must therefore be determined using higher order gyrokinetic calculations [105, 106, 107]. In these cases, the plasma is “free to rotate” at any velocity, since  $E_r$  in Equation 2.1 is no longer constrained and the velocity  $V$  therefore now becomes a free parameter. This

remains the case as long as the flow values are modest, but even a perfectly quasi-symmetric device would not be allowed to rotate at nearly sonic speeds at low collisionality in the way that a tokamak can, because particle flux becomes non-ambipolar again at large values of  $E_r$  in any non-axi-symmetric system [108].

Any real device cannot be perfectly symmetric, though. It can be shown that in the case of a stellarator, even leaving aside as-built device considerations, no configuration exists that is perfectly quasi-symmetric without being axisymmetric [23]. So all real devices have some non-zero ripple, which will lead to some amount of non-ambipolar neoclassical particle transport. This in turn causes there to be a finite number of neoclassically predicted roots at which each surface must have the specified value of  $E_r$  in order for the particle transport to be ambipolar. In the absence of other current or momentum sources, any deviation from this value will drive a radial current which will quickly change the potential on the surfaces until  $E_r$  satisfies the ambipolarity constraint and equilibrium is reached.  $E_r$ , and subsequently the rotation velocity, would then be expected to be fixed to this neoclassically determined value for any real device with finite ripple, including all tokamaks, if the neoclassical term was the only term in the momentum balance. This is in conflict with experimental observations of arbitrary rotation velocities in tokamaks [49], demonstrating that there is some finite amount of ripple that is acceptable while still allowing arbitrary rotation and radial electric field values.

If the non-ambipolar neoclassical particle transport is reduced to a small enough value, then the turbulence-driven Reynolds stress can provide enough torque to rotate the plasma and set  $E_r$  to a different value that still results in zero net radial current when all of the stresses are accounted for [109]. The competition of these two effects, neoclassical viscosity and Reynolds stress, will now be explained in further detail.

The momentum equation summed over all species is

$$\mathbf{J} \times \mathbf{B} - \nabla p = \nabla \cdot (\rho \mathbf{V} \mathbf{V} + \boldsymbol{\pi}) + \frac{\partial(\rho \mathbf{V})}{\partial t}. \quad (2.9)$$

Here  $\boldsymbol{\pi}$  represents the sum of both the neoclassical and turbulent components of the viscous stress, and  $\rho \mathbf{V} \mathbf{V}$  is the Reynolds stress. Decomposing the current and magnetic field into equilibrium and fluctuating components due to turbulence ( $\mathbf{J} \rightarrow \mathbf{J}_0 + \mathbf{J}_1$ ,  $\mathbf{B} \rightarrow \mathbf{B}_0 + \mathbf{B}_1$ , where  $\mathbf{J}_0 \times \mathbf{B}_0 = \nabla p_0$ ), taking the scalar product of Equation 2.9 in the direction of quasi-symmetry  $\hat{e}_\beta$  and averaging over a flux surface,  $\langle \dots \rangle$ , gives (following reference [109], but taking an arbitrary direction  $\hat{e}_\beta$ )

$$\frac{\partial \langle \rho \mathbf{V} \cdot \hat{e}_\beta \rangle}{\partial t} = \langle \nabla \cdot (\rho \mathbf{V} \mathbf{V} + \boldsymbol{\pi} + \mathbf{M}) \cdot \hat{e}_\beta \rangle, \quad (2.10)$$

with the Maxwell stress  $\mathbf{M}$  defined as

$$\mathbf{M} = \frac{1}{\mu_0} \left( \frac{B_1^2}{2} \mathbf{I} - \mathbf{B}_1 \mathbf{B}_1 \right). \quad (2.11)$$

In steady state, the left hand side of Equation 2.10 goes to zero, and the flow drive and damping terms on the right hand side are brought into equilibrium. In the case of HSX, low  $\beta$  operation results in the Maxwell stress term becoming small compared to the Reynolds stress and viscosity terms, as demonstrated in Section 2.3.2. Thus in steady state, these are the only two terms that are expected to contribute, so that in a fully ionized plasma with no injected momentum,

$$\langle \nabla \cdot (\rho \mathbf{V} \mathbf{V} + \boldsymbol{\pi}) \cdot \hat{e}_\beta \rangle = 0, \quad (2.12)$$

where the Reynolds stress and neoclassical damping balance each other in the direction of symmetry to determine the global rotation.

In a non-optimized stellarator, the neoclassical viscosity term is large, so the fluctuating terms vanish to leading order in the momentum balance equation. Over short radial scale lengths, variations may exist in the form of zonal flows, but the global rotation is determined by neoclassical processes. When neoclassical viscosity is sufficiently reduced, however, the fluctuating Reynolds

stress and Maxwell stress terms become relevant again, and all of the terms must be taken into account, as they need to be in tokamaks [26]. The next obvious question which this leads to is: at what point does this transition happen? How close to quasi-symmetry must a configuration be before the fluctuating terms in the momentum balance begin to compete with the neoclassical one, and how should this level of symmetry be quantified? In order to investigate these questions in HSX, the configurational space of the HSX device must first be understood.

### 2.4.1 Magnetic configurations in HSX

Along with the main coil set, HSX has a set of planar auxiliary coils which can be energized in order to break the designed quasi-symmetry. The effects of magnetic geometry on the properties of confinement and flows can then be explored. The “Mirror” configuration used in this work [99] is designed in such a way that it adds an additional large  $n=4, m=0$  mode to the magnetic spectrum while attempting to balance positive and negative toroidal flux so as to leave the rotational transform relatively unchanged from the QHS configuration. Experiments are also run in the “Flip-1-4” configuration, which includes a smaller amplitude  $n=4, m=0$  mode as well as an  $n=8, m=0$  mode. This allows the axis to be aligned with the axis position in the QHS configuration so that stationary diagnostics are properly aligned in the core. Figure 2.11 shows the rotational transform profile as a function of the square root of toroidal flux normalized to the flux surface average field strength ( $\sqrt{\Phi}/\langle|B|\rangle$ ) for the QHS, Flip-1-4 (labeled “FL14”) and Mirror magnetic configurations from vacuum VMEC equilibria. Plotting the horizontal axis in this way as opposed to the normalized flux value  $\rho = \sqrt{\psi/\psi_{LCFS}}$  demonstrates the difference in volume between the configurations.

The lowest order rational surfaces ( $n, m \leq 20$ ) with values of  $n$  divisible by 4 (the field periodicity of HSX) are also plotted in Figure 2.11. Finite bootstrap current would reduce the rotational



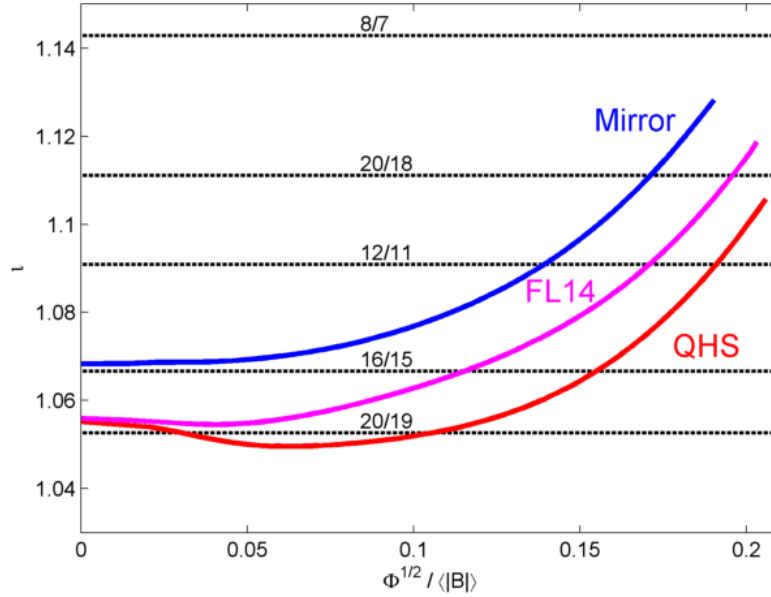


Figure 2.11 Rotational transform profiles for the QHS, Flip-1-4 (labeled FL14) and Mirror configurations along with the lowest order rational surfaces.

transform, but the plasma current which is measured is not sufficiently large to change the rotational transform profile enough in any of these configurations to introduce low order islands into the confinement region.

Although the QHS configuration has been optimized to be dominated by a single helical mode in the magnetic field strength in the Boozer decomposition [20] (the  $n=4$ ,  $m=1$  mode), there are many additional modes with finite amplitude across the minor radius of the plasma. These are presented in Figure 2.12(a), which gives the largest 8 modes in the spectrum for the QHS configuration, evaluated at the outermost flux surface. These modes are small compared to the main  $n=4$ ,  $m=1$  mode, but they play an important role in the finite amount of neoclassical non-ambipolar transport which is being studied here. The main  $1\text{ T } n=0$ ,  $m=0$  term is not plotted here.

The Mirror configuration alters the equilibrium from the QHS baseline primarily by greatly increasing the  $n=4$ ,  $m=0$  term in the spectrum, which is plotted in Figure 2.12(b). The addition of the large secondary mode to the magnetic spectrum leads to an increase in flow damping and

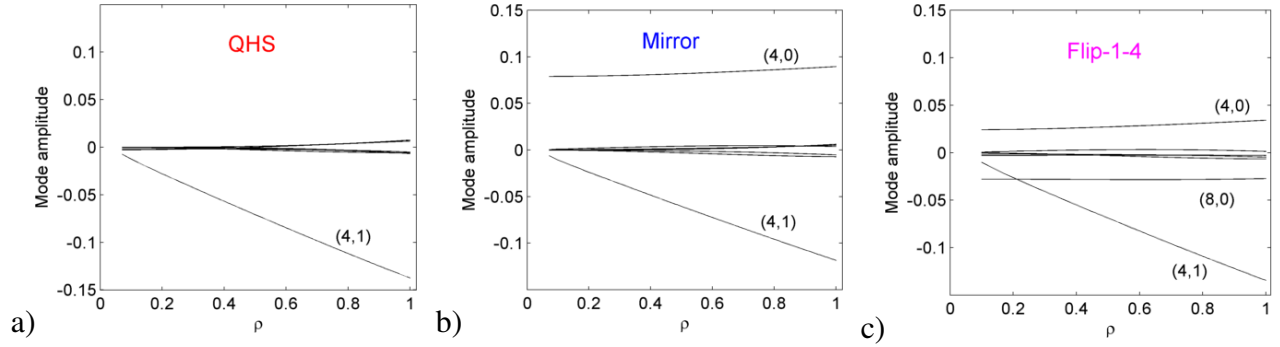


Figure 2.12 Boozer spectra for the dominant harmonics in the (a) QHS, (b) Mirror and (c) Flip-1-4 configurations.

neoclassical particle and heat transport throughout the plasma [99, 34]. The effect of the modes in the Flip-1-4 configuration are similar, although the mode amplitudes of the symmetry breaking terms are smaller, as seen in Figure 2.12(c).

While magnetic configurations with larger symmetry breaking terms such as an  $n=1$  or  $n=2$  perturbation would increase the neoclassical transport beyond that of the Mirror configuration used in this work, generating these non-stellarator symmetric configurations using the existing HSX coil set and vacuum vessel is not effective due to the close fit of the coils to the plasma. Further explanation of this and analysis of other configurations, both stellarator symmetric and non-stellarator symmetric, are given in Appendix B.

### 2.4.2 Effective ripple

One parameter which may be used to approximate how close a magnetic configuration is to quasi-symmetry is the effective ripple ( $\epsilon_{eff}$ ), which quantifies the thermal neoclassical particle losses at low collisionality [110]. In the low collisionality regime, the neoclassical particle and energy losses scale with  $\epsilon_{eff}^{3/2}/\nu$ . If achieving non-neoclassical rotation is dependent on reducing the neoclassical non-ambipolar particle transport, then the effective ripple should quantify this

transport well in the low collisionality regime and therefore be a relevant quantity for determining the threshold for non-neoclassical rotation.

Figure 2.13 shows the effective ripple in the QHS, Flip-1-4 and Mirror configurations of HSX used in this work across the minor radius, along with that of the unoptimized stellarators TJ-II [111] and LHD [112, 113], and the spherical tokamak NSTX with RMP coils energized [114]. The “inward shifted” configuration in LHD was one designed to reduce the neoclassical transport in the core relative to the “standard” configuration.

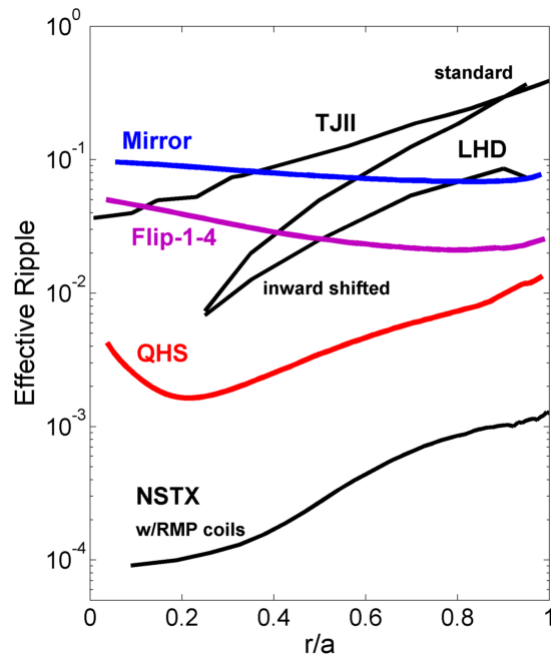


Figure 2.13 Effective ripple in HSX QHS, Flip-1-4 and Mirror configurations compared to other devices [111, 112, 113, 114, 115].

A larger-scale tokamak like ITER would have an effective ripple two or more orders of magnitude lower than that shown here for NSTX with RMP coils [114]. As seen in Figure 2.13, the QHS configuration of HSX has an effective ripple somewhere between that of a conventional stellarator and a tokamak with non-axisymmetric perturbations, while the Mirror configuration has

neoclassical transport properties similar to that of unoptimized stellarators. This makes it an interesting case in examining the transition from configurations which have their radial electric field determined by neoclassical processes, like stellarators, to configurations which are close enough to quasi-symmetric to allow other terms to dominate the momentum balance, like tokamaks. The Flip-1-4 configuration has an effective ripple between that of the QHS and Mirror configurations, and will be used as an intermediate step between the two.

In HSX, thermal ions are not in the low collisionality regime anywhere across the minor radius of the plasma, but thermal electrons are, and are therefore subject to the enhanced transport at low collisionality which is quantified using the effective ripple. The normalized collisionality  $\nu^*$  can be expressed as

$$\nu^* = \frac{\nu R_0}{\iota_{eff} v_T}, \quad (2.13)$$

where  $\nu$  is the particle collisionality,  $v_T$  is its thermal velocity,  $R_0$  is the major radius of the device, and  $\iota_{eff} = |n - m\iota|$  is the effective rotational transform. The normalized collisionality  $\nu^*$  for thermal electrons and ions using data from the QHS configuration is plotted in Figure 2.14, assuming that the  $n=4, m=1$  term is dominant in the magnetic spectrum for the value of  $\iota_{eff}$ . Particles are in the Pfirsch-Schlüter regime if  $\nu^* > 1$ , the low collisionality “banana” regime if  $\nu^* < \epsilon_h^{3/2}$ , and the “plateau” regime for collisionalities between those values [116, 117]. Here  $\epsilon_h$  is the dominant helical ripple, taken for HSX as the  $n=4, m=1$  term as plotted in Figure 2.12. The important transition for this work is between the plateau and low collisionality regimes, where the bounce frequency of a particle becomes larger than the collision frequency, and below which there is a differential particle flux between electrons and ions for most values of the radial electric field. This transition is plotted as a dashed red line in Figure 2.14.

As seen in Figure 2.14, electrons in HSX are in the collisionless regime while ions are in the plateau regime across the minor radius, although some particles of each species would be in different collisionality regimes in a thermalized plasma with a range of particle velocities.

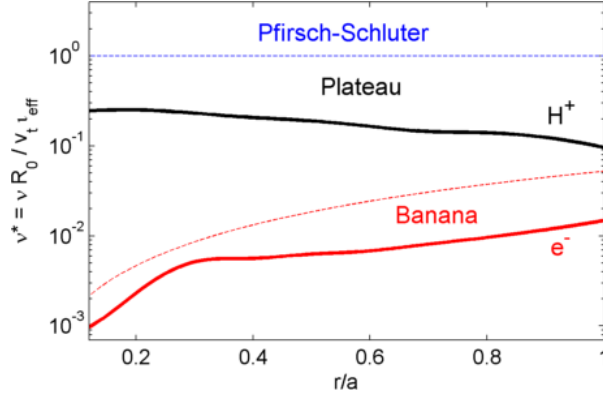


Figure 2.14 Normalized collisionality  $\nu^*$  for thermal electrons and ions in the QHS configuration of HSX.

### 2.4.3 Observations of intrinsic rotation in tokamaks

Experimentally, in low-ripple tokamak plasmas without large sources of injected momentum such as neutral beams, there exists some level of “intrinsic rotation” in the toroidal direction that is apparently sustained by the plasma itself [49]. Exploring this observed intrinsic rotation in tokamaks may provide some insight into what level of intrinsic rotation might be expected in a sufficiently optimized quasi-symmetric stellarator.

For tokamaks very close to axisymmetry, a common empirical scaling has been found for the intrinsic rotation of H-mode plasmas [49]. Using regression analysis to fit sets of data from 6 different tokamak devices, a dimensionless scaling for the intrinsic rotation was found in which the Alfvén mach number  $M_A$  follows the trend

$$M_A = 0.65\beta_T^{1.4}q_*^{2.3}, \quad (2.14)$$

where  $\beta_T \equiv 2\mu_0\langle P \rangle / B_T^2$  is the toroidal plasma beta and  $q_* \equiv 2\pi\kappa a^2 B / \mu_0 R I_p$  is the normalized inverse rotational transform. The Alfvén mach number is related to the velocity by  $v = M_A \frac{B}{\sqrt{\mu_0 \rho}}$ , where  $\rho = n_i m_i$  is the mass density. Interestingly, there was no correlation of the intrinsic rotation in these devices with either collisionality or the normalized gyro-radius, which might be expected if turbulent processes were the cause of the rotation. This result is not understood, as most models

and some experimental evidence of the intrinsic rotation implicate microturbulence as the source of intrinsic rotation [118].

In plasmas in the Alcator C-Mod tokamak, core rotation was found to scale with the edge temperature gradient,  $V_\phi(0) \sim \nabla T|_{edge}/B_\theta$  [119], which is evidence that torque may be supplied at the edge via the residual stress and is then transported inwards to the core.

In L-mode tokamak plasmas, which are more similar to HSX discharges than the H-mode studies discussed above, it has been observed that the intrinsic toroidal rotation can change direction at some density threshold. This intrinsic rotation bifurcation has been associated with a change in the dominant microinstability from trapped electron modes to ion temperature gradient turbulence based on measured density fluctuations [120]. While causation of these two observations is not definitive, it is suggestive that the fluctuations driven by microturbulence may be responsible for the observed intrinsic rotation. No such transport or rotation change has yet been observed in HSX, but it may occur if ion heating were ever implemented and the ratio of ion to electron heating were to be scanned. Investigation into this type of rotation bifurcation (or lack thereof) would give further insight into the nature of the intrinsic rotation in HSX.

Most of the work here concerns non-neoclassical rotation drive, because it is not intuitive that large rotation velocities above the level that is predicted neoclassically should be measured without any injected momentum. Rotation damping, however, is also measured to be anomalously large in tokamaks (above the neoclassical and neutral damping levels) where the neoclassical flow damping is small in the toroidal direction [84, 121]. This is a further indication that other physics may become important when the neoclassical term in the momentum balance has been minimized.

Neoclassical physics may also play a role in tokamaks when toroidal field ripple is large enough or when 3D non-axisymmetric perturbations are applied. Neoclassical toroidal viscosity in tokamaks generally provides a torque in the counter-direction, which opposes the normally-observed co-rotation of H-mode tokamaks [76, 122, 123]. This is closely related to stellarator rotation, where

the non-ambipolar neoclassical particle transport sets some finite level of rotation. The intrinsic rotation of a tokamak is driven toward this neoclassical offset rotation and scales with  $(\delta B/B)^2$  when ripple is added [76, 124].

The competition between the neoclassical effects and the intrinsic rotation which exists due to the non-neoclassical effects discussed here will be crucially important to predicting and understanding the flows in next-generation devices, in both tokamaks and quasi-symmetric stellarators.

## 2.5 Predictions of limits of non-neoclassical $E_r$ determination in HSX

In Section 2.4 it was demonstrated that if the amount of ripple in the magnetic field strength is sufficiently reduced, then other terms in the momentum balance may compete with the neoclassical one to determine the radial electric field. Some estimates of the limits of this effect and calculations applying the theory to HSX plasmas will now be presented.

### 2.5.1 Helander and Simakov estimates

Work by Helander and Simakov predicts that a plasma may have a mean  $E_r$  that deviates from the neoclassical ambipolar root over a radial region  $N$  ion gyroradii wide when the effective ripple satisfies the condition that [26]

$$\epsilon_h^{3/2} < \frac{L}{N\lambda_{MFP}}, \quad (2.15)$$

where  $L$  is the macroscopic scale length and  $\lambda_{MFP}$  is the mean-free path of a thermal ion. This is an order-of-magnitude approximation for when the Reynolds stress may compete with the neoclassical viscosity to determine the global rotation. It was derived by comparing the radial current due to non-ambipolar neoclassical particle diffusion with an estimate of the radial current resultant from the Reynolds stress. Ions and electrons were both assumed to be in the collisionless  $1/\nu$  regime in this analysis, although ions are in the plateau regime in HSX, which would lead to an over prediction of the importance of the neoclassical term when applied to HSX experimental

parameters. This would affect Equation 2.15 by increasing the allowable effective ripple on the left hand side for HSX and making non-neoclassical rotation more accessible than the expression suggests.

To evaluate whether the inequality given in Equation 2.15 is satisfied, the effective ripple in HSX is plotted alongside the right hand side of Equation 2.15 in Figure 2.15(a) for several values of  $N$ . Solving for  $N$  and evaluating for the radial width over which the estimate predicts that an arbitrary mean  $E_r$  may be maintained, this critical radial distance becomes

$$\Delta r_{crit} = N \rho_i = \frac{L}{\epsilon_h^{3/2} \lambda_{MFP}} \rho_i. \quad (2.16)$$

Equation 2.16 has been solved for experimental parameters in HSX and is plotted for the outer half radius in Figure 2.15(b). Figure 2.15(b) is therefore the solution of the intersection of the curves in Figure 2.15(a), with the value of  $N$  applied to give a radial distance. As a reference, the total flux surface averaged minor radius of the plasma up to the given radial location is also plotted as a dotted line.

It is clear that using this estimate, the inner portion of the plasma which has the lowest effective ripple in the QHS configuration ( $r/a < \sim 0.6$ ) is capable of rotating at a velocity determined by processes other than neoclassical transport alone. In this region, the radial width over which non-neoclassical rotation may occur is predicted to be greater than the minor radius of the plasma. In the outer portion of the plasma, the extent of the region over which a deviation from the neoclassical  $E_r$  may be maintained is less than the plasma radius, which suggests that the plasma rotation is primarily determined by neoclassical non-ambipolar transport in this region.

In the far edge region where probe measurements are made ( $r/a > \sim 0.85$ ), the critical value of  $\Delta r$  is at a minimum, on the order of  $\sim 1$  cm. If this estimation for critical  $\Delta r$  were true, the measured radial electric field over this approximate scale size would be expected to average to the neoclassical value. This contradicts Langmuir probe measurements which will be presented in



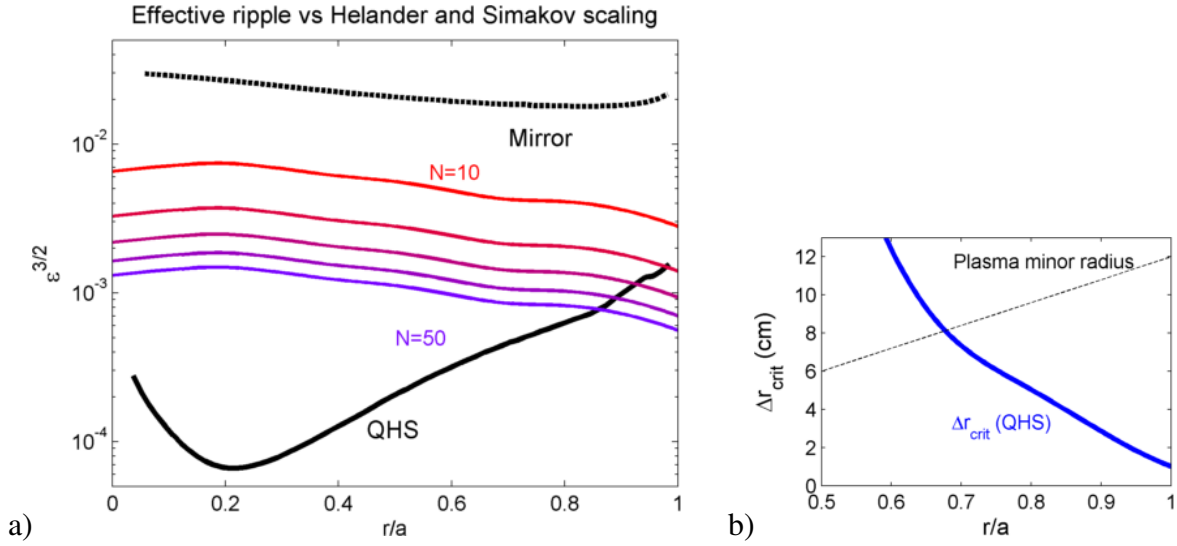


Figure 2.15 a)  $\epsilon_{eff}^{3/2}$  across the minor radius for the QHS and Mirror configurations, along with the RHS of Equation 2.15 plotted for several values of  $N$ , and b) the intersection of these curves: the average radial distance ( $\Delta r_{crit} = N_{crit} \rho_i$ ) over which a mean  $E_r$  may be maintained which deviates from the neoclassical value.

Chapter 4 which show that over a radial region of  $\sim 3$  cm (flux surface averaged  $r$ ), the measured  $E_r$  value does not average out to the neoclassical calculation, as it might in the case of a zonal flow. The measured quantity is consistently more positive than the neoclassical value. This has also been observed in previous experiments in HSX, which will be described later in Section 2.6. This discrepancy may be explained by the fact that the ion collisionality in HSX is higher than it is in the derivation behind Equation 2.16, which leads to reduced neoclassical ion losses from what this basic model assumes. Since ions in the edge of HSX are in the plateau regime, a longer mean-free path does not necessarily lead to greater neoclassical particle losses, as this scaling assumes. The limits given by Reference [26] and Equation 2.15 which are evaluated for HSX in Figure 2.15 should therefore be considered a lower limit on the amount of ripple acceptable in HSX before the radial electric field may be determined by non-neoclassical processes. Because the edge region is approaching the limit for non-neoclassical  $E_r$  determination in Equation 2.15, then, it may be that

the Reynolds stress is capable of being larger than the neoclassical term in the momentum balance in this region.

### 2.5.2 Calculations of closeness to quasi-symmetry by Calvo et. al.

Recent analytical work by Calvo et. al. has also attempted to answer the question of how far from quasi-symmetry a stellarator can be before the determination of the long-wavelength radial electric field is dominated by neoclassical transport processes [21]. This work additionally addresses the separate problem of whether a stellarator is close enough to quasi-symmetry to allow fast rotation in the presence of momentum injection. These analyses can be directly applied to HSX, which is close to quasi-symmetry but not perfectly quasi-symmetric. A summary of the derivation and results from [21] is presented here, along with its application to HSX.

If the magnetic field strength of an approximately quasisymmetric device is decomposed into a quasi-symmetric component and a component which deviates from quasi-symmetry, it can be expressed for flux surface  $\psi$  as

$$B(\psi, \Theta, \zeta) = B_{0,0}(\psi) + B_{N,M}(\psi)\cos(N\zeta - M\Theta) + \sum_{n,m} B_{n,m}(\psi)\cos(n\zeta - m\Theta), \quad (2.17)$$

where  $B_{n,m}$  is the Fourier component of the magnetic field strength with toroidal and poloidal helicity  $n$  and  $m$ , and  $N$  and  $M$  are the toroidal and poloidal mode numbers of the quasi-symmetric component of the magnetic field ( $N = 4$ ,  $M = 1$  in HSX). There are only cosine terms in Equation 2.17 because the magnetic field (as designed) is stellarator symmetric. Another consequence of this is that in HSX, the only non-zero terms in the summation will have values of  $n$  which are multiples of 4 due to the periodicity of the device.

Once the field has been decomposed in this manner, the deviation from true quasisymmetry can be expressed as a small parameter  $\alpha$ , quantified for a given Fourier component of the magnetic

field  $(n, m)$  in HSX as

$$\alpha = \left| \frac{B_{n,m}}{B_{4,1}} \right|, \quad (2.18)$$

where  $B_{4,1}$  is the quasi-symmetric component of the magnetic field strength. This  $\alpha$  in Equation 2.18 is distinct from the effective ripple  $\epsilon_{eff}$  (discussed in Section 2.4.2) in that it only accounts for a single non-quasi-symmetric harmonic in the magnetic field strength, rather than attempting to account for all helical ripples as  $\epsilon_{eff}$  does. Calculations are then made to compare this small parameter  $\alpha$  with other plasma parameters which determine the radial electric field. In this derivation ([21]), standard gyrokinetic ordering is assumed to find that the flux surface averaged radial current, which is used to determine the ambipolarity constraint, is given as

$$\langle \mathbf{J} \cdot \nabla_R \psi \rangle_\psi = O(\alpha)^2, \quad (2.19)$$

so that to first order in  $\alpha$ , the ambipolarity constraint is satisfied for any value of  $E_r$ .

It is found in Reference [21] that if this parameter  $\alpha$  is larger than  $\rho_i/L$ , then the radial electric field must be determined neoclassically. In this case,  $\rho_i$  is the ion gyroradius and  $L$  is the macroscopic scale size, taken here as the minor radius  $a$ .

The second result of reference [21] is that for  $\alpha > \sqrt{\rho_i/L}$ , the plasma may not rotate rapidly, even under the influence of a strong torque such as neutral beams. “Rapid” rotation being allowed in this case does not mean near-sonic flow velocities, because even a perfectly quasi-symmetric configuration cannot rotate at these velocities [108], but rather that  $V_i \gg (\rho_i/L)v_{ti}$  is allowed.

Applying these two tests to HSX, Figure 2.16 plots the factor  $\alpha$  from Equation 2.18 for the largest non-quasi-symmetric modes in HSX using Boozer coordinates, along with the quantities  $\rho_i/a$  as a dashed red line and  $\sqrt{\rho_i/a}$  as a dashed black line. If the value of  $\alpha$  for any mode plotted is larger than the red line ( $\rho_i/a$ ), then according to the analysis,  $E_r$  should be determined neoclassically. The same is true for the black line ( $\sqrt{\rho_i/a}$ ), so that all modes must be smaller than this term for the configuration to allow rapid rotation. The Boozer decomposition of the magnetic

field [125] differs slightly from that given in Reference [21] and shown in Equation 2.17, but it should be a sufficient approximation for these purposes.

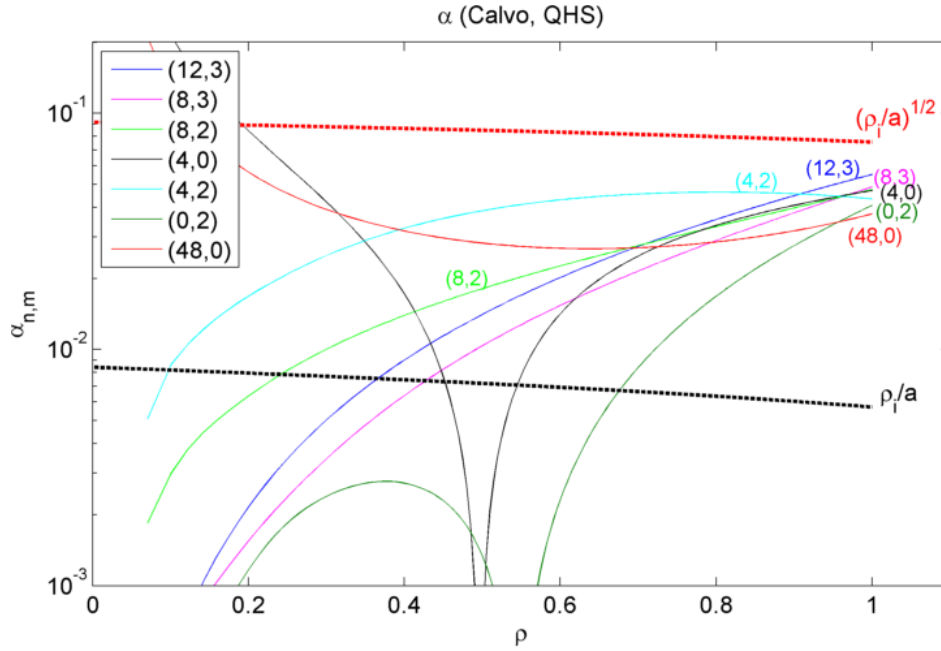


Figure 2.16  $\alpha$  from ref. [21] along with the parameters with which it is to be compared: If  $\alpha > \rho_i/a$ ,  $E_r$  is said to be determined neoclassically (black dotted line), and if  $\alpha > \sqrt{\rho_i/a}$ , then fast rotation is not allowed (red dotted line).

The ordering used in the derivation here requires that  $\alpha \hat{\mathbf{b}}_0 \cdot \nabla_{\mathbf{R}} B_1 > \hat{\mathbf{b}}_0 \cdot \nabla_{\mathbf{R}} B_0$ , where  $B_0$  is the quasi-symmetric component and  $B_1$  is the non-quasi-symmetric component of the magnetic field strength. In general this means that the helicity and amplitude of the perturbation must be large enough compared to the quasi-symmetric field helicity so that new wells are not generated in the large magnetic field gradient regions. This is well-satisfied in the outer radii of HSX, but not in the region where  $r/a < 0.3$ , so the analysis is explicitly not valid in this core region.

As seen in Figure 2.16, although the QHS configuration is optimized to minimize the non-quasi-symmetric modes, there are modes which have values of  $\alpha$  larger than  $\rho_i/a$  across the minor radius of the plasma. The claim is that the radial electric field in HSX should therefore always be dictated by neoclassical processes. This is in contradiction to previous measurements of  $E_r$  in HSX

that will be shown in Section 2.6, as well as the measurements in Chapter 4 which were performed for this work.

All values of  $\alpha$  are less than  $\sqrt{\rho_i/a}$  across the minor radius in Figure 2.16 where the ordering is valid, suggesting that a plasma in HSX may be allowed to rotate at large velocities if there were sufficient torque applied. If neutral beam injection were ever added to HSX, this might be an interesting issue to explore aside from the intrinsic rotation studied in this work.

As a comparison to the calculations for the QHS configuration, the values of  $\alpha$  for the Boozer spectrum in the Mirror configuration is plotted in Figure 2.17. It is clear from this that the (4,0) term which is added to break the symmetry is sufficiently large that fast rotation is no longer possible in this configuration, and that the radial electric field would certainly be expected to be determined dominantly by neoclassical processes.

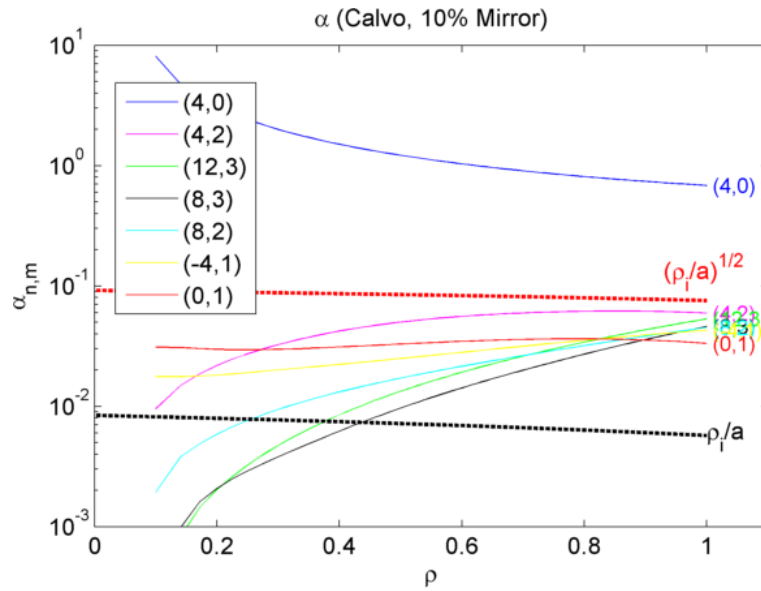


Figure 2.17  $\alpha$  in the Mirror configuration.

It may not be surprising that the result for allowing fast rotation ( $\alpha^2 < \rho_i/a$ ) produces a similar  $(\delta B/B)^2$  scaling for the rotation braking as tokamaks find [76], as discussed in Section 2.4.3.

The result for the radial electric field determination (neoclassical if  $\alpha < \rho_i/a$ ) produces some more questionable implications, however. First, the scaling is linear with  $\alpha$ , where one might expect a scaling of the neoclassical ripple to the  $3/2$  power for ripple-trapped particles, as there is in the scaling presented in the previous section by Helander and Simakov [26]. This discrepancy may be due to the fact that only a single symmetry-breaking term in the magnetic spectrum is considered in the analysis, so that ripple-trapped particles are not properly accounted for. If the neoclassical non-ambipolar particle transport is not properly accounted for in this model, then it would not be expected to accurately describe the limits of when this transport dominates the momentum balance.

### **2.5.3 Comparison of non-ambipolar neoclassical particle flux to total experimental particle flux**

Although there is some differential particle flux that is calculated to result from a neoclassically non-ambipolar particle flux, this differential flux is meaningless unless compared with other fluxes to determine its relative importance. In Sections 2.5.1 and 2.5.2, this neoclassical radial current was compared with estimates of the torque driven by Reynolds stress. Now the neoclassical differential particle flux will be compared directly to the total measured particle flux in HSX as an estimate of what portion of the total particle flux would need to be non-ambipolar in order to balance the neoclassical non-ambipolar fluxes.

The experimentally inferred flux surface averaged particle flux is plotted in black in Figure 2.18 for a set of discharges in the QHS configuration using a logarithmic vertical axis. This has been calculated using the DEGAS Monte-Carlo neutral particle code, which uses particle balance to determine the total electron particle flux per unit area  $\Gamma$  based on H-alpha measurements that are used to scale the source rates in the DEGAS calculation. The static background plasma is determined using fits of electron temperature and density profiles from Thomson scattering and ion

temperature profiles from CHERS (DEGAS calculations courtesy of Laurie Stephey). The differential neoclassical particle flux  $\Gamma_i - \Gamma_e$  for a non-ambipolar value of  $E_r$  is then plotted as a dashed red line in Figure 2.18 for comparison. A representative deviation from the ambipolar solution of  $\Delta E_r = 3$  kV/m was taken for this calculation, which is approximately the experimentally measured deviation where probe measurements are made in the edge. The non-ambipolar fluxes scale approximately linearly with  $\Delta E_r$  in this regime.

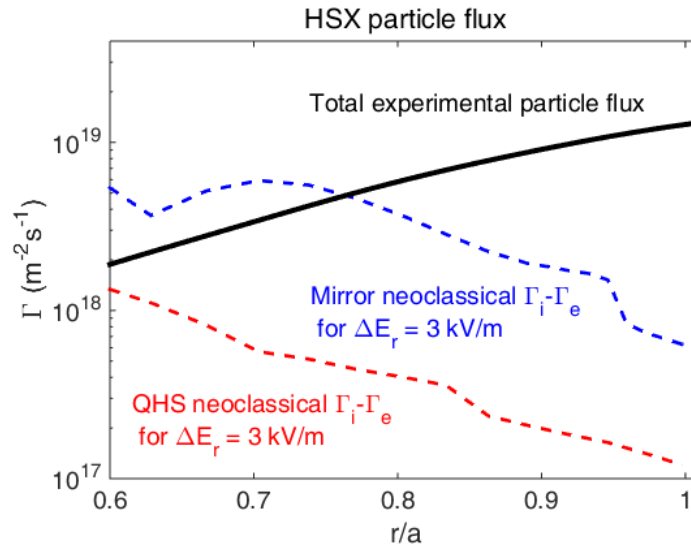


Figure 2.18 Comparison of calculated neoclassical non-ambipolar particle flux to total experimentally measured particle flux in HSX for the QHS and Mirror configurations [particle flux calculations courtesy of Laurie Stephey].

Most of the differential neoclassical particle flux is ion flux in the edge of the QHS configurations in the cases, as demonstrated by the plots of species-dependent particle flux later in Figure 4.3(a). There is therefore very little ambipolar neoclassical particle flux that would account for the experimentally measured fluxes. Figure 2.18 demonstrates that in the edge region of the QHS configuration where probe measurements are taken ( $r/a > 0.85$ ), the total experimentally measured particle flux is about a factor of  $\sim 100$  larger than the calculated neoclassical non-ambipolar particle fluxes. If there were a deviation from intrinsic ambipolarity in the turbulent particle flux on the

scale of  $\sim 1\%$ , this would be comparable to the neoclassical radial current calculated by PENTA in the edge and could be capable of canceling out the neoclassical charge flux.

In the Mirror configuration, differential neoclassical particle fluxes are increased for non-ambipolar solutions of  $E_r$  relative to the QHS configuration, as shown later in Figure 4.4. These differential neoclassical particle fluxes are plotted for the Mirror configuration as a blue dashed line in Figure 2.18, again for a sample deviation from the neoclassically calculated ambipolar solution of  $\Delta E_r = 3 \text{ kV/m}$ . In the Mirror configuration, the neoclassical fluxes are still smaller in the edge than the total experimental fluxes, but only by a factor of  $\sim 10$  rather than  $\sim 100$  as in the QHS configuration. In the Mirror case, it would therefore be much less likely that the turbulent particle flux could be non-ambipolar on the scale necessary to compete with the neoclassical component.

## 2.6 Previous comparisons of measured flows in HSX to neoclassical calculations

Many of the previous experiments on HSX have focused on comparisons of measurements to neoclassical calculations of the relevant parameters [33, 34, 55, 99]. Some of these experiments involved either the experimental flow damping or the intrinsic flows measured in discharges with no source of external momentum which may be relevant to the research performed in this work.

### 2.6.1 Flow damping

Some of the first measurements made on HSX were of experimental flow damping rates. The plasma was “spun up” using a biased electrode to impose a  $\mathbf{J} \times \mathbf{B}$  torque, then the bias was turned off, and the damping rate of the flows was measured using a 2D Gundestrup probe on a surface [99]. It was found that in the direction of minimum flow damping (the direction optimized for quasi-symmetry), the QHS configuration has greatly reduced flow damping relative to the Mirror configuration. This result is shown in Figure 2.19 (reproduced from [99]), which plots the



measured damping rate in both configurations across the portion of the minor radius which was measured using Langmuir probes.

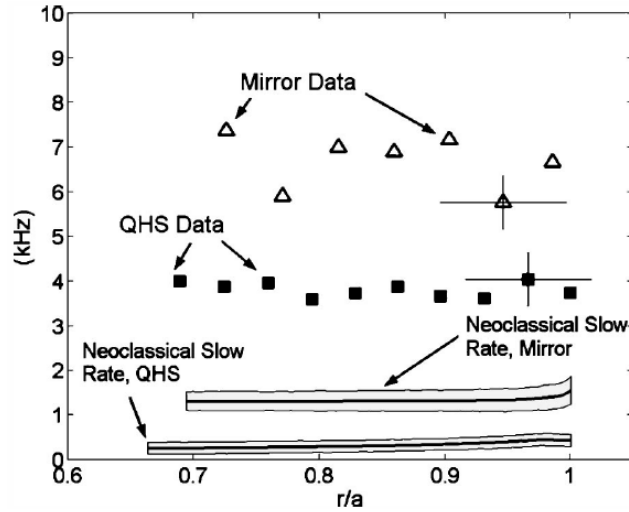


Figure 2.19 Measured flow damping rates in the quasi-helically symmetric direction in HSX compared to calculated neoclassical damping rates in both the QHS and Mirror configurations (from [99]).

Aside from the major result that the damping rate is reduced in the QHS configuration, this plot demonstrates another important point, that the damping rate is dominated by non-neoclassical processes once the configuration has been optimized to minimize the neoclassical damping. Neutral damping was accounted for in these calculations, and in fact dominates the damping rate for the QHS configuration. The additional damping in both the QHS and Mirror configurations is unaccounted for, but is most likely due to plasma turbulence. The idea that turbulence can significantly influence the flows in a quasi-symmetric configuration, as opposed to the flows being determined predominantly by neoclassical processes, is a focal point for much of this work.

### 2.6.2 CHERS intrinsic flow measurements

In addition to measurements of flow damping, more recently a CHarge Exchange Recombination Spectroscopy (CHERS) system has been implemented in HSX to measure the intrinsic flows

in the plasma [74]. The measured radial electric field from CHERS in 100 kW QHS plasmas is given in Figure 2.20, along with the predicted neoclassical values from both DKES (“Without Momentum Conservation”) and PENTA (“With Momentum Conservation”) [33]. Momentum conservation produces small adjustments to the calculated neoclassical radial electric field, and the PENTA-calculated value is the one that will be compared against for this work.

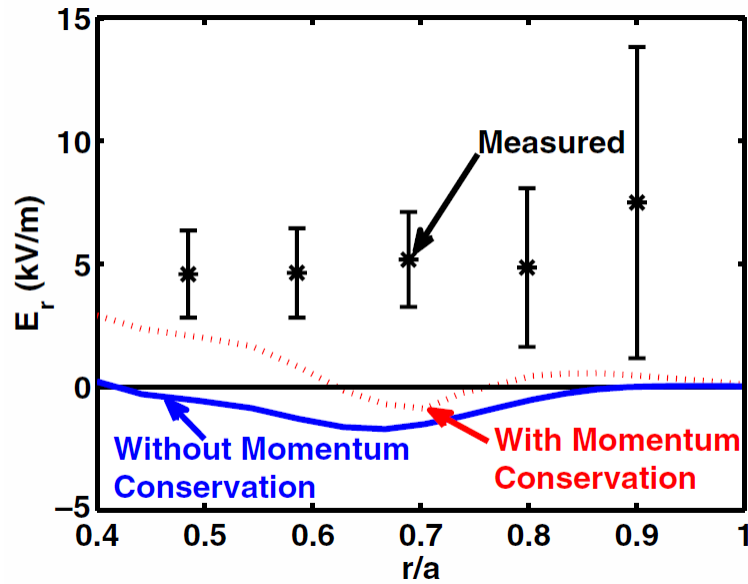


Figure 2.20 Measured  $E_r$  profile from CHERS in HSX compared to neoclassical calculations [33].

Figure 2.20 shows that the radial electric field predicted by neoclassical calculations does not accurately predict the measured flows in HSX. Based on sensitivity studies of the inputs to the neoclassical calculations, the uncertainty of the neoclassical calculations are small ( $\leq 1$  kV/m) compared to the difference between the calculation and the measurement. This is in contrast to measurements in other stellarator devices, as shown in Section 2.2.2, which do not have configurations optimized to reduce neoclassical losses, and measure radial electric fields similar to the neoclassically calculated values.

The plasmas represented in Figure 2.20 have been doped with carbon by using  $\text{CH}_4$  as the working gas to enable the measurement of an impurity recombination event. The changes to the ion species have been accounted for as completely as possible in the neoclassical calculations. While there are uncertainties in the behavior of ions near the value of the poloidal resonance, as discussed in Section 2.2.2.1, this does not meaningfully change the outcome of the neoclassical calculations plotted in Figure 2.20 due to the near-zero value of the predicted  $E_r$ .

### 2.6.3 Probe floating potential

Using Langmuir probes, a negative floating potential gradient ( $dV_{fl}/dr$ , where  $V_{fl} = \Phi_p - \mu \frac{T_e}{e}$  as discussed later in Section 3.1.1) has been measured in the edge of QHS configuration discharges across a wide variety of plasma regimes [99, 40, 82]. Due to the positive contribution of a physically relevant (negative)  $\nabla T_e$  to the floating potential gradient for low  $T_e$ , this means that  $E_r = -\nabla \Phi_p$  is necessarily more positive than the value calculated using only  $\nabla \Phi_{fl}$  with no temperature gradient. This positive definite  $E_r$ , which is consistently observed by Langmuir probes in the edge of QHS discharges, does not agree with neoclassical calculations which consistently predict a near-zero or small negative radial electric field in the edge where the probe measurements are taken.

Chapter 4 of this work presents qualitatively similar results of positive radial electric field measurements using probes and compares them with neoclassical calculations. It is shown that the edge floating potential gradient again deviates from what one would expect based on purely neoclassical predictions, and shows that the edge Reynolds stress profile may be responsible for this  $E_r$ , which cannot be explained by neoclassical transport processes alone.

## 2.7 Measurements of Reynolds stress in other devices

Measurements of the Reynolds stress and its contribution to the momentum balance have been made in several other experiments prior to the work presented here. In the cylindrical plasma device CSDX, mean azimuthal flow has been measured which is sustained against viscosity by the Reynolds stress [126, 127]. In these experiments, Langmuir probes were used to measure the electric field fluctuations in the azimuthal (analogous to the poloidal direction in a toroidal system) and radial directions in order to infer the corresponding velocity fluctuations which determine the Reynolds stress ( $\langle \tilde{v}_r \tilde{v}_\theta \rangle = -\langle \tilde{E}_\theta \tilde{E}_r \rangle / B_0^2$  for electrostatic turbulence). The azimuthal rotation calculated by balancing this measured Reynolds stress with the calculated ion-ion and ion-neutral viscosity was found to agree well with the rotation found by time delay estimation techniques using adjacent probe pins. This data is reproduced in Figure 2.21, with the force balance value based on the measured Reynolds stress plotted as a line and the poloidal flow measured using a time delay estimation technique (TDE) plotted as diamonds.

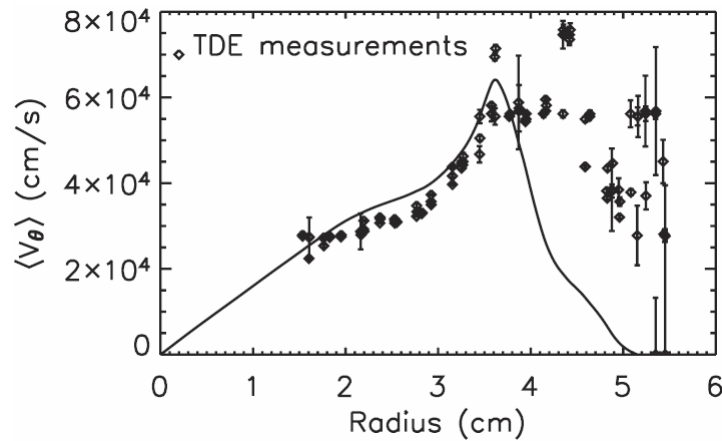


Figure 2.21 Azimuthal rotation in the CSDX linear device, as measured by a time delay estimation technique (TDE, plotted as diamonds) and calculated from force balance using the measured Reynolds stress (plotted as a line) [126].

This same procedure has been loosely followed for the experiments presented in Chapter 5, where fluctuations are measured via the floating potential and balanced against a calculated viscosity to predict the resulting flow. The experimental setup of the probes presented in Chapter 3 is also similar to those in the CSDX experiments, although the probes in HSX include an additional set of ion saturation pins in order to measure the parallel flow. This parallel flow measurement enables the three orthogonal components of the velocity fluctuations to all be measured simultaneously, which is important for a fully 3D system, as opposed to a linear device like CSDX.

In experiments at DIII-D, measurements of the Reynolds stress were made using Langmuir probes in the edge as well. These measurements were not shown to explain the intrinsic torque that must exist to drive the observed toroidal flows in H-mode plasmas, however [96, 128]. The measured Reynolds stress actually applied a torque in the opposite direction compared to the measured intrinsic rotation. In this case, a kinetic model of thermal ion orbit loss accounted for approximately half of the inferred torque in the co-direction at the edge. The remaining intrinsic toroidal rotation was unaccounted for. These experiments were performed in diverted H-mode plasmas with hot ions, which has significantly different edge physics than the HSX plasmas studied here, but it is nonetheless interesting to note that there is observed rotation that cannot be fully explained using measurements of the Reynolds stress in addition to existing models of intrinsic torque.

This chapter has presented the theoretical basis for the experiments presented later regarding Reynolds stress and intrinsic rotation in HSX. It has been shown that due to the quasi-symmetric optimization of HSX, the momentum balance may not be dominated by neoclassical processes, as it is thought to be in unoptimized stellarators. After examining each term in the momentum balance, the Reynolds stress was shown to be the most likely candidate to compete with the neoclassical term in the direction of symmetry. Previous relevant experiments from HSX and other devices have been summarized in order to provide context for the experiments which will be detailed in the rest of this document.

## References

20. Boozer, A. H. Transport and isomorphic equilibria. *Physics of Fluids* **26**, 496 (1983).
21. Calvo, I., Parra, F. I., Velasco, J. L. & Alonso, J. A. Stellarators close to quasisymmetry. *Plasma Physics and Controlled Fusion* **55**, 125014 (2013).
23. Garren, D. A. & Boozer, A. H. Existence of quasihelically symmetric stellarators. *Physics of Fluids B: Plasma Physics* **3**, 2822 (1991).
26. Helander, P. & Simakov, A. Intrinsic Ambipolarity and Rotation in Stellarators. *Physical Review Letters* **101**, 145003 (2008).
30. Proll, J. H. E., Helander, P., Connor, J. W. & Plunk, G. G. Resilience of Quasi-Isodynamic Stellarators against Trapped-Particle Instabilities. *Physical Review Letters* **108**, 245002 (2012).
33. Briesemeister, A, Zhai, K, Anderson, D. T., Anderson, F. S. B. & Talmadge, J. N. Comparison of the flows and radial electric field in the HSX stellarator to neoclassical calculations. *Plasma Physics and Controlled Fusion* **55**, 014002 (2013).
34. Canik, J., Anderson, D. T., Anderson, F. S. B., *et al.* Experimental Demonstration of Improved Neoclassical Transport with Quasihelical Symmetry. *Physical Review Letters* **98**, 085002 (2007).
35. Gerhardt, S., Talmadge, J. N., Canik, J. & Anderson, D. T. Experimental Evidence of Reduced Plasma Flow Damping with Quasisymmetry. *Physical Review Letters* **94**, 015002 (2005).
40. Wilcox, R. S., van Milligen, B. P., Hidalgo, C., *et al.* Measurements of bicoherence and long-range correlations during biasing in the HSX stellarator. *Nuclear Fusion* **51**, 083048 (2011).

41. Sabbagh, S. A., Sontag, A. C., Bialek, J. M., *et al.* Resistive wall stabilized operation in rotating high beta NSTX plasmas. *Nuclear Fusion* **46**, 635 (2006).
42. Fitzpatrick, R. Interaction of tearing modes with external structures in cylindrical geometry (plasma). *Nuclear Fusion* **33**, 1049 (1993).
43. Hegna, C. C. Healing of magnetic islands in stellarators by plasma flow. *Nuclear Fusion* **51**, 113017 (2011).
44. Terry, P. W. Suppression of turbulence and transport by sheared flow. *Reviews of Modern Physics* **72**, 109165 (2000).
45. Burrell, K. H. Effects of ExB velocity shear and magnetic shear on turbulence and transport in magnetic confinement devices. *Physics of Plasmas* **4**, 1499 (1997).
46. Biglari, H., Diamond, P. H. & Terry, P. W. Influence of sheared poloidal rotation on edge turbulence. *Physics of Fluids B* **2**, 1 (1990).
47. Mynick, H. E., Pomphrey, N. & Xanthopoulos, P. Reducing turbulent transport in toroidal configurations via shaping. *Physics of Plasmas* **18**, 056101 (2011).
48. Schmitz, L., Holland, C., Rhodes, T. L., *et al.* Reduced electron thermal transport in low collisionality H-mode plasmas in DIII-D and the importance of TEM/ETG-scale turbulence. *Nuclear Fusion* **52**, 023003 (2012).
49. Rice, J. E., Ince-Cushman, A., deGrassie, J. S., *et al.* Inter-machine comparison of intrinsic toroidal rotation in tokamaks. *Nuclear Fusion* **47**, 1618–1624 (2007).
50. Rosenbluth, M. N. & Hinton, F. L. Plasma rotation driven by alpha particles in a tokamak reactor. *Nuclear fusion* **36**, 55 (1996).
51. Mynick, H. E. & Hitchon, W. N. G. Effect of the ambipolar potential on stellarator confinement. *Nuclear Fusion* **23**, 1053 (1983).

52. Hirshman, S. P., Shaing, K. C., van Rij, W. I., Beasley, C. O. & Crume, E. C. Plasma transport coefficients for nonsymmetric toroidal confinement systems. *Physics of Fluids* **29**, 2951 (1986).
53. Lore, J., Guttenfelder, W., Briesemeister, A., *et al.* Internal electron transport barrier due to neoclassical ambipolarity in the Helically Symmetric Experiment. *Physics of Plasmas* **17**, 056101 (2010).
54. Hirshman, S. P., Van Rij, W. I. & Merkel, P. Three-dimensional free boundary calculations using a spectral Green's function method. *Computer Physics Communications* **43**, 143155 (1986).
55. Schmitt, J. C., Talmadge, J. N. & Anderson, D. T. Measurement of a helical Pfirsch-Schlüter current with reduced magnitude in HSX. *Nuclear Fusion* **53**, 082001 (2013).
56. Hirshman, S. P., Sanchez, R. & Cook, C. R. SIESTA: A scalable iterative equilibrium solver for toroidal applications. *Physics of Plasmas* **18**, 062504 (2011).
57. Reiman, A. & Greenside, H. Calculation of Three-Dimensional MHD Equilibria With Islands and Stochastic Regions. *Computer Physics Communications* **43**, 157 (1986).
58. Hudson, S. R., Dewar, R. L., Dennis, G., *et al.* Computation of multi-region relaxed magnetohydrodynamic equilibria. *Physics of Plasmas* **19**, 112502 (2012).
59. van Rij, W. I. & Hirshman, S. P. Variational bounds for transport coefficients in three-dimensional toroidal plasmas. *Physics of Fluids B* **1**, 563 (1989).
60. Beidler, C. D. & D'haeseleer, W. D. A general solution of the ripple-averaged kinetic equation (GSRAKE). *Plasma Physics and Controlled Fusion* **37**, 463 (1995).
61. Canik, J. *John Canik's Dissertation, University of Wisconsin - Madison* 2007.



62. Baldzuhn, J., Kick, M. & Maassberg, H. Measurement and calculation of the radial electric field in the stellarator W7-AS. *Plasma Physics and Controlled Fusion* **40**, 967 (1998).
63. Matsuoka, S., Satake, S., Yokoyama, M. & Wakasa, A. Radial Electric Field Formation Including Electron Radial Drift for a Core Electron-Root Confinement (CERC) Plasma in LHD. *Plasma and Fusion Research* **6**, 1203016 (2011).
64. Wakasa, A., Murakami, S., Itagaki, M. & Oikawa, S.-i. Construction of neoclassical transport database for large helical device plasma applying neural network method. *Japanese Journal of Applied Physics* **46**, 1157 (2007).
65. Satake, S., Kanno, R. & Sugama, H. Development of a Non-Local Neoclassical Transport Code for Helical Configurations. *Plasma and Fusion Research* **3**, S1062 (2008).
66. Yokoyama, M., Wakatani, M. & Shaing, K. C. Non-linear incompressible poloidal viscosity and its implications for H mode in stellarator/heliotron plasmas. *Nuclear Fusion* **35**, 153 (1995).
67. Beidler, C. D., Isaev, M. Y., Kasilov, S. V., *et al.* in *Proc. 16th Int. Stellarator/Heliotron Workshop (Toki, Japan)* (2007).
68. Landreman, M., Smith, H. M., Mollén, A. & Helander, P. Comparison of particle trajectories and collision operators for collisional transport in nonaxisymmetric plasmas. *Physics of Plasmas* **21**, 042503 (2014).
69. Briesemeister, A. *Alexis Briesemeister's Dissertation, University of Wisconsin - Madison* 2013.
70. Spong, D. A. Generation and damping of neoclassical plasma flows in stellarators. *Physics of Plasmas* **12**, 056114 (2005).

71. Sugama, H. & Nishimura, S. How to calculate the neoclassical viscosity, diffusion, and current coefficients in general toroidal plasmas. *Physics of Plasmas* **9**, 4637 (2002).
72. *Private communications with Jason Smoniewski*, 2014.
73. Solomon, W. M., Burrell, K. H., deGrassie, J. S., *et al.* Momentum confinement at low torque. *Plasma Physics and Controlled Fusion* **49**, B313–B324 (2007).
74. Briesemeister, A., Zhai, K., Anderson, D. T., *et al.* Flow Velocity Measurements Using ChERS in the HSX Stellarator. *Contributions to Plasma Physics* **50**, 741–744 (2010).
75. Callen, J. D., Cole, A. J. & Hegna, C. C. Toroidal flow and radial particle flux in tokamak plasmas. *Physics of Plasmas* **16**, 082504 (2009).
76. Nave, M. F. F., Johnson, T., Eriksson, L.-G., *et al.* Influence of Magnetic Field Ripple on the Intrinsic Rotation of Tokamak Plasmas. *Physical Review Letters* **105**, 105005 (2010).
77. Ida, K. & Rice, J. Rotation and momentum transport in tokamaks and helical systems. *Nuclear Fusion* **54**, 045001 (2014).
78. Hasegawa, A. & Wakatani, M. Self-Organization of Electrostatic Turbulence in a Cylindrical Plasma. *Physical Review Letters* **59**, 1581 (1987).
79. Diamond, P. H. & Kim, Y. Theory of mean poloidal flow generation by turbulence. *Physics of Fluids B* **3**, 1626 (1991).
80. Diamond, P. H., McDevitt, C. J., Gürçan, O. D., *et al.* Physics of non-diffusive turbulent transport of momentum and the origins of spontaneous rotation in tokamaks. *Nuclear Fusion* **49**, 045002 (2009).
81. Guttenfelder, W., Lore, J., Anderson, D. T., *et al.* Effect of Quasihelical Symmetry on Trapped-Electron Mode Transport in the HSX Stellarator. *Physical Review Letters* **101**, 215002 (2008).

82. Guttenfelder, W., Anderson, D. T., Anderson, F. S. B., *et al.* Edge turbulence measurements in electron-heated Helically Symmetric Experiment plasmas. *Physics of Plasmas* **16**, 082508 (2009).
83. Scott, S. D., Diamond, P. H., Fonck, R. J., *et al.* Local measurements of correlated momentum and heat transport in the TFTR tokamak. *Physical Review Letters* **64**, 531 (1990).
84. deGrassie, J. S., Baker, D. R., Burrell, K. H., *et al.* Toroidal rotation in neutral beam heated discharges in DIII-D. *Nuclear fusion* **43**, 142 (2003).
85. Nishijima, D, Kallenbach, A, Günter, S, *et al.* Experimental studies of toroidal momentum transport in ASDEX Upgrade. *Plasma Physics and Controlled Fusion* **47**, 89–115 (2005).
86. Hahm, T. S., Diamond, P. H., Gürçan, O. D. & Rewoldt, G. Nonlinear gyrokinetic theory of toroidal momentum pinch. *Physics of Plasmas* **14**, 072302 (2007).
87. Lee, W., Rice, J., Marmor, E., *et al.* Observation of Anomalous Momentum Transport in Tokamak Plasmas with No Momentum Input. *Physical Review Letters* **91**, 205003 (2003).
88. Gürçan, O. D., Diamond, P. H., Hahm, T. S. & Singh, R. Intrinsic rotation and electric field shear. *Physics of Plasmas* **14**, 042306 (2007).
89. Solomon, W. M., Burrell, K. H., Garofalo, A. M., *et al.* Advances in understanding the generation and evolution of the toroidal rotation profile on DIII-D. *Nuclear Fusion* **49**, 085005 (2009).
90. Ding, W., Lin, L., Brower, D., *et al.* Kinetic Stress and Intrinsic Flow in a Toroidal Plasma. *Physical Review Letters* **110**, 065008 (2013).
91. Kuritsyn, A., Fiksel, G., Almagri, A. F., *et al.* Measurements of the momentum and current transport from tearing instability in the Madison Symmetric Torus reversed-field pinch. *Physics of Plasmas* **16**, 055903 (2009).

92. van Milligen, B. P., García, L., Carreras, B. A., *et al.* MHD mode activity and the velocity shear layer at TJ-II. *Nuclear Fusion* **52**, 013006 (2012).
93. Scott, B. Three-dimensional computation of drift Alfvén turbulence. *Plasma Physics and Controlled Fusion* **39**, 1635 (1997).
94. Catto, P. J., El Nadi, A. M., Liu, C. S. & Rosenbluth, M. N. Stability of a finite- $\beta$  inhomogeneous plasma in a sheared magnetic field. *Nuclear Fusion* **14**, 405 (1974).
95. Shaing, K. C. & Crume, E. C. J. Bifurcation Theory of Poloidal Rotation in Tokamaks: A Model for the L-H Transition. *Physical Review Letters* **63**, 2369 (1989).
96. Müller, S. H., Boedo, J. A., Burrell, K. H., *et al.* Experimental Investigation of the Role of Fluid Turbulent Stresses and Edge Plasma Flows for Intrinsic Rotation Generation in DIII-D H-Mode Plasmas. *Physical Review Letters* **106**, 115001 (2011).
97. Catto, P. J., Helander, P., Connor, J. W. & Hazeltine, R. D. Neutral particle and radiation effects on Pfirsch-Schlüter fluxes near the edge. *Physics of Plasmas* **5**, 3961 (1998).
98. Simakov, A. N & Helander, P. Plasma rotation in a quasi-symmetric stellarator. *Plasma Physics and Controlled Fusion* **53**, 024005 (2011).
99. Gerhardt, S. P., Talmadge, J. N., Canik, J. M. & Anderson, D. T. Measurements and modeling of plasma flow damping in the Helically Symmetric eXperiment. *Physics of Plasmas* **12**, 056116 (2005).
100. Idei, H., Ida, K., Sanuki, H., *et al.* Transition of the Radial Electric Field by Electron Cyclotron Heating in the CHS Heliotron/Torsatron. *Physical Review Letters* **71**, 2220 (1993).
101. Radder, J. *Jerahmie Radder's Preliminary Exam, University of Wisconsin - Madison* 2012.
102. Wang, L. & Diamond, P. H. Gyrokinetic Theory of Turbulent Acceleration of Parallel Rotation in Tokamak Plasmas. *Physical Review Letters* **110**, 265006 (2013).

103. Rutherford, P. H. Collisional Diffusion in an Axisymmetric Torus. *Physics of Fluids* **13**, 482 (1970).
104. Hinton, F. L. & Hazeltine, R. D. Theory of plasma transport in toroidal confinement systems. *Reviews of Modern Physics* **48**, 239 (1976).
105. Parra, F. I. & Catto, P. J. Turbulent transport of toroidal angular momentum in low flow gyrokinetics. *Plasma Physics and Controlled Fusion* **52**, 059801 (2010).
106. Parra, F. I., Barnes, M. & Catto, P. J. Sources of intrinsic rotation in the low-flow ordering. *Nuclear Fusion* **51**, 113001 (2011).
107. Calvo, I. & Parra, F. I. Long-wavelength limit of gyrokinetics in a turbulent tokamak and its intrinsic ambipolarity. *Plasma Physics and Controlled Fusion* **54**, 115007 (2012).
108. Sugama, H., Watanabe, T.-H., Nunami, M. & Nishimura, S. Quasisymmetric toroidal plasmas with large mean flows. *Physics of Plasmas* **18**, 082505 (2011).
109. Helander, P. & Simakov, A. N. Gyrokinetic Theory of Rotation in Stellarators. *Contributions to Plasma Physics* **50**, 695–700 (2010).
110. Nemov, V. V., Kasilov, S. V., Kernbichler, W. & Heyn, M. F. Evaluation of  $1/\nu$  neoclassical transport in stellarators. *Physics of Plasmas* **6**, 4622 (1999).
111. Seiwald, B., Kasilov, S. V., Kernbichler, W., *et al.* Optimization of energy confinement in the  $1/\nu$  regime for stellarators. *Journal of Computational Physics* **227**, 6165 (2008).
112. Wakasa, A., Murakami, S., Maassberg, H., *et al.* Monte Carlo Simulations Study of Neoclassical Transport in Inward Shifted LHD Configurations. *J Plasma Fusion Res Ser* **4**, 408–412 (2001).
113. Murakami, S., Wakasa, A., Maassberg, H., *et al.* Neoclassical transport optimization of LHD. *Nuclear fusion* **42**, L19 (2002).

114. *Private communications with Don Spong and John Canik, ORNL, 2010.*
115. Canik, J. M., Anderson, D. T., Anderson, F. S. B., *et al.* Reduced particle and heat transport with quasisymmetry in the Helically Symmetric Experiment. *Physics of Plasmas* **14**, 056107 (2007).
116. Wesson, J. & Connor, J. W. *Tokamaks* (Clarendon Press, Oxford; New York, 1987).
117. Wakatani, M. *Stellarator and Heliotron Devices* p. 287 (Oxford University Press, 1998).
118. Diamond, P. H., Kosuga, Y., Gürçan, O. D., *et al.* An overview of intrinsic torque and momentum transport bifurcations in toroidal plasmas. *Nuclear Fusion* **53**, 104019 (2013).
119. Rice, J. E., Hughes, J. W., Diamond, P. H., *et al.* Edge Temperature Gradient as Intrinsic Rotation Drive in Alcator C-Mod Tokamak Plasmas. *Physical Review Letters* **106**, 215001 (2011).
120. Rice, J. E., Cziegler, I., Diamond, P. H., *et al.* Rotation Reversal Bifurcation and Energy Confinement Saturation in Tokamak Ohmic L-Mode Plasmas. *Physical Review Letters* **107**, 265001 (2011).
121. Askinazi, L. G., Golant, V. E., Lebedev, S. V., Rozhanskij, V. A. & Tendler, M. Radial current in a tokamak caused by a biased electrode. *Nuclear Fusion* **32**, 271 (1992).
122. Cole, A., Hegna, C. & Callen, J. Effect of Neoclassical Toroidal Viscosity on Error-Field Penetration Thresholds in Tokamak Plasmas. *Physical Review Letters* **99**, 065001 (2007).
123. Cole, A., Callen, J., Solomon, W., *et al.* Observation of Peak Neoclassical Toroidal Viscous Force in the DIII-D Tokamak. *Physical Review Letters* **106**, 225002 (2011).
124. Shaing, K. C. Magnetohydrodynamic-activity-induced toroidal momentum dissipation in collisionless regimes in tokamaks. *Physics of Plasmas* **10**, 1443 (2003).

125. Boozer, A. H. Plasma equilibrium with rational magnetic surfaces. *Physics of Fluids* **24**, 1999 (1981).
126. Holland, C., Yu, J., James, A., *et al.* Observation of Turbulent-Driven Shear Flow in a Cylindrical Laboratory Plasma Device. *Physical Review Letters* **96** (2006).
127. Tynan, G. R., Holland, C, Yu, J. H., *et al.* Observation of turbulent-driven shear flow in a cylindrical laboratory plasma device. *Plasma Physics and Controlled Fusion* **48**, S51–S73 (2006).
128. Solomon, W. M., Burrell, K. H., deGrassie, J. S., *et al.* Characterization of intrinsic rotation drive on DIII-D. *Nuclear Fusion* **51**, 073010 (2011).

## Chapter 3

### Experimental setup

The main diagnostic used in this work is a set of Langmuir probes designed to acquire spatially localized and time-resolved measurements of plasma parameters. The physics of the Langmuir probe measurements will be described in Section 3.1, and the specific design and implementation of the HSX Reynolds stress probe system will then be given in Section 3.2. Section 3.3 describes the positioning of the probes in the device as well as the magnetic geometry at each location. In Section 3.4, tests of the probes' perturbation on the plasma are presented.

#### 3.1 Langmuir probes

Langmuir probes are commonly used to study edge plasmas in magnetic confinement devices. By physically inserting a conducting probe tip surrounded by insulating material into the plasma during a discharge, spatially and temporally localized measurements can be made and plasma parameters may be calculated from these measurements. Similar localization can be difficult with other, less invasive diagnostics. These localized measurements come at the cost, however, of being inherently perturbative. The assumption that the plasma is relatively unaffected by the probe can be difficult to verify, especially given the highly localized nature of the measurements and perturbations. In the data presented here, no macroscopic changes to the HSX plasmas' stored energy, toroidal current, or radiated power were observed with other diagnostics while the probes were inserted, nor were probe measurements indicative of non-physical plasma behavior observed unless otherwise noted. Using multiple instances of probes, experiments were also run to test the



influence of one probe's perturbation on the measurement using the second. The results of these measurements are given in Section 3.4.

While the voltage applied to Langmuir probes is often swept over time in cold plasmas to gather information about the plasma parameters, this is a more difficult problem in hot, well confined plasmas where both high frequency fluctuations are present and the voltage range to be swept over is large. When swept probes are used to measure fluctuations of local plasma parameters, high frequency resolution is lost unless the voltage is swept at a frequency higher than that of the fluctuations, which often extend to  $\sim 300$  kHz in HSX plasmas. Fast-switching probes have been successfully used to simultaneously monitor multiple fluctuating plasma parameters at high frequencies in Alcator C-Mod [129, 130], but this is a technically difficult problem.

Another method of gathering information from a hot plasma using Langmuir probes, which is especially useful for measuring fluctuation data, is by statically biasing the probe tip at strategic points along the characteristic probe I-V curve. This provides time resolved measurements of plasma parameters with a simplified experimental setup, and results in many more realizations which reduce the statistical uncertainty of the measurement. Making this simplification requires an assumption that the electron distribution function is a Maxwellian. In sufficiently well confined, collisional plasmas, this assumption will be valid, although the effect of a deviation from a Maxwellian on the measurements will be discussed in the analysis below.

### 3.1.1 Floating potential

One of the basic measurements that can be made using Langmuir probes is the floating potential, defined as the potential at which a probe in the plasma draws no net current. To measure this voltage, a non-zero amount of current must actually be drawn, so that the voltage across a resistor can be recorded. The net resistance of the voltage divider circuit must therefore be large enough that the load line of the resistor circuit ( $I = -V/R_{tot}$ ) intercepts the characteristic probe

I-V curve at approximately the value of the floating potential, where  $I$  becomes vanishingly small. The voltage divider circuit used to measure the floating potential in HSX is shown in Figure 3.1.

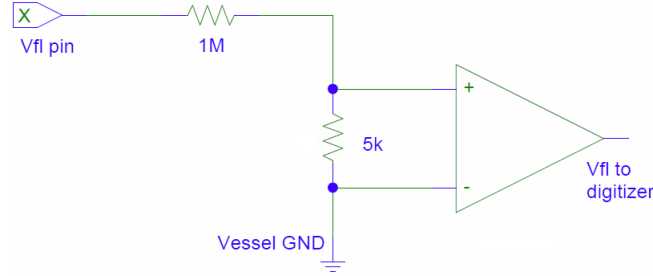


Figure 3.1 Floating potential circuit for HSX Langmuir probes.

The relevant physical quantity that the floating potential is generally used to investigate is the plasma potential. The plasma potential  $\Phi_p$  differs from the measured quantity by a voltage drop across the sheath that is proportional to the electron temperature, such that

$$V_{fl} = \Phi_p - \mu \frac{T_e}{e}. \quad (3.1)$$

where  $V_{fl}$  is the measured floating potential and  $T_e/e$  is the normalized electron temperature. Because of the extensive use of floating potential measurements in this work, the factor  $\mu$  will be derived as accurately as possible for these experiments.

Making the assumption of a Maxwellian electron distribution, the electron temperature coefficient  $\mu$  from Equation 3.1 is determined by [131]

$$\mu = \ln \left( \frac{(1 - \gamma_e) A_e}{(1 + \gamma_i) A_i} \sqrt{\frac{T_e}{T_e + T_i}} \sqrt{\frac{m_i}{2\pi m_e}} \right), \quad (3.2)$$

where  $A_e/A_i$  is the ratio of the effective probe collection areas for electrons and ions, and  $\gamma_e$  and  $\gamma_i$  are the secondary electron emission coefficients caused by electrons and ions, respectively. The dominant term is the mass ratio, especially when most of the standard cold plasma assumptions like  $A_e \approx A_i$ ,  $T_e \gg T_i$  and  $\gamma_e \approx \gamma_i \approx 0$  are made.

These assumptions are not valid in many relevant situations, however. First, in a magnetized plasma, the effective probe collection area depends on the relative sizes of the probe and the gyro-radius of a particle. In the edge of HSX, the gyroradius of thermal hydrogen ions ( $\rho_i \approx 0.7mm$ ) is larger than the probe radius ( $r_p \approx 375\mu m$ ), so that the ions are effectively unmagnetized and the probe collection area for ions is therefore taken to be equivalent to the full conducting surface area of the probe. For electrons, the gyroradius ( $\rho_e \approx 25\mu m$ ) is significantly smaller than the probe dimensions, so that the effective probe collection area is approximately  $2\hat{\mathbf{b}} \cdot \mathbf{S}$ , where  $\hat{\mathbf{b}}$  is the unit vector in the direction of the magnetic field and  $\mathbf{S}$  is the conducting surface of the probe. If the length of the exposed cylindrical conducting probe tip is  $l_p$ , the ratio of the collection areas is then  $A_e/A_i = 4r_p l_p / (\pi r_p^2 + 2\pi r_p l_p)$  for magnetized electron collection and unmagnetized ion collection. For the probe tips used in this work,  $r_p \approx 375\mu m$  and  $l_p \approx 750\mu m$ , giving the ratio  $A_e/A_i \cong 0.5$  in Equation 3.2.

As for the temperature factor in Equation 3.2, at the edge of HSX where the probe measurements are taken, the approximate electron and ion temperatures are on the order of  $T_e \sim 60eV$  and  $T_i \sim 25eV$ . Electron temperatures are from Thomson scattering, and ion temperature is estimated by taking measured carbon temperature profiles using CHERS in similar plasmas with the fueling gas switched from hydrogen to  $CH_4$ , and scaling the temperatures by the predicted effect of the removal of carbon ions. In this case, this meant reducing the CHERS-measured  $T_i$  [69] by 25%, because the charge exchange losses from background neutrals are reduced when a significant population of carbon ions are present [132].

The secondary emission coefficient due to ion impacts,  $\gamma_i$ , is calculated to be small with the low ion temperatures in HSX, but this is not necessarily the case for secondary emission due to electrons [133]. This term,  $\gamma_e$ , can be approximated by the expression [133]

$$\frac{\gamma_e}{\gamma_{e,m}} = (2.72)^2 \frac{E_p}{E_{p,m}} \exp \left( -2 \sqrt{\frac{E_p}{E_{p,m}}} \right), \quad (3.3)$$

where  $E_p$  is the primary particle energy in eV, and  $\gamma_{e,m}$  is the maximum secondary emission for a given material, which occurs at a material-dependent primary particle energy  $E_{p,m}$ . For the tungsten probe tips used in this work,  $\gamma_e$  in Equation 3.3 is approximately 0.5 for 60 eV electrons. Substituting graphite probe tips would increase  $\gamma_e$  to  $\approx 0.6$  for the same  $E_p$ .

Taking all of these terms together in Equation 3.2,  $\mu \approx 1.3$  for a typical 60 eV pure-hydrogen plasma just inside the last closed flux surface of HSX ( $r/a \approx 1$ ). This is significantly different than the commonly assumed value of about 3 [82], and  $\mu$  is not a weak function of  $T_e$  because of the strong secondary emission in the presence of hot electrons.

The total effect of the electron temperature on the floating potential measurement, using all  $T_e$ -dependent terms included in Equation 3.2, is plotted in Figure 3.2.  $T_i$  is assumed to be constant and equal to 25 eV for this plot; however, realistic deviations from this assumption would not strongly affect the curve, since  $\mu$  is a weak function of  $T_i$  in Equation 3.2. The measured floating potential would be the sum of the term plotted in Figure 3.2 and the plasma potential, which is the physical quantity that will be extracted from the measurement. A constant value of  $\mu$  in Equation 3.1 would lead to a straight line in Figure 3.2, and a region of small gradients indicates that the gradient of the  $V_{fl}$  measurement (used to determine  $E_r$ ) is relatively insensitive to the electron temperature.

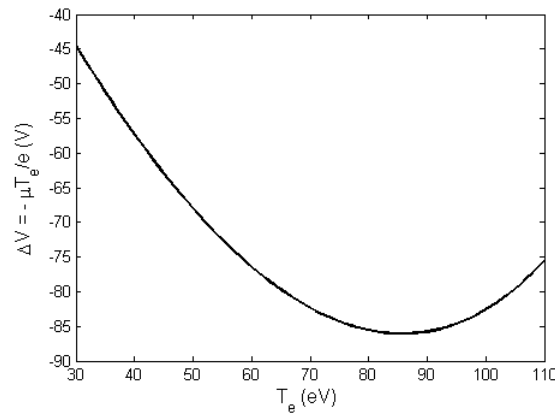


Figure 3.2 Calculated contribution of  $T_e$  to  $V_{fl}$  measurements for probes in HSX.

Because this work uses the spatial gradient of the floating potential signals as a measure of the electric field, the primary concern is the effect of a  $T_e$  *gradient* on the measurement, rather than deducing the exact value of the plasma potential itself from the measured  $V_{fl}$ . For the normal range of electron temperatures observed near the last closed flux surface of HSX ( $\sim 50 - 90$  eV), it can be seen from Figure 3.2 that a physically realistic  $\nabla T_e$  results in a slightly more negative contribution to the  $V_{fl}$  measurement as the probe is inserted further. At high electron temperatures, especially above about 100 eV, this is no longer true, as secondary emission becomes a dominant effect and  $\partial(\mu T_e)/\partial T_e$  changes sign. For this and other reasons (including damage to the probes), probe measurements in HSX are limited to regions where  $T_e \leq 100$  eV when possible to ensure a trustworthy interpretation of the results.

There are additional effects which may impact the value of  $\mu$  in Equation 3.1, and therefore the measurement of  $V_{fl}$ . First, the presence of a large impurity population would increase the value of  $\mu$  by a factor of  $\ln(\sqrt{m_i/m_H})$ . Based on radiated power measurements in HSX plasmas with boronized walls, impurity concentrations should be small enough that this term, and more importantly for this application, its gradient, would be negligible. Next, if the electron energy distribution function is sufficiently non-Maxwellian, such as in the presence of a fast electron population, then  $\mu$  can increase by factors of order unity from what is given in Equation 3.2 [134]. There is, however, no evidence of such a fast electron population in the high density HSX plasmas studied here. As discussed in Section 2.3.5 and plotted in Figure 2.10, the ECE signals and diamagnetic loop both show indications of fast electron populations in low density HSX plasmas, but there is no such evidence in these experiments at high density. The values of  $\mu$  calculated here are therefore expected to lead to a valid translation of the floating potential gradients to measured electric fields.

### 3.1.2 Ion saturation current

By biasing a probe tip with a large negative voltage, electrons are repelled from the probe and all of the ions that enter the sheath are collected. The current that the biased probe collects can give an estimate of the plasma density, because the current measured may be interpreted as entirely ion current without any contribution from electron current. The magnitude of bias for this condition to be met is approximately 3 times the largest expected  $T_e/e$  (the electron temperature in terms of volts), at which point the exponential term  $e^{-eV/T_e}$  in the derivation of the sheath equations becomes negligible. Once this bias level is reached, any additional voltage applied to the probe will only effectively serve to increase the size of the sheath, without increasing the total current collected beyond the effect of increased surface area. As long as the sheath size is small compared to the probe dimensions, the increased current collection from an increase in sheath surface area is negligible. The sheath size is on the order of a few Debye lengths, so for realistic probe sizes in laboratory plasmas, this condition is generally satisfied.

The radius of the Langmuir probe tips used for the work here is  $r_p = 375\mu m$ , and the Debye length for a typical HSX discharge near the last closed flux surface is approximately  $50\mu m$ . This justifies the assumption that once the applied voltage is high enough to enter the ion saturation regime, the exact value of applied voltage does not greatly affect the analysis. Since the maximum electron temperature in the region of the probes was expected to be  $70 - 80eV$  from previous Thomson scattering measurements, 250V, 200mA Acopian power supplies were chosen to supply the bias for the Langmuir probe pins. Although the bias is listed by the manufacturer as 250 V, because the power supply is unregulated, the actual voltage applied is about 290 V.

A low-resistance sense resistor is used to measure the ion saturation current collected. Similar to the floating potential circuit, this will necessarily affect the current collected by a finite amount. If the resistance of the sense resistor is small enough, this effect is negligible, because the load line

of the circuit used with a small resistor ( $I_{sat, meas} = (V_{bias} - V)/R_{sense}$ ) intersects the characteristic probe I-V curve near the value of the ion saturation current. The circuit used to bias a probe pin to measure ion saturation current is shown in Figure 3.3.

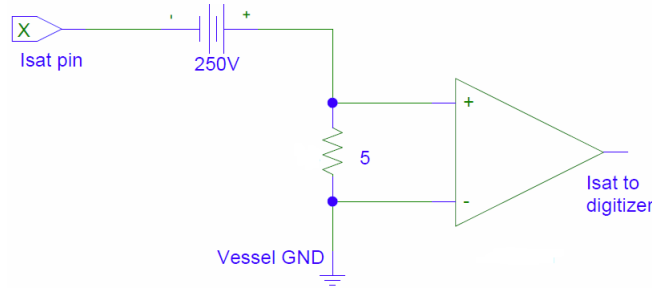


Figure 3.3 Circuit for measuring the ion saturation current in HSX.

If the probe tip is biased sufficiently into the ion saturation regime, then the current drawn by the probe in a thermalized plasma is approximately [135]

$$I_{i,sat} \simeq 0.6n_ieA_i\sqrt{\frac{T_e}{m_i}}, \quad (3.4)$$

where  $A_i$  is the probe collection area for ions. For this work, the ion saturation current is measured at two pins in the form of a mach probe in order to determine the flow velocity of the plasma.

### 3.1.3 Mach probes

By biasing two Langmuir probe tips into the ion saturation regime as discussed in Section 3.1.2 and separating them by an insulating barrier, the flow velocity in the direction along which the probes are aligned can be inferred from the ion saturation current at the two probes.

The parallel flow velocity is calculated using the measured ion saturation currents and the relationship [136]

$$\frac{\Gamma_{up}}{\Gamma_{down}} = \exp(KV_{flow}/c_s), \quad (3.5)$$

where  $c_s = \sqrt{(T_e + T_i)/m_i}$  is the ion sound speed,  $K$  is a constant that depends on the model, and  $\Gamma_{up}$  and  $\Gamma_{down}$  are the upstream and downstream ion saturation fluxes, respectively. If the ion

gyroradius is larger than the characteristic probe dimension,  $\rho_i > r_p$ , then an unmagnetized model for the mach probe should be used. Because the ion gyroradius of hydrogen in the edge of HSX is approximately 0.7 mm and the probe radius is approximately 0.4 mm, an unmagnetized model of the plasma flow in the presence of a probe by Hutchinson has been used for this work [136]. In this model, the value of  $K$  in Equation 3.5 was determined to be  $\approx 1.34$  for  $T_i/ZT_e < 3$ , using a two dimensional particle-in-cell simulation [136]. Since only electron heating is available in HSX, this assumption is valid in all experimental regimes, and the calculated value for the constant  $K$  is expected to be accurate.

One feature of this mach probe design is that by putting the two pins on the same magnetic surface, normalizing the two probe fluxes to each other in Equation 3.5 eliminates the uncertainty in the electron temperature and ion mass in Equation 3.4. Since the probe collection areas are never identical, however, the fluxes to each probe tip need to be normalized properly to calibrate out the collection area effect from Equation 3.4 (flux  $\Gamma = I/A$ , and the current  $I$  is the measured quantity). To calibrate this probe collection area, multiple measurements are taken with the probe in the same spatial location and in similar plasma conditions, but with the orientation of the probe rotated  $180^\circ$  for one measurement, so that the upstream pin is downstream and the downstream pin is upstream. By assuming that the mach number is the same in both cases, Equation 3.5 is used to find that the ratio of the collection areas of the two pins is related to the  $I_{\text{sat}}$  measurements by

$$\frac{A_2}{A_1} = \sqrt{\frac{I_{2,\text{orig}} I_{2,\text{rot}}}{I_{1,\text{orig}} I_{1,\text{rot}}}}, \quad (3.6)$$

where  $A_2/A_1$  is the relative probe collection area of the two pins, and  $I$  denotes the current measured from each pin (1 or 2) in either the original or rotated position.

Once the relative surface areas of the probes are known, the factor  $\frac{A_2}{A_1}$  calculated from equation Equation 3.6 is multiplied by all signals measured by pin 1, and Equation 3.5 is used to calculate the parallel ion flow in the plasma. The relative surface area of the probes was found to be about



1.15 for each of the two mach probes, which is within the expected tolerance of the probe collection areas.

### 3.2 Reynolds stress probe design

Two sets of Langmuir probes were designed and installed to measure the radial electric field, parallel ion flow and Reynolds stress profiles in HSX to determine the contribution of the Reynolds stress to the momentum balance. Tungsten is used as the conducting probe pin material for its high conductivity and high melting point. Tungsten is a standard material used for conducting Langmuir probe pins, although graphite is sometimes used when there is a desire to keep high-Z materials from contaminating a plasma [137]. High purity boron nitride is used as the insulating material, which is also a standard choice. Besides its low electrical conductivity, boron nitride also has a high thermal conductivity, which allows the insulator to absorb heat flux from the plasma without generating large thermal gradients within the material, and a low thermal expansion coefficient which prevents it from breaking easily.

Two pictures of the probe on the low-field side of the device are given in Figure 3.4. The purpose of this specific probe configuration is to find the mean parallel flow velocity as well as the local fluctuating velocity components in each of the three orthogonal directions. Labels on the left picture indicate which pins are biased to measure the floating potential and ion saturation current, and labels on the right show the pairs of pins that are compared to infer the three local velocity components.

Three of the pins of the probe are aligned perpendicular to the direction of the magnetic field lines, two of which are positioned on the same flux surface and a third that is recessed radially from the leading pins. By measuring the floating potential at each of these three points, the instantaneous radial and bi-normal electric fields  $E_r$  and  $E_\theta$  are extracted to infer the bi-normal and radial plasma velocities  $v_\theta$  and  $v_r$ , respectively. The bi-normal direction  $\hat{\theta}$  (approximately “poloidal”) is defined

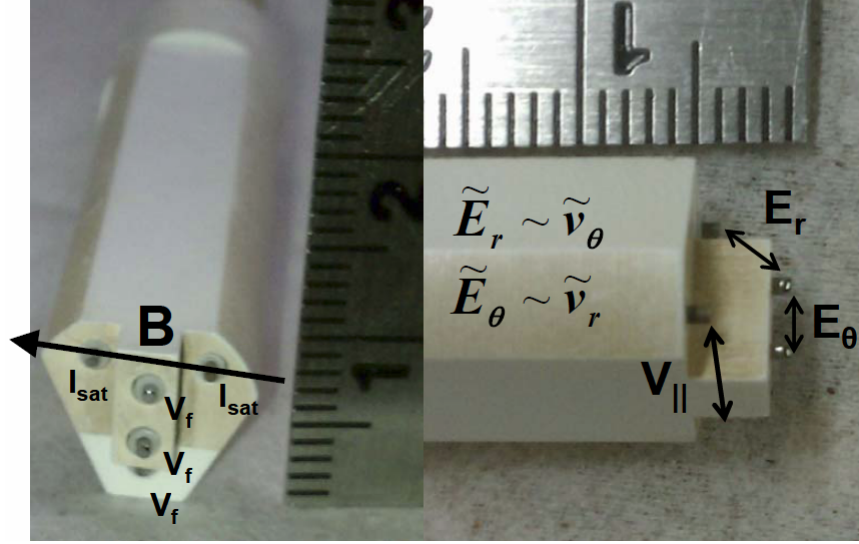


Figure 3.4 Pictures of the Reynolds stress probe. **Left:** From the perspective of the plasma with  $\vec{B}$  from right to left, with pins labeled according to which signal it is biased to measure. **Right:** Profile view, with  $\vec{B}$  going approximately into the page. The velocity components which each of the pin signals are used to infer are labeled.

here as the direction of positive  $\vec{E}_r \times \vec{B}_0$  flow, so that

$$\tilde{v}_\theta = \frac{\tilde{\vec{E}}_r \times \vec{B}_0}{|B_0|^2} \approx \frac{\tilde{V}_{f2} - \tilde{V}_{f3}}{|B_0|}, \quad (3.7)$$

$$\tilde{v}_r = -\frac{\tilde{\vec{E}}_\theta \times \vec{B}_0}{|B_0|^2} \approx -\frac{\tilde{V}_{f2} - \tilde{V}_{f1}}{|B_0|}, \quad (3.8)$$

where the floating potential signals  $V_{f1} \rightarrow V_{f3}$  are taken from the pins ordered 1→3 from top to bottom in the center vertical row of the probe on the left in Figure 3.4. It is assumed that the fluctuations are purely electrostatic, which should be valid in low  $\beta$  HSX plasmas, where the turbulence is expected to be dominated by electrostatic microinstabilities [82] (see also Figure 2.9). This formulation for the fluctuating quantities accounts for any mean  $T_e$  gradients that may exist between the pins, as the  $\tilde{V}_f$  quantities are mean-free, but it does not account for fluctuating components of  $T_e$  on the length scale of the probe tip separation. Electron temperature fluctuations have been shown to be significant in the quantitative interpretation of differential Langmuir probe  $V_f$  signals as  $E_\theta$  fluctuations [138]. Despite this, because there are no measurements available to

quantify  $T_e$  fluctuations directly, this effect is neglected in this work in order to get an estimate of the fluctuating plasma potential  $\tilde{\phi}_p$  from the floating potential measurements.

The separation distance between the floating potential pins was chosen to ensure that a negligible fraction of particle trajectories that are incident on one pin would have also been collected by another pin, while minimizing the size of the probe to reduce the perturbation to the plasma. The pins are aligned to avoid shadowing by the magnetic field and the poloidal separation between the pins is 3 mm center-to-center. Each pin has a 0.75 mm diameter, so there are about 3 thermal ion gyroradii between the pins ( $\rho_i \approx 0.7\text{mm}$  in the edge where the probes measure). It is also important that the probe sheaths do not overlap, but this is generally not an issue in HSX plasmas, where the Debye length is on the order of  $\sim 50\ \mu\text{m}$  in the edge.

Two additional pins are then configured as a mach probe to measure the ion saturation current on either side of an insulating barrier, and are aligned on a field line to infer the parallel ion flow velocity using the relationship given in Equation 3.5. The mach probe collection areas are calibrated using the method described in Section 3.1.3. The probe measurements during this calibration were repeatable from shot to shot as the measured line-averaged density from the interferometer was, giving confidence that this calculated area factor  $A_{up}/A_{down}$  is accurate to within  $< 5\%$ . The calibration procedure was also repeated after several months of operation with similar results, indicating that the surface conditioning of the probes do not change over time or exposure to plasma enough to have a measurable effect on the measurement.

Signals from the probes are sampled at 2.5 MHz using high-impedance digitizers connected to the sense resistor for each signal by a 50 Ohm coaxial cable. Because of the high frequency resolution necessary for this work and the failure of previous high bandwidth amplifier hardware to produce accurate measurements, no amplifiers are used. A digital filter is applied above 300 kHz to reduce the noise from radio signals above 1 MHz. This does not produce any substantive changes to the results, except where noted for some analysis of fluctuating  $I_{\text{sat}}$  measurements.

### 3.3 Probe positioning and magnetic geometry

Two Reynolds stress probes are located in regions near the maximum of the variation of magnetic geometry on a flux surface. One probe is in a region of low field and “bad curvature” ( $\kappa \cdot \nabla\psi > 0$ ) with small flux expansion ( $\nabla\psi > \langle \nabla\psi \rangle$ ), and the other is in a region of high field and “good curvature” ( $\kappa \cdot \nabla\psi < 0$ ) with large flux expansion ( $\nabla\psi < \langle \nabla\psi \rangle$ ). Details of these quantities at each probe location relative to the rest of the flux surface will be presented in Section 3.3.3. Turbulent instabilities are expected to be influenced in the same way by each of these effects: they should be destabilized at the low-field side location (LFS) and stabilized at the high-field side location (HFS) [139]. Due to the helical structure of the magnetic field in HSX, both the LFS and HFS probes are located on the outboard side of the device. The physical locations of the probes used in this work on HSX are shown in Figure 3.5.

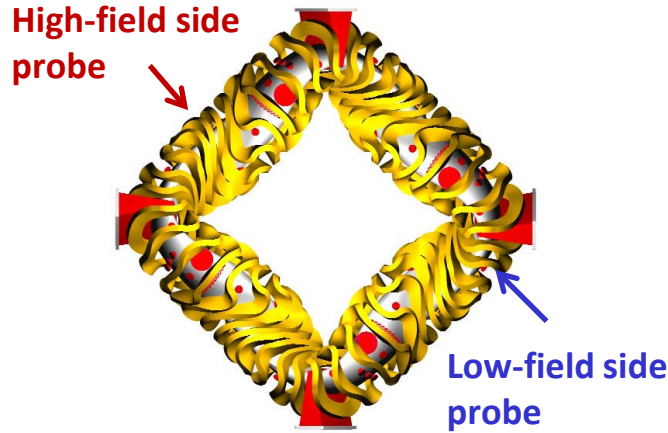


Figure 3.5 Top view of HSX with locations of Reynolds stress probes indicated.

The cross section of the magnetic surfaces at each of the probe locations is given in Figure 3.6 as calculated by vacuum field line following in the QHS configuration. The relative magnetic field strength is indicated by the color at each point, with red being the highest field strength and blue the lowest field strength. Probe insertion points are plotted as arrows and accessible sampling points

are plotted with black circles. The shaping of the magnetic surfaces does not change dramatically when the configuration is changed from QHS to Mirror, although the changes will be discussed later. Based on VMEC calculations, finite-beta effects are not expected to change the shaping of the surfaces significantly at the locations of the probes.

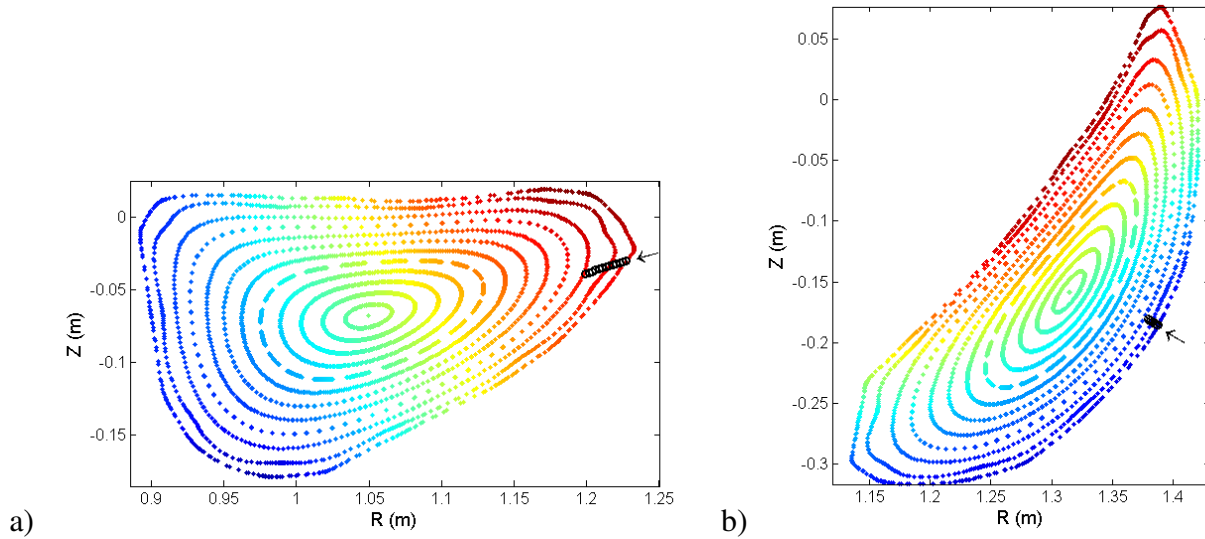


Figure 3.6 Magnetic surface cross sections at probe insertion locations on (a) the high-field side and (b) the low field side probe locations in HSX, with colors indicating field strength at each surface point.

As seen in Figure 3.6(a), the magnetic surfaces at the probe insertion point on the HFS port are not normal to the plane of the probe slide. The shape of the HFS probe is adjusted to account for this change in the angle of incidence compared to the picture of the LFS probe given in Figure 3.4.

The topology of magnetic surfaces could be strongly influenced by the presence of magnetic islands, which are not included in the VMEC models. Although there are not expected to be large islands in the confinement region in HSX for these experiments, based on vacuum field line following, there is a small island chain near  $r/a \approx 0.93$  which has a non-negligible width at the HFS probe location. This surface is where  $\iota \approx 12/11$  based on the rotational transform profile given in Figure 2.11. A detailed Poincaré plot of this island chain with a dense mesh of surfaces is given

in Figure 3.7 at the probe insertion point. The probe sampling points are again plotted in red, so it can be seen that because of the oblique insertion angle, the island is the width of about 3 sampling points in the radial scan, which are spaced at 0.25 cm along the axis of the probe.

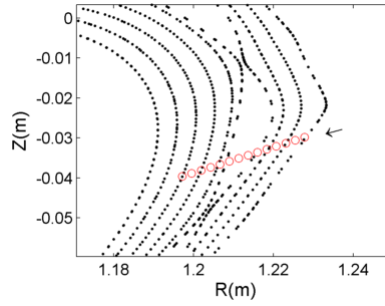


Figure 3.7 Poincaré plot of the 12/11 island chain at the location of the high-field side probe.

### 3.3.1 Probe alignment to the magnetic field

Each Reynolds stress probe has two pins separated by an insulated barrier which are biased to ion saturation and designed to measure the parallel flow, as shown in Figure 3.4.

The angles of magnetic field lines to the vertical in the axis of the probe slide were calculated for each probe measurement location. These angles are then used to align the Mach probe pins to the magnetic field lines at each of these positions using a plumb line. Considering the finite physical flex in the rotational dial on the probe shaft, this alignment is expected to be accurate within 5 degrees. Due to the finite width of the tungsten probe tips, the short distance between the mach probe tips and the finite ion gyro radius, it is calculated that a misalignment of this size would not meaningfully affect the measurement.

The local magnetic shear in this region of the plasma is small, so that the angle of the field line in the axis of the probe slide only changes by approximately 0.5 degrees between the last closed flux surface and  $r/a=0.7$  in the QHS configuration. In the Mirror configuration, the pitch of the field lines also changes by approximately 0.5 degrees relative to the QHS configuration, and the local magnetic shear is similar across configurations. This gives confidence that the probe orientation

does not need to be adjusted either as the probe is inserted deeper into the plasma or when the magnetic configuration is changed.

The bi-normal electric field measurement may also be dependent upon the rotational position of the probe, but because the fluctuations being measured are expected to be drift waves with long parallel wavelengths, the positioning of the floating potential pins is less sensitive to the rotation than the position of the mach probe pins. These  $V_{\parallel}$  pins should be well aligned when the recessed ion saturation current pins are aligned.

### 3.3.2 Radial positioning of probes

In order to compare the probe measurements with measurements using other diagnostics as well as with calculations from neoclassical modeling, the probe position must be mapped with the radial location in magnetic coordinates. Using a digital arm to measure the location of each probe in a retracted position in lab space, the probe's location is then extrapolated along the axis of the linear probe slide to find its location in flux space based on the VMEC equilibrium. This approximated position is then used as an initial guess for the last closed flux surface (LCFS), and the data from the radial probe scan is used to further refine the probe position.

Figure 3.8 shows the radial location of both the LFS and HFS Reynolds stress probes calculated from the VMEC equilibria for the QHS, Flip-1-4 and Mirror configurations. Although the geometric shaping factors do not change significantly at the positions of the probes when the magnetic configuration is changed (this will be shown in Section 3.3.3), the surfaces move in lab space, and this must be accounted for with the positioning of the probes. The probe locations are given as the distance along the axis of the probe slide relative to the modeled position of the vacuum vessel. The radial location is given in normalized flux space, where  $\rho = \sqrt{\psi/\psi_{LCFS}}$ . Figure 3.8 is also used to find the local  $\nabla\psi$  term to calculate radial derivatives for determining the flux surface averaged values of  $E_r$ .

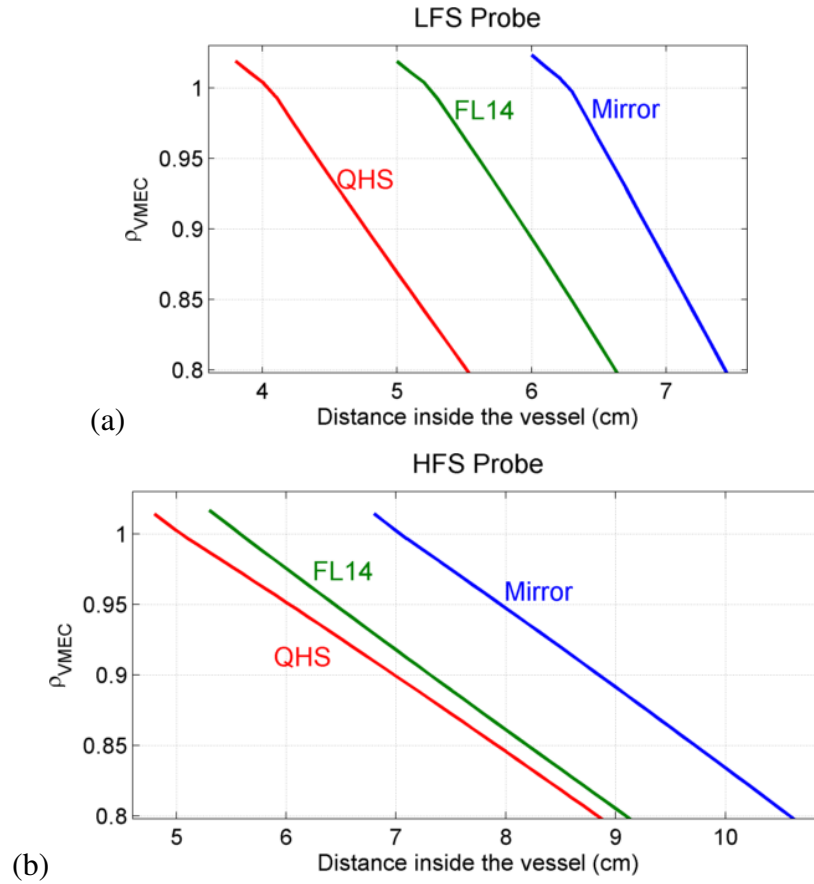


Figure 3.8 Radial locations in normalized flux space from VMEC equilibria of the (a) low-field side and (b) high-field side Reynolds stress probes along the axis of the probe slide in the QHS, Flip-1-4 and Mirror configurations relative to the modeled location of the vessel.

The location is referenced to the original design model of the vacuum vessel, which has been found to deviate by as much as 5 mm from the actual vessel location. Nevertheless, the relative positions of the LCFS in different magnetic configurations is assumed to be accurate. Experimental probe scans are used to determine the actual location of the last closed flux surfaces as a function of position on the linear probe slides. The values calculated in Figure 3.8 are then used to translate the location of the probe on the linear slides to a radial coordinate based on the experimentally determined last closed flux surface.



The ion saturation current is proportional to both the density and the square root of electron temperature ( $I_{sat} \simeq 0.6n_i e A_i \sqrt{\frac{T_e}{m_i}}$  from Equation 3.4), and it is therefore expected that the  $I_{sat}$  signal should increase monotonically as the probe is inserted towards the heating and particle sources, and the gradient of the  $I_{sat}$  signal should increase as the probe enters a region of improved confinement. This observation is used to experimentally determine the location of the last closed flux surface in HSX. Figure 3.9 shows radial scans of the  $I_{sat}$  signals of the LFS Reynolds stress probes in the QHS and Mirror configurations, along with the location which was determined to be the last closed flux surface (LCFS) for both configurations based on these measurements.

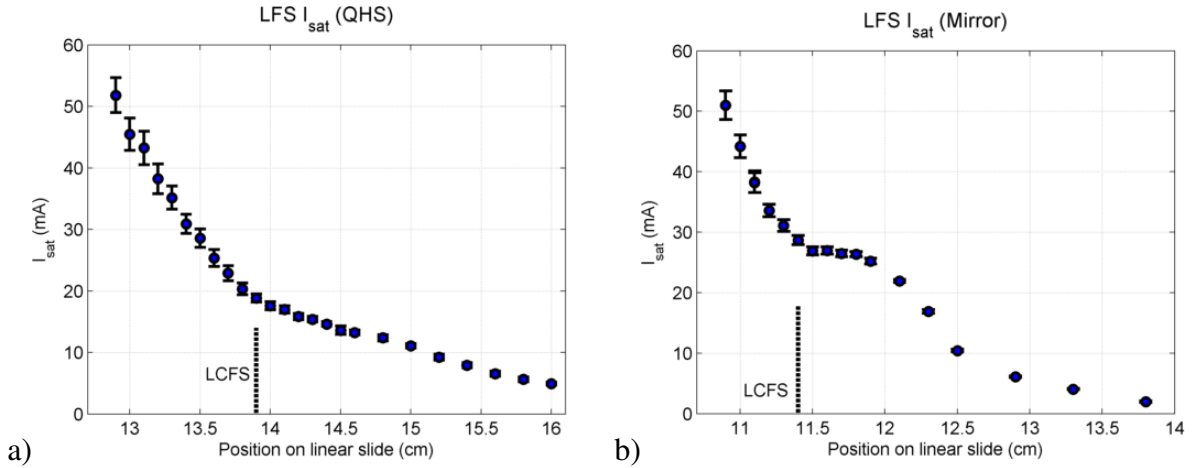


Figure 3.9 Radial profiles of  $I_{sat}$  signals at the LFS probe position in (a) the QHS and (b) Mirror configurations.

The ion saturation current is measured by the Reynolds stress probe using two pins on either side of an insulating barrier, so these signals are combined as  $I_{sat,tot} = I_{sat,1} + I_{sat,2}$  to approximate the total local  $I_{sat}$  signal as if there were no barrier. The values plotted in Figure 3.9 are taken to be the mean of the total  $I_{sat}$  signal over the final 20 ms of quiescent plasma, and the errorbars indicate the standard deviation of the moving mean over the 20 ms using 1 ms moving time windows. The floating potential profiles also demonstrate gradient changes near the last closed flux surface in many cases, although this is not shown here.

### 3.3.3 Magnetic geometry at probe locations

In order to investigate the variation of the Reynolds stress on a flux surface, the two probe locations were chosen to be located in regions near the extrema of magnetic field strength and normal curvature on a flux surface. Turbulence caused by microinstabilities is thought to be the source of the fluctuations which lead to the Reynolds stress in magnetized plasmas. For experimental parameters in HSX, trapped electron modes are calculated to be the most unstable modes and the dominant instability contributing to transport in the edge of the plasma [81, 82].

There are a few important factors which are expected to play a role in determining the growth rates of these microinstabilities in the plasma. One factor is the magnetic field strength normalized to the flux surface averaged value,  $|B|/\langle B \rangle$ , which determines the local trapped particle population. This is plotted for the QHS configuration in Figure 3.10(a) as a function of toroidal angle  $\phi$  and poloidal angle  $\theta$  in VMEC coordinates, where blue is low magnetic field strength relative to the flux surface average, and red is high magnetic field strength. The locations of the probes are indicated by white X's, with the low-field side (LFS) probe near  $\phi \approx 1.3$  and the high-field side (HFS) probe located near  $\phi \approx 4$ . Both probes are located on the outboard side of the device, where the outboard midplane is  $\theta = 0$ .

The second factor which is expected to influence the local turbulence stability is the normal curvature of the surface,  $\kappa_n$ . The curvature vector is defined as

$$\vec{\kappa} = \left( \hat{\mathbf{b}} \cdot \nabla \right) \hat{\mathbf{b}}, \quad (3.9)$$

where  $\hat{\mathbf{b}}$  is the unit vector in the direction of the magnetic field. The normal curvature is then given as  $\kappa_n = \kappa \cdot \hat{\mathbf{n}}$ , where  $\hat{\mathbf{n}} = \frac{\nabla \psi}{|\nabla \psi|}$  is the vector normal to the surface, pointed outward.

The normal curvature for a magnetic surface at  $r/a \approx 0.82$  in the QHS configuration is plotted in Figure 3.10(b), where blue is the largest “bad” curvature and red is the largest “good” curvature. The surface was traced using line following and the poloidal coordinates are determined by

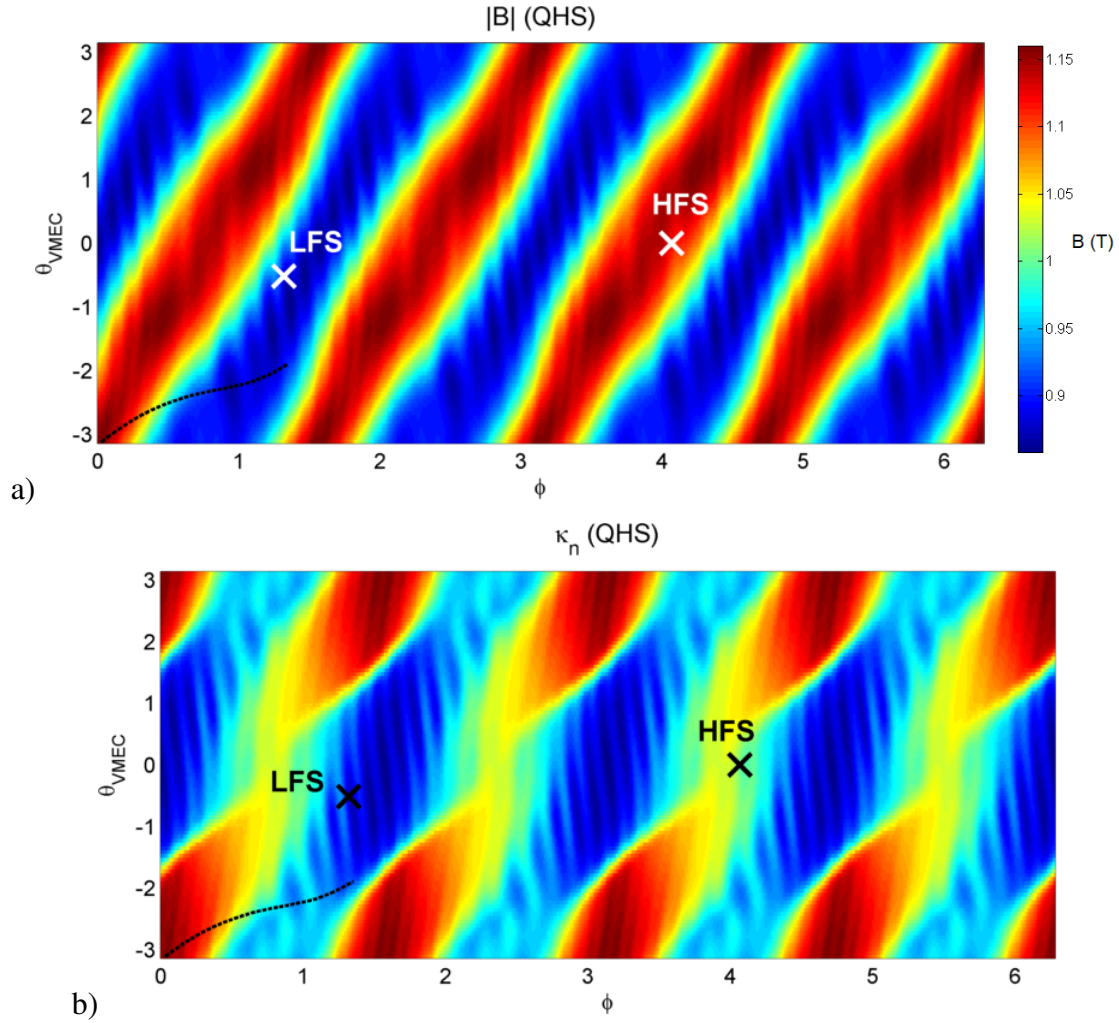


Figure 3.10 (a) Magnetic field strength and (b) normal curvature on a surface near  $r/a \approx 0.82$  in the QHS configuration in VMEC coordinates. Probe locations are marked with X's and labeled LFS and HFS, and a representative field line is given as a dashed black line.

mapping the surface points onto the VMEC equilibrium. The Reynolds stress probe locations are indicated with black X's.

As shown in Figure 3.10, the LFS probe is in a region near the minimum of curvature on a flux surface (largest “bad” curvature), while the HFS probe is in a region with only slightly higher than zero curvature (only slightly “good” curvature). The regions that are most accessible to probes are near the outboard mid-plane of the torus, which corresponds to the area around  $\theta \approx 0$  in the plots

in Figure 3.10. Because of this, the slightly positive  $\kappa_n$  value at the HFS probe is the location with the most favorable curvature that is accessible using existing ports in HSX which are capable of supporting a probe.

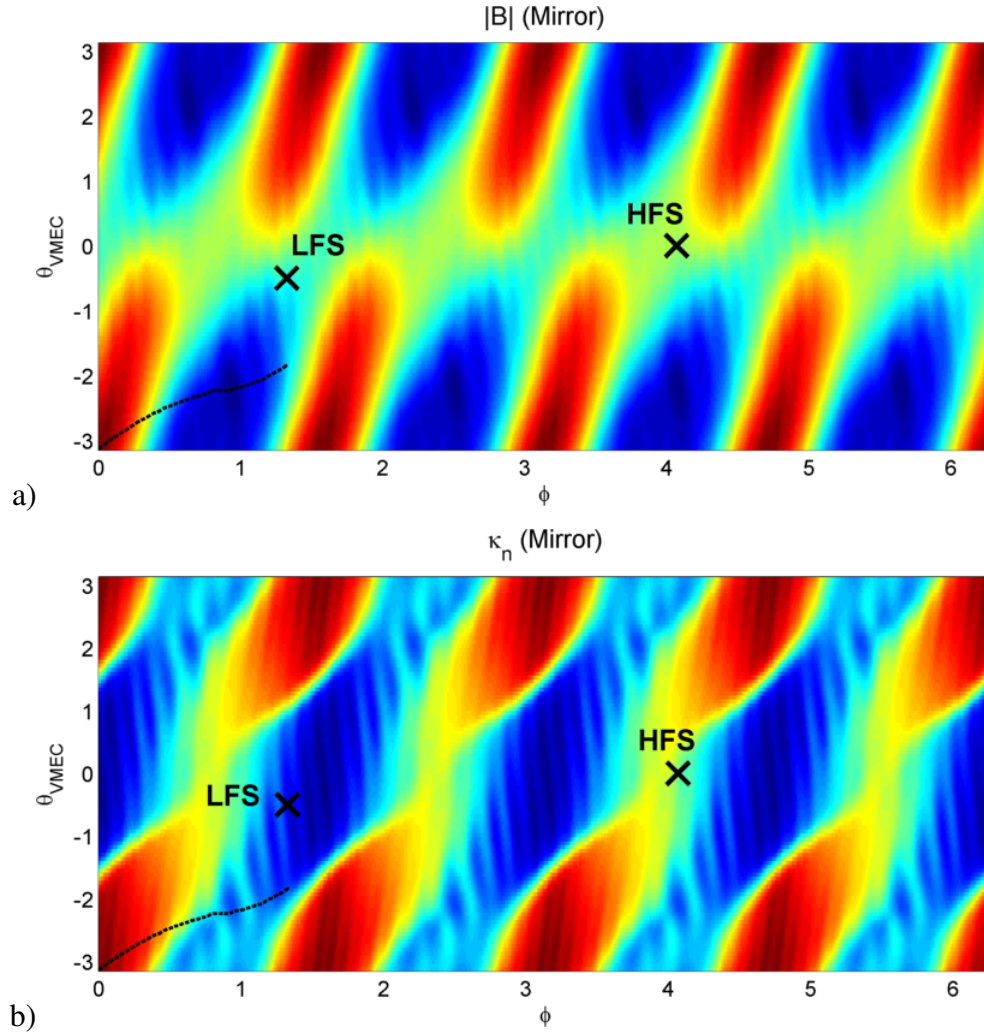


Figure 3.11 (a) Magnetic field strength and (b) normal curvature on a surface around  $r/a \approx 0.82$  in the Mirror configuration in VMEC coordinates. Probe locations are marked with black X's and labeled LFS and HFS, and a representative field line is given as a dashed black line.

The magnetic geometry factors  $|B|$  and  $\kappa_n$  are plotted again for the Mirror configuration in Figure 3.11. As seen by comparing figures 3.10 and 3.11, the normal curvature at the probes does not change significantly between the QHS and Mirror configurations, however, the difference in

magnetic field strength is smaller between the two probes in the Mirror configuration than it is in the QHS configuration. The field strength at all outboard ports (near  $\theta = 0$ ) is similar in the Mirror configuration due to the combination of the  $n=4, m=1$  main field harmonic and the  $n=4, m=0$  term which is added to break the symmetry.

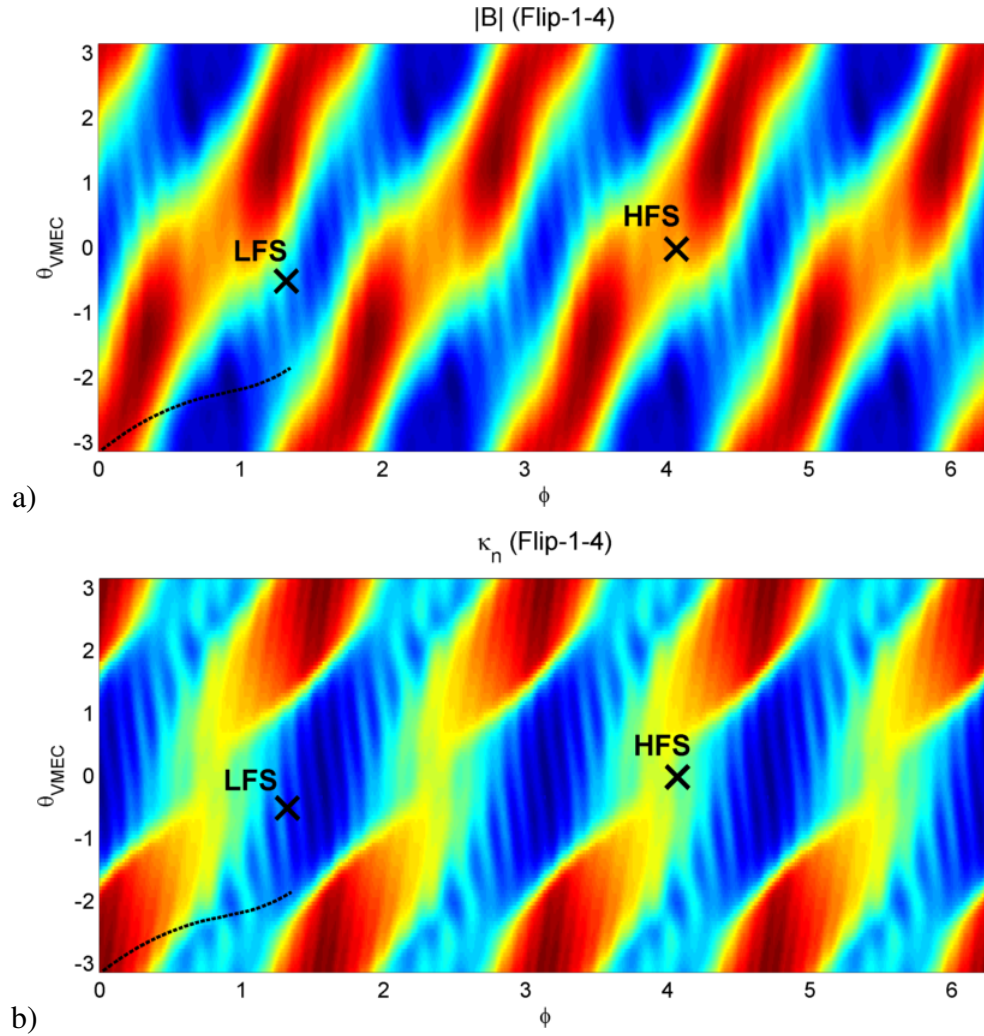


Figure 3.12 (a) Magnetic field strength and (b) normal curvature on a surface around  $r/a \approx 0.83$  in the Flip-1-4 configuration in VMEC coordinates. Probe locations are shown with black X's and labeled LFS and HFS, and a representative field line is given as a dashed black line.

The magnetic field strength and normal curvature in the Flip-1-4 configuration is plotted in Figure 3.12. Again, the curvature is not significantly affected by the change in configuration, however, the field strength at the probes changes relative to both the QHS and Mirror configurations.

Another quantity of interest is the local magnetic shear, although this value is small in HSX relative to most tokamaks. The rotational transform  $\iota$  has a small range over the minor radius of HSX, as shown in Figure 2.11, and given the large aspect ratio ( $\sim 10$ ), the local magnetic shear should be small enough that it does not play a significant role in turbulence stabilization, although the calculation of turbulence stabilization due to magnetic shear has not yet been performed.

### 3.4 Probe perturbation tests

One important aspect of these measurements with Langmuir probes is the assumption that the probes are not perturbing the plasma and changing the parameters which are being measured. In this work, no macroscopic changes to the plasma due to probe insertion are observed in the electron temperature or density from Thomson scattering, the electron density from the interferometer, the radiated power from the bolometers, and the stored energy from the diamagnetic loop in the discharges used here. The only thing that changes is the amount of gas puff which is necessary to achieve the same line-averaged density, which increases slightly as the high-field side probe is inserted deeply into the confinement region, but is apparently unaffected by the location of the low-field side probe. The resulting density profiles measured by Thomson scattering and the interferometer are indistinguishable.

As a further test of the effect of the probes' physical presence in the plasma on the measurements which they are making, one probe was inserted into the plasma while the other was scanned across the minor radius in the edge. Because both probes are distantly spaced toroidally on the outboard side of the device (see Figure 3.5) and the rotational transform in HSX is approximately

1, the parallel connection length between the two probes is long, so that they will not be directly “shadowing” each other.

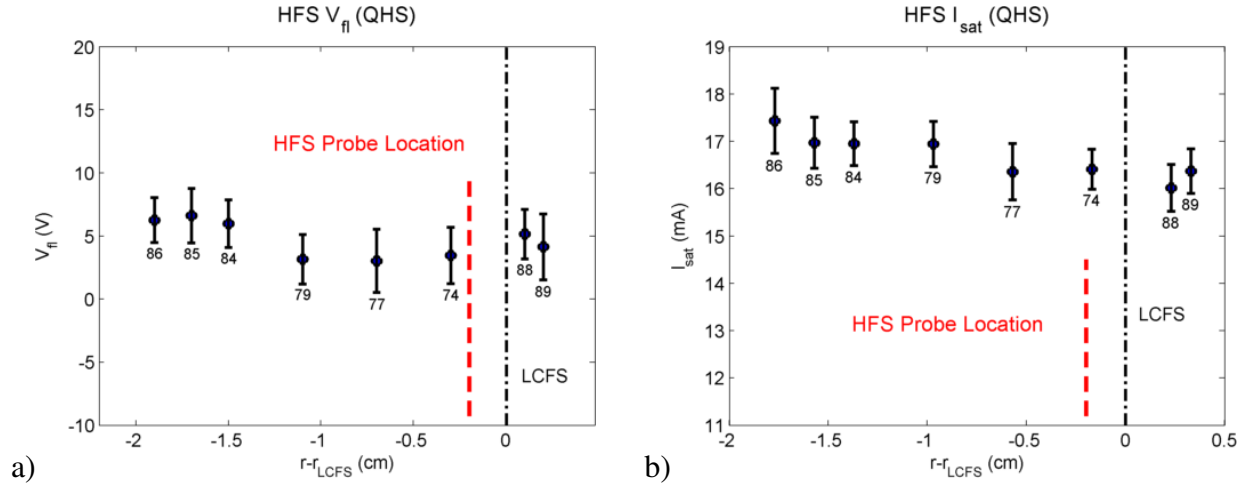


Figure 3.13 Low field side probe perturbation test. Measurements of (a)  $V_{fl}$  and (b)  $I_{sat}$  using the stationary LFS probe while HFS probe scanned across the edge.

Measurements of floating potential and ion saturation current using the high field side Reynolds stress probe are given in Figures 3.13 (a) and (b), respectively as the LFS probe is scanned radially. Each data point is the measurement using the HFS probe from one discharge with the LFS probe location relative to the estimated last closed flux surface (LCFS) given by the horizontal axis, and the approximate radial location of the stationary HFS probe is given by the dashed red line. The floating potential measurement given is the average of the two leading  $V_{fl}$  pins and the ion saturation current measurement is the sum of the two recessed  $I_{sat}$  pins that are used to measure the parallel flow. There are 20 ms of data used for each discharge, and the plotted point is the average of the moving mean of the signals using a 1 ms boxcar average. The errorbars indicate the standard deviation of the moving mean, which is different for each sample time.

Based on Figure 3.13, it appears that the presence of the LFS probe does not have a meaningful effect on the measurements taken at the HFS probe. The floating potential signals show almost no change as the LFS probe is scanned radially, and the ion saturation current measurements change

slightly as the probe is scanned, but the change is roughly within the level of the scatter in the measurement within a single discharge.

The same experiment was also performed by leaving the LFS probe stationary while scanning the HFS probe across the minor radius. The measurements from this experiment using the LFS probe are given in Figure 3.14 for (a) the floating potential and (b) the ion saturation current signals. The approximate radial position of the LFS probe is given as a red line, and the shot numbers are shown underneath each data point to demonstrate the lack of hysteresis and the repeatability of discharges and measurement trends over time.

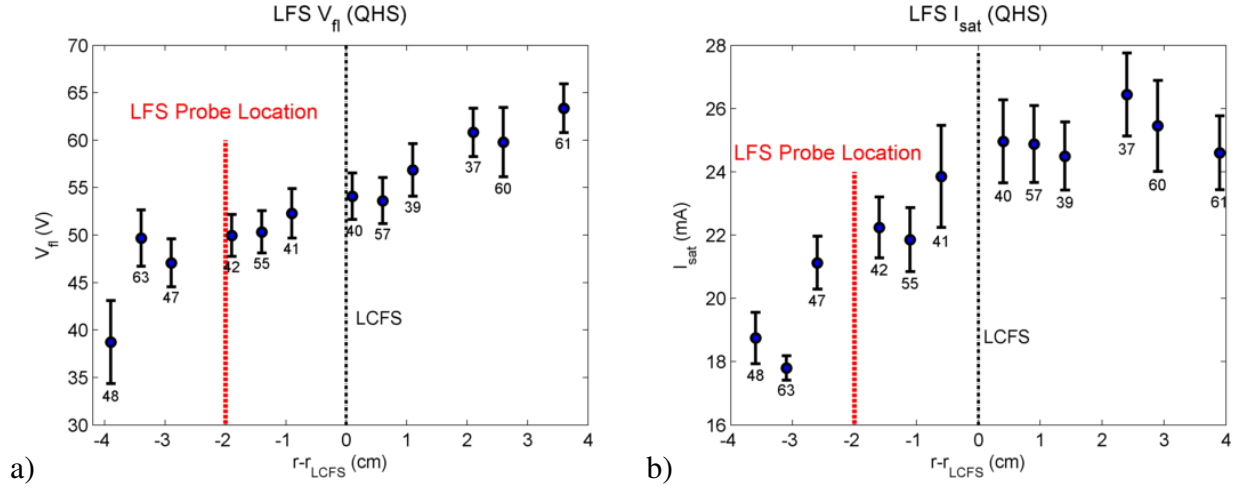


Figure 3.14 High field side probe perturbation test. Measurements of (a)  $V_{fi}$  and (b)  $I_{sat}$  using the stationary LFS probe while HFS probe scanned across the edge.

From Figure 3.14, it can be seen that the probe measurements made at the LFS location are altered by the presence of the HFS probe beyond the standard millisecond-to-millisecond variation of the signal within a discharge. This perturbation is strongest when the HFS probe is positioned further inside the plasma than the LFS probe location (more negative  $r - r_{LCFS}$ ), but the perturbation is finite for the floating potential signal immediately as the HFS probe is inserted into the plasma from the scrape-off layer. It is intuitively understandable that the HFS probe would be more perturbative than the LFS one, because the flux expansion is larger for this location, so that



the intersection of closed field lines with the probe is about 3 times larger for the HFS probe than the LFS one for a given radial position in flux space. This can be seen from Figure 3.8, where the same location in radial flux space is about 3 times as far into the plasma linearly on the HFS probe than the LFS one. This is also the reason for the difference in the range over which the probes were scanned between Figures 3.13 and 3.14.

While it would be advantageous to measure plasma parameters with both probes simultaneously in the same plasmas, Figure 3.14 indicates that the HFS probe influences the measurements made using the LFS probe. Due to this result, measurements made using both probes simultaneously in the plasma are avoided in the remainder of this work, and the two probes are scanned independently in separate sets of discharges.

Another implication of the results from Figure 3.14 is that the mean values of the floating potential scan using the high field side probe may not be reliable as the probe is inserted into the plasma. The presence of the HFS probe is having some effect on the local plasma parameters that causes the measured floating potential to be reduced, although the Thomson scattering and interferometer measurements do not show any changes large enough to measure using those diagnostics. It is unclear how this would also affect the fluctuation measurements.

This chapter has introduced the diagnostic setup used in the experiments presented later. The Langmuir probe theory and setup in HSX was given, along with information about the magnetic geometry at each probe location. Probe perturbation tests demonstrated that the low-field side (LFS) probe does not appear to influence measured plasma parameters far away from it, but that the presence of the high-field side (HFS) probe does in fact influence these measurements.

## References

69. Briesemeister, A. *Alexis Briesemeister's Dissertation, University of Wisconsin - Madison* 2013.
81. Guttenfelder, W., Lore, J., Anderson, D. T., *et al.* Effect of Quasihelical Symmetry on Trapped-Electron Mode Transport in the HSX Stellarator. *Physical Review Letters* **101**, 215002 (2008).
82. Guttenfelder, W., Anderson, D. T., Anderson, F. S. B., *et al.* Edge turbulence measurements in electron-heated Helically Symmetric Experiment plasmas. *Physics of Plasmas* **16**, 082508 (2009).
129. LaBombard, B. & Lyons, L. Mirror Langmuir probe: A technique for real-time measurement of magnetized plasma conditions using a single Langmuir electrode. *Review of Scientific Instruments* **78**, 073501 (2007).
130. LaBombard, B., Golfinopoulos, T., Terry, J. L., *et al.* New insights on boundary plasma turbulence and the quasi-coherent mode in Alcator C-Mod using a Mirror Langmuir Probe. *Physics of Plasmas* **21**, 056108 (2014).
131. Schrittwieser, R., Balan, P., Hron, M., *et al.* Measurements with an emissive probe in the CASTOR tokamak. *Plasma Physics and Controlled Fusion* **44**, 567 (2002).
132. *Private communication, calculations performed by Christopher Clark*, 2012.
133. Thomas, E. W. Data Compendium for Plasma-Surface Interactions. *Nuclear Fusion* **24**, S9 (1984).
134. Demidov, V., DeJoseph, C. & Kudryavtsev, A. Anomalous High Near-Wall Sheath Potential Drop in a Plasma with Nonlocal Fast Electrons. *Physical Review Letters* **95**, 215002 (2005).

135. Hershkowitz, N. in *Plasma Diagnostics* 113 (1989).
136. Hutchinson, I. H. Ion collection by a sphere in a flowing plasma: I. Quasineutral. *Plasma Physics and Controlled Fusion* **44**, 1953 (2002).
137. Yan, L., Hong, W., Zhao, K., *et al.* Novel design for zonal flow probe arrays in the HL-2A tokamak. *Review of Scientific Instruments* **77**, 113501 (2006).
138. Gennrich, F. P. & Kendl, A. Analysis of the temperature influence on Langmuir probe measurements on the basis of gyrofluid simulations. *Plasma Physics and Controlled Fusion* **54**, 015012 (2012).
139. Horton, W. Drift waves and transport. *Reviews of Modern Physics* **71**, 735–778 (1999).

## Chapter 4

### Measurements of $E_r$ and $V_{||}$ and comparisons with neoclassical modeling

Measurements of the time-averaged radial electric field and parallel ion flows have been made using the Langmuir probe system introduced in Chapter 3. The probes are scanned radially from shot to shot over a set of discharges which are similar according to macroscopic diagnostics such as the interferometer and diamagnetic loop, and each probe is scanned independently so that the presence of one does not affect the measurements of the other. Both a forward and backward radial scan were performed with the probe for each data set to check for measurement consistency. Any long term changes in the plasma as the data was taken, due to wall conditioning or changes in the heating power, for example, would be clear from the redundant data sets.

Section 4.1 presents calculations of the predicted radial electric field and parallel flows from the neoclassical ambipolarity constraint using PENTA. The characteristics of the raw data from the Langmuir probes are introduced in Section 4.2, and measured values of the radial electric field using the floating potential are presented in Section 4.3, where they are also compared to the neoclassical calculations. Section 4.4 then compares the measurements of parallel ion flow from the mach probes to the neoclassical calculations, as well.

#### 4.1 Neoclassical ambipolarity calculations

In order to compare the measured flows and radial electric field to what would be expected if neoclassical transport and damping were dominant in the momentum balance, the PENTA code

[53, 70] is used here to calculate the neoclassical ambipolar solution for  $E_r$  based on experimental plasma parameters. The details of the code's methodology, dependencies and assumptions are given in Section 2.2.

#### 4.1.1 Inputs to PENTA

As its inputs, PENTA takes the electron temperature and density profiles measured via Thomson scattering, along with an ion temperature profile based on measurements using CHERS under similar plasma conditions. The transport coefficients calculated by DKES can be taken along with these experimental values to calculate the particle flux for each species. These particle fluxes are then used to calculate the predicted radial electric field from the neoclassical ambipolarity condition.

The Thomson scattering electron temperature and density profiles used as inputs into PENTA for the QHS configuration are given in Figure 4.1. This profile was generated using data from the same ensemble of shots which was used to take measurements with the Reynolds stress probe.

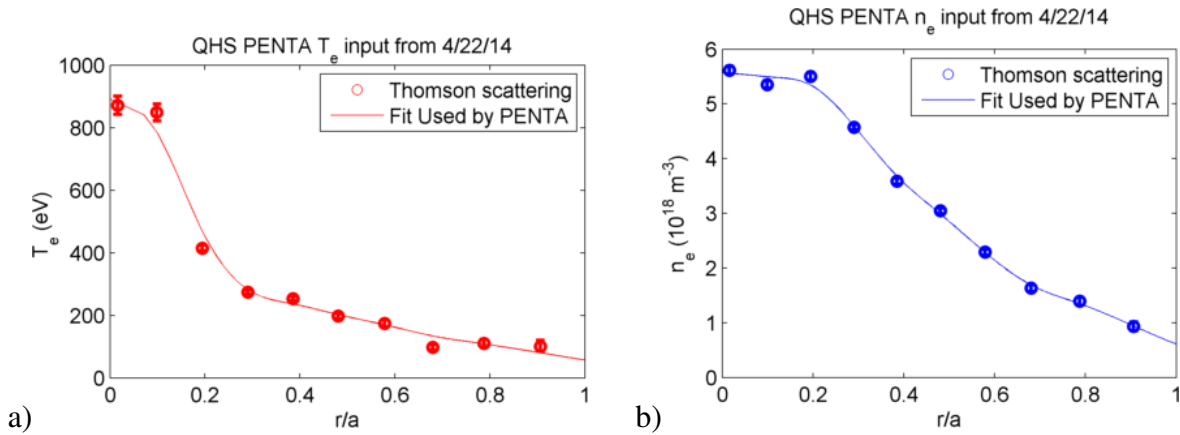


Figure 4.1 (a)  $T_e$  and (b)  $n_e$  profiles from Thomson scattering in QHS plasmas and their fits used as inputs to PENTA.

The fits line which are shown in Figure 4.1 are generated by mirroring the profiles across the axis and using a cubic spline fitting routine. This ensures smooth, continuous gradients across

the minor radius. PENTA then uses the values of this fit as its inputs, since there are many more radial points in the PENTA (VMEC/DKES) mesh than there are in the HSX Thomson scattering diagnostic. The fitted  $T_e$  profiles given in Figure 4.1(a) agree well in the edge with the probe measurements given later in Figure 4.9 which are used in the calculations of  $E_r$ .

#### 4.1.1.1 Ion temperature

The ion temperature profile is measured using CHERS in discharges similar to the ones presented here (line-averaged density  $\bar{n}_e \approx 4 \times 10^{18} \text{ m}^{-3}$ , QHS configuration, 44 kW injected ECRH), with the exception that  $\text{CH}_4$  is used as the fueling gas in order to acquire a measureable impurity signal using the spectrometers. The addition of carbon is necessary because the CHERS system is designed to measure carbon ion temperatures, and does not directly measure the hydrogen ion temperatures in relatively pure hydrogen plasmas. The measured carbon ion temperature profile is plotted in Figure 4.2. Both a linear and quadratic fit match reasonably well with the data given the errorbars in the measurement, and the linear fit was chosen because the normalized gradients become large relative to the measurement certainty in the edge of the parabolic fit, and this is where the probe measurements are taken. Because charge exchange losses with background neutrals dominate ion heat transport, there is no intuitive form for how the shape of the ion temperature profile “should” be. The choice of fit and changes to the ion temperature profile in general produce only minimal changes in the predicted  $E_r$  profile, and do not qualitatively change any of the results of the neoclassical transport calculations. This will be demonstrated later in Section 4.1.3.

These measured  $T_i$  values are then scaled down to attempt to account for the presence of carbon in the CHERS-measured discharges. Using ADAS [140] and assuming a coronal equilibrium, Chris Clark calculated that the replacement of a  $\text{CH}_4$  plasma with a pure hydrogen plasma would reduce the ion temperature by a factor of  $\approx 25\%$ , so all measured values from  $\text{CH}_4$  plasmas are scaled down by this factor before they are used as inputs to the neoclassical calculations [132].

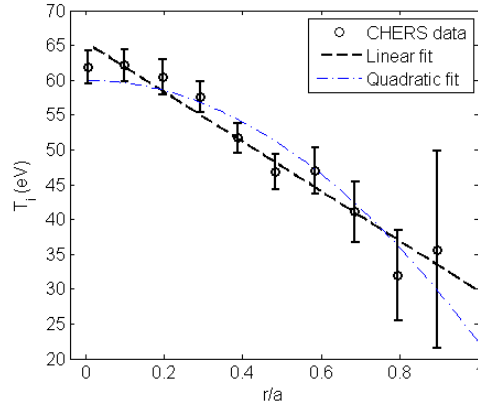


Figure 4.2 Ion temperature measurements from CHERS (courtesy of A. Briesemeister).

This assumes that charge exchange losses dominate transport in the ion temperature determination, which should be valid given that the ion thermal transport time scale is much longer than the charge exchange frequency. Changes in  $T_i$  up to a factor of about 50% are calculated to have relatively small effects on the change in the neoclassically ambipolar  $E_r$  solution calculated by PENTA.

#### 4.1.2 Calculated neoclassical particle fluxes and ambipolar solution for $E_r$

Using the measured plasma parameters described in Section 4.1.1 as inputs to PENTA, the particle fluxes are calculated for main ions and electrons across the minor radius of HSX. An example of the calculated fluxes for electrons and hydrogen ions for a surface at  $r/a \approx 0.95$  in the QHS configuration is given in Figure 4.3(a).

Assuming that the neoclassical fluxes of these two species are the dominant source of non-ambipolar particle flux and that there is no additional source of momentum in the system, the particle fluxes as a function of  $E_r$  are used to predict the radial electric field in steady state using the ambipolarity constraint, so that  $\Gamma_i(E_r) = \Gamma_e(E_r)$  at each surface for a pure hydrogen plasma. This is equivalent to finding the intersection of the calculated curves in Figure 4.3 for each surface. A more detailed explanation of this calculation and the underlying physics was provided in Section

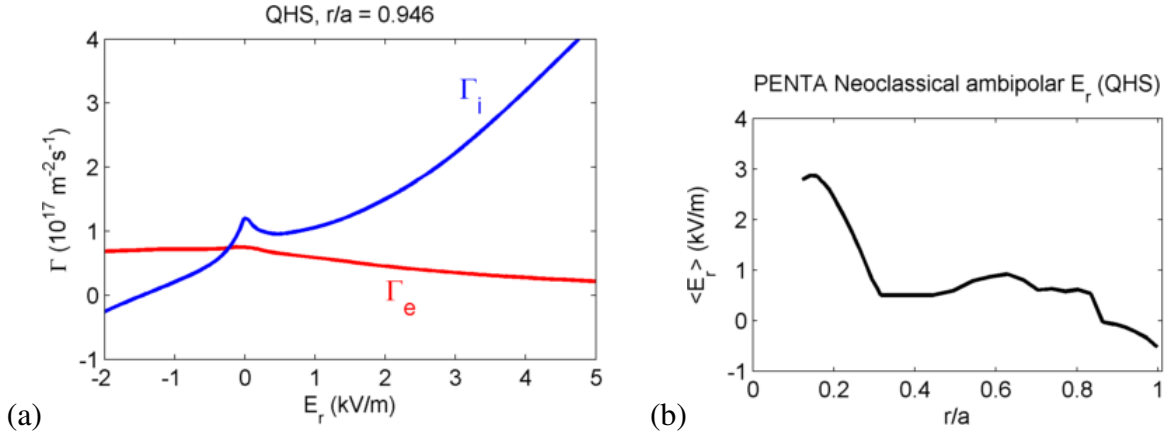


Figure 4.3 (a) Neoclassical particle fluxes as a function of  $E_r$  for hydrogen ions (blue) and electrons (red) calculated by PENTA for HSX experimental parameters at  $r/a \approx 0.95$  in the QHS configuration, and (b) the predicted radial  $E_r$  profile resulting from these calculations using the ambipolarity constraint for each surface in QHS.

2.2. The full radial profile which results from this calculation for the discharges studied here in the QHS configuration is plotted in Figure 4.3(b).

It has been shown that the addition of experimentally relevant quantities of impurity ions such as carbon results in minimal changes to the resulting calculated neoclassical ambipolar solution for the radial electric field in HSX [18]. Because of this and the low impurity concentrations indicated by low radiated power measurements in these experiments, no additional impurity species were included in the neoclassical modeling.

In the Mirror configuration, the neoclassical particle fluxes are expected to be larger than in the QHS configuration due to the addition of a large  $n=4, m=0$  term to the magnetic spectrum. This is confirmed with the PENTA calculations of the particle fluxes as a function of  $E_r$  plotted in Figure 4.4 using solid lines for the Mirror configuration, along with dashed lines for the fluxes in the QHS configuration.

A radial electric field which deviates from the neoclassical ambipolar root (the intersection of the electron and ion flux curves) would result in a non-ambipolar particle flux and therefore a radial current.  $E_r$  is driven toward the neoclassical ambipolar solution on a timescale proportional to the



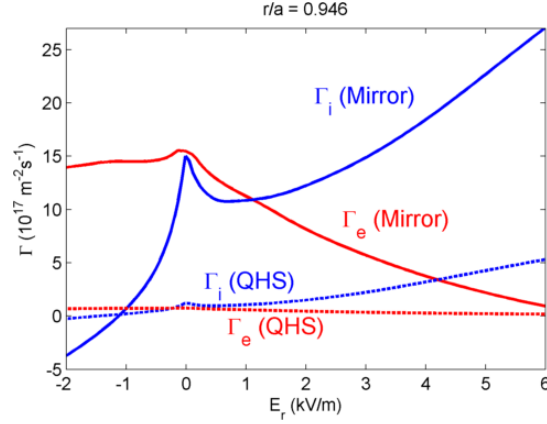


Figure 4.4 Neoclassical particle fluxes as a function of  $E_r$  for hydrogen ions (blue) and electrons (red) calculated by PENTA for HSX experimental parameters at  $r/a \approx 0.95$  in both the Mirror (solid lines) and QHS configurations (dashed lines).

differential particle flux,  $\frac{\partial E_r}{\partial t} \propto (\Gamma_e - \Gamma_i)$  assuming that the gradient of the radial electric field is small enough that diffusion can be neglected [141, 142]. In this sense, the differential neoclassical particle flux can be considered a torque being applied to the plasma as the momentum relaxes toward the ambipolar solution. As seen in Figure 4.4, this differential particle flux would be much larger in the Mirror configuration than in the QHS configuration for most non-ambipolar values of  $E_r$ , resulting in a larger neoclassical torque in the Mirror case.

### 4.1.3 Sensitivity studies

In order to calculate an estimate of the error in the neoclassical calculation, the inputs into the PENTA calculation were varied within the bounds of possible experimental measurement error. For the most-positive limits of the ambipolar  $E_r$  solution, the ion flux was reduced by reducing  $T_i$  by 20% and the electron flux was increased by increasing  $T_e$  by 20% compared to their measured values. The ion flux is more sensitive to changes in the density input, so the density was chosen as 20% less than the measured value from Thomson scattering, which is more than the statistical error in the measurement. This decrease in density reduces both particle fluxes and results in a more-positive  $E_r$  solution. For the most-negative limits of the ambipolar  $E_r$  solution, the opposite

assumptions were made: smaller  $T_e$ , larger  $T_i$  and an increase to the density input. The resulting  $E_r$  calculated in this manner for the neoclassical ambipolarity calculations are shown as dashed lines in Figure 4.5, along with the solution from Figure 4.3(b) as a solid line.

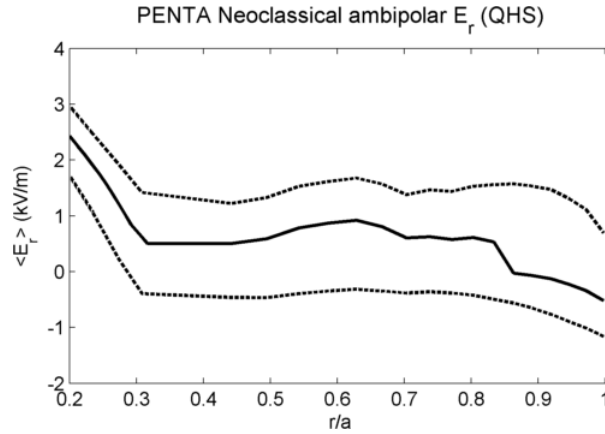


Figure 4.5 Approximate limits of the neoclassical ambipolar solutions calculated by PENTA given conservative estimates of experimental measurement uncertainties.

As demonstrated by Figure 4.5, the calculated errorbars in the edge region of the plasma where probe measurements are taken is  $\leq \sim 1$  kV/m in either direction. These errorbars are very conservative, in that the measurement error is almost certainly smaller than what has been used here, and even if one measurement were incorrect by this amount, all three would almost certainly not be simultaneously wrong in the correct directions for the effects to combine in this way. Changing only one parameter within experimental uncertainties, even  $\nabla T_i$ , which has the largest uncertainty of any of the inputs, does not produce differences in the final ambipolar solution for  $E_r$  as large as those plotted in Figure 4.5. The resilience of this calculated result is due to the fact that the electron flux is relatively small compared to the ion flux, and the ion flux is approximately linear in the plateau collisionality regime, as seen in Figure 4.3(a). Modest changes to the fluxes in this region of the plasma therefore do not result in large changes in the intersection of the two curves. However, these calculated errorbars only indicate error due to measurement uncertainties, and do

not include any possible errors from the coupled numerical codes VMEC, DKES and PENTA themselves.

## 4.2 Raw Langmuir probe data and synthesis

For each discharge, data is acquired from the probe ion saturation current and floating potential signals at a sampling rate of 2.5 MHz for a time that extends from 5 ms before the ECRH is launched until 20 ms after the heating has terminated, including the full 50 ms of time that the ECRH is heating the plasma. The data presented here only uses the time series for the last 20 ms of heating time, which is when the plasma has generally stabilized and most of the macroscopic plasma parameters are in a quiescent state.

An example of raw data from probe pins measuring the floating potential and ion saturation current are plotted in Figure 4.6 (a) and (b), respectively. The moving average of the data using 1 ms time windows is plotted as a green line, and the average of this moving mean is given as a dashed white line. For the mean-value measurements of floating potential and parallel ion flow, the dashed line average will be used as the data point for each of these pins in the shot-by-shot radial scans presented later. The standard deviation of the moving mean will be used as the errorbars for the mean measurement. Each of these values is given above the plots for the discharge presented in Figure 4.6. Although there are intermittent, large amplitude fluctuations on both signals, these are less frequent than they may appear from the plots because there is 600 ms of data plotted with a sample frequency of 2.5 MHz.

The fluctuations on the two ion saturation current signals from opposite sides of the insulating barrier are highly correlated up to high frequencies, indicating that the fluctuations in the  $I_{\text{sat}}$  signal plotted in Figure 4.6(b) are predominantly due to density fluctuations rather than fluctuations of the parallel flow.

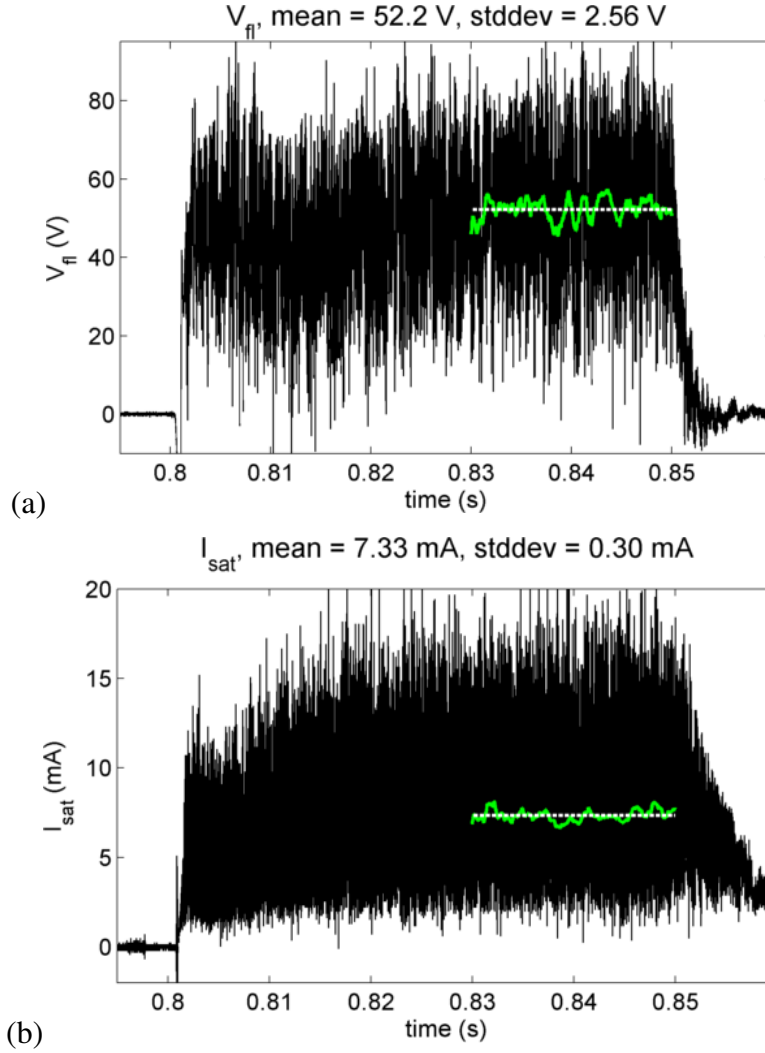


Figure 4.6 Raw data and averages taken from pins measuring (a) floating potential and (b) ion saturation current.

For the data presented here, no coherent modes were detected in the fluctuation spectrum unless otherwise noted. The auto-power spectrum from a sample floating potential signal from the low-field side probe near  $r/a = 0.9$  in the QHS configuration is given in Figure 4.7. The final 20 ms of data from a discharge was split into 20 discrete 1 ms realizations, and the spectrum of each realization was averaged to give the curve in Figure 4.7, which therefore has a frequency resolution of 1 kHz - 1.25 MHz. The noise which is plotted is the spectrum of the signal for the 5 ms of data which is taken before the ECRH is turned on, using the same 1 ms discrete time windows.

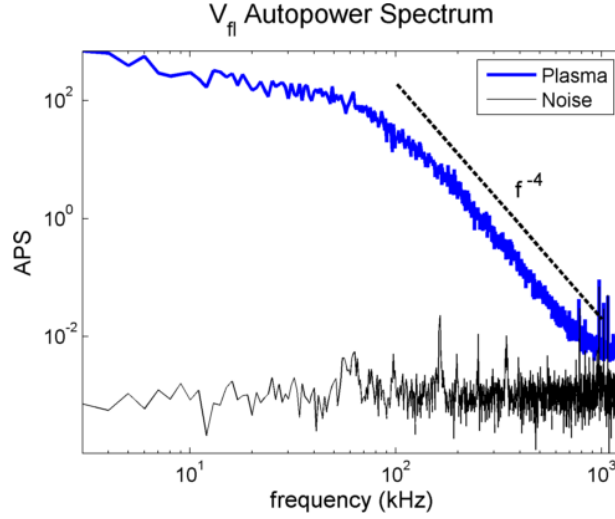


Figure 4.7 Auto-power spectrum of fluctuations from a probe pin measuring the floating potential.

The floating potential fluctuation spectrum in Figure 4.7 exhibits a power law decay of the fluctuation intensity with frequency in the inertial range (the frequency range between the generation and dissipation frequencies of the turbulence, above about 100 kHz) with an exponent of approximately -4. This is the same value for the exponent which was measured previously for fluctuations in HSX discharges where the main magnetic field strength  $B_0 = 0.5$  T [143]. This Kolmogorov-like power-law decay is expected for saturated, high Reynolds number turbulence [144]. The autocorrelation time of the potential fluctuations in the confined plasma region is approximately  $10 \mu\text{s}$ .

The ion saturation current measurement signals did not exhibit the same characteristic decay of fluctuations in the inertial frequency range, as shown in Figure 4.8(a), where relevant power remains in fluctuation frequencies up to the Nyquist frequency (1.25 MHz). The fluctuation amplitude still falls with frequency, but it does so more slowly for the  $I_{sat}$  signals than it did for the  $V_{fl}$  signals. The cause of these observed fluctuations up to very high frequencies remains uncertain, but a circuit component with a nonlinear transfer function at high frequencies is suspected of producing this result. A digital filter is therefore applied above the frequencies that are determined to

be real plasma fluctuations based on the  $V_{fl}$  signals (above 250 kHz). The filtered and unfiltered signals for both  $I_{sat}$  and  $V_{fl}$  measurements are plotted in Figure 4.8.

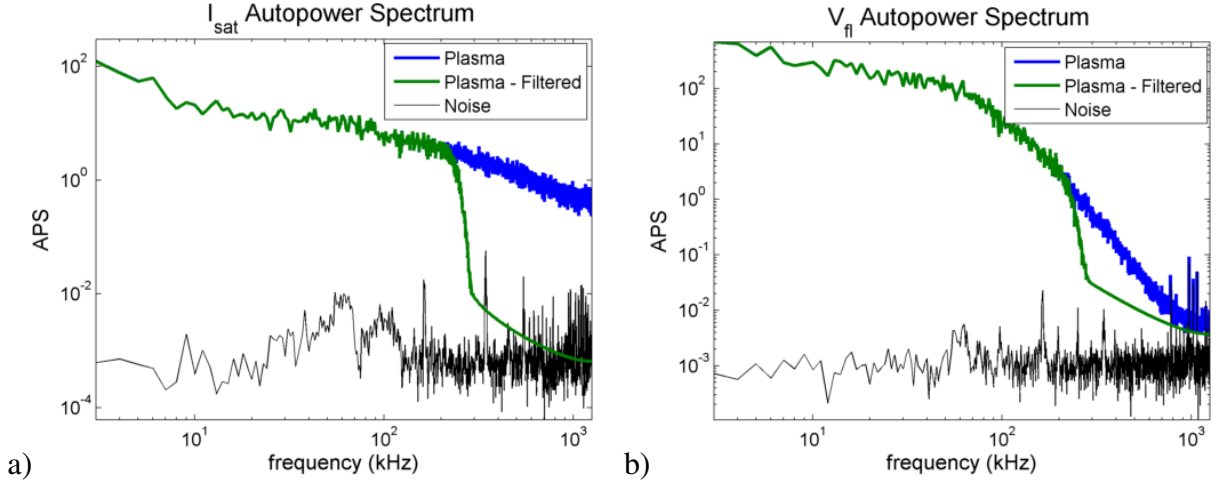


Figure 4.8 Auto-power spectra of fluctuations from probe pins measuring (a) the ion saturation current and (b) the floating potential, with and without an applied digital filter at 250 kHz.

The filtering of the  $V_{fl}$  signals at 250 kHz results in a reduction of the total fluctuating quantities of less than 0.5%, demonstrating that the majority of the real plasma fluctuations are left intact by the filter. The spikes in the  $V_{fl}$  fluctuation spectrum around 1 MHz were determined to be radio stations, and the filter effectively eliminates these from the analysis. The reduction in  $I_{sat}$  fluctuations due to filtering is  $\sim 10\text{-}20\%$ , depending on the discharge.

### 4.3 Radial electric field measurements

Using the leading pins of the Reynolds stress probe to measure floating potential, the radial electric field can be found by accounting for the effect of  $T_e$  on the floating potential measurement ( $V_{fl} = \Phi_p - \mu \frac{T_e}{e}$  from Equation 3.1), then fitting the resulting potential profile and taking the spatial derivative. The value is then scaled to the flux surface average value of  $E_r$  to account for the distance in flux space along the linear path of the probe at its insertion point. This method uses the assumption that both  $\phi$  and  $T_e$  are constant on a flux surface, and that these are the only

contributions to  $V_{fl}$  that change as the probe moves through the plasma. Although extrapolating the Thomson scattering measurements in the edge has been used effectively as an estimate of  $T_e$ , a potentially more accurate estimate of the local electron temperature is implemented here using the existing measurements from the Langmuir probes.

### 4.3.1 Measurement of $T_e$ from fluctuating signals

A technique for estimating the local electron temperature at the probe location in a given discharge has been developed for this work. Assuming an adiabatic electron response, fluctuating electron density and plasma potential can be related by the expression

$$\frac{\tilde{n}_e}{n_e} = e^{\tilde{\phi}/T_e} - 1, \quad (4.1)$$

where  $\tilde{n}_e$  and  $\tilde{\phi}$  are the fluctuating components of the electron density and plasma potential, respectively. For the relatively collisional edge where the probe measurements are taken, the adiabatic assumption should be approximately valid.

Rearranging Equation 4.1 results in an expression for the electron temperature in terms of the fluctuating potential and density components, each of which can be approximated using probe measurements:

$$\frac{T_e}{e} = \frac{\tilde{\phi}}{\ln\left(\frac{\tilde{n}_e}{n_e} + 1\right)}. \quad (4.2)$$

If quasi-neutrality is assumed and electron temperature fluctuations are neglected, then the term  $\frac{\tilde{n}_e}{n_e}$  can be approximated by the fluctuating component of the ion saturation current as  $\frac{\tilde{n}_e}{n_e} \approx \frac{\tilde{I}_{sat}}{I_{sat}}$  ( $I_{sat} = 0.6n_ieA_i\sqrt{\frac{T_e}{m_i}}$  from Equation 3.4). Because the ion saturation current is measured by the Reynolds stress probe using two pins on either side of an insulating barrier, these signals are combined as  $I_{sat,tot} = I_{sat,1} + I_{sat,2}$  to get the total local  $I_{sat}$  signal for the  $\frac{\tilde{n}_i}{n_i}$  term in Equation 4.2. Here the mean signal which is subtracted to find the fluctuating component is taken from discrete

sub-windows rather than a moving mean to enable error analysis. The differences between the resulting calculations using the two mean-finding methods are minor.

The fluctuating potential  $\tilde{\phi}$  is then taken to be the standard deviation of the floating potential signals from the leading pins, assuming that the floating potential fluctuations are dominated by the plasma potential ( $V_{fl} = \Phi_p - \mu \frac{T_e}{e}$  from Equation 3.1). For both the fluctuating  $V_{fl}$  and  $I_{sat}$  signals, the electron temperature fluctuations are assumed to be small compared to the plasma potential and density fluctuations. This effect should be small for the ion saturation current, but for the floating potential signal, it could be significant. For example, based on the value of  $\mu \approx 1.3$  from Section 3.1.1, an electron temperature fluctuation of  $\frac{\tilde{T}_e}{T_e} = 1\%$  would lead to an overestimate of the calculated  $\tilde{\phi}$ , and therefore  $T_e$ , by approximately 5% based on measurements made with the probe positioned near the last closed flux surface. Because the gradient of this  $T_e$  is used in the analysis to calculate  $E_r$ , this is not expected to change the result significantly, unless there is also a large  $\nabla \frac{\tilde{T}_e}{T_e}$ .

Using Equation 4.2 and the assumptions given above, the estimated electron temperature profile in a series of QHS discharges is given in Figure 4.9 using both the LFS and HFS probes. Discrete 200  $\mu s$  time windows are used for mean subtraction to determine the fluctuating components of the  $V_{fl}$  and  $I_{sat}$  signals at each point. The variance of the fluctuating components of  $V_{fl}$  and  $I_{sat}$  across the discrete time windows is then used to determine the total variance of the measurement  $\sigma_T^2$  such that

$$\frac{\sigma_T^2}{T_e^2} = \frac{\sigma_{\tilde{\phi}}^2}{\tilde{\phi}^2} + \frac{\sigma_N^2}{N^2}, \quad (4.3)$$

where  $\sigma_{\tilde{\phi}}$  is taken as the standard deviation of the floating potential fluctuations over the time windows,  $N = \ln(\frac{\tilde{n}}{n} + 1)$  and  $\sigma_N$  is the standard deviation of this term  $N$  over the time windows.

The  $T_e$  measurements from Thomson scattering are plotted alongside the estimate of  $T_e$  from the probe fluctuations in Figure 4.9. It should be noted that the photon counts in this Thomson data set were low, and the temperature profile from the probe is similar to an estimated  $T_e$  gradient based



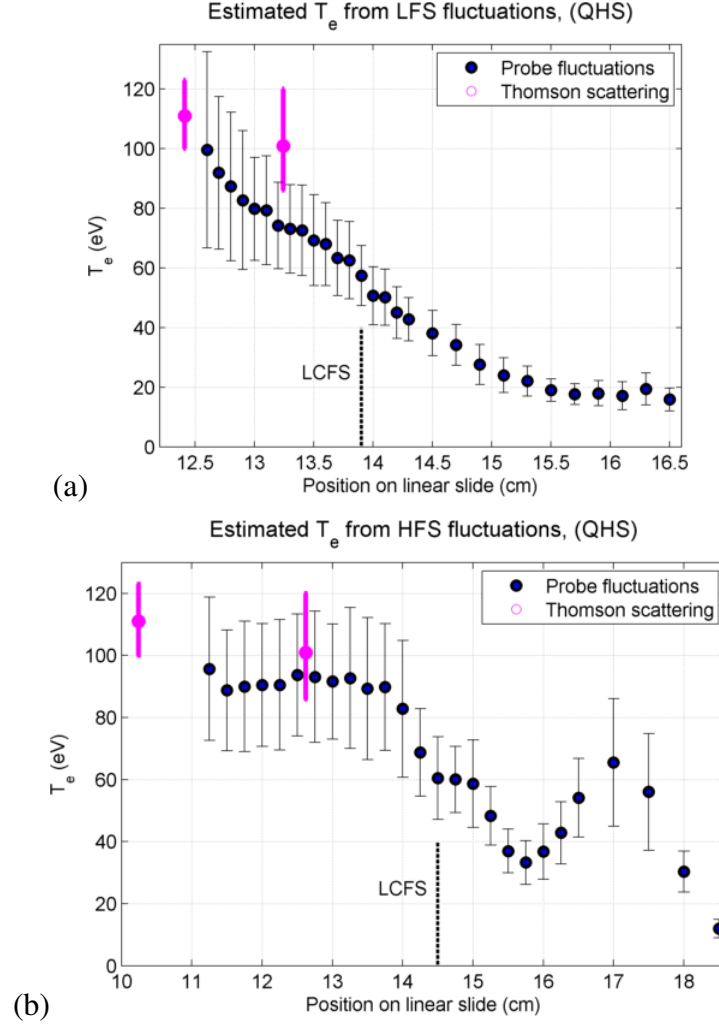


Figure 4.9 Electron temperature profiles estimated from  $V_{fl}$  and  $I_{sat}$  fluctuations based on Equation 4.2 using the (a) LFS and (b) HFS Reynolds stress probes in the QHS configuration.

on previous Thomson scattering profiles in the outer half radius of QHS plasmas. The outermost Thomson scattering point at  $r/a \approx 0.9$  is generally measured to be closer to 70-80 eV, rather than the 100 eV measurement made with large errorbars in this data set.

Inside the confinement region (approximately  $< 13.9$  cm on the LFS in Figure 4.9(a) and  $< 14.5$  cm on the HFS in Figure 4.9(b)), the measured fluctuation values that resulted in these calculated temperatures were  $\tilde{n}/n \approx 20\text{-}30\%$ . A digital low-pass filter has been applied at 250 kHz to eliminate fluctuations measured at high frequency that are not thought to be real plasma fluctuations,

as explained in Section 4.2. Each data point is taken on a different discharge, and the scans of the HFS and LFS probes were each performed over the course of a different set of discharges. The differences between the electron temperature in the confinement region calculated from the measurements using the two probes may be a measurement error, may be due to changes in the plasma over the course of the experiments, or may also be from real differences in edge plasma parameters in the two data sets, possibly due to the presence of the probes. Based on the evidence from Figure 3.14 demonstrating that the HFS probe changes the measured values at the LFS probe as it is inserted, this estimate of  $T_e$  may be further evidence that the presence of the HFS probe has a meaningful impact on the edge plasma parameters.

There is also the possibility that the island shown in Figure 3.7 is the reason for the flattening of  $T_e$  at the HFS probe location when the probe location is inside about 14 cm. However, based on vacuum line following, the width of this island is calculated to be  $\approx 0.75$  cm along the axis of the probe, and the  $T_e$  profile is flat over a much wider region in Figure 4.9(b).

When the same technique is applied to a set of discharges in the Mirror configuration, the resulting electron temperature profile is given in Figure 4.10, again using both the LFS and HFS Reynolds stress probes. These profiles again match closely with Thomson scattering data, even more so than they did in the QHS data from Figure 4.9, giving further confidence in the technique as an estimate of  $T_e$ .

For each discharge, the plasma potential at the radial location of the probe is then calculated using Equation 3.1 with the floating potential signal and this estimate of  $T_e$  plotted in Figures 4.9 and 4.10. This gives better profile resolution to the measurements than the Thomson scattering, and also tracks any changes in the local plasma parameters from shot to shot which may be caused by slight differences in parameters like the absorbed heating power or impurity content.

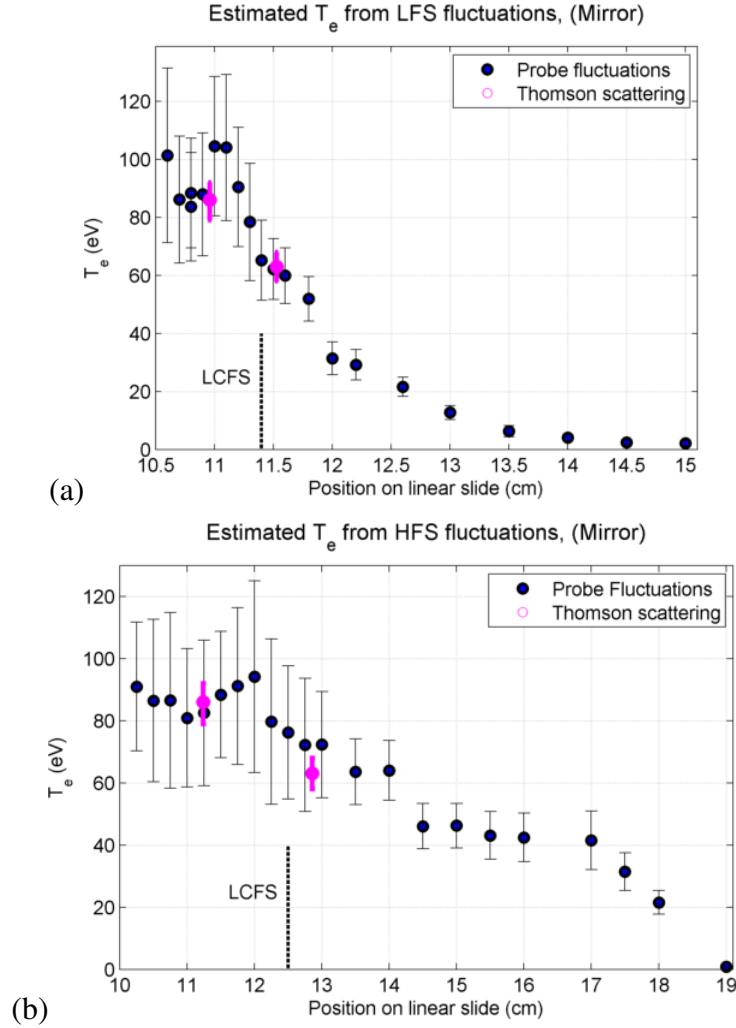


Figure 4.10 Electron temperature profiles estimated from  $V_{fl}$  and  $I_{sat}$  fluctuations using the (a) LFS and (b) HFS Reynolds stress probes in the Mirror configuration.

### 4.3.2 $E_r$ profile and comparison to neoclassical calculations

Using the procedure outlined in Section 4.3.1 to account for the contribution of the electron temperature to the floating potential signal ( $\Phi_p = V_{fl} + \mu_e^{T_e}$  from Equation 3.1), the plasma potential profile in the confinement region of the QHS configuration measured by the LFS probe is given in Figure 4.11(a). The  $V_{fl}$  measurement is taken from the moving mean of the  $V_{fl}$  signal using 1

ms time windows. The variance of this moving mean,  $\sigma_{fl}^2$ , is used to propagate the errorbars and calculate the uncertainty in the final plasma potential.

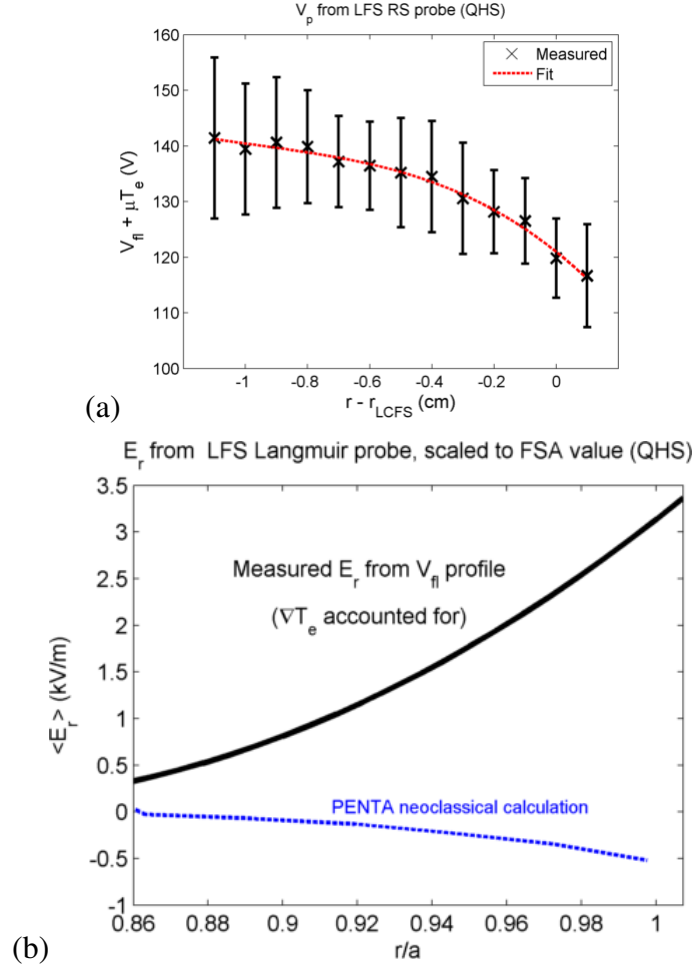


Figure 4.11 (a) Potential profile with a polynomial fit and (b) the resulting flux-surface averaged  $E_r$  measured by the LFS Reynolds stress probe in the QHS configuration, and a comparison with neoclassical calculations from PENTA.

The errorbars indicate the standard deviation of the plasma potential  $\sigma_p$ , which is calculated from the variance in the  $V_{fl}$  measurement ( $\sigma_{fl}^2$ ) and the variance in the  $T_e$  measurement ( $\sigma_T^2$ ) as

$$\sigma_p^2 = \sigma_{fl}^2 + \mu^2 \sigma_T^2, \quad (4.4)$$

based on  $\Phi_p = V_{fl} + \mu \frac{T_e}{e}$  from Equation 3.1, where  $\mu$  is the coefficient calculated in Equation 3.2, the variance of which is neglected as small for this calculation. The value for  $\sigma_T$  is taken from the

errorbars on the measurement of  $T_e$  calculated in Section 4.3.1 and plotted in Figures 4.9 and 4.10. The variance in the temperature measurement is the largest source of error here.

The potential profile is fit to a polynomial using a nonlinear weighted fit (MATLAB's "nlinfit" function), where the weight at each data point is taken as the inverse of the variance of the data. This fit is also plotted in Figure 4.11(a) as a dashed red line, and the derivative of the fit is taken to calculate the local radial electric field. Assuming that the plasma potential  $\phi$  is constant on a flux surface, the local radial electric field along the axis of the probe slide  $l$  is  $E_{probe} = -\frac{d\Phi}{d\psi} \frac{d\psi}{dl}$ . Here  $\frac{d\psi}{dl}$  is the local change in flux along the axis of the probe slide, taken from Figure 3.8. This quantity varies depending on the local geometry and must be translated to a flux surface averaged value of  $E_r$  for comparison with neoclassical theory. The measured value is therefore scaled by a geometric factor to find the flux surface averaged value  $\langle E_r \rangle$ , so that

$$\langle E_r \rangle = -\frac{d\Phi}{d\psi} \frac{d\psi}{dl} \frac{dl}{d\langle r \rangle}, \quad (4.5)$$

where the term  $\frac{dl}{d\langle r \rangle}$  is the ratio of the linear distance each probe travels to the change in flux surface average radial coordinate  $r$  used by PENTA. This geometric factor is calculated to be approximately 1.7 for the LFS probe and 0.6 for the HFS probe in the QHS configuration.

Taking the locally calculated potential from Figure 4.11 and accounting for the local flux expansion along the axis of the probe according to Equation 4.5, the measured radial electric field using the LFS probe is plotted in Figure 4.11(b). The values of  $E_r$  calculated by PENTA using the neoclassical ambipolarity constraint, calculated in Section 4.1, are also plotted as a blue dashed line for comparison. The measured radial electric field is significantly more positive than the predicted neoclassical value calculated by PENTA, especially in the region where  $r/a > 0.9$ .

Based on previous measurements of  $E_r$  using CHERS in  $\text{CH}_4$  plasmas, as plotted in Figure 2.20, the radial electric field is expected to be  $\approx 5$  kV/m at  $r/a=0.8$  (albeit with large errorbars,  $\pm 3$  kV/m). This is larger than the values of  $E_r$  given by the probe measurements plotted in Figure 4.11. It

could be that the influence of the presence of the probe on the shot-to-shot floating potential profile causes the measured  $E_r$  to be reduced. This was the case using the HFS probe in the perturbation experiments presented in Figure 3.14, but the same experiment for the LFS seemed to demonstrate that the floating potential was not affected by the presence of the probe. However, this experiment necessitated that the HFS probe be inserted for all of the discharges, which may have distorted the results of the LFS probe perturbation test.

Using the HFS probe, the result of the mean radial electric field measurement made using the LFS probe could not be reproduced. The potential profile using the HFS probe is presented in Figure 4.12.

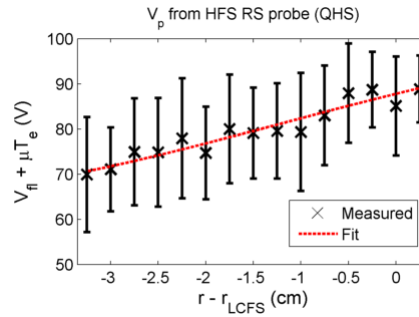


Figure 4.12 Potential profile measured by the perturbative HFS probe in the QHS configuration.

The discrepancy between the LFS and HFS probes is most likely due to the perturbation introduced to the plasma as the HFS probe is inserted, as demonstrated in Figure 3.14, where the floating potential signal at the stationary LFS probe was reduced as the HFS probe was inserted into the plasma. There will therefore be no analysis performed using the time-averaged floating potential measurements to estimate the radial electric field using the HFS probe.

#### 4.4 Parallel flow measurements

Another mean plasma parameter measured by the Reynolds stress probes that can be compared to neoclassical calculations is the parallel ion flow. The parallel ion flow is measured using the two

ion saturation pins of the Reynolds stress probe configured as a mach probe, as described in Section 3.1.3. The measurement given by the probe is the parallel mach number  $M_{||} = V_{||}/(Kc_s)$ , where  $c_s = \sqrt{(T_e + T_i)/m_i}$  is the ion sound speed and  $K$  is a constant determined by the model. This is translated to a parallel velocity by assuming hydrogen ions and using the same  $T_e$  and  $T_i$  profiles that are used as inputs to PENTA which were given in Section 4.1.1. As explained in Section 3.1.3, an unmagnetized model by Hutchinson has been used to determine the value of  $K = 1.34$  for this work [136].

The total local parallel ion flow can be expressed as [69, 147]

$$V_{||i} = \left( \frac{\langle V_{||i} B \rangle}{\langle B^2 \rangle} + \left( \frac{1}{enZ_i} \frac{dp_i}{d\psi} + \frac{d\Phi}{d\psi} \right) h \right) \mathbf{B}, \quad (4.6)$$

where  $\langle \dots \rangle$  indicates a flux surface average,  $\frac{dp_i}{d\psi}$  is the ion pressure gradient,  $\frac{d\Phi}{d\psi}$  is the radial potential gradient, and  $h$  is a geometric factor equivalent to the normalized Pfirsch-Schlüter current ( $h\mathbf{B}\nabla p = \mathbf{J}_{||,PS}$ ) [145, 146, 147]. The first term in the parenthesis is the flux surface constant  $\frac{\langle V_{||i} B \rangle}{\langle B^2 \rangle}$ , which is calculated from PENTA. The second term is the contribution of Pfirsch-Schlüter flows and will be discussed in Section 4.4.1. All of the terms combined will then be calculated and compared with experimental measurements in HSX in Section 4.4.2.

The parallel ion flow over the local magnetic field strength that would result from a given value of the radial electric field is plotted in Figure 4.13, as calculated by PENTA. This represents the term  $\frac{\langle V_{||i} B \rangle}{\langle B^2 \rangle}$  in Equation 4.6. The relationship between  $E_r$  and  $V_{||,i}/B$  in Figure 4.13 is mostly linear in the region where these experiments are concerned near  $E_r=0$ , and it does not change significantly across the radial range over which the probe is scanned.

#### 4.4.1 Pfirsch-Schlüter component of the parallel ion flow

The Pfirsch-Schlüter component of the parallel flow may be written for species  $a$  as [146, 147]

$$V_{||,a,PS} = \left( \frac{d\Phi}{d\psi} + \frac{1}{q_a n_a} \frac{dp_a}{d\psi} \right) h \mathbf{B}. \quad (4.7)$$

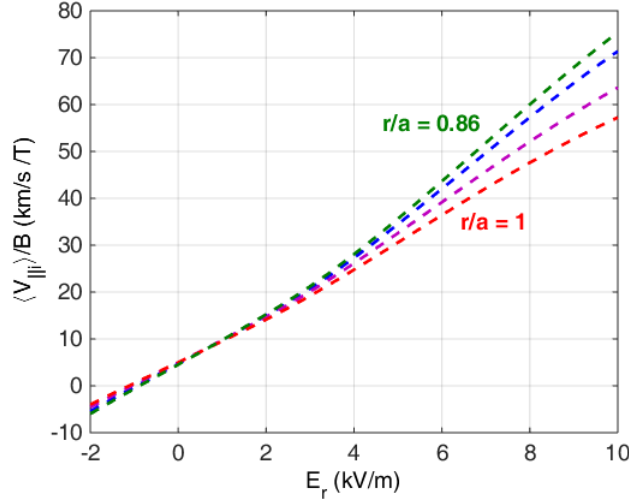


Figure 4.13 Parallel ion flow divided by the local magnetic field strength ( $B \approx 1$  T) as a function of  $E_r$  for a selection of radial locations in the edge of the QHS configuration, calculated by PENTA.

For hydrogen ions, equation 4.7 can then be expressed in terms of the experimentally measured quantities  $E_r$  and  $\frac{dp_i}{dr}$  as

$$V_{||,i,PS} = \left( -E_r + \frac{1}{en_i} \frac{dp_i}{dr} \right) \frac{dr}{d\psi} h\mathbf{B} \quad (4.8)$$

where the derivatives in flux space have been translated to measured spatial derivatives. The term  $\frac{dr}{d\psi}$  is derived as

$$\begin{aligned} \frac{r}{a} &= \sqrt{\frac{\psi}{\psi_a}} \\ \frac{dr}{d\psi} &= \frac{a}{2} \frac{1}{\sqrt{\psi\psi_a}}, \end{aligned} \quad (4.9)$$

where  $\psi_a$  is the flux through the last closed flux surface and  $a$  is the flux surface averaged minor radius of the plasma.

Based on Equation 4.8, the contribution of Pfirsch-Schlüter flows to the local parallel ion velocities at each measurement location of the LFS and HFS probes in the QHS configuration are given in Figure 4.14. The contributions to  $V_{||,PS}$  from the ion pressure gradient and radial electric field terms are broken out and plotted as blue and red X's, respectively, and the sum total of these are given as black circles. A representative value of  $E_r = 2$  kV/m was used to calculate the contribution



due to the radial electric field, where this term scales linearly with  $E_r$ . The ion pressure gradient was calculated using the same values of  $T_i$  from CHERS measurements that is used as the PENTA input file (the scaled-down linear fit from Figure 4.2), so the uncertainty of this term is large, of order  $\sim 50\%$ . Changes in  $\nabla p_i$  within the measurement uncertainty are not calculated to generate significant changes to the total flows.

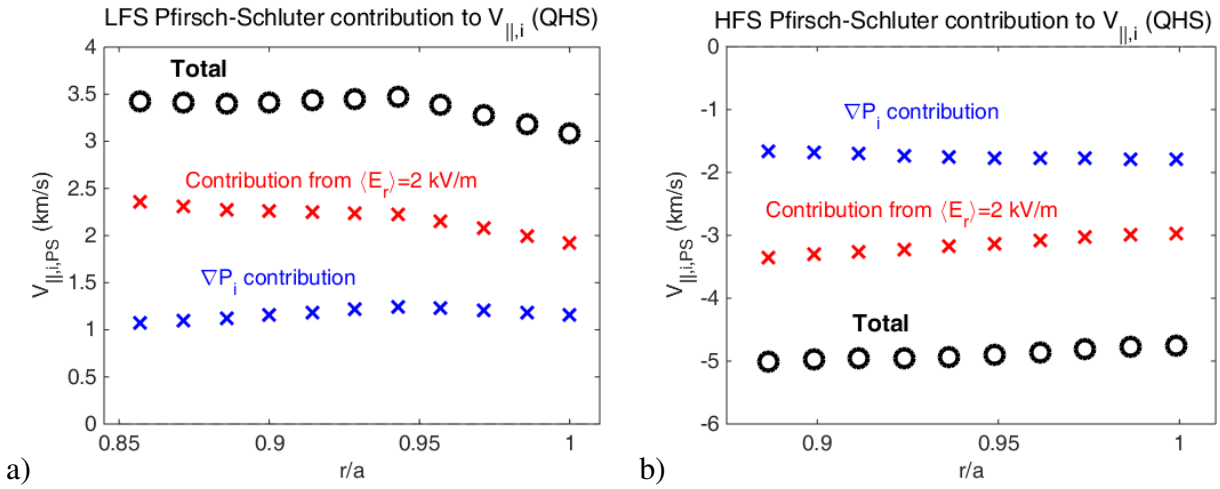


Figure 4.14 Contributions of Pfirsch-Schlüter flows to the parallel ion velocity given assumed ion pressure gradients and radial electric fields at (a) the LFS and (b) HFS probe locations in the QHS configuration.

Figure 4.14 demonstrates that the magnitude of the Pfirsch-Schlüter flows at the locations of the probes (in km/s) is on the order of a few km/s, depending on the value of  $E_r$ . These calculated Pfirsch-Schlüter flows will be included using the appropriate values of  $E_r$  in the comparisons of measurements to neoclassical modeling in the sections to follow.

#### 4.4.2 Total measured $V_{||}$ profiles and comparison to neoclassical calculations in QHS

The parallel ion velocity given the measured mach numbers and assumed temperature profiles is shown in Figure 4.15. Each value plotted is the average of the moving mean of the processed signals over the final 20 ms of each discharge using a 1 ms boxcar average, and the errorbars

indicate the standard deviation of the moving mean. The parallel ion flow that is calculated to result from the neoclassical ambipolar solution for  $E_r$  using Equation 4.6 is also plotted in blue. The  $\frac{\langle V_{||i} B \rangle}{\langle B^2 \rangle}$  term is calculated directly by PENTA as plotted in Figure 4.13, and the local contribution from the Pfirsch-Schüter flows for the PENTA-calculated ambipolar solution of  $E_r$  is calculated using Equation 4.8.

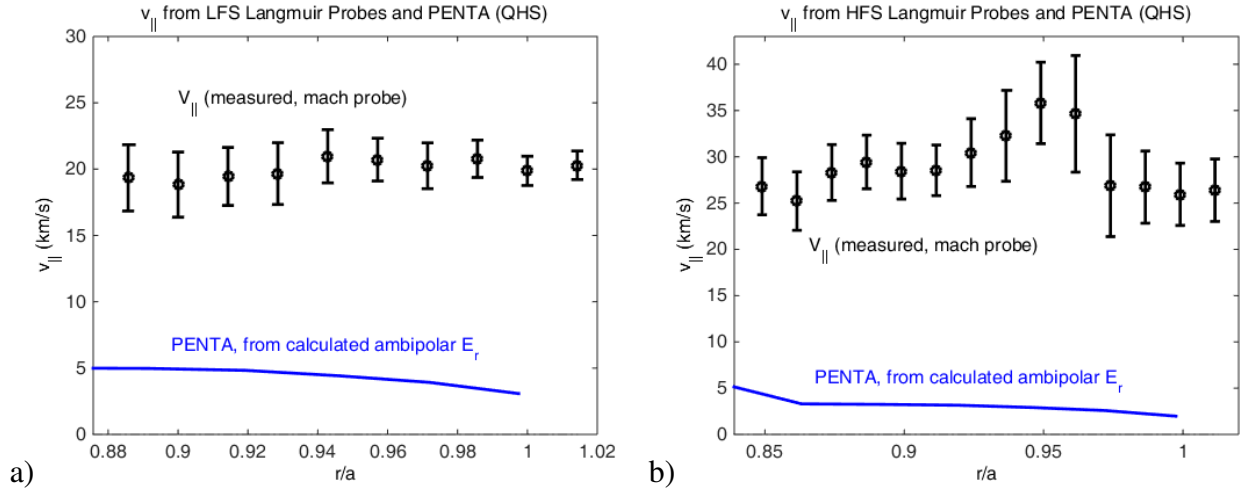


Figure 4.15 Parallel ion flow in the QHS configuration measured by the (a) LFS and (b) HFS mach probes, compared with neoclassical predictions from PENTA.

The parallel flows measured on both the LFS and HFS probes that are depicted in Figure 4.15 deviate significantly from the values calculated to result from the neoclassical ambipolarity condition by PENTA. This is another piece of evidence that the neoclassical non-ambipolar transport calculated by DKES and PENTA is not properly accounting for all of the terms in the transport and momentum balance equations in the QHS configuration. Each probe measures a parallel velocity profile that is relatively consistent across the minor radius with the exception of the HFS probe in the radial region around  $r/a \approx 0.95$ , which is approximately the region of the 12/11 magnetic island, as plotted in Figure 3.7.

After accounting for an estimate of the local Pfirsch-Schüter flows and the change in local velocity due to the field strength as described in Equation 4.6, the measurements of  $V_{||}$  in Figure

4.15 give the flux surface averaged component of the parallel flow  $\langle V_{||i} \rangle \approx 20$  km/s at the LFS probe and  $\approx 30$  km/s at the HFS probe. The discrepancy between the two measurements could be caused by a miscalibration of the probe collection areas on one or both of the probes, or by local perturbations introduced by the insertion of the probes, or by real changes in the background plasma between the independent sets of discharges used for each probe scan.

Taking a flux surface averaged parallel flow of  $\langle V_{||} \rangle \approx 20 - 30$  km/s and applying it to the curve of  $\langle E_r \rangle$  versus  $V_{||}/B$  from Figure 4.13, the measured parallel flow would imply  $\langle E_r \rangle \approx 3 - 5$  kV/m. Comparing this  $E_r$  to the value calculated using the LFS floating potential profile which is plotted in Figure 4.11, the radial electric field inferred from the  $V_{||}$  measurement matches the LFS  $\nabla V_{fl}$  measurement just inside the last closed flux surface, but it is larger than what was measured using the floating potential further inside the plasma. This may be an indication that the probe is perturbing the plasma enough to affect the floating potential measurement as it is inserted, because the velocity measurements are relatively consistent across the radius, while the measured value of  $E_r$  decreases as the probe is inserted further into the plasma.

Possible sources of error in the  $V_{||}$  measurement are changes in the  $T_i$  and  $T_e$  values relative to the assumed profiles that were used to translate the measured flux ratio between the two  $I_{sat}$  pins into a parallel flow velocity. An overestimate of either  $T_i$  or  $T_e$  or an underestimate of  $m_i$  due to impurity ions would lead to an overestimate of the  $V_{||}$  calculated from the measured differential  $I_{sat}$  fluxes.

## 4.5 $E_r$ and $V_{||}$ measurements in other configurations

The measurements presented in sections 4.3.2 and 4.4 for the QHS configuration were taken again in the Mirror and Flip-1-4 configurations. In the Mirror configuration, the neoclassical damping term is largest, and the drive toward the neoclassical ambipolar solution is the largest, as demonstrated by the differential fluxes in Figure 4.4 ( $\frac{\partial E_r}{\partial t} \propto (\Gamma_e - \Gamma_i)$ ). As explained in Section

4.1.2, the expectation for the Mirror configuration is therefore that the flows would be closer to the neoclassical calculations than they are in the QHS configuration.

#### 4.5.1 $E_r$ and $V_{||}$ measurements in the Mirror configuration

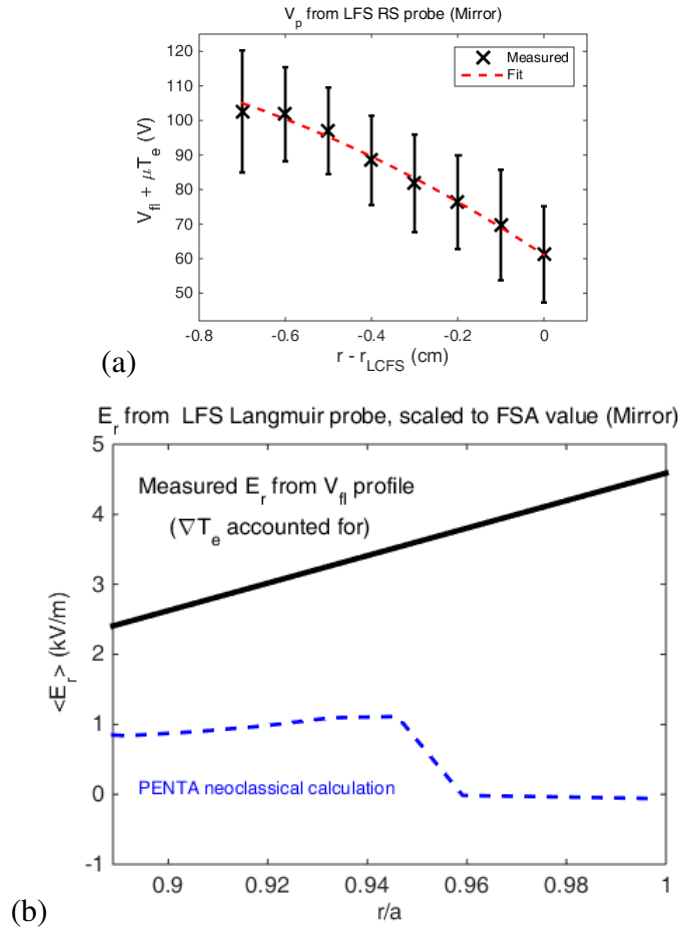


Figure 4.16 (a) Potential profile with a polynomial fit and (b) the resulting flux-surface averaged  $E_r$  measured by the LFS Reynolds stress probe in the Mirror configuration, and a comparison with neoclassical calculations from PENTA.

The measured potential profile, its fit, and resulting radial electric field using the LFS probe in the Mirror configuration are plotted in Figure 4.16. The radial electric field is again calculated from the potential profile along the axis of the probe according to Equation 4.5. Contrary to expectations,

the radial electric field deviates from the neoclassical value calculated by PENTA by more in the Mirror configuration than in the QHS configuration (from Figure 4.11).

The normalized parallel flow that is calculated to result from a given value of  $E_r$  by PENTA in the Mirror configuration is plotted in Figure 4.17. These parallel flows are smaller than those in the QHS configuration plotted in Figure 4.13 for equivalent values of  $E_r$  because the additional terms in the magnetic spectrum in the Mirror configuration increase the parallel flow damping.

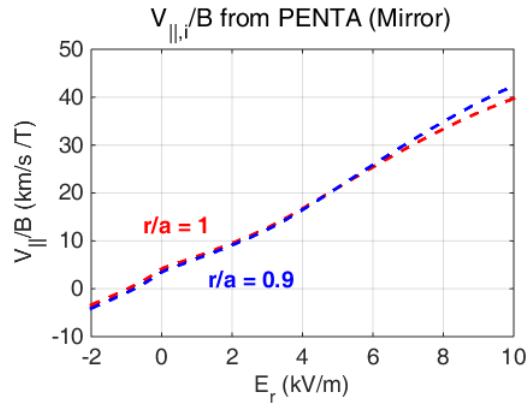


Figure 4.17 Parallel ion flow divided by the local magnetic field strength ( $B \approx 1$  T) as a function of  $E_r$  for a selection of radial locations in the edge of the Mirror configuration, calculated by PENTA.

The parallel flow measurements in the Mirror configuration are plotted in Figure 4.18(a) using the LFS probe and Figure 4.18(b) using the HFS probe. Based on the relationship between  $E_r$  and  $V_{||}$  shown in Figure 4.17, these parallel flows are much larger than would be expected given the measured values of  $E_r$  from Figure 4.16.

The Pfirsch-Schlüter factor  $h$  in all configurations used here is similar to that in the QHS configuration at both probe locations, so that the values plotted in Figure 4.14 are a good estimate of the contribution of Pfirsch-Schlüter flows at each probe location for the given value of  $E_r$ . The difference between the measured flows using the LFS and HFS probes implies a radial electric field of  $E_r \approx 8$  kV/m around  $r/a=0.95$ , which is larger than the values approximated by the floating potential gradient plotted in Figure 4.17. If this  $E_r \approx 8$  kV/m from the Pfirsch-Schlüter calculations

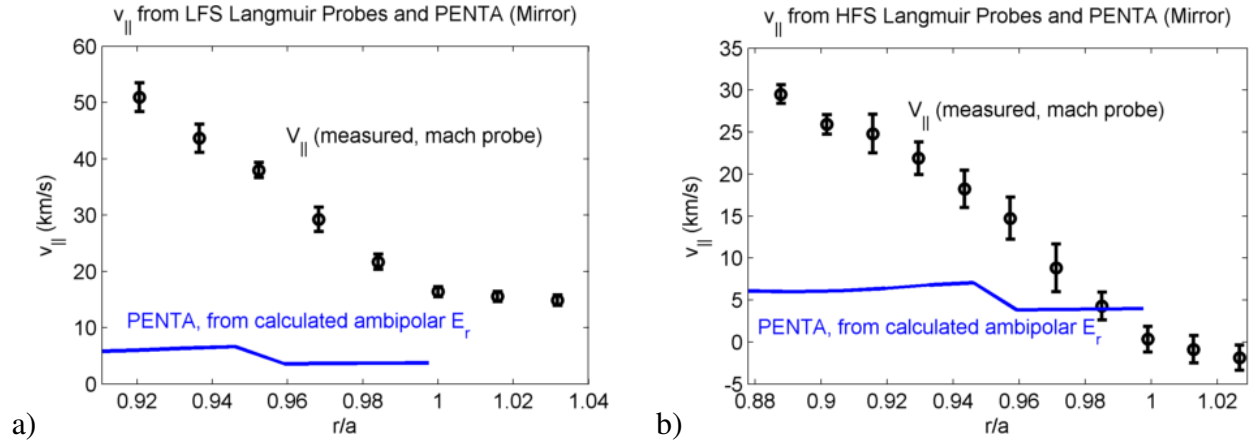


Figure 4.18 Parallel ion flow in the Mirror configuration measured by the (a) LFS and (b) HFS mach probes, compared with neoclassical predictions from PENTA.

were applied to the curve of  $V_{\parallel}$  as a function of  $E_r$  from Figure 4.18, however, it yields a value of the parallel flow that is similar to that measured directly by the probes,  $V_{\parallel i}/B \approx 30$  km/s. Although these parallel flow values may be overestimated due to incorrect assumptions of  $T_e$ ,  $T_i$  or  $m_i$ , based on this analysis of the parallel flows, the radial electric field is most likely even larger than the values plotted in Figure 4.17 as measured using the gradient of the floating potential profile.

The large flows in the Mirror configuration plotted in Figure 4.18 are a second independent measurement (along with  $E_r$  from Figure 4.16(b)) demonstrating that the flows deviate even more from the neoclassical ambipolar solution calculated by PENTA in the Mirror configuration than they did in the QHS configuration. One possible explanation for this is that the neoclassical transport codes do not accurately capture the collisionless electron losses due to the magnetic ripple in the Mirror configuration. DKES and PENTA modeling is radially local and assumes a Maxwellian distribution, so that non-local transport such as collisionless loss orbits will not be properly accounted for. Additional ripple-trapped electron losses that are unaccounted for by DKES and PENTA would drive the ambipolar solution to a more-positive value of  $E_r$  relative to what is calculated. This hypothesis will be tested first by measuring the intrinsic flows in the Flip-1-4 configuration, which has neoclassical drive and damping terms that are between those of the QHS

and Mirror configurations, as demonstrated by the effective ripple for each configuration plotted in Figure 2.13. If the problem was only that the ripple was too large in the Mirror configuration to be modeled appropriately, and the reduction in ripple going to the Flip-1-4 configuration was sufficient to solve this problem, then the flows might be expected to more closely match the neoclassical calculations in the Flip-1-4 configuration.

#### 4.5.2 $E_r$ and $V_{||}$ measurements in the Flip-1-4 configuration

The Flip-1-4 configuration has an effective ripple in the edge that is between that of the QHS and Mirror configurations, as shown in Figure 2.13. Based on the measurements of the flows in the Mirror configuration given in Section 4.5.1, the collisionless loss orbits in the Mirror configuration may be driving  $E_r$  to a much larger value than what is calculated neoclassically. By reducing the ripple compared to the Mirror configuration, measurements can be compared again with neoclassical modeling to explore the scaling of the flows with ripple. In Chapter 5, the contribution of the Reynolds stress to the flows in each configuration will also be examined, where it will be shown that the measured Reynolds stress is smaller in the configurations with the symmetry broken than it is in the QHS configuration.

The measured potential profile, its fit, and the resulting radial electric field using the LFS probe in the Flip-1-4 configuration are plotted in Figure 4.19, with  $E_r$  again calculated according to Equation 4.5. The parallel flow measurements in the Flip-1-4 configuration using the LFS and HFS probes are then also plotted in Figures 4.20(a) and 4.20(b), respectively. There is a small  $n=20$ ,  $m=18$  island at  $r/a=0.97$  at the HFS probe location that could be influencing the flows, but the island width is smaller than the radial step size of the probe scan.

Unlike in the Mirror configuration, the difference between the parallel flows measured on the LFS and HFS probes cannot be reconciled by the inclusion of Pfirsch-Schlüter flows with a large value for  $E_r$  while preserving some consistency with the flux surface average parallel flow. For

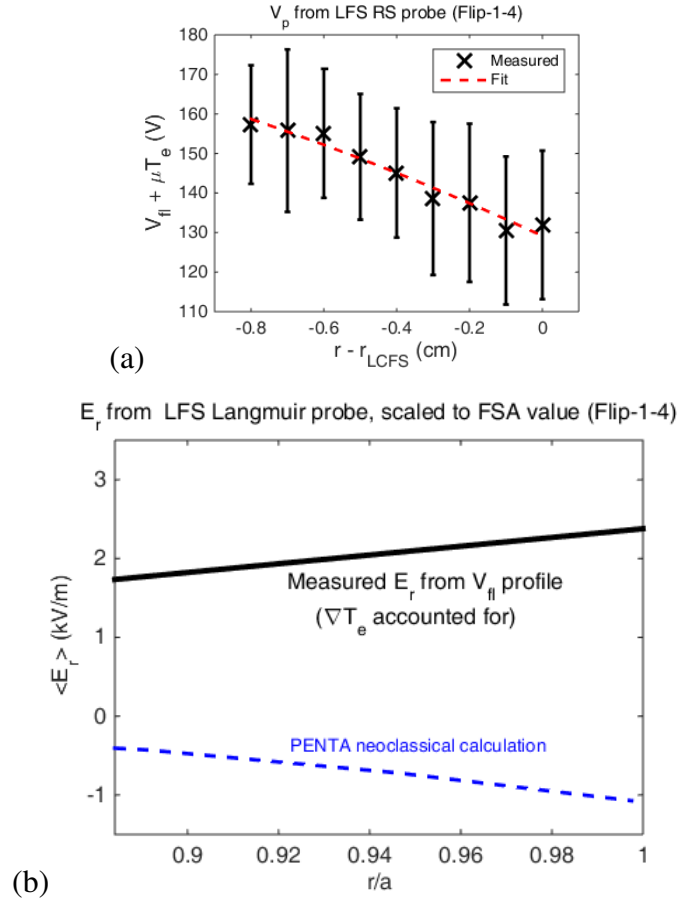


Figure 4.19 (a) Potential profile with a polynomial fit and (b) the resulting flux-surface averaged  $E_r$  measured by the LFS Reynolds stress probe in the Flip-1-4 configuration, and a comparison with neoclassical calculations from PENTA.

$V_{||LFS} \approx 30$  km/s and  $V_{||HFS} \approx 10$  km/s,  $E_r$  would need to be  $\approx 8$  kV/m to cause this level of Pfirsch-Schlüter flow, but this would be expected to lead to a significantly larger flux surface averaged parallel flow than what is measured. Nonetheless, the large parallel flows measured are much larger than what would be expected neoclassically based on calculations by PENTA. Both  $E_r$  and  $V_{||}$  are again indicative of additional electron particle flux that is not accounted for using the neoclassical transport codes, but the radial electric field and parallel flows measured by the LFS probe (which is less perturbative than the HFS probe) are reduced relative to those measured in the Mirror configuration.



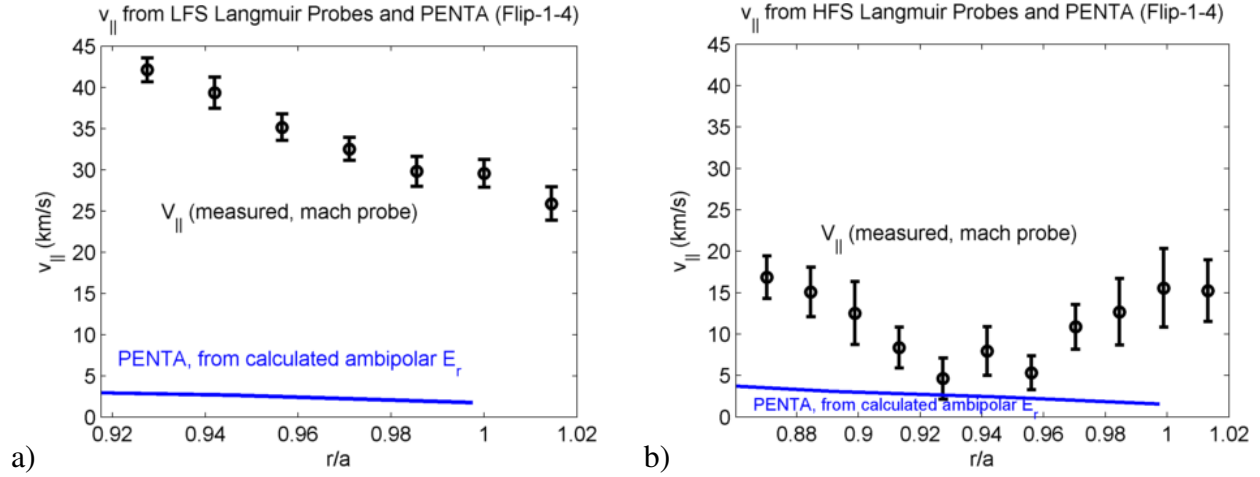


Figure 4.20 Parallel ion flow in the Flip-1-4 configuration measured by the (a) LFS and (b) HFS mach probes, compared with neoclassical predictions from PENTA.

This chapter has presented measurements of the radial electric field and parallel ion flows from the Reynolds stress probes in multiple magnetic configurations, as well as calculations of flows considering neoclassical physics alone using the PENTA code. The measurements are shown to deviate from the neoclassical calculations in the QHS configuration. This was shown to be possible in Chapter 2 because of the competition between the neoclassical term and the Reynolds stress in the momentum balance when the magnetic configuration is optimized towards quasi-symmetry. Chapter 5 will present the Reynolds stress measurements in support of this argument.

This chapter then also presented measurements of  $E_r$  and  $V_{\parallel}$  in the Mirror and Flip-1-4 configurations. In both of these configurations, the expectation was that the value of  $E_r$  would be determined neoclassically due to the increased non-ambipolar transport relative to the QHS configuration, and would therefore be accurately predicted by PENTA. In both cases, however, the radial electric field and parallel flows were large, and more importantly, the deviation from the calculated neoclassical solution was greater than in the QHS configuration in both cases. This deviation of the flows from neoclassical calculations appears to scale qualitatively with effective ripple. If the measured Reynolds stress were larger in these alternate configurations, then the Reynolds stress

may be responsible for the additional rotation. However, it will be shown in Chapter 5 that the local Reynolds stress is actually smaller in both cases. Further discussion of these unexpected results will be presented in Chapter 6.

## References

18. Lore, J. *Jeremy Lore's Dissertation, University of Wisconsin - Madison* 2010.
53. Lore, J., Guttenfelder, W., Briesemeister, A., *et al.* Internal electron transport barrier due to neoclassical ambipolarity in the Helically Symmetric Experiment. *Physics of Plasmas* **17**, 056101 (2010).
69. Briesemeister, A. *Alexis Briesemeister's Dissertation, University of Wisconsin - Madison* 2013.
70. Spong, D. A. Generation and damping of neoclassical plasma flows in stellarators. *Physics of Plasmas* **12**, 056114 (2005).
132. *Private communication, calculations performed by Christopher Clark*, 2012.
136. Hutchinson, I. H. Ion collection by a sphere in a flowing plasma: I. Quasineutral. *Plasma Physics and Controlled Fusion* **44**, 1953 (2002).
140. Summers, H. P. *The ADAS User Manual, version 2.6* <http://www.adas.ac.uk> (2004).
141. Shaing, K. C. Stability of the radial electric field in a nonaxisymmetric torus. *Physics of Fluids* **27**, 1567 (1984).
142. Shaing, K. C. Plasma flows and radial electric field in nonaxisymmetric toroidal plasmas. *Physics of Fluids* **29**, 2231 (1986).
143. Guttenfelder, W. *Walter Guttenfelder's Dissertation, University of Wisconsin - Madison* 2008.
144. Kolmogorov, A. N. The local structure of turbulence in incompressible viscous fluid for very large Reynolds numbers. *Dokl. Akad. Nauk SSSR* **30**, 299–303 (1941).

145. Nemov, V. V. Calculations of the magnetic surface function gradient and associated quantities in a torsatron. *Nuclear Fusion* **28**, 1727 (1988).
146. Coronado, M. & Wobig, H. On the definition of Pfirsch-Schlüter and bootstrap currents in toroidal systems. *Physics of Fluids B* **4**, 1294 (1992).
147. Coronado, M. & Talmadge, J. N. Evolution of the plasma rotation and the radial electric field for a toroidal plasma in the Pfirsch-Schlüter and plateau regimes subject to a biased electrode. *Physics of Fluids B: Plasma Physics* **5**, 1200 (1993).

## Chapter 5

### Measurements of Reynolds stress using Langmuir probes

Using the Langmuir probe system introduced in Chapter 3, measurements of the local fluctuating velocity components have been made at two discrete locations in HSX in order to calculate the contribution of the Reynolds stress to the momentum balance. The two probes are located near the extremes of the variation of magnetic geometry on a flux surface. Each probe is scanned radially from shot to shot using discharges which are similar according to macroscopic diagnostics (interferometer, diamagnetic loop, etc.), and each probe is scanned independently so that one does not affect the measurements of the other. Data points within the scan were taken non-sequentially to ensure that long-term changes in the plasma parameters over the course of a run day were not mistaken for changes in the radial profiles.

In Section 5.1, measurements of the local Reynolds stress using both the LFS and HFS probes in the QHS configuration will be presented. The local gradients of these measurements will then be assumed to be indicative of a flux surface average, and these Reynolds stress drives will be modeled to balance against an analytically calculated viscosity. The flows resulting from the evolution equations will be presented in Section 5.2. Section 5.3 then examines the role of the measured Reynolds stress in configurations where the symmetry is degraded and neoclassical transport is expected to dominate the momentum balance.

## 5.1 Local Reynolds stress measurements

Assuming a local slab geometry, the divergence of the local Reynolds stress tensor can be written as

$$\begin{aligned}
 \nabla \cdot (\tilde{\mathbf{V}}\tilde{\mathbf{V}}) &= \left( \hat{\rho} \frac{\partial}{\partial \rho} + \hat{b} \frac{\partial}{\partial b} + \hat{\theta} \frac{\partial}{\partial \theta} \right) \cdot (\tilde{\mathbf{V}}\tilde{\mathbf{V}}) \\
 &= \hat{\rho} \frac{\partial}{\partial \rho} \tilde{v}_\rho^2 + \hat{b} \frac{\partial}{\partial \rho} (\tilde{v}_\rho \tilde{v}_\parallel) + \hat{\theta} \frac{\partial}{\partial \rho} (\tilde{v}_\rho \tilde{v}_\theta) \\
 &\quad + \hat{\rho} \frac{\partial}{\partial b} (\tilde{v}_\rho \tilde{v}_\parallel) + \hat{b} \frac{\partial}{\partial b} \tilde{v}_\parallel^2 + \hat{\theta} \frac{\partial}{\partial b} (\tilde{v}_\parallel \tilde{v}_\theta) \\
 &\quad + \hat{\rho} \frac{\partial}{\partial \theta} (\tilde{v}_\rho \tilde{v}_\theta) + \hat{b} \frac{\partial}{\partial \theta} (\tilde{v}_\parallel \tilde{v}_\theta) + \hat{\theta} \frac{\partial}{\partial \theta} \tilde{v}_\theta^2,
 \end{aligned} \tag{5.1}$$

where  $\hat{\rho} = \nabla\psi/|\nabla\psi|$  is the unit vector in the direction normal to the flux surface,  $\hat{b}$  is the unit vector in the direction of the magnetic field and  $\hat{\theta}$  is the “bi-normal” direction, defined here as the unit vector perpendicular to the magnetic field, but within the flux surface ( $\hat{\rho} \times \hat{b} = \hat{\theta}$ ). The coordinates are defined in this way because these are the three orthogonal directions which are relevant for the turbulence, and they are approximately the three directions in which the Reynolds stress probes measure velocity fluctuations. The use of a slab geometry neglects additional terms due to torsion and curvature, but the terms given here should be dominant considering the small size of the probe relative to the plasma shaping. The flux surface average of this Reynolds stress term is included in the momentum balance equation as described in Section 2.3.

From Equation 5.1, the terms that drive flows in the radial direction are ignored, because the flow drive within the surface is being examined rather than radial transport, and these terms are expected to be formally smaller. Next, the terms with parallel derivatives ( $\frac{\partial}{\partial b} \dots$ ) are neglected as small compared to the other terms, because drift wave turbulence is expected to have  $k_\parallel \ll k_\perp$ . Finally, because the main phenomenon being investigated and that is expected to dominate is radial momentum transport, and also because there is no measurement of the gradients in the bi-normal direction ( $\frac{\partial}{\partial \theta} \dots$ ), these terms are neglected as well. This leaves only two terms in the expression

to consider for the probe measurements,

$$\langle \nabla \cdot (\tilde{\mathbf{V}}\tilde{\mathbf{V}}) \rangle_{probes} = \hat{b} \left\langle \frac{\partial}{\partial \rho} (\tilde{v}_\rho \tilde{v}_\parallel) \right\rangle + \hat{\theta} \left\langle \frac{\partial}{\partial \rho} (\tilde{v}_\rho \tilde{v}_\theta) \right\rangle, \quad (5.2)$$

where  $\langle \dots \rangle$  indicates a time-average. These two terms correspond to the radial transport of parallel and perpendicular flow, which are each measured and included in the analysis of Reynolds stress flow drive in HSX in this work.

Measuring the local fluctuating velocity components using the setup and methodology described in Section 3.2, the probability density function of the instantaneous radial and bi-normal velocity fluctuations as measured by the LFS probe at two different locations in a radial scan is plotted in Figure 5.1 as a visualization of the  $r - \theta$  component of the Reynolds stress. The fluctuating  $\tilde{v}_r$  and  $\tilde{v}_\theta$  values are calculated for these plots for each sample time using a moving  $30 \mu s$  mean (about 3 turbulence decorrelation times). The domain is then discretized and each grid square is colored to represent how frequently the combination of  $\tilde{v}_r$  and  $\tilde{v}_\theta$  fluctuations within those velocity ranges coincided with each other, with red being the most frequent and blue being the least frequent.

Near the last closed flux surface, where the data from Figure 5.1(b) was taken, the fluctuations are mostly isotropic. Positive radial fluctuations correlate roughly equivalently with both positive and negative bi-normal velocity fluctuations, and likewise for negative radial fluctuations. Further inside the plasma, where the data from Figure 5.1(a) was taken, positive  $\tilde{v}_r$  fluctuations correlate more frequently with negative  $\tilde{v}_\theta$  fluctuations and vice-versa. The integrated result of this skewed PDF is a negative value of the time-averaged Reynolds stress term  $\langle \tilde{v}_r \tilde{v}_\theta \rangle$ .

The fluctuations depicted in Figure 5.1 could also be considered a visualization of the local tilt of the turbulent eddies. If it is assumed that the locally measured fluctuations are indicative of a flux surface average value of the Reynolds stress in the bi-normal direction, then the change in Reynolds stress across the minor radius demonstrated by the fluctuation PDFs in Figure 5.1 implies

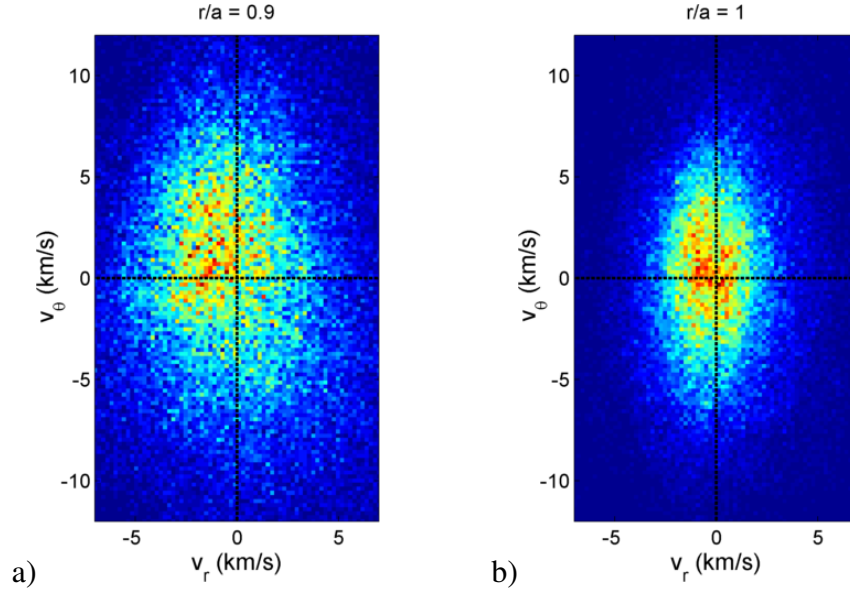


Figure 5.1 Probability density functions of radial and bi-normal velocity fluctuations from the LFS probe (a) inside the plasma at  $r/a \approx 0.9$  and (b) near the last closed flux surface.

a flow drive in the bi-normal direction according to Equation 5.2, since the Reynolds stress torque in this direction is proportional to the gradient of  $\langle \tilde{v}_r \tilde{v}_\theta \rangle$ .

### 5.1.1 Reynolds stress profiles in the QHS configuration

In order to calculate the local Reynolds stress based on the measured fluctuation quantities, a time average of the measurements must be taken for the time series of data from each discharge. For the profiles presented below, the final 20 ms of data from each 50 ms discharge was discretized into  $50 \mu\text{s}$  time windows for mean subtraction, and the average Reynolds stress in these time windows is the quantity plotted. The dependence of the results on this time averaging is discussed in Section 5.1.2.

To estimate the contribution to the momentum that would result from the measured Reynolds stress, a gradient must then be calculated from the measured shot-by-shot profile, because the Reynolds stress drive term is proportional to the radial gradient of  $\langle \tilde{v} \tilde{v} \rangle$ , as shown in Equation 5.2. Taking gradients by finite differencing produces spuriously noisy results given the variability



between discharges and individual time windows. The measured points are instead fit to a curve, and the derivative of the curve is taken to estimate the time-averaged Reynolds stress force. In the cases presented here, a second order polynomial fit was found to agree sufficiently well with the data. This curve fitting is justified by the appropriately dense radial scan and the generally small deviation of the individual points from the fit.

The measured Reynolds stress profiles using the LFS probe in the QHS configuration are plotted in Figure 5.2 along with the fitted curves. The bi-normal component of the Reynolds stress,  $\langle \tilde{v}_r \tilde{v}_\theta \rangle$ , is plotted in Figure 5.2(a), and the parallel component,  $\langle \tilde{v}_r \tilde{v}_\parallel \rangle$ , is plotted in Figure 5.2(b). The errorbars indicate the standard deviation of the discrete time windows used in the ensemble for each discharge.

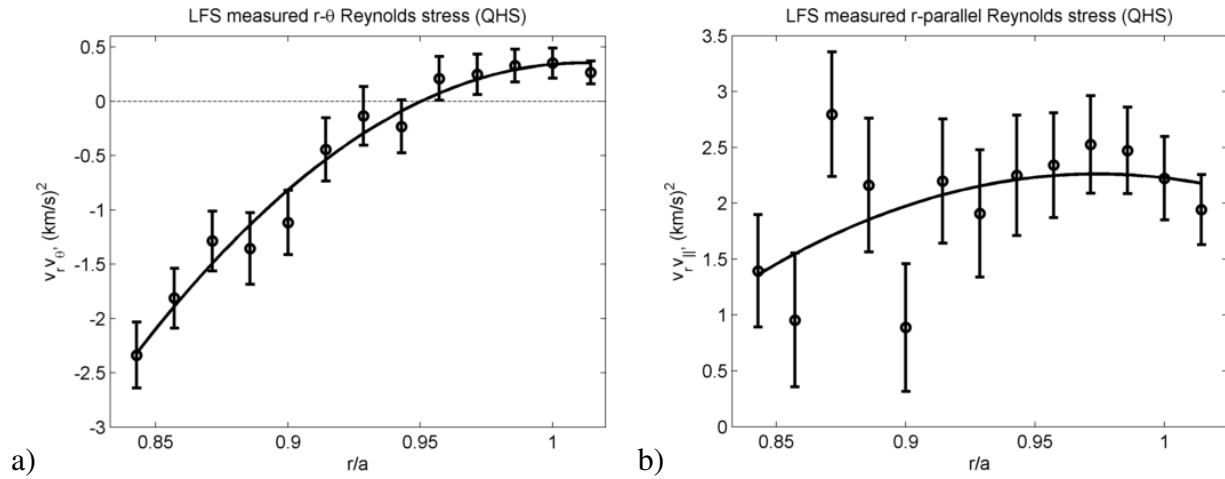


Figure 5.2 Radial profiles of (a)  $\langle \tilde{v}_r \tilde{v}_\theta \rangle$  and (b)  $\langle \tilde{v}_r \tilde{v}_\parallel \rangle$  measured by the LFS probe in the QHS configuration, along with polynomial fits.

The errorbars in Figure 5.2 only represent the statistical variation of the fluctuation data over the time windows, and do not reflect any systematic errors or any uncertainty that would be added by changing time window size. Although there is a gradient to the fitted curve of the parallel Reynolds stress in Figure 5.2(b), the gradient is small relative to the statistical uncertainty and

radial variability of the measurement. This is in contrast to the bi-normal Reynolds stress in Figure 5.2(a), which shows a clear, consistent radial gradient across the region spanned by the probe.

The Reynolds stress profiles measured by the HFS probe is then plotted in Figure 5.3(a) for the bi-normal component and Figure 5.3(b) for the parallel component.

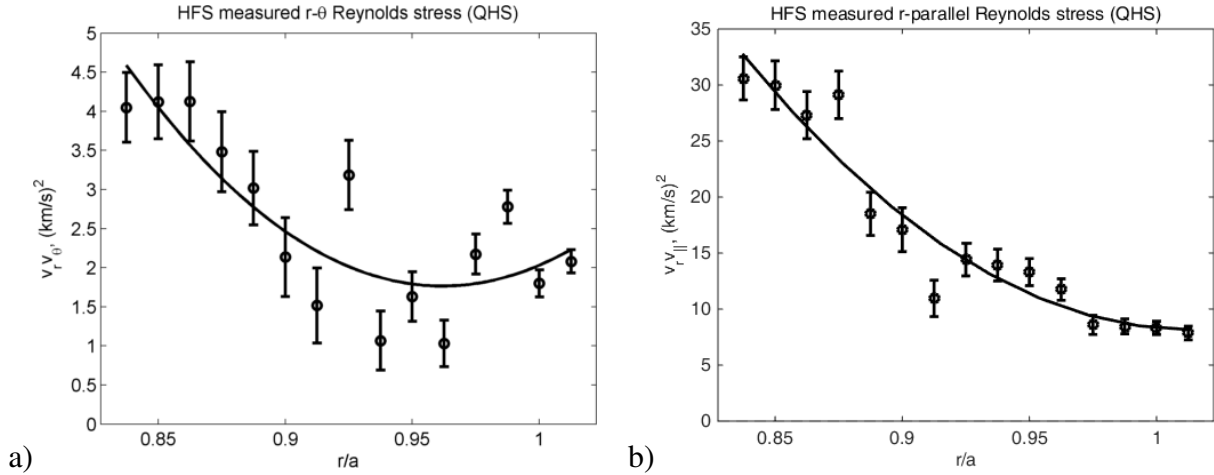


Figure 5.3 Radial profiles of (a)  $\langle \tilde{v}_r \tilde{v}_\theta \rangle$  and (b)  $\langle \tilde{v}_r \tilde{v}_{||} \rangle$  measured by the HFS probe in the QHS configuration, along with polynomial fits.

There are several things to consider when comparing the Reynolds stress profiles measured by the LFS and HFS probe. First, the flux expansion is larger at the HFS probe location than at the LFS probe, so that the spatial derivative will be smaller for the same distance that is spanned in flux space by the HFS probe. There is also a small island near  $r/a \approx 0.93$  at the HFS probe location, as shown in Figure 3.7. Next is that although the direction of the probe insertion is toward the magnetic axis, it is not strictly along the radial direction, so that the derivative taken to estimate the Reynolds stress flow drive has some poloidal component to it, as well. Finally, the HFS probe was shown to be perturbative to time-averaged measurements made by the LFS probe in Section 3.4, so it may be likely that the presence of the probe could be affecting the plasma quantities that are being measured.

With these caveats in mind, the Reynolds stress measurements made using the HFS probe in Figure 5.3 differ in both magnitude and gradient from those made at the LFS probe location from Figure 5.2. The differences are significant enough that a general statement cannot be made regarding the flux surface average of the Reynolds stress based on the measurements at these two discrete locations. Coupling these measurements with gyrokinetic modeling, however, could allow the measured quantities to be scaled based on the calculated value of the Reynolds stress at the probe location and its contribution to the total flux surface averaged Reynolds stress from the gyrokinetic simulations.

### 5.1.2 Time averaging of the Reynolds stress

The length of the time windows used for mean subtraction to find the fluctuating components of the probe signals determines the frequencies of fluctuations that are included in the analysis. It is expected that the Reynolds stress is driven by drift wave turbulence, so that the majority of the Reynolds stress should be contained in fluctuations that are averaged over a few turbulent decorrelation times ( $\tau_d \approx 10\mu s$ ). Averaging over shorter time scales than this neglects low frequency turbulent fluctuations, but averaging over time scales that are too long may cause the analysis to misinterpret macroscopic changes in the plasma parameters as fluctuations from microturbulence. Changes in the plasma on transport time scales are neglected in other terms of the momentum balance, so they should not be included here, either.

The bi-normal Reynolds stress profiles measured by the LFS probe using a range of values for the time window size used for mean subtraction are presented in Figure 5.4. A linear fit is also plotted for each set of data in order to extract the average gradient over the region for the calculation of the Reynolds stress drive. Figure 5.4 shows that the linear fit to the data has a similar gradient regardless of the time window size used for mean subtraction, although for larger time windows that include low frequency fluctuations, the fit does not agree well with the data.

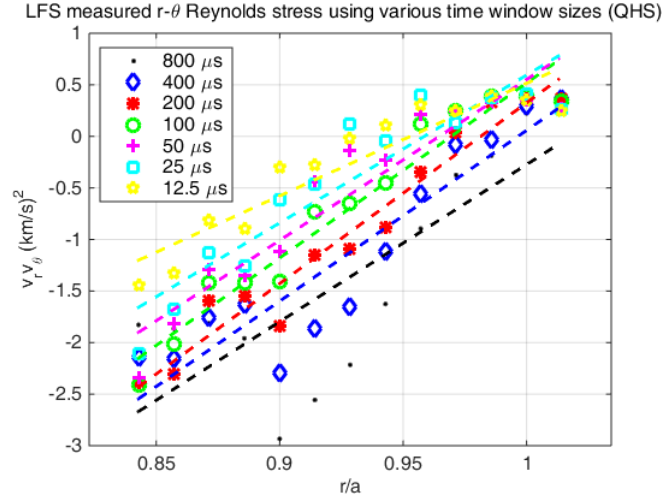


Figure 5.4 Radial profiles of  $\langle \tilde{v}_r \tilde{v}_\theta \rangle$  measured by the LFS probe in the QHS configuration and linear fits using a range of time windows for mean subtraction.

To clarify and expand this comparison, the radial gradient of a linear fit to the Reynolds stress profiles in the bi-normal and parallel directions is plotted in Figure 5.5 (a) and (b) respectively for the range of time window sizes used for mean subtraction in Figure 5.4. These radial gradients are used as the drive term in the momentum evolution, as shown in Equation 5.2. A linear fit is used here rather than a quadratic used elsewhere for simplicity so that the simple comparison in Figure 5.5 could be made. The data given in Figure 5.5 is taken using the LFS probe in the QHS configuration, and the errorbars indicate the standard deviation of the data to the linear fit.

As demonstrated in Figure 5.5, varying the time window size for mean subtraction does not significantly affect the resulting calculated Reynolds stress drive for a range of approximately  $30\mu s < \tau_a < 100\mu s$ . This result suggests that the Reynolds stress being measured is indeed a result of the microturbulence, because most of the fluctuations contributing to the measurement occur within the timescale of a few turbulent decorrelation times.

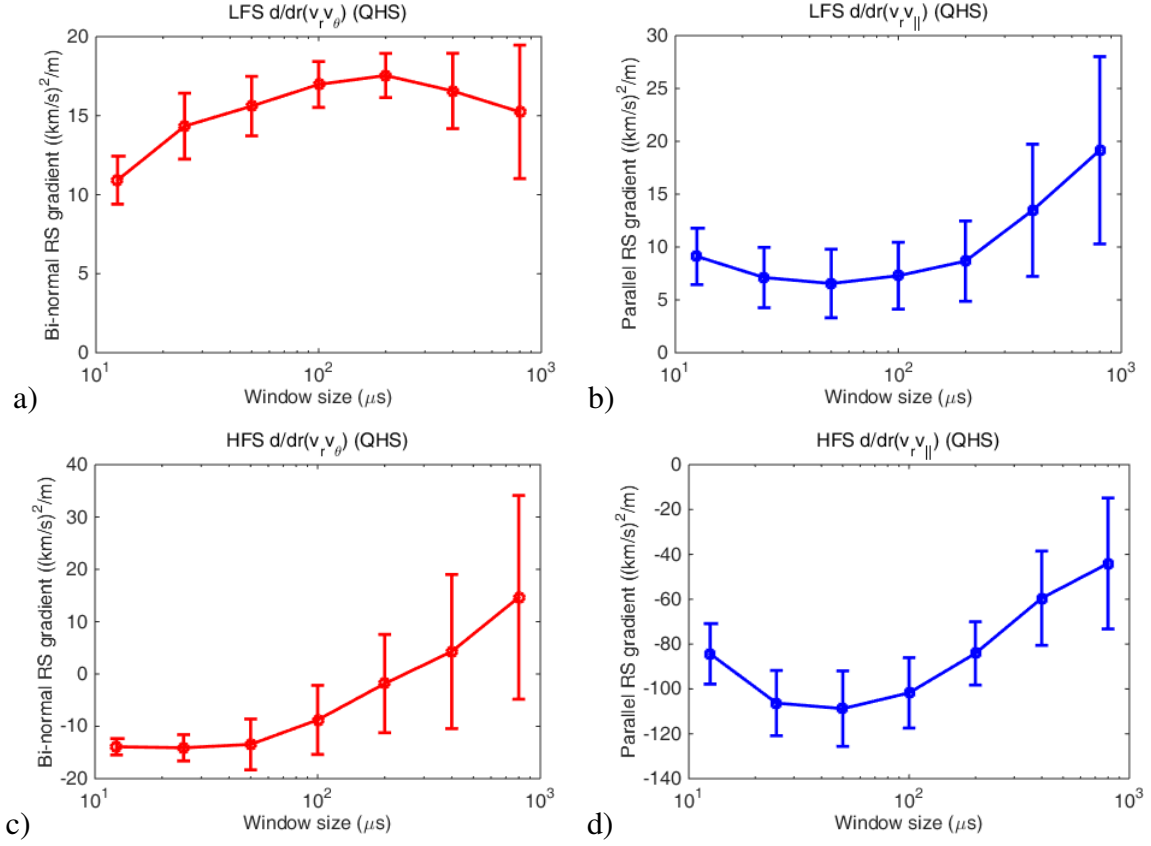


Figure 5.5 Gradients of the radial Reynolds stress profiles in the QHS configuration using a range of time windows for mean subtraction, for (a)  $\langle \tilde{v}_r \tilde{v}_\theta \rangle$  and (b)  $\langle \tilde{v}_r \tilde{v}_{||} \rangle$  profiles from the LFS probe and (c)  $\langle \tilde{v}_r \tilde{v}_\theta \rangle$  and (d)  $\langle \tilde{v}_r \tilde{v}_{||} \rangle$  profiles from the HFS probe.

### 5.1.3 Contribution of turbulent particle flux to Reynolds stress

The standard formulation of the Reynolds stress is  $\frac{\partial}{\partial r} \langle \tilde{V} \tilde{V} \rangle$  (from Equation 2.5, for example), but arriving at this term from the momentum balance involves discarding a particle transport term that should be included if it is on the same order as the fluctuating velocity terms. The Reynolds stress divergence component of the flow drive from Equation 2.9 is

$$\left( \frac{\partial(\rho \mathbf{V})}{\partial t} \right)_{RS} = -\nabla \cdot (\rho \mathbf{V} \mathbf{V}), \quad (5.3)$$

where  $\rho = nm$  is the mass density and  $V$  is the velocity vector. For radial momentum transport, this divergence becomes a radial derivative, so that the Reynolds stress in Equation 5.3 in an arbitrary

direction  $\beta$  within a flux surface becomes [80]

$$\Pi_{r,\beta} = \langle n \rangle \langle \tilde{V}_r \tilde{V}_\beta \rangle + \langle \tilde{n} \tilde{V}_r \rangle \langle V_\beta \rangle + \langle \tilde{n} \tilde{V}_r \tilde{V}_\beta \rangle, \quad (5.4)$$

where the brackets  $\langle \dots \rangle$  indicate an average over time and over the flux surface, and  $\langle \tilde{n} \tilde{V}_r \tilde{V}_\beta \rangle$  represents the nonlinear flux, as opposed to the quasi-linear fluxes. This last nonlinear term is generally neglected for simplicity, but may play a role in momentum transport [80]. The turbulent particle flux term,  $\langle \tilde{n} \tilde{V}_r \rangle$ , is also generally neglected as small compared to the  $\langle \tilde{V}_r \tilde{V}_\beta \rangle$  term in tokamaks. This may not be the case for HSX, which has significant particle fueling throughout the minor radius of the plasma and particle flux through the edge.

For a typical QHS discharge in the edge,  $\langle \tilde{V}_r \tilde{V}_\theta \rangle \approx 1 \times 10^6 \text{ (m/s)}^2$  from Figure 5.2, and the mean density in this region is approximately  $n_e \approx 1 \times 10^{18} \text{ m}^{-3}$ , so that the total magnitude of the first term in Equation 5.4 is  $\langle n \rangle \langle \tilde{V}_r \tilde{V}_\theta \rangle \approx 1 \times 10^{24} \text{ m}^{-1} \text{s}^{-2}$ . Fluctuations resulting in Reynolds stress in the parallel direction are similar in magnitude to those in the bi-normal direction.

The locally measured turbulent particle flux  $\langle \tilde{n} \tilde{V}_r \rangle$  is not available using the Reynolds stress probe, because the alignment of the pins was not designed for this measurement. Based on modeling of the QHS configuration of HSX, however, the flux surface averaged particle flux near the last closed flux surface is calculated to be approximately  $\Gamma_r \approx \langle \tilde{n} \tilde{V}_r \rangle \approx 1 \times 10^{19} \text{ m}^{-2} \text{s}^{-1}$  (plotted in Figure 2.18) [148]. These calculations were made by Laurie Stepheie using the DEGAS neutral gas code, which uses an array of H-alpha detectors to scale the particle source rate along with the density profile from Thomson scattering to calculate the total particle flux. The two mean flow velocities in the QHS configuration were approximately  $V_{||} \approx 20 \text{ km/s}$  from Figure 4.15 and  $V_\theta \approx E_r B_0 \approx 2 \text{ km/s}$  from Figure 4.11. Based on this, the larger of the two particle flux terms is  $\langle \tilde{n} \tilde{V}_r \rangle \langle V_{||} \rangle \approx 2 \times 10^{23} \text{ m}^{-1} \text{s}^{-2}$ . While this term is smaller than the Reynolds stress term measured by the probes ( $\langle n \rangle \langle \tilde{V}_r \tilde{V}_\theta \rangle \approx 1 \times 10^{24} \text{ m}^{-1} \text{s}^{-2}$  from above), these are rough estimates, each value of which varies over the radial profile, and the particle flux term does not appear to be negligibly

small. The Reynolds stress term is also locally measured rather than a flux surface average value, so that a flux surface average value may lead the Reynolds stress term to be smaller and more comparable to the particle flux term.

The sign of the particle flux term will necessarily be positive, while the measured Reynolds stress in the bi-normal direction tends to be negative at the LFS probe based on Figure 5.2(a) and positive at the HFS probe based on Figure 5.3(a). It is not obvious, then, whether the addition of the (most likely smaller) particle flux component will increase or decrease the gradient of the measured Reynolds stress. The contribution of the particle flux term decreases further into the plasma as the particle sourcing is reduced.

#### 5.1.4 Potential sources of measurement error

There are several possible systematic sources of error in these measurements that cannot be easily quantified, but should be understood by anyone examining the data. First, by only including the fluctuating component of each signal for the Reynolds stress measurements, any changes to the signal caused by differences in the mean or low frequency  $T_e$  relative to assumptions will have no affect on the analysis. However, there could be errors introduced to the measurements by a fluctuating electron temperature on the length scale of the pin separation and a time scale shorter than the window time used for mean subtraction of the probe signals. Assuming that these  $\tilde{T}_e$  contributions are negligible is standard practice in Langmuir probe experiments, simply because it is a difficult effect to account for. Gyrofluid calculations used as a synthetic diagnostic for Langmuir probes, however, have shown that electron temperature fluctuations in realistic plasma parameters would indeed distort the translation of the measured floating potential signals to plasma potential fluctuations [138]. In the case studied in these gyrofluid simulations, which used plasma parameters on the same order as those measured in HSX, the electron temperature fluctuations led to an overestimate of the poloidal electric field fluctuations by a factor of  $\sim 3-4$ . Although the

exact number would almost certainly change in the case of HSX parameters, it is reasonable to assume that the fluctuating electric fields  $\tilde{E}_r$  and  $\tilde{E}_\theta$  are being overestimated by a factor of order unity in this work due to  $T_e$  fluctuations being interpreted through the floating potential as potential fluctuations. This could lead to an overestimate of the resulting Reynolds stress drive by a factor of  $\sim 10$ .

There could also be some error introduced to the analysis of the bi-normal component of the Reynolds stress because the two measurements sharing a pin that measures the same  $V_{fl}$ . Noise on this pin would be interpreted as velocity fluctuations in both directions, so that the measured  $\langle \tilde{V}_r \tilde{V}_\theta \rangle$  would be finite over a time average. On the LFS probe, a positive  $V_{fl}$  fluctuation on the shared pin would be interpreted as a positive electric field fluctuation for both the  $E_r$  and the  $E_\theta$  signals. A negative fluctuation would likewise lead to a negative electric field fluctuation on both pins. The result of this correlated noise would lead to a more-positive total  $\langle \tilde{V}_r \tilde{V}_\theta \rangle$ , which is the opposite result of the negative value which is generally measured using this probe, as seen in Figure 5.2(a). At the HFS probe, the configuration of the pins is changed so that correlated noise on the shared pin would lead to a more-negative  $\langle \tilde{V}_r \tilde{V}_\theta \rangle$ . This is again the opposite result from the measurement of positive  $\langle \tilde{V}_r \tilde{V}_\theta \rangle$ , shown in Figure 5.3(a). This demonstrates that the measurements presented in Section 5.1.1 are not an artifact of the two electric field measurements sharing a single floating potential pin, and this effect will therefore be neglected.

Careful shielding of the transmission lines to provide grounded return paths for the signal current was implemented to avoid correlated noise between different pins. The length of the coaxial cabling between the probes and digitizers was also minimized to reduce ringing of high frequency components of the signals. Because of these efforts, errors due to systematic issues such as external noise or cross-talk of the signals as they travel between the probe and digitizer are expected to be small.



## 5.2 Momentum evolution and steady state solution

To estimate the rotation that would result from the measured Reynolds stress, the inferred torque from the measured Reynolds stress profile is balanced against a calculated viscosity. Assuming that neoclassical viscosity and ion-neutral friction are the dominant damping mechanisms that are balancing the Reynolds stress as the dominant drive term, the flow evolution equations can be written in the form of a pair of coupled differential equations as [99]

$$\begin{aligned}\frac{\partial \langle \mathbf{B} \cdot \mathbf{V} \rangle}{\partial t} &= -\frac{1}{n_i m_i} \langle \mathbf{B} \cdot \nabla \cdot \Pi \rangle - \nu_{in} \langle \mathbf{B} \cdot \mathbf{V} \rangle - B_0 \left\langle \frac{\partial}{\partial \rho} (\tilde{v}_\rho \tilde{v}_\parallel) \right\rangle \\ \frac{\partial \langle \mathbf{B}_P \cdot \mathbf{V} \rangle}{\partial t} &= -\frac{1}{n_i m_i} \langle \mathbf{B}_P \cdot \nabla \cdot \Pi \rangle - \nu_{in} \langle \mathbf{B}_P \cdot \mathbf{V} \rangle - B_P \left\langle \frac{\partial}{\partial \rho} (\tilde{v}_\rho \tilde{v}_\theta) \right\rangle,\end{aligned}\tag{5.5}$$

where  $\mathbf{B}_P$  is the poloidal component of the main field,  $\rho = \frac{\nabla \psi}{|\nabla \psi|}$  is the radial coordinate,  $\nu_{in}$  is the damping rate due to ion-neutral collisions and  $\langle \dots \rangle$  indicates a flux surface average. The Reynolds stress terms are also taken as a time-average. Here  $\nu_{in}$  will be calculated as [149]

$$\nu_{in} \approx N_n 10^{-14} T_i^{0.318},\tag{5.6}$$

where  $N_n$  is the neutral particle density in  $\text{m}^{-3}$ . The bi-normal fluctuating velocity component  $v_\theta$  has been approximated to be in the poloidal direction for these calculations. The neoclassical parallel and poloidal viscosity can be calculated analytically for ions in the plateau collisionality regime as [150, 151]

$$\begin{aligned}\langle \mathbf{B} \cdot \nabla \cdot \Pi \rangle &= (n_i m_i B_0) v_{ti} \frac{\sqrt{\pi}}{2} [(\iota \alpha_P + \alpha_C) U^\alpha + (\iota \alpha_C + \alpha_T) U^\zeta] \\ \langle \mathbf{B}_P \cdot \nabla \cdot \Pi \rangle &= (n_i m_i B_P) v_{ti} \frac{\sqrt{\pi}}{2} \iota (\alpha_P U^\alpha + \alpha_C U^\zeta),\end{aligned}\tag{5.7}$$

where  $\iota$  is the rotational transform,  $v_{ti}$  is the ion thermal velocity,  $U^\alpha$  and  $U^\zeta$  are the flows in the Hamada poloidal and toroidal directions, respectively,  $\alpha_T = \sum n^2 b_{n,m}^2 / |n - m|$ ,  $\alpha_P = \sum m^2 b_{n,m}^2 / |n - m|$ ,  $\alpha_C = -\sum n m b_{n,m}^2 / |n - m|$ , and each of the sums are taken over all spectral components  $b_{n,m}$  in the configuration. In the QHS configuration, the  $n=4, m=1$  mode

dominates the neoclassical damping, but the total evolution time of the flows in the edge region is dominated by the neutral viscosity. This result, that the analytically calculated damping in the quasi-symmetric direction is dominated by the neutral viscosity, was previously reported for 0.5 T plasmas in HSX [35]. The neutral density profiles are calculated using the DEGAS Monte Carlo neutral gas modeling code as well as measurements from an array of H-alpha detectors and Thomson scattering. These modeled atomic and molecular hydrogen densities are plotted in Figure 5.6 [148].

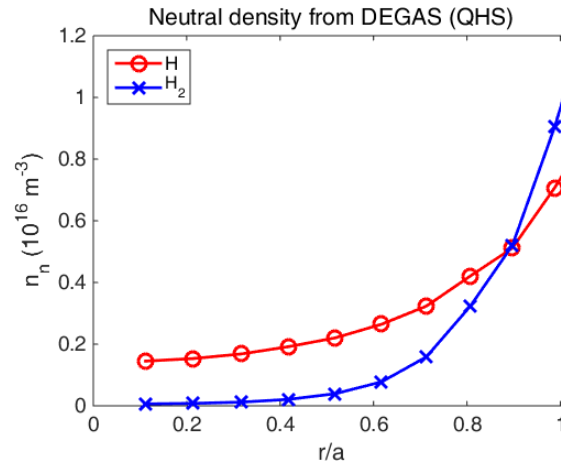


Figure 5.6 Neutral particle density for viscosity calculations, as modeled by DEGAS (calculations courtesy of Laurie Stephey).

Given the fit to the  $r - \theta$  Reynolds stress measurements from Figure 5.2(a), the bi-normal Reynolds stress drive is inserted into Equation 5.5 and the coupled flows are evolved by integrating the equations until they are sufficiently saturated. The resulting time-dependent flows are presented in Figure 5.7, starting from a zero-flow initial condition. The parallel component of the Reynolds stress has been neglected for this example calculation. All values used in the calculations plotted here were taken from a radial location of  $r/a=0.9$ .

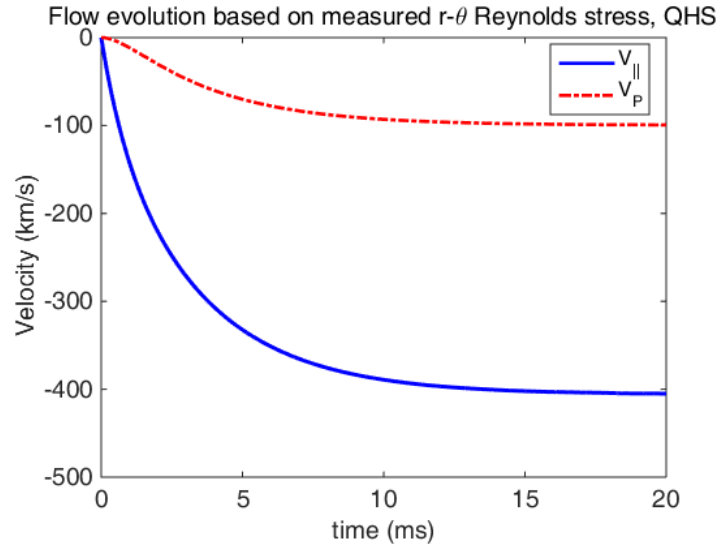


Figure 5.7 Momentum evolution from Equation 5.5 in the QHS configuration near  $r/a=0.9$  resulting from the bi-normal component of the Reynolds stress measured by the LFS probe.

As demonstrated in Figure 5.7, the flows that are calculated to result from the measured Reynolds stress are many times larger than the experimentally measured values in the QHS configuration from Sections 4.3.2 and 4.4. It should be noted again, however, that the Reynolds stress should be taken as a flux surface averaged value, where here it has been measured locally and the local measurement is assumed to be indicative of a flux surface average for the purposes of evaluating the magnitude of the drive. For the rest of this work, only the final steady-state velocities will be used, since all of the data analyzed here is from experiments in quiescent, steady state plasmas.

This method is similar to the one utilized in the linear device CSDX to calculate a rotation profile that matched the measured rotation in the azimuthal direction, as outlined in Section 2.7 [126, 127]. Calculating the viscosity in HSX is much more complicated than in a collisional linear device, however, and previous experiments have demonstrated that the experimental viscosity in HSX is several times larger than what is calculated using this analytic method [99].

Assuming that the local Reynolds stress measured using probe is indicative of a flux surface average, the resulting saturated parallel velocities calculated by the momentum evolution using

Equation 5.5 is given in Figure 5.8. The integration of the momentum evolution equations was calculated for 50 ms, and the final flow values after the 50 ms were taken, regardless of whether or not the flows had saturated, since this is the length of an HSX discharge. Both the parallel and bi-normal components of the Reynolds stress are included in this calculation.

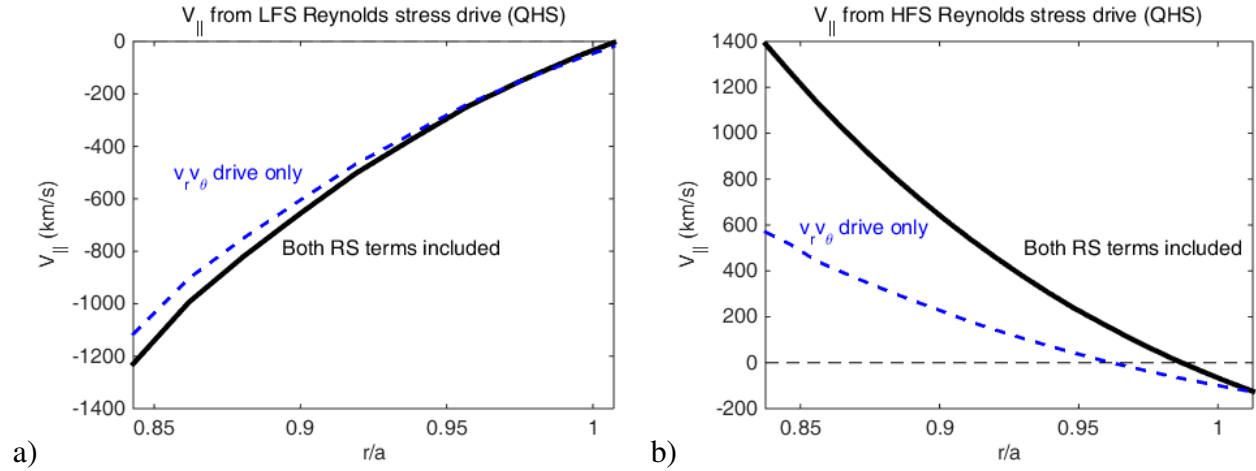


Figure 5.8 Parallel flow inferred from the saturated evolution of Equation 5.5 in the QHS configuration using both the parallel and bi-normal components of the Reynolds stress drive measured by the (a) LFS and (b) HFS probes.

Figure 5.8 shows that the Reynolds stress profiles measured at the LFS and HFS probe locations both lead to large flow drive terms, and that they actually drive the flows in opposite directions. More information about the variation of the Reynolds stress on a surface is required to fully account for the flux surface average Reynolds stress in the momentum balance.

In order for the momentum evolution from Equation 5.5 to saturate at flow values that are similar to those observed experimentally near the last closed flux surface ( $V_{\parallel} \approx 20$  km/s based on measurements from Section 4.4.2), the flux surface averaged gradient of the bi-normal Reynolds stress would need to be  $\approx 0.1$  (km/s)<sup>2</sup>/m. This is about a factor of 20 smaller than the average gradient across the edge region using the LFS probe. Due to the fact that the neutral viscosity dominates the modeled damping in the QHS configuration and that the neutral density gradient is

large in the edge, the necessary Reynolds stress that is calculated to drive the flows would decrease rapidly further inside the plasma, as well.

### 5.3 Contribution of Reynolds stress to flows in different configurations

In Section 4.5, it was shown that  $E_r$  and  $V_{||}$  in the Mirror and Flip-1-4 configurations deviated more from the neoclassically calculated solutions for the flows than they did in the QHS configuration. This result is in contradiction to expectations that plasmas in these configurations would be driven more strongly toward the neoclassical solutions. One reason for this observation could be that the Reynolds stress is larger in these configurations than it is in the QHS configuration, but this section presents measurements showing that this is not the case.

#### 5.3.1 Expectation of Reynolds stress scaling

As shown by the differences between the measurements of the Reynolds stress made using the LFS and HFS probes, it may not be appropriate to extrapolate two local measurements to a flux surface average. To estimate how the Reynolds stress scales with measured fluctuating quantities, the Diamond and Kim scaling of the Reynolds stress drive is used here, which gives [79]

$$J_r \approx n_0 e c_s \left( \frac{e \tilde{\phi}}{T_e} \right)^2 k_\theta \rho_s, \quad (5.8)$$

where  $c_s = \sqrt{(T_e + T_i)/m_i}$  is the sound speed,  $\rho_s = c_s/\Omega_i$  is the sound speed over the ion gyro-radius, and  $k_\theta$  is the wavenumber in the bi-normal direction. Here the scale size of the instability is assumed to be on the order of  $k_\theta \rho_s \approx 0.5$  in all experimental cases, which is expected to be the approximate peak of the growth rate for the TEM turbulence which is dominant in HSX based on gyrokinetic simulations [143].

Although it contains no cross-phase information, the scaling from Equation 5.8 finds that the Reynolds stress drive is expected to scale approximately with the fluctuating potential squared. If

adiabatic electrons are assumed so that  $\frac{e\phi}{T_e} \approx \frac{\tilde{n}}{n}$ , then the normalized density fluctuations can be estimated from the ion saturation current measurements. Using  $I_{sat} = 0.6n_i e A_i \sqrt{\frac{T_e}{m_i}}$  from Equation 3.4 and assuming quasi-neutrality and that electron temperature fluctuations are negligible, the measurement can be related directly to the fluctuating density so that  $\frac{\tilde{n}}{n} \approx \frac{\tilde{I}_{sat}}{I_{sat}}$ . This is the same approximation used in Section 4.3.1 to calculate an estimate of the local mean value of  $T_e$  from probe signal fluctuations. Using this approximation, the normalized density fluctuations as measured by the LFS probe in the QHS, Flip-1-4 and Mirror configurations are plotted in Figure 5.9. The  $I_{sat}$  measurements from each side of the insulating barrier of the mach probe are added together for the total  $I_{sat}$  signal in this analysis.

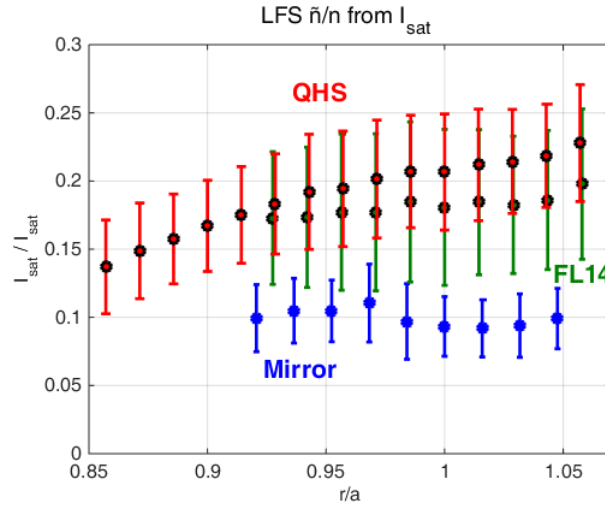


Figure 5.9 Normalized density fluctuation profiles,  $\frac{\tilde{I}_{sat}}{I_{sat}}$ , in the QHS, Flip-1-4 and Mirror configurations.

In the Mirror configuration, the normalized magnitude of the density fluctuations is about half as large as they are in the QHS configuration in the radial region measured by the probes. Fluctuations in the Flip-1-4 configuration are also reduced slightly relative to the QHS configuration. The launched power was the same in all configurations here, but the absorbed power was less in the Mirror and Flip-1-4 cases than in the QHS configuration, so that the total heat flux through the last

closed flux surface is reduced in these cases. This may explain the result of reduced fluctuations in the Mirror and Flip-1-4 configuration, which had reduced heat flux through the edge.

Based on these measurements and the simple estimate of the scaling from Figure 5.9, the Reynolds stress drive would be expected to be about 4 times larger in the QHS case than in the Mirror configuration. This would mean that the Reynolds stress is not responsible for the additional deviation from neoclassical ambipolarity in the measured flows in the Mirror configuration. If the scaling in Equation 5.8 holds, then there would need to be an additional term in the momentum balance aside from the Reynolds stress and the neoclassical transport as modeled by PENTA to account for the flows observed in the Mirror and Flip-1-4 configurations. The cross phase of the fluctuations may be important, so the locally measured Reynolds stress profiles in the Flip-1-4 and Mirror configurations will be presented next to find the local gradients and calculated resulting Reynolds stress drive.

### 5.3.2 Measured Reynolds stress and calculated resulting flows

The measured Reynolds stress profiles using the LFS probe in the Mirror configuration are plotted in Figure 5.10(a) for the bi-normal component and in Figure 5.10(b) for the parallel component. These measurements were made using the same discharges as those used for the parallel flow and  $E_r$  measurements in the Mirror configuration in Section 4.5.1.

The bi-normal and parallel components of the measured Reynolds stress profiles using the HFS probe are then plotted in Figure 5.11 (a) and (b), respectively, along with polynomial fits to the data. Again, due to the observed perturbation to the plasma parameters caused by the HFS probe, the analysis of the data using this probe will be weighted less heavily than that using the LFS probe.

Using the fits of the Reynolds stress profiles measured by the probes from Figures 5.10 and 5.11, the Reynolds stress is included in the momentum balance in the Mirror configuration, as described for the QHS configuration in Section 5.2. The resulting saturated parallel flows using

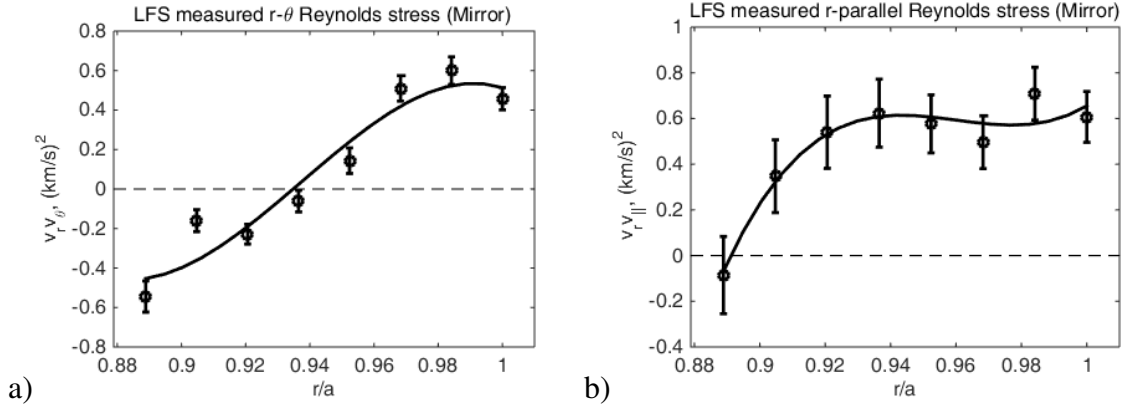


Figure 5.10 Radial profiles of (a)  $\langle \tilde{v}_r \tilde{v}_\theta \rangle$  and (b)  $\langle \tilde{v}_r \tilde{v}_\parallel \rangle$  measured by the LFS probe in the Mirror configuration, along with polynomial fits.

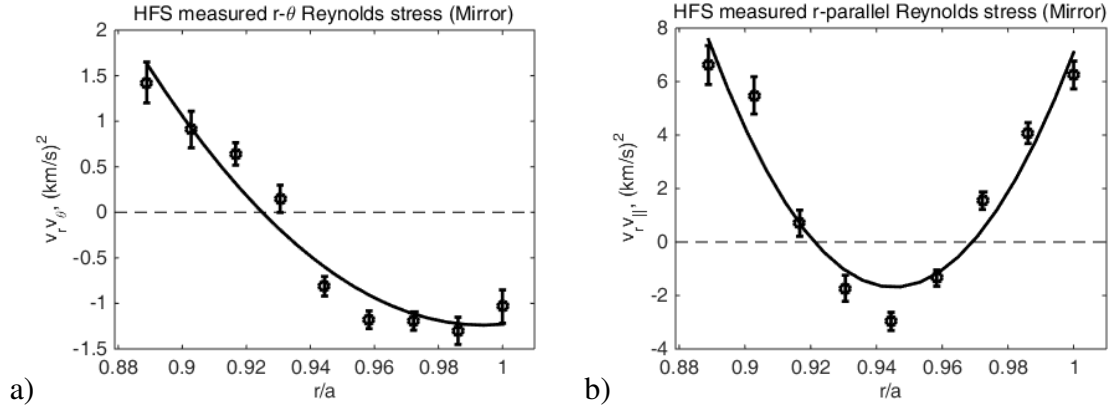


Figure 5.11 Radial profiles of (a)  $\langle \tilde{v}_r \tilde{v}_\theta \rangle$  and (b)  $\langle \tilde{v}_r \tilde{v}_\parallel \rangle$  measured by the HFS probe in the Mirror configuration, along with polynomial fits.

Equation 5.5 are plotted in Figure 5.12(a) for the data from the LFS probe and Figure 5.12(b) for the data from the HFS probe.

As shown in Figure 5.12, the measured Reynolds stress in the Mirror configuration is still calculated to play a large role in the momentum balance, although it is smaller than the QHS configuration on the LFS. The HFS Reynolds stress measurements imply similar flows as those in the QHS configuration, but not significantly larger. This does not account for the back-reaction of the neoclassical non-ambipolar transport driving the flows back toward the neoclassical solution, but



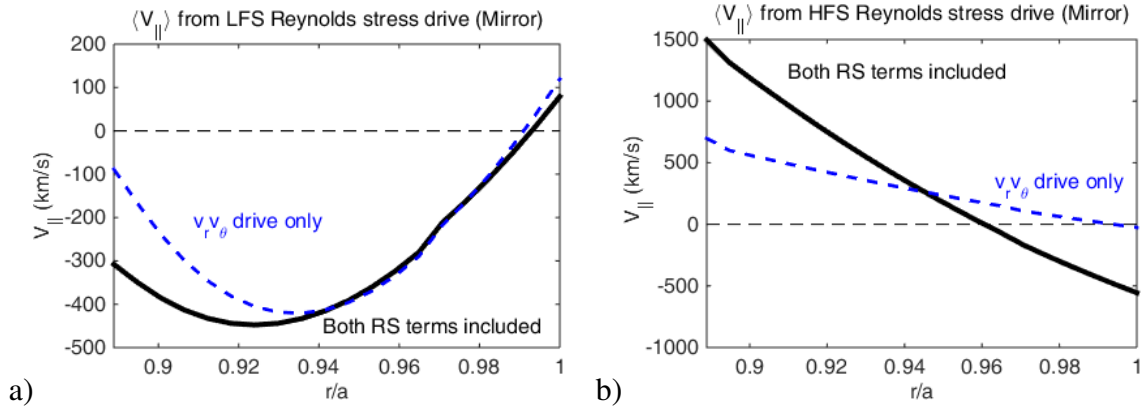


Figure 5.12 Saturated parallel flows resulting from Reynolds stress profiles in the Mirror configuration using the (a) LFS and (b) HFS probes.

these neoclassical radial currents are calculated to be much smaller than the effect of the measured Reynolds stress extrapolated to the entire flux surface.

Finally, the measured Reynolds stress profiles using the LFS probe in the Flip-1-4 configuration are plotted in Figure 5.13(a) for the bi-normal component and in Figure 5.13(b) for the parallel component.

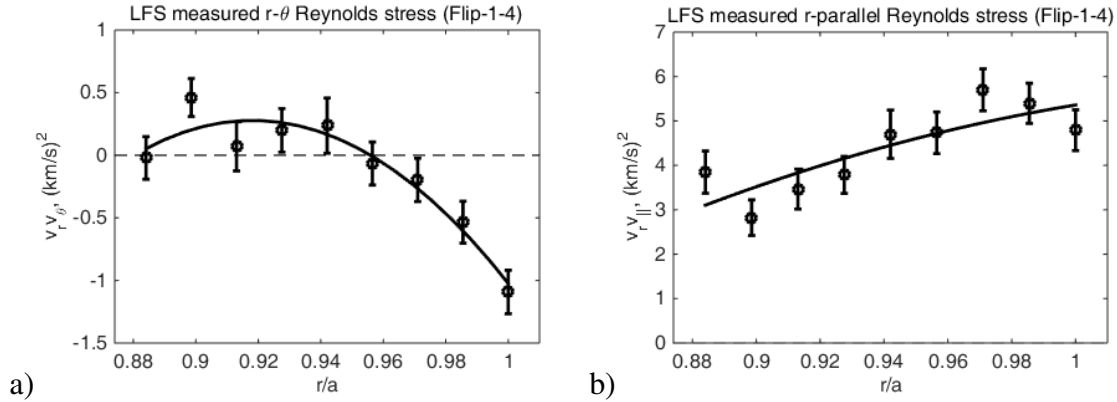


Figure 5.13 Radial profiles of (a)  $\langle \tilde{v}_r \tilde{v}_{\theta} \rangle$  and (b)  $\langle \tilde{v}_r \tilde{v}_{\parallel} \rangle$  measured by the LFS probe in the Flip-1-4 configuration, along with polynomial fits.

The bi-normal and parallel components of the measured Reynolds stress profiles using the HFS probe are then plotted in Figure 5.11 (a) and (b), respectively, along with polynomial fits to the data.

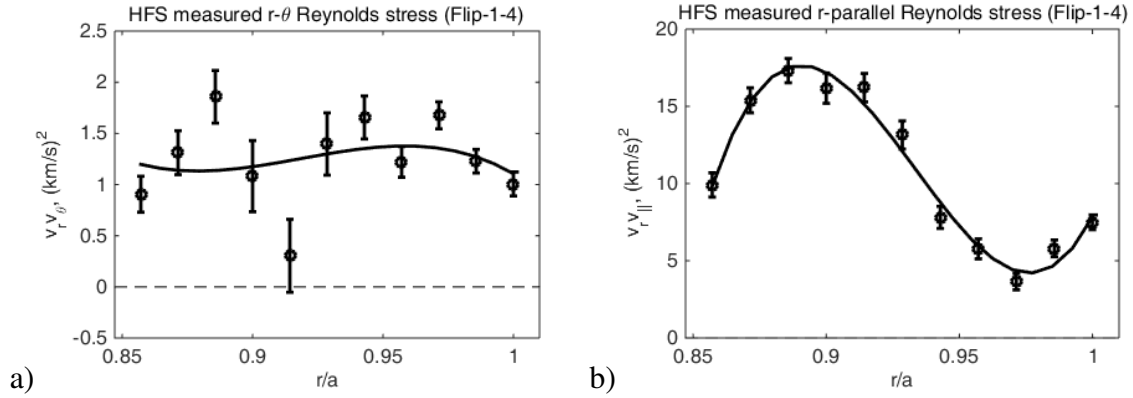


Figure 5.14 Radial profiles of (a)  $\langle \tilde{v}_r \tilde{v}_\theta \rangle$  and (b)  $\langle \tilde{v}_r \tilde{v}_{||} \rangle$  measured by the HFS probe in the Flip-1-4 configuration, along with polynomial fits.

Using the fits of the Reynolds stress profiles measured by the probes from Figures 5.13 and 5.14, the Reynolds stress is included in the momentum balance in the Flip-1-4 configuration. The resulting saturated parallel flows using Equation 5.5 are plotted in Figure 5.15(a) for the data from the LFS probe and Figure 5.15(b) for the data from the HFS probe.

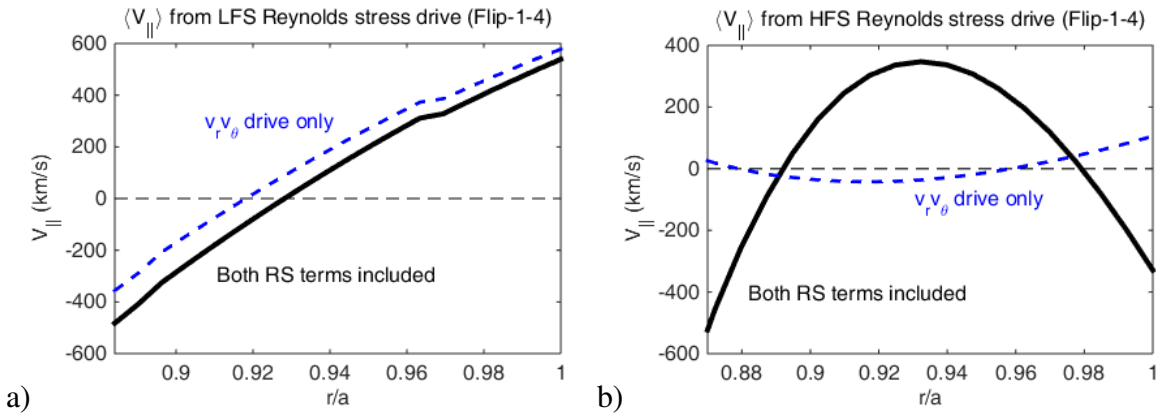


Figure 5.15 Saturated parallel flows resulting from Reynolds stress profiles in the Flip-1-4 configuration using the (a) LFS and (b) HFS probes.

As shown in Figure 5.15, the measured Reynolds stress in the Flip-1-4 configuration is calculated to play a large role in the momentum balance while being reduced compared to the QHS configuration. The Reynolds stress results in the Flip-1-4 and Mirror configurations are similar in this regard.

Based on the measured Reynolds stress profiles and the resulting calculated flows in Figures 5.12 and 5.15, the Reynolds stress may still be a large and important term in the momentum balance in these configurations, but it does not account for the increase in flows observed relative to the QHS configuration.

This chapter has presented measurements of Reynolds stress profiles using the LFS and HFS probes in multiple magnetic configurations as well as the calculated rotation that this Reynolds stress would imply if it were extrapolated to a flux surface average. The resulting flows from this calculation were much larger than the observed flows presented in Chapter 4. It was shown that the Reynolds stress measured in two locations on a flux surface with different magnetic geometries resulted in dramatically different rotation drive, suggesting that a small number of measurement points is insufficient to properly sample the flux surface averaged quantity as it enters into the momentum balance. In configurations with the symmetry degraded, the measured Reynolds stress and its associated drive are decreased relative to the QHS configuration. This suggests that the Reynolds stress is not responsible for the additional rotation in the Mirror and Flip-1-4 configurations that is not predicted by the neoclassical modeling using PENTA.

## References

35. Gerhardt, S., Talmadge, J. N., Canik, J. & Anderson, D. T. Experimental Evidence of Reduced Plasma Flow Damping with Quasisymmetry. *Physical Review Letters* **94**, 015002 (2005).
79. Diamond, P. H. & Kim, Y. Theory of mean poloidal flow generation by turbulence. *Physics of Fluids B* **3**, 1626 (1991).
80. Diamond, P. H., McDevitt, C. J., Gürcan, O. D., *et al.* Physics of non-diffusive turbulent transport of momentum and the origins of spontaneous rotation in tokamaks. *Nuclear Fusion* **49**, 045002 (2009).
99. Gerhardt, S. P., Talmadge, J. N., Canik, J. M. & Anderson, D. T. Measurements and modeling of plasma flow damping in the Helically Symmetric eXperiment. *Physics of Plasmas* **12**, 056116 (2005).
126. Holland, C., Yu, J., James, A., *et al.* Observation of Turbulent-Driven Shear Flow in a Cylindrical Laboratory Plasma Device. *Physical Review Letters* **96** (2006).
127. Tynan, G. R., Holland, C, Yu, J. H., *et al.* Observation of turbulent-driven shear flow in a cylindrical laboratory plasma device. *Plasma Physics and Controlled Fusion* **48**, S51–S73 (2006).
138. Gennrich, F. P. & Kendl, A. Analysis of the temperature influence on Langmuir probe measurements on the basis of gyrofluid simulations. *Plasma Physics and Controlled Fusion* **54**, 015012 (2012).
143. Guttenfelder, W. *Walter Guttenfelder's Dissertation, University of Wisconsin - Madison* 2008.
148. *Private communication with Laurie Stephey*, 2014.

149. Cornelis, J., Sporken, R., Oost, G. & Weynants, R. Predicting the radial electric field imposed by externally driven radial currents in tokamaks. *Nuclear Fusion* **34**, 171 (1994).
150. Coronado, M. & Wobig, H. Parallel and toroidal viscosity for nonaxisymmetric toroidal plasmas in the plateau regime. *Physics of Fluids* **29**, 527 (1986).
151. Shaing, K. C., Hirshman, S. P. & Callen, J. D. Neoclassical transport fluxes in the plateau regime in nonaxisymmetric toroidal plasmas. *Physics of Fluids* **29**, 521 (1986).

## Chapter 6

### Conclusions

This document has presented measurements of plasma flows and localized Reynolds stress using Langmuir probes in the HSX stellarator. This chapter begins with a summary and discussion of the results from this work in Section 6.1. Some possible directions of future work are then presented in Section 6.2 for further investigation into momentum transport in HSX.

#### 6.1 Summary and discussion of results

Based on predictions presented in Section 2.5, the torque provided by neoclassical non-ambipolar transport was compared to the estimated torque provided by turbulence via the Reynolds stress. Based on these models, the QHS configuration of HSX is expected to be approaching the limit where it would be quasi-symmetric enough to allow non-neoclassical rotation, but the quasi-symmetry is broken enough that the radial electric field is expected to be determined predominantly by neoclassical processes. The models used to reach this conclusion, however, were derived using assumptions that may not be valid for the plasmas studied here, such as ions in the low collisionality regime.

Experimentally, the radial electric field and parallel flows measured using Langmuir probes in the edge of the QHS configuration do not match predictions based on the neoclassical transport code PENTA, as shown in Chapter 4. Measurements presented in Chapter 5 show that the Reynolds stress seems to play an important role in the intrinsic rotation in QHS based on the gradients in the

locally measured Reynolds stress profile and their calculated contribution to the momentum balance. By extrapolating these local measurements of the Reynolds stress to a flux surface averaged value and solving for the flows in the momentum evolution equation, the saturated values of the inferred flows is many times larger than the observed flows.

Due to the variation in the locally measured Reynolds stress at two locations on a flux surface, however, a direct causal connection cannot be drawn between the Reynolds stress fluctuations and the observed flow. Measurements made at two different locations on the device differ greatly across the radial region where the probe measurements are made. This suggests that interpreting a flux surface average value of the Reynolds stress based on these two measurements is not possible without further modeling.

Contrary to expectations, measurements made in configurations with the quasi-symmetry intentionally broken exhibit deviations from the neoclassically calculated velocity profiles even larger than in the QHS configuration, while measured fluctuations are reduced, indicating that additional terms may be important in the momentum balance in these cases. In both the Mirror and Flip-1-4 configurations, the radial electric field and parallel flows were much larger than the values predicted by neoclassical calculations using PENTA, and the deviations from the neoclassical calculations were larger than those in the QHS configuration. This was not expected because both the neoclassical drive and damping terms for these configurations are larger for a value of  $E_r$  that deviates from the neoclassical solution than they are in the QHS configuration. The normalized fluctuations are also reduced in these plasmas relative to those in the QHS configuration, although the locally measured Reynolds stress profiles still imply significant drive if extrapolated to a flux surface average.

### 6.1.1 Possible additional sources of momentum

The large deviations of measured rotation from neoclassical calculations in configurations with the symmetry broken suggest that additional terms may be important in the momentum balance in these cases. A broad range of possible momentum sources aside from the Reynolds stress and neoclassical transport were discussed in Section 2.3, but the most likely candidates are ECRH-driven flux and additional non-ambipolar electron transport that is not properly modeled by DKES and PENTA.

Given that as the effective ripple was increased, the measured radial electric field became more-positive relative to the neoclassical prediction (as presented in Section 4.5), the most likely explanation for this observation is that there is additional electron particle flux that is not properly accounted for by the neoclassical modeling. One possible mechanism for this is increased ECRH-driven electron fluxes due to loss cones in velocity space as the ripple is increased. As particles are heated into these loss cones, they are quickly lost from the confined plasma, and this electron flux is not accounted for by PENTA when it predicts the solution for  $E_r$  which satisfies the ambipolarity constraint. As demonstrated by the ECE signals in Figure 2.10, non-thermal electron distributions were not observed in the plasmas which were studied in this work, but the ECRH-driven fluxes would not need to be large to account for the observed radial electric field. The ECRH absorption is expected to be small in the edge, but small non-ambipolar particle losses could lead to large flows, and this should be properly quantified.

Another possible cause of the observed rotation is thermal particle flux that is not appropriately modeled by DKES and PENTA, particularly near the last closed flux surface. Based on the measurements from LHD shown in Figure 2.5, neoclassical modeling does not accurately predict  $E_r$  near the plasma boundary, where the measured value of  $E_r$  is much more positive than the values calculated using the neoclassical ambipolarity constraint [63]. It may be that the ripple-trapped



particles that are lost collisionlessly in this region are not appropriately captured using simple diffusive models like DKES.

### **6.1.2 Implications for other devices**

For next-generation quasi-symmetric stellarator devices with significantly lower collisionality than that measured in HSX, it will be increasingly difficult to achieve non-neoclassical rotation. This is because at low collisionality, the non-ambipolar particle losses for experimentally realistic values of effective ripple and radial electric field become large compared to the flow drive generated by the Reynolds stress, as emphasized by Helander and Simakov [26] and described by the scaling in Section 2.5.1. This work could nonetheless inform experiments for next generation quasi-symmetric devices, if any were ever built. In a device with similar or lower effective ripple than HSX and only slightly lower collisionality than that in HSX, the Reynolds stress may still compete with the neoclassical term in the momentum balance.

For tokamaks with small non-axisymmetric components to the magnetic field, this work may also be a step toward providing a threshold for the amount of non-axisymmetric field that may be allowed while still enabling “free rotation” in the toroidal direction, particularly in the rippled edge. Predicting the rotation in future devices is extremely important for larger tokamaks, particularly ITER, which is expected to have rotation dominated by intrinsic flows [17]. Momentum transport and intrinsic rotation could potentially be an area of mutually beneficial collaboration between tokamaks and quasi-symmetric stellarators.

## **6.2 Suggestions for future work**

There are several directions that would need to be taken to advance this work beyond these initial studies. Some suggestions will be given here, starting with the most tractable and necessary work and moving toward the more difficult problems.

### 6.2.1 Quantify ECRH-driven electron flux

One important piece of physics that has been left out of this work is the contribution of ECRH-driven electron flux to the neoclassical particle transport and the impact that this has on the calculation of  $E_r$  using the ambipolarity constraint. Although the region of the plasma studied here is well outside the central deposition region, there may still be a meaningful amount of electron particle flux driven by the ECRH. This flux needs to be compared to the neoclassical radial current for a non-ambipolar  $E_r$  solution as calculated by PENTA so that it can either be ruled out as a contributing factor or included in the calculation of the ambipolar solution.

These calculations are especially important given the results from Section 4.5 showing that the measured values of  $E_r$  and  $V_{||}$  deviate from the neoclassical solutions more in configurations with the symmetry broken than they do in the QHS configuration. These flows are consistent with additional electron flux, and they are larger in the Mirror configuration than in the Flip-1-4 configuration. This could be an indication that increasing the ripple leads to increased ECRH-driven flux, and that this term is important to the momentum balance.

### 6.2.2 Parameter scans, measure flows using CHERS

When the gyrotron power supplies are upgraded to allow simultaneous heating with both gyrotrons injecting a total of 200 kW of ECRH into HSX, a broad parameter scan could be performed to measure the intrinsic flows across a range of collisionalities. Although it is difficult to perform experiments with Langmuir probes across a range of heating powers and collisionalities due to their sensitivity to suprathermal electrons, the CHERS system could be used to take measurements across a range of plasmas for comparison with neoclassical models and expectations for Reynolds stress drive. A parameter scan has been performed while measuring flows with CHERS in the QHS and Flip-1-4 configuration by Alexis Briesemeister using up to 100 kW of heating [69], but

including the Mirror configuration and doubling the heating power could greatly improve the understanding of the scaling of intrinsic rotation in HSX and under which conditions the Reynolds stress is important.

There are several momentum transport mechanisms to consider which may be important as heating power is increased. First is the direct ECRH-driven electron flux, which drives the plasma toward a more-positive value of  $E_r$  as discussed in the previous section. The next is the thermal neoclassical non-ambipolar particle flux, which would increase for radial electric fields that are not in agreement with the neoclassical ambipolarity condition, generating a larger drive back toward the PENTA-calculated solution.

The greater effect of increased heating, though, may be increased fluctuation levels which lead to an increase in the Reynolds stress drive term. In this case, regardless of the neoclassically calculated solution, one would expect the flows to be larger with additional heating than in the case with less heating.

Because each high-spatial resolution probe scan takes an entire run day using both probes, passive turbulence diagnostics such as the reflectometer and interferometer could be used to monitor the turbulence during the parameter scan. If there is an interesting phenomenon, then it may be useful to take more measurements using the Reynolds stress probes to further investigate the physics in the interesting cases.

### **6.2.3 Gyrokinetic Reynolds stress simulations**

Work performed at DIII-D compared measured poloidal rotation velocities with neoclassical theory, as well as with a gyrokinetic model for the Reynolds stress and a model which accounted for fast ion friction [152]. It was found that the measured poloidal rotation generally agreed well with neoclassical theory when there was sheared flow present, but did not agree well at all with

neoclassical calculations or with the calculated Reynolds stress when the turbulence was not suppressed.

If similar simulations could be run for HSX, then comparisons could be made to measurements of both the Reynolds stress using probes at the edge as well as the radial electric field throughout the plasma using CHERS. This would need to be done using the fully 3D gyrokinetic code GENE [153] has been developed for stellarators. GENE has recently been expanded to include a full flux surface version [154], which simulates an entire flux surface rather than single flux tubes at a time, since each flux tube of a stellarator is unique. This project may also involve some code development in order to extract the local fluctuating velocity components from the saturated turbulence and calculate the total flux surface averaged Reynolds stress from this.

From these gyrokinetic simulations, several experimentally relevant parameters could be extracted. First, the Reynolds stress at the two locations of the probe could be calculated using two flux tube simulations to compare against the experimentally measured values. If these calculated velocity fluctuations were found to agree reasonably well with experiment, then the full surface calculation could be performed. The experimentally measured quantities could then be extrapolated based on the calculated contribution of the local Reynolds stress to its total flux surface average value. The intrinsic torque due to the flux surface averaged Reynolds stress could also be calculated directly for any set of surfaces that were simulated. However, because a radial gradient is needed for this calculation, at least two nearby surfaces would need to be simulated for this last calculation, and radial coupling may be important, which is not included in the simulations.

These calculations would be very computationally expensive. In order to properly model the Reynolds stress torque, each surface would need to be simulated using a full-flux surface calculation with kinetic electrons and ions to simulate the trapped electron mode. Simulating two flux tubes starting at the two probe locations, on the other hand, would be tractable on a relatively short

timescale. This would be a good starting point toward comparing measurements to gyrokinetic modeling.

#### 6.2.4 Add ion heating

In the event of an upgrade to the HSX device that included either neutral beam injection or ICRH to heat ions, studies of the intrinsic rotation in HSX could be significantly expanded. First, the role of neoclassical non-ambipolar transport in the momentum balance would be expected to be larger if ions entered the low collisionality regime. Additionally, by scaling the ion to electron heating, the transition from TEM-dominated turbulence to an ITG-dominant regime could be explored. If the turbulence and resultant Reynolds stress are indeed responsible for the intrinsic flows in HSX, one would expect this transition in the dominant instability to coincide with a change in the flow profile in HSX. This is the mechanism invoked for core rotation reversals in the Alcator C-Mod tokamak [120].

To study intrinsic rotation in HSX heated by neutral beams, the injected torque using multiple beams would need to be carefully balanced. Using unbalanced neutral beam injection, the residual stress component of the Reynolds stress could be measured experimentally by attempting to cancel out the intrinsic flows, similar to the experiments in DIII-D [89] discussed in Section 2.3.1.

With neutral beam heating, the Reynolds stress measurements may also be made without having to use Langmuir probes by implementing a Beam Emission Spectroscopy (BES) system. This would allow more spatial coverage of the diagnostic and would not be as perturbative to the plasma as the Langmuir probes. The density in HSX could also be increased if NBI-heated discharges were not limited by the ECRH cutoff density. Among other things, this would decrease the neutral penetration and most likely reduce the turbulent particle flux that complicates the analysis of the Reynolds stress, as discussed in Section 5.1.3.

This chapter has provided a summary of the work in this document and suggested directions for future work to expand on the progress made here. Turbulent momentum transport is an important area of study in both tokamaks and quasi-symmetric stellarators, and understanding the competition between neoclassical and turbulent components of the momentum balance is crucial to predicting and controlling rotation in future devices.

## References

17. Shimada, M, Campbell, D. J., Mukhovatov, V, *et al.* ITER Physics Basis, Chapter 1: Overview and summary. *Nuclear Fusion* **47**, S1–S17 (2007).
26. Helander, P. & Simakov, A. Intrinsic Ambipolarity and Rotation in Stellarators. *Physical Review Letters* **101**, 145003 (2008).
63. Matsuoka, S., Satake, S., Yokoyama, M. & Wakasa, A. Radial Electric Field Formation Including Electron Radial Drift for a Core Electron-Root Confinement (CERC) Plasma in LHD. *Plasma and Fusion Research* **6**, 1203016 (2011).
69. Briesemeister, A. *Alexis Briesemeister's Dissertation, University of Wisconsin - Madison* 2013.
89. Solomon, W. M., Burrell, K. H., Garofalo, A. M., *et al.* Advances in understanding the generation and evolution of the toroidal rotation profile on DIII-D. *Nuclear Fusion* **49**, 085005 (2009).
120. Rice, J. E., Cziegler, I., Diamond, P. H., *et al.* Rotation Reversal Bifurcation and Energy Confinement Saturation in Tokamak Ohmic L-Mode Plasmas. *Physical Review Letters* **107**, 265001 (2011).
152. Chrystal, C. in (Presented at the 55th APS-DPP Annual Meeting, Denver, CO, 2013).
153. Jenko, F., Dorland, W., Kotschenreuther, M. & Rogers, B. N. Electron temperature gradient driven turbulence. *Physics of Plasmas* **7**, 1904 (2000).
154. Helander, P, Beidler, C. D., Bird, T. M., *et al.* Stellarator and tokamak plasmas: a comparison. *Plasma Physics and Controlled Fusion* **54**, 124009 (2012).

## Appendix A: Zonal flows

Zonal flows are radially localized perpendicular flows that are driven by turbulence, which also act as the nonlinear saturation mechanism for some turbulent micro-instabilities. A linearized theory of electrostatic turbulence driving poloidal rotation was first derived by Hasegawa and Wakatani [78]. For those interested in a more thorough discussion, Reference [155] is a good theoretical review of zonal flows in plasmas and their effects on confinement.

In the poloidal plane, zonal flows are driven by 3-wave coupling between high- $k$  fluctuations and the low- $k$  zonal mode. The wave momentum in this 3-wave coupling process follows the conservation rule  $k_1 + k_2 = k_3$ , where  $k_3$  is the wave number of the resulting mode. If  $k_1 \approx -k_2$ , then the resulting fluctuation will be a long wavelength mode near the scale size of the system. This is the case of zonal flows in a torus, which results in the  $n=0, m=0$  zonal flow mode, localized radially with a finite radial wavenumber  $k_r$ . The radial wavelength is on the order of a few ion gyroradii. Although the zonal flow is zero-frequency, this mode has a finite spectral width, determined by collisional damping, which allows it to be observed by looking for coherent potential fluctuations at low frequencies at multiple points on a flux surface [156]. Zonal flows do not lead to transport, as opposed to the turbulent modes that drive them, and they therefore act as a benign energy dump for the free energy source which does not flatten the temperature or density gradients.

One of the theories of L-H transitions also suggests that these zonal flows are (at least partially) responsible for the initial poloidal rotation which leads to an increase in the pressure gradient that triggers a confinement transition near the separatrix [79, 157, 158]. Experiments have found evidence that this mechanism may play a role in spontaneous confinement transitions using bicoherence analysis [159] in both tokamaks [160] and stellarators [161, 162]. While there are other theories for spin-up mechanisms which trigger L-H transitions, such as ion orbit loss [95] or



Stringer spin-up [163], it is important to note that these mechanisms are not necessarily mutually exclusive, and that the initial radial electric field required for the confinement bifurcation to occur may be the result of any combination of sources.

In tokamaks, zonal flow modes consist of two branches: a zero frequency component that is often what people intend when they refer generically to zonal flows [164], and a finite frequency GAM (geodesic acoustic mode) component [165]. In a stellarator with multiple terms in the magnetic spectrum, another branch of the zonal flow, distinct from the GAM, appears as low frequency oscillations which may also be observed experimentally [166].

## A.1 Zonal flows in HSX

Because of the expected beneficial effects of zonal flows on confinement, the existence of zonal flows in HSX was investigated in order to study the effects of quasi-symmetry on zonal flow formation and damping. As discussed in Section 1.3.1, it has been predicted that non-axisymmetric magnetic configurations with reduced neoclassical transport may also have reduced anomalous transport through an enhanced zonal flow response relative to unoptimized configurations [36]. This is because in unoptimized stellarators, the non-zero average radial drift of electrons in helical ripples leads to the zonal potential being effectively shorted out. Experiments to test this hypothesis have been performed in HSX, where long-range correlations indicative of zonal flows were observed during biasing [40]. The goal was to test whether or not the zonal flow response is greater in the QHS configuration than in a similar configuration with the quasi-symmetric optimization broken (in this case, the “Flip-1-4” configuration was used, rather than the “Original Mirror” configuration).

Results of the configurational comparison were inconclusive, with similar long-range correlations and broadband bicoherence of  $E_\theta$  fluctuations being detected in both configurations during biasing, and neither being observed before the applied bias. It is suspected that the results of the

two configurations were similar because the large  $E_r$  that was imposed in order to excite these signatures eliminated the difference between the neoclassical particle fluxes between the two configurations. No signatures of zonal flows have been detected in HSX without the imposition of a large  $E_r$  with a bias probe. This is an indication that measured radial electric fields in the edge of HSX are due to mean flows as opposed to radially localized zonal modes. What follows in this section is a brief review and further analysis of the experimental results from [40].

### A.1.1 Auto-bicoherence of $E_\theta$ fluctuations

Bicoherence analysis can be used to find indications of 3-wave coupling between drift waves and zonal flows [167]. The idea is to look directly at local fluctuating electric field and density quantities and calculate the coherence of 3-wave couplings in the search for coupling to the near-zero frequency branch of the zonal flow.

By measuring the differential floating potential at two Langmuir probe pins poloidally separated on a surface (similar to the setup and methods used to measure  $E_\theta$  in Section 3.2, although using a different set of probes), the auto-bispectrum of poloidal electric field fluctuations can be determined using the expression

$$B(\omega_1, \omega_2) = \hat{X}^*(\omega) \hat{X}(\omega_1) \hat{X}(\omega_2), \quad (\text{A.1})$$

where  $\hat{X}$  is the Fourier transform of the signal,  $\hat{X}^*$  is the complex conjugate of  $\hat{X}$ , and  $\omega = \omega_1 + \omega_2$  is the sum frequency of the fluctuations to which coupling is being calculated. From this, the auto-bicoherence is then obtained as

$$b^2(\omega_1, \omega_2) = \frac{|\langle B(\omega_1, \omega_2) \rangle|^2}{\langle |\hat{X}(\omega)|^2 \rangle \langle |\hat{X}(\omega_1) \hat{X}(\omega_2)|^2 \rangle}, \quad (\text{A.2})$$

where the brackets indicate an average over realizations.

In both the experiments performed here and at TJ-II [161], fluctuations in the poloidal electric field quantities were found to exhibit auto-bicoherence above the noise level, while no meaningful

levels of cross-bicoherence (above the noise) were found between any two sets of fluctuating probe signals. The auto-bicoherence of  $E_\theta$  fluctuations both before and after biasing at several radial locations in QHS plasmas is plotted in Figure A.1.

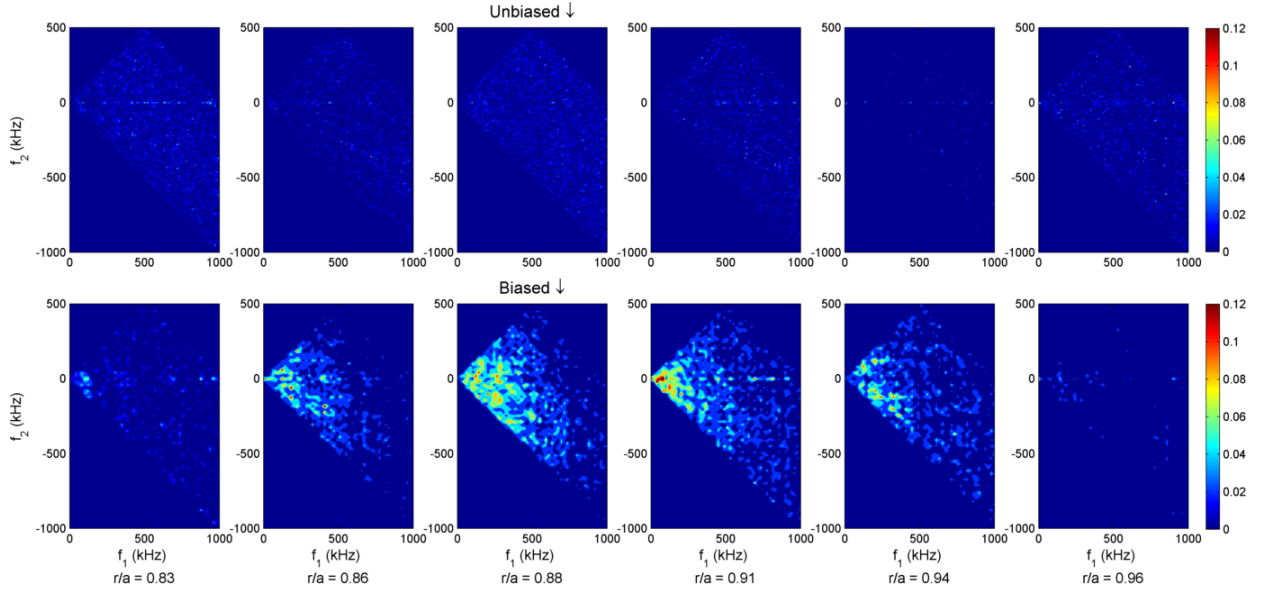


Figure A.1 Auto-bicoherence of  $E_\theta$  fluctuations at several radial locations in QHS, both with (top) and without (bottom) an applied bias.

Before the bias is applied, there is no measurable 3-wave coupling in the poloidal plane significantly above the noise level (0.005). Once the bias is applied, the  $E_\theta$  fluctuations show signs of broadband bicoherence, but no coupling to a coherent mode at low frequencies are observed as one would expect for a zonal flow. No meaningful difference was observed between the data measured in these QHS plasmas and those measured in the Flip-1-4 configuration. This is also the same pattern of broadband bicoherence which was observed in biased discharges in TJ-II [161].

For a comparison of what one might expect to see if there were signatures of 3-wave coupling to a zonal flow mode, a plot of the auto-bicoherence of  $E_\theta$  in a TJ-II discharge during a spontaneous confinement transition is given in Figure A.2(a) [161], and the auto-bicoherence of  $I_{\text{sat}}$  signals during an L-H transition in the tokamak CCT is shown in Figure A.2(b) [160].

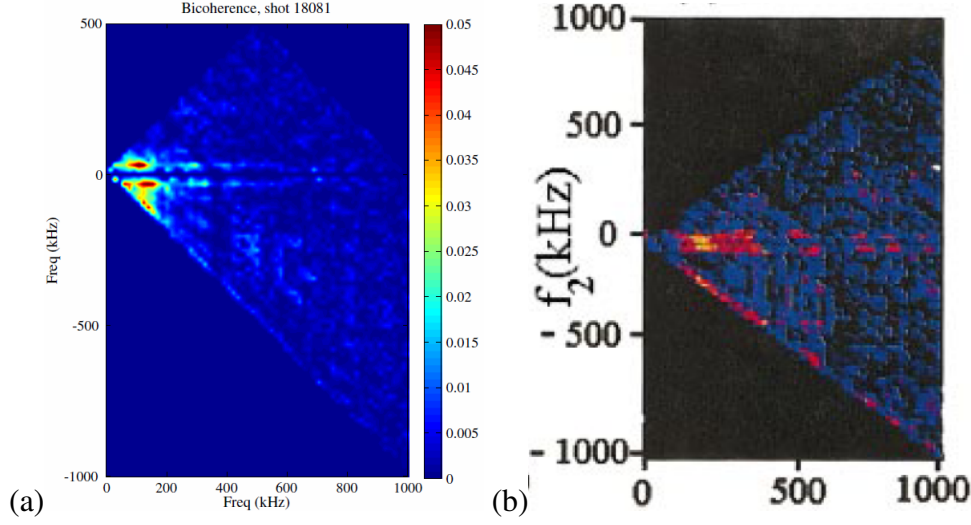


Figure A.2 Auto-bicoherence of fluctuations for discharges more indicative of zonal flows in (a)  $E_\theta$  signals in TJ-II [161] and (b)  $I_{\text{sat}}$  signals in CCT [160].

The TJ-II and CCT data demonstrate the higher coherence of 3-wave interactions which sum to the near-zero frequency zonal flow. This is manifested as brighter lines in regions where some combination of  $\omega_1$  on the x-axis,  $\omega_2$  on the y-axis, and the sum frequency  $\omega_1 + \omega_2$  sum to approximately zero. This coupling to a coherent mode is not evident in any of the HSX data shown in Figure A.1. There is no spontaneous confinement transition in the HSX discharges, though, which is when the behavior in Figure A.2 is observed, so this type of coupling may not be expected.

### A.1.2 Long-range correlations

Using Langmuir probes to measure the floating potential at two different points on a flux surface, separated both toroidally and poloidally, long range correlations of potential fluctuations were observed during biasing, but not before the bias was applied. This was done during the same set of discharges as the data used above in Section A.1.1. A reference probe was left stationary in a single radial location as the second probe was scanned radially across the edge region. Figure A.3 plots the power spectra of the scanning probe, the relative phase and the coherence of low frequency ( $<10$  kHz) floating potential fluctuations between the two distantly separated Langmuir probe pins

as the scanning probe was moved radially. This radial scan is performed on a shot-by-shot basis in the same manner as the data presented in Chapters 4 and 5, with similarly repeatable discharges. The radial location of the fixed reference probe is indicated by a dotted line. Phase wrapping is used to smooth the phase plots, which leads to values slightly higher than  $\pi$  in some cases.

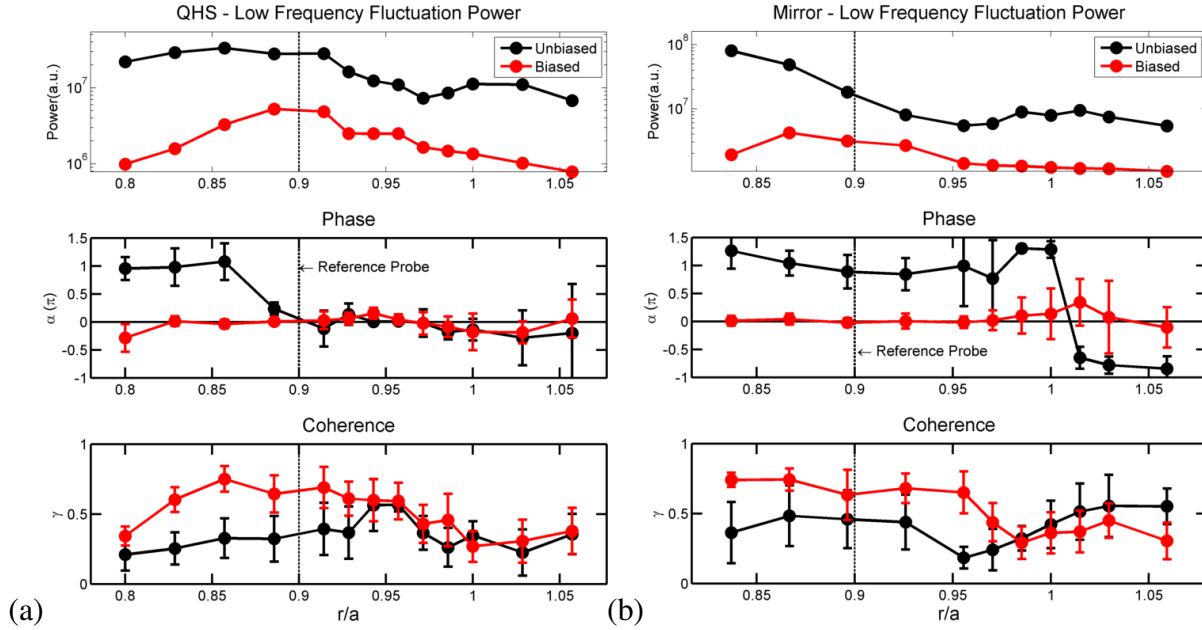


Figure A.3 Long-range correlations of low-frequency fluctuations between a scanning probe potential and a stationary reference probe on the far side of the machine in the (a) QHS and (b) Mirror (FL14) configurations. All values are for fluctuations  $< 10$  kHz.

Before the bias is applied, the coherence is at or below the noise level ( $\sim 0.3$ ), which makes the measured phase of the fluctuations meaningless in those cases. When the bias is applied, the phase of the low frequency fluctuations goes approximately to zero, and the coherence increases significantly above the noise level.

As with the bicoherence results, there is no qualitative difference between the data in the QHS and Mirror configurations for the biased fluctuation data with high coherence. One might expect that any difference in particle orbits, neoclassical transport or intrinsic flows between the two configurations may be overwhelmed by the effects of the applied bias. If intrinsic zonal flows

were ever detected in HSX without applying a bias, then revisiting these experiments to determine the effects of the magnetic configuration on the zonal flows could be useful. It may be the case that even relatively small deviations from quasi-symmetry on the scale of those in HSX's QHS configuration are enough to prevent the build-up of zonal potential and the development of zonal flows.

## A.2 GAMs in HSX

Because zero-frequency zonal flows are notoriously difficult to observe and study, the finite-frequency GAM (geodesic acoustic mode) [165] can be used as a more experimentally accessible observation for testing zonal flow theories. This mode is not expected to be beneficial to confinement in the same way as the zero-frequency branch of the zonal flow, however.

In a tokamak, GAM oscillations arise from the poloidal asymmetry of the  $E \times B$  flow. The poloidal velocity  $v_\theta$  is larger on the high field side than it is on the low field side, causing a poloidal pressure gradient (up-down in a tokamak,  $\tilde{p} \propto \sin(\theta)$ ). This  $\nabla \tilde{p} \times \vec{B}$  leads to a perturbed radial polarization current  $\tilde{j}_r$ , which in turn drives a poloidal rotation  $\tilde{v}_\theta$  in the opposite direction as the initial perturbation. By equating the polarization current of this flow to the perturbed  $\tilde{j}_r$ , a differential equation describing GAM oscillations can be obtained as [168]

$$\frac{d^2 E_r}{dt^2} + \omega_{GAM} E_r = 0, \quad (\text{A.3})$$

where, in a tokamak, the GAM frequency is

$$\omega_{GAM} = \frac{1}{R_0} \sqrt{\frac{\xi_1 T_i + \xi_2 T_e}{m_i}}, \quad (\text{A.4})$$

with  $\xi_1 \approx \xi_2 \approx 1$ . The damping rate scales like  $\gamma \sim \omega_{GAM} e^{-q^2}$ , and comes collisionlessly from ion Landau damping.

While fundamentally similar, GAM oscillations in stellarators are generally more complicated than in tokamaks due to the complex magnetic mode structure. With quasi-symmetry, however,

there is only a single dominant harmonic to consider in the magnetic spectrum. Watari et. al. have formulated an approximation for a system with a single helicity in which the real frequency can be described by [169]

$$\omega_{GAM}^2 = \left(T_e + \frac{7}{4}T_i\right) M^2 \frac{b_{M,N}^2}{2rm_i} + \xi k_{||,M,N}^2 v_{Ti}^2, \quad (A.5)$$

with

$$\xi \equiv \frac{(T_e + \frac{23}{8}T_i)}{(T_e + \frac{7}{4}T_i)} \approx 1 \quad (A.6)$$

and

$$k_{||,M,N} = \frac{1}{B_0}(MB^\theta - NB^\zeta), \quad (A.7)$$

where  $r$  is the average local minor radius,  $b_{M,N}$  is the amplitude of the dominant harmonic, and  $M$  and  $N$  are the poloidal and toroidal mode numbers, respectively. The collisionless damping rate is then expressed as

$$\gamma_{GAM} = \frac{\sqrt{\pi}}{2\sqrt{2\left(\frac{T_e}{T_i} + \frac{7}{4}\right)}} \omega_{GAM} \zeta_{M,N} \left(\zeta_{M,N}^4 + \zeta_{M,N}^2 + \frac{1}{2}\right) \exp(-\zeta_{M,N}^2), \quad (A.8)$$

with the parameter  $\zeta_{M,N}$  defined as

$$\zeta_{M,N}^2 = \frac{\omega^2}{k_{||,M,N}^2 v_{Ti}^2}. \quad (A.9)$$

Using the Watari single helicity approximation from Equations A.5 and A.8 for the  $n=4$ ,  $m=1$  helicity in HSX, the GAM frequency and damping rates are plotted in Figure A.4. A standard high density 50 kW QHS plasma profile was assumed for this calculation, with measured electron temperatures from Thomson scattering peaked at  $\sim 900$  eV on axis down to  $\sim 60$  eV at  $r/a=0.9$ , and densities ranging from  $\sim 5 \times 10^{18} \text{ m}^{-3}$  in the core to  $\sim 1 \times 10^{18} \text{ m}^{-3}$  at the edge. Both collisional and collisionless mechanisms are capable of dominating GAM damping.

As demonstrated in Figure A.4, the collisionless damping rate of GAM oscillations is larger than the mode frequency across most of the minor radius in HSX. Unless the mode were strongly

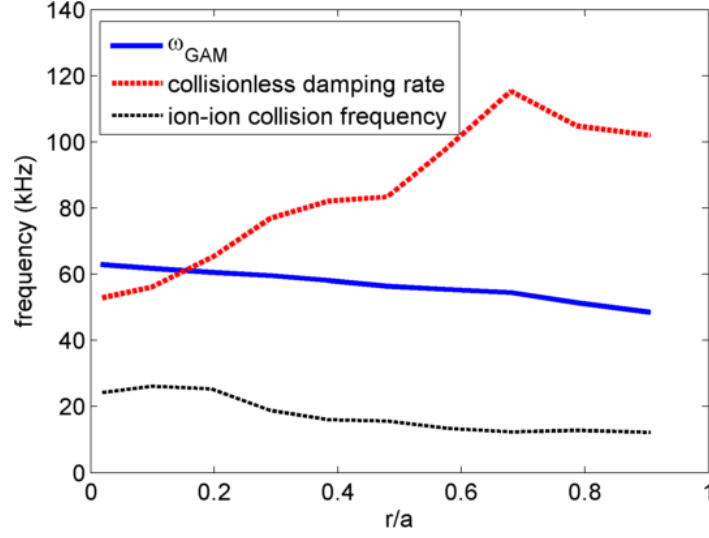


Figure A.4 GAM oscillation frequency and damping rate in HSX using the Watari single helicity model with a standard QHS plasma profile.

driven, this would most likely lead to the oscillating mode being unobserved in the plasma. This result is robust across many different plasma profiles, and is consistent with the lack of observations of GAMs on any of the diagnostics in HSX. It is also consistent with nonlinear gyrokinetic results predicting that the perturbed potential on a surface would damp away directly to the residual flow rather than oscillating at the GAM frequency during the damping phase.

From Equation A.8, the GAM damping goes like  $\sim e^{-(1/\iota)^2}$ . Because HSX has a high “effective” rotational transform,  $\iota_{eff} = |n - m\iota| = 4 - \iota \approx 3$ , this leads to a large damping rate relative to a similar tokamak. Helical ripples also enhance the GAM damping [170].

If there were to be GAM oscillations in HSX, they would be expected to appear as a coherent mode in both density and potential in the  $\sim 40$ - $60$  kHz range. The mode of the density fluctuations would be expected to follow the  $|B|$  contours of the magnetic field, and therefore have an  $n=4$ ,  $m=1$  spatial mode structure. The oscillating potential would have an  $n=0$ ,  $m=0$  mode structure, just like the zero frequency zonal flow.



## References

36. Sugama, H. & Watanabe, T. Dynamics of Zonal Flows in Helical Systems. *Physical Review Letters* **94**, 115001 (2005).
40. Wilcox, R. S., van Milligen, B. P., Hidalgo, C., *et al.* Measurements of bicoherence and long-range correlations during biasing in the HSX stellarator. *Nuclear Fusion* **51**, 083048 (2011).
78. Hasegawa, A. & Wakatani, M. Self-Organization of Electrostatic Turbulence in a Cylindrical Plasma. *Physical Review Letters* **59**, 1581 (1987).
79. Diamond, P. H. & Kim, Y. Theory of mean poloidal flow generation by turbulence. *Physics of Fluids B* **3**, 1626 (1991).
95. Shaing, K. C. & Crume, E. C. J. Bifurcation Theory of Poloidal Rotation in Tokamaks: A Model for the L-H Transition. *Physical Review Letters* **63**, 2369 (1989).
155. Diamond, P. H., Itoh, S. I., Itoh, K. & Hahm, T. S. Zonal flows in plasma - a review. *Plasma Physics and Controlled Fusion* **47**, 35–161 (2005).
156. Hahm, T. S., Burrell, K. H., Lin, Z., Nazikian, R. & Synakowski, E. J. Zonal flow measurements concept I. *Plasma Physics and Controlled Fusion* **42**, A205 (2000).
157. Diamond, P. H., Liang, Y., Carreras, B. A. & Terry, P. W. Self-Regulating Shear Flow Turbulence: A Paradigm for the L to H Transition. *Physical Review Letters* **72**, 2565 (1994).
158. Carreras, B. A., Newman, D., Diamond, P. H. & Liang, Y. Dynamics of low to high ("L" to "H") confinement bifurcation: Poloidal flow and ion pressure gradient evolution. *Physics of Plasmas* **1**, 4014 (1994).
159. Ritz, C. P., Powers, E. J. & Bengtson, R. D. Experimental measurement of three-wave coupling and energy cascading. *Physics of Fluids B: Plasma Physics* **1**, 153 (1989).

160. Tynan, G. R., Moyer, R. A., Burin, M. J. & Holland, C. On the nonlinear turbulent dynamics of shear-flow decorrelation and zonal flow generation. *Physics of Plasmas* **8**, 2691 (2001).
161. van Milligen, B. P., Kalhoff, T., Pedrosa, M. A. & Hidalgo, C. Bicoherence during confinement transitions in the TJ-II stellarator. *Nucl. Fusion* **48**, 115003 (2008).
162. Shats, M., Solomon, W. & Xia, H. Turbulent Transport Reduction and Randomization of Coherent Fluctuations by Zonal Flows in Toroidal Plasma. *Physical Review Letters* **90**, 125002 (2003).
163. Hassam, A. B., Antonsen, T. M. J., Drake, J. F. & Liu, C. S. Spontaneous Poloidal Spin-Up of Tokamaks and the Transition to H Mode. *Physical Review Letters* **66**, 309 (1991).
164. Hinton, F. L. & Rosenbluth, M. N. Dynamics of axisymmetric and poloidal flows in tokamaks. *Plasma Physics and Controlled Fusion* **41**, A653 (1999).
165. Winsor, N., Johnson, J. L. & Dawson, J. M. Geodesic Acoustic Waves in Hydromagnetic Systems. *Physics of Fluids* **11**, 2448 (1968).
166. Helander, P., Mishchenko, A., Kleiber, R. & Xanthopoulos, P. Oscillations of zonal flows in stellarators. *Plasma Physics and Controlled Fusion* **53**, 054006 (2011).
167. Diamond, P. H., Rosenbluth, M. N., Sanchez, E., *et al.* In search of the elusive zonal flow using cross-bicoherence analysis. *Physical Review Letters* **84**, 4842 (2000).
168. Watari, T., Hamada, Y., Notake, T., Takeuchi, N. & Itoh, K. Geodesic acoustic mode oscillation in the low frequency range. *Physics of Plasmas* **13**, 062504 (2006).
169. Watari, T., Hamada, Y., Fujisawa, A., Toi, K. & Itoh, K. Extension of geodesic acoustic mode theory to helical systems. *Physics of Plasmas* **12**, 062304 (2005).
170. Sugama, H. & Watanabe, T. Collisionless damping of zonal flows in helical systems. *Physics of Plasmas* **13**, 012501 (2006).

## Appendix B: Alternative configurations in HSX

The original “symmetry breaking” configuration for HSX (referred to as “Mirror” in this work and “Old Mirror” in some codes and documentation), was designed to introduce the largest possible perturbation to the magnetic spectrum, which is easiest to do with low mode numbers [35]. This configuration predominantly introduces a single, large amplitude  $n=4$ ,  $m=0$  harmonic to the magnetic spectrum.

Unfortunately, this configuration poses a problem when doing core transport studies, because the Thomson scattering beam line and diagnostic neutral beam are statically positioned to pass through the axis in the QHS configuration, and the axis shifts inward with this “Original Mirror” configuration. Therefore, a new configuration was implemented for core transport studies which aligned the axis with the static diagnostics. This configuration, internally dubbed the “Flip-1-4” configuration, has been referred to somewhat ambiguously as the “Mirror” configuration in subsequent HSX publications [40, 115].

In this work, one of the differences that was investigated between the optimized quasi-symmetric configuration and the Original Mirror configuration was the level of non-ambipolar neoclassical particle transport. The neoclassical particle transport can be described for a thermalized plasma in the long mean free path regime using the effective ripple parameter,  $\epsilon_{eff}$  [110], as discussed in Section 2.4.1. In this appendix, the effective ripple in several configurations is calculated to determine which configuration provides the largest change in neoclassical transport compared to QHS.

### B.1 Stellarator symmetric configurations

For both computational as well as experimental purposes, the auxiliary coils in HSX are normally energized in a stellarator symmetric fashion, such that each half field period remains the

same as every other. The polarities of some of the most relevant stellarator symmetric configurations are given in Table B.1. While it would be best for this work to select a configuration which holds the rotational transform relatively constant, the Hill and Well configurations are included for completeness.

Table B.1 Aux coil polarity for stellarator symmetric configurations.

<b>Configuration</b>	<b>1</b>	<b>2</b>	<b>3</b>	<b>4</b>	<b>5</b>	<b>6</b>
Old Mirror	+	+	+	-	-	-
Flip 1-4	-	+	+	+	-	-
Flip 3-6	+	+	-	-	-	+
Every Other Coil	+	-	+	-	+	-
Hill	+	+	+	+	+	+
Well	-	-	-	-	-	-

The “Every other coil” configuration given here introduces dominantly high mode number perturbations to the magnetic spectrum ( $n=24$ ). There is no reason to expect this configuration to greatly increase transport relative to the other configurations, but it is presented as an example of what happens with arbitrary configurations which are not targeted toward low mode number perturbations.

The effective ripple for each of the configurations listed in table B.1 is plotted in figure B.1. 11% of the main coil current is used as the auxiliary coil current for each configuration except the 9% Well case, which is the standard operating point for that configuration. The “anti-” configurations, plotted as dashed lines, have the polarity for each coil reversed.

Figure B.1 shows that the “Old Mirror” configuration has the largest effective ripple of any of the configurations tested. While the effective ripple of the “anti-Old Mirror” configuration is slightly higher than the standard version, this configuration has poor ECRH absorption due to a

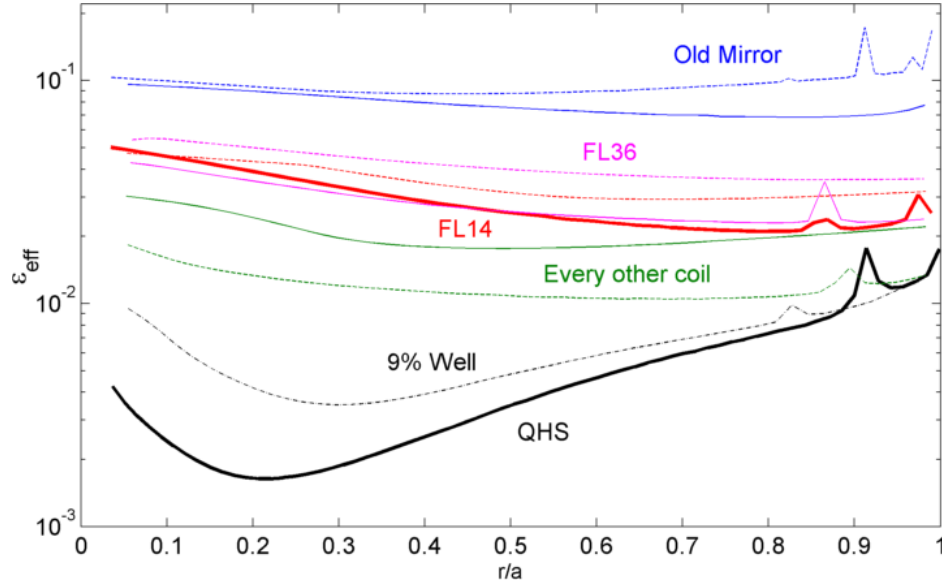


Figure B.1 Effective ripple for several configurations in HSX. Solid lines are the standard configuration, dashed are the “anti-” configuration, with the polarities of all aux coils reversed.

magnetic well in the ECRH deposition region [171]. The effective ripple calculation shown here uses a line following routine which is not valid near rational surfaces, leading to the spikes in each configuration around  $r/a \approx 0.9$  near the surface where the rotational transform is  $12/11$ . The 6% Hill configuration which is sometimes used is excluded from figure B.1 due to the presence of large islands which encompass much of the plasma volume.

## B.2 Non-stellarator symmetric configurations

The planar auxiliary coils in HSX are aligned with the main modular coils, meaning that they predominantly influence the toroidal mode structure. Relaxing the constraint of stellarator symmetry allows for large amplitude, low mode number toroidal harmonics to be introduced to the magnetic spectrum, which increases non-ambipolar particle fluxes beyond the level of stellarator symmetric terms.

Because the standard field solver for HSX, “grid interp” [172], uses stellarator symmetry to reduce computational time, an additional database of field values using non-stellarator symmetric coil sets was generated for the grid interp routine and implemented for these calculations.

### **B.2.1 $n=1$ perturbation**

The neoclassical transport scales with the magnitude of the non-quasi-symmetric modes squared, so the perturbations to the magnetic field which drive the most neoclassical transport are the long wavelength ones which can be pumped up to large magnitudes. The  $n=1$ ,  $m=0$  mode is the longest wavelength mode that may be produced with the HSX auxiliary coils, and would be expected to drive the most neoclassical transport for a given amount of auxiliary coil current. To generate a configuration where this mode is dominant, 24 aux coils on one half of the machine are energized to increase the magnitude of the field generated by the main coils, and the 24 on the other half are energized to decrease the field.

Unfortunately, when the coils are energized with the standard amount of current for an auxiliary configuration (11% of the main coil current), the additional torsion of the surfaces causes the field lines to get too close to the coils and they no longer form closed flux surfaces. The aux coil current must be reduced to  $\sim 5\%$  to get any closed surfaces at all, and at  $\sim 2.5\%$  aux coil current, there is enough volume that heat deposition would be feasible and most diagnostics could be effective at measuring the relevant quantities. The surfaces for this 2.5%  $n=1$  configuration are plotted along with the vessel in Figure B.2 for toroidal slices at the boxports ( $\phi=0$ , right) and joint flanges ( $\phi=\pi/4$ , left). The toroidal location of each cross section is relatively arbitrary, since the phase of the  $n=1$  perturbation could be oriented to align any particular cross section in any field period.

While minor changes to the configuration could be made by changing where the node of the  $n=1$  perturbation was made (e.g., between coils 1 and 2 instead of at the boxport), this phase shift does not qualitatively change any of the results explained here.

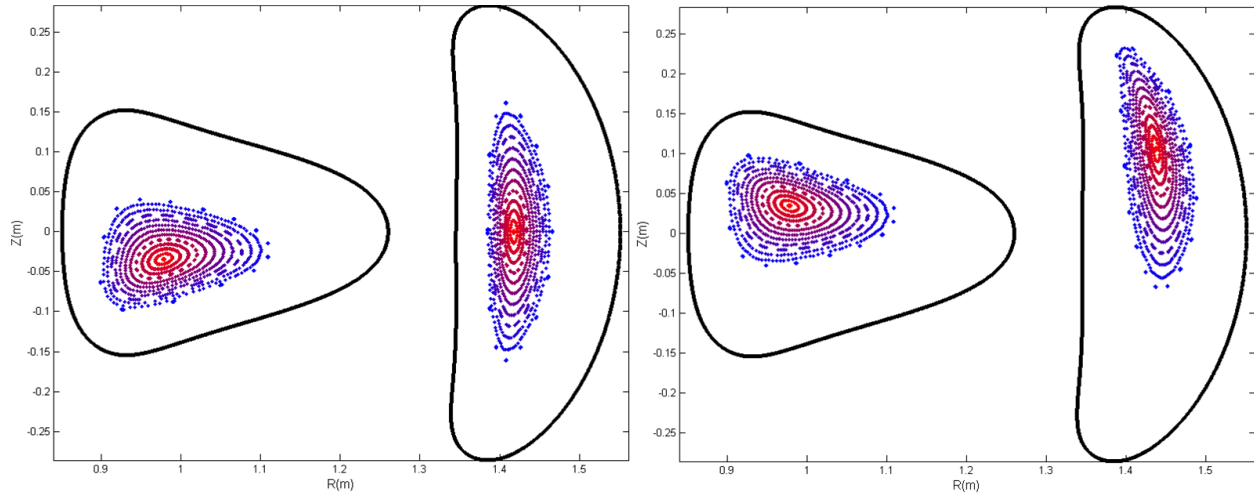


Figure B.2 Poincaré plots for 2.5%  $n=1$  configuration.

### B.2.2 $n=2$ perturbation

Another configuration worth investigating is one with an  $n=2$  ( $m=0$ ) perturbation to the main field. This has the advantage of introducing a longer-wavelength term to the spectrum than the stellarator symmetric  $n=4$  one which the standard Mirror configuration excites, while moving the surfaces less in real space compared to the  $n=1$  configuration discussed above. Poincaré plots at the boxports and joint flanges of HSX for a magnetic configuration with an  $n=2$  perturbation using the standard 11% of the main coil current are given in Figure B.3.

Because this configuration again sacrifices much of the plasma volume, a configuration using only 5% of the main field coil current in the auxiliary coils can be investigated to find if it would sufficiently break the symmetry while leaving more of the plasma volume intact as closed surfaces.

To compare these non-stellarator symmetric configurations, the effective ripple has been calculated for each and plotted alongside the effective ripple of standard stellarator symmetric configurations in Figure B.4. Here the minor radial locations of each configuration are normalized to the last closed surface, so that the change in volume for each configuration is not reflected in the radial coordinate.

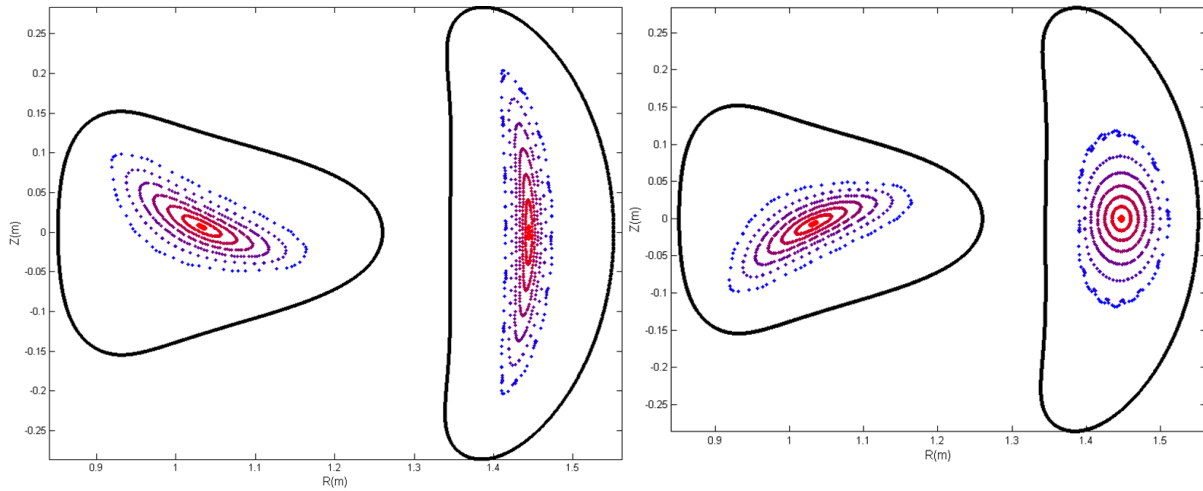


Figure B.3 Poincare plots for 11%  $n=2$  configuration.

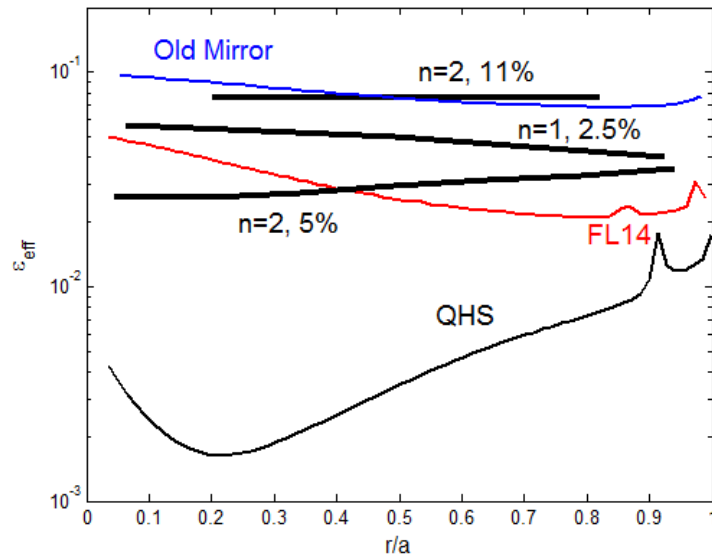


Figure B.4 Effective ripple for non-stellarator symmetric configurations.

As seen in figure B.4, the only non-stellarator symmetric configuration that increases the effective ripple as much as the “Old Mirror” configuration used throughout this work is the 11%  $n=2$  configuration. However, because the volume is reduced and the surfaces move substantially, which greatly affects diagnostic access, this is not a sufficient improvement to justify using it for these experiments as opposed to the standard Mirror configuration.



Due to the large aspect ratio and torsion of the axis of HSX, as well as the closeness of the coils and vessel to the confinement region, any non-stellarator symmetric perturbation to the designed field leads to a reduction in volume, because the additional torsion moves the plasma toward the vessel and coils. It was therefore determined that for this thesis, the “Original Mirror” configuration is the best option for a configuration which breaks the symmetry as much as possible.

## References

35. Gerhardt, S., Talmadge, J. N., Canik, J. & Anderson, D. T. Experimental Evidence of Reduced Plasma Flow Damping with Quasisymmetry. *Physical Review Letters* **94**, 015002 (2005).
40. Wilcox, R. S., van Milligen, B. P., Hidalgo, C., *et al.* Measurements of bicoherence and long-range correlations during biasing in the HSX stellarator. *Nuclear Fusion* **51**, 083048 (2011).
110. Nemov, V. V., Kasilov, S. V., Kernbichler, W. & Heyn, M. F. Evaluation of  $1/\nu$  neoclassical transport in stellarators. *Physics of Plasmas* **6**, 4622 (1999).
115. Canik, J. M., Anderson, D. T., Anderson, F. S. B., *et al.* Reduced particle and heat transport with quasisymmetry in the Helically Symmetric Experiment. *Physics of Plasmas* **14**, 056107 (2007).
171. *Private communications with Konstantin Likin*, 2014.
172. Probert, P. High-Performance Interpolation of Stellarator Magnetic Fields. *IEEE Transactions on Plasma Science* **39**, 1051–1054 (2011).